# Zeolitic Imidazolate Framework-8: Control of Particle Size and Shape and its Self-Assembly

**Civan Avci**

Universitat Autònoma de Barcelona

# Zeolitic Imidazolate Framework-8: Control of Particle Size and Shape and its Self-Assembly

**Civan Avci**

Doctorate Thesis

**Thesis Directors:**

Prof. Dr. Daniel Maspoch
Dr. Inhar Imaz

**Thesis Tutor:**
Prof. Dr. Félix Busqué

Catalan Institute of Nanoscience and Nanotechnology (ICN2)
Chemistry Department-Science Faculty
Universidad Autonoma de Barcelona
**2018**

Memoria presentada per aspirar al Grau de Doctor per Civan Avci.

Vist i plau

Prof. Dr. Daniel Maspoch

Supramolecular Nanochemistry and Materials Group.

Institut Català de Nanociencia i Nanotecnologia (ICN2)

Dr. Inhar Imaz

Supramolecular Nanochemistry and Materials Group.

Institut Català de Nanociencia i Nanotecnologia (ICN2)

Prof. Dr. Félix Busqué

Departament de Quimica

Universidad Autònoma de Barcelona

Bellaterra, 14 de novembre de 2018

**T**he present PhD Thesis has been carried out at the Supramolecular NanoChemistry and Materials Group of the Catalan Institute of Nanoscience and Nanotechnology (ICN2) following the doctoral program in Materials Science of Autonomous University of Barcelona (UAB). According to the decision of the PhD Commission, this PhD Thesis is presented as a compendium of publications.

All publications are listed below in the order of their appearance in the Thesis:

**Publication 1.** "Post-Synthetic AnisotropicWet-Chemical Etching of Colloidal Sodalite ZIF Crystals" C. Avci, J. Ariñez-Soriano, A. Carné-Sánchez, V. Guillerm, C. Carbonell, I. Imaz, D. Maspoch, *Angew. Chem. Int. Ed*. **2015**, 54, 14417

**Publication 2.** "Sequential Deconstruction−Reconstruction of Metal−Organic Frameworks: An Alternative Strategy for Synthesizing (Multi)-Layered ZIF Composites" C. Avci, A. Yazdi, M. Tarrés, E. Bernoud, N. G. Bastús, V. Puntes, I. Imaz, X. Ribas, D. Maspoch, *ACS Appl. Mater. Interfaces* **2018**, 10, 23952

**Publication 3.** "Self-Assembly of Polyhedral Metal–Organic Framework Particles into Three-Dimensional Ordered Superstructures" C. Avci, I. Imaz, A. Carné-Sánchez, J. Angel Pariente, N. Tasios, J.Pérez-Carvajal, M. Isabel Alonso, A. Blanco, M. Dijkstra, C. López, D. Maspoch, *Nat. Chem.* **2018**, 10, 78

# Table of Contents

Table of Contents……i
Abstract……iii
Acknowledgements……vii
CHAPTER 1: Introduction to Porous Materials, Metal-Organic Frameworks, Zeolitic Imidazolate Frameworks and Zeolitic Imidazolate Framework-8 ..... 1
1. Porosity ..... 2
1.1. From Natural to Synthetic Porous Materials ..... 5
1.2. Definition, Classification and Important Parameters of Porous Materials ..... 5
**1.2.1. Standard Definition of Porous Materials** ..... 5
**1.2.2. Specific Surface Area** ..... 5
**1.2.3. Pore Volume and Pore Size Distribution** ..... 6
2. Metal-Organic Frameworks (MOFs) ..... 7
2.1. Definition ..... 7
2.2. Properties of MOFs: Highly Porous, Lightweight and Stable Crystals ..... 10
**2.2.1. Porosity of MOFs** ..... 10
**2.2.2. Density of MOFs** ..... 12
**2.2.3. Stability of MOFs** ..... 13
2.3. Applications of MOFs ..... 13
**2.3.1. $H_2$ and $CH_4$ Storage for Fuel Applications** ..... 13
**2.3.2. $CO_2$ Capturing and Sequestration** ..... 17
**2.3.3. Other Adsorption and Controlled Release Applications** ..... 22
**2.3.4. MOFs as Nanomaterials** ..... 23
3. Zeolitic Imidazolate Frameworks (ZIFs) ..... 31
3.1. Description ..... 31
3.2. Discovery and Properties ..... 32
4. ZIF-8 ..... 37
4.1. Structural Properties ..... 37
4.2. Thermal Properties ..... 39
4.3. Mechanical Properties ..... 40
4.4. Applications ..... 41
**4.4.1. Molecular Sieving** ..... 42
**4.4.2. Sensing** ..... 43

**4.4.3. Heterogeneous Catalysis** ..... 43
**4.4.4. Drug delivery** ..... 45
4.5. Crystallization and Morphology ..... 47
4.6. Synthesis ..... 48
**4.6.1. Evolution of the Synthesis of ZIF-8** ..... 48
**4.6.2. Effect of the Solvent** ..... 50
**4.6.3. Effect of the Metal Source** ..... 50
**4.6.4. Effect of the Added Base** ..... 51
**4.6.5. Effect of the Added Surfactant** ..... 52
4.7. Post-Synthetic Modification and Engineering of ZIF-8 ..... 54
**4.7.1. Top-down Shaping of ZIF-8** ..... 55
**4.7.2. Bottom-up Shaping of ZIF-8** ..... 60
5. References ..... 64
CHAPTER 2: Objectives ..... 75
Objectives ..... 76
CHAPTER 3: Post-Synthetic Anisotropic Wet-Chemical Etching of Colloidal Sodalite ZIF Crystals ..... 79
CHAPTER 4: Sequential Deconstruction−Reconstruction of Metal−Organic Frameworks: An Alternative Strategy for Synthesizing (Multi)-Layered ZIF Composites ..... 110
CHAPTER 5: Self-Assembly of Polyhedral Metal-Organic Framework Particles into Three-Dimensional Ordered Superstructures ..... 139
CHAPTER 6: Conclusions ..... 179
Conclusions ..... 180

# Abstract

The present Thesis aims to give the reader new insights on the controlled manipulation of Metal-Organic Framework (MOF) materials with nano-scale precision and its consequences in the final properties and applications. The study presented here hopes to form a bridge between MOFs and Nanotechnology; which means, bridging the classical expectations from the bulk properties of MOFs with novel functions that can arise upon the manipulation at the nano-scale. Here we demonstrate this bridging with a prototypical MOF, namely Zeolitic-Imidazolate Framework-8 (ZIF-8), which is one of the most studied MOF, due to its easy synthesis and promising properties including high porosity and exceeding thermal, chemical and water stability.

The Thesis is organized into two parts. Chapter 1 constitutes the first part where the reader will find an introduction of the concept of porosity, with examples of naturally porous materials. This Chapter continues with a brief introduction of MOFs, an extensive introduction to ZIFs and, even more extensive introduction to ZIF-8. Thanks to the carefully selected examples and concepts, this introductory Chapter attempts to draw attention of the reader to the main point of this Thesis, which is the manipulation of MOFs at the nano-scale in order to reach beyond the classical aspects.

The second part of this Thesis starts with a description of the objectives in Chapter 2. Then, each chapters 3, 4 and 5 includes a publication related to the manipulation of ZIF-8 at the nano-scale using ZIF-8 and -in some cases- other MOFs. In these studies, we followed three main approaches: 1. Post-synthetic top-down approach; 2. Post-synthetic bottom-up approach; and 3. In-situ modulation and self-assembly of particles.

The publication in Chapter 3 is related to the post-synthetic top-down approach, explaining the anisotropic etching of ZIF-8 crystals to reach unprecedented shapes that are unachievable by conventional synthetic methods. The publication also attempts to explain the underlying mechanism of this anisotropic etching of ZIF-8 crystals. Also, to shed light on other MOFs and to prove the generality of the method, anisotropic etching of ZIF-67 crystals is demonstrated.

The second publication, which constitutes Chapter 4, is centered on the post-synthetic bottom-up approach where the size, shape, composition and architecture of ZIF-8 and ZIF-67 crystals are modified using post-synthetic wet-chemistry. This publication explains the manipulation of MOF crystals by post-synthetic growing steps of other MOF layers, the

functionalization of MOF particles with inorganic nanoparticles (InNPs) and finally, the design of complex multi-layered MOF-InNP composite materials that can be used as catalysts in cascade reactions.

The last publication presented in this Thesis, in Chapter 5, is related to the *in-situ* modulation and self-assembly of MOF particles. This publication includes the production of MOF particles with very high size and shape monodispersity using surfactants as modulators. In this sense, highly monodisperse ZIF-8 and UiO-66 particles with various sizes and shapes were produced using CTAB and PVP, respectively, with polydispersive index < 5% for ZIF-8 and < 8% for UiO-66. It also includes the colloidal self-assembly of these MOF crystals via a fast droplet evaporation method to form ordered superstructures with well-defined crystalline superlattices that can be used as 3D photonic crystals when the particle size is selected appropriately. Finally, the photonic properties of these MOF photonic crystals and evaluation of this sensing capability of alcohol vapors are exploited.

# Acknowledgements

I would like to first express my gratitude to my supervisors Daniel Maspoch and Inhar Imaz for their educative guidance and helpful attitude during all my PhD study. The highly competitive environment of the NanoUP group along with the scientific atmosphere of ICN2 have constantly fed me with inspiration and motivation.

As in my master thesis, I dedicate this PhD thesis as well to my lovely parents Nurten and Hüseyin Avcı who have always been there for me in every term and to my brother Can Onur Avcı who has been an exemplary scientist in front of me shedding light to my embryonic scientific career. None of these could happen without them.

My deepest thanks are for Ceren Çamur who has been a very special person to me, my life partner and also my best colleague during my PhD, with whom I shared everything with. Even though things have evolved differently, as one of my closest friend now and forever, I will never forget her contribution to my life in general.

My other special thanks are for Mustafa who is my best friend for 16 years, for being always there to support me and provide me happiness even from far distances.

Special mentions to my dearest colleagues Xavi, Amirali and Javier (Perez) for their excellent collaborations and generous contributions in my projects. None of these happen without you either.

I also offer my thanks to my labmates (of my generation) Jordi, Luis Carlos, Claudia, Carles, Jorge, Gerard, Ivan, Abraham and Heng with whom I had so much fun working together and doing social activities, dinners, drinkings along with the previous and current postdocs Sabina, Kyriakos, Arnau, Vincent, Thais and Javier (Troyano). I would like to thank to our previous group manager Raquel who always spread joy to everybody with her cheerful face. I also had so much fun with some other members of our group that I will call the “lunch team”, Sonia, Mary, Marta (Ruiz) and Rosa. I think I improved most of my Spanish on that table thanks to you. Also thanks to our technicians Marta (Sanmarti) and Jose for enduring my occasional lack of order on my bench. I am also pleased to meet Najmeh as a valuable friend, and relatively newer members of our group: Yang, Anna, Borja, Yunhui, Hossein, Farnoosh and Asier.

I also thank to my “team Renfe”: Nuria, Federico, Kumara, Dani and Fabian for the wonderful train rides full of laughs on our way to work in the morning and back home in the evening. Thank you guys, really.

Finally, many thanks to my lovely Turkish community in Barcelona: Kutlu, Alican, İnci, Başak, Gülçin, Onur, Emre and Didem who made my weekends full of fun with (ironically) Chinese food, drinks, teatime chats, concerts and many other events. I love you all guys.

# CHAPTER 1

# Introduction to Porous Materials, Metal-Organic Frameworks, Zeolitic Imidazolate Frameworks and Zeolitic Imidazolate Framework-8

# 1. Porosity

## 1.1. From Natural to Synthetic Porous Materials

Nature is an immense laboratory inspiring scientists since the beginning of the noteworthy achievements. Porosity in substances is one of the fascinating formation largely encountered in nature, especially in biological tissues. For instance, a pair of adult human lungs that weigh only 1.3 kg have evolved to have some fascinating ~2400 km long macro- and micro-airways to ease the chemisorption of oxygen that the body needs to keep its temperature constant at 37°.[1] Animal skins and other membranes that cover living mechanisms are also examples to natural porous formations since they exhibit semipermeability which is a vital feature for living mechanisms. Inspired by these and many other natural structures exhibiting porous features, scientists have started to do new, synthetic porous materials that resembles to the ones found in nature. To do so, several methodologies that can be the subject of the more general field named Nanotechnology have been developed.

Nanotechnology is described as the controlled miniaturization of materials down to nanometer-levels in order to reveal new properties due to the increased surface-to-volume ratio compared to their bulk forms. The main idea is to increase the interaction capability of the material by keeping its mass at its minimum. One of the most straightforward routes to do this is to miniaturize the material down to nanometer-sized particles (nanoparticles) with top-down (e.g. mechanical grinding) or bottom-up (e.g. wet chemistry) approaches. The scientific community is controllably producing nanoparticles from every conceivable material that is accessible since Faraday made the first description of the very thin gold and silver flakes, and their unprecedented properties in 1857.[2] Although nanoparticles might have exceeding electronic, plasmonic, optical and catalytic properties along with a high active surface area; they do not offer great adsorption or any filtration related capabilities due to their 0-dimensional structure. Besides, their colloidal form, aggregation issues and non-recyclability are the major drawbacks. These issues have been intended to overcome using solid substrate reinforcements. However, in this case, the advantage of using less material to do "more things" is somehow sacrificed. Another possible way of increasing the interactive surface of solids by maintaining the material amount at its lowest is to create small cavities in the bulk material itself. In this way, very high interaction area can be achieved while conserving the bulkiness of the solid. For instance, a material that has nanometer-sized cavities (i.e. nanopores) with

very thin pore walls can be considered as the "negative" (as in the photolithographic patterns) of the same sized nanoparticles of that material (**Figure 1**). Therefore by creating pores in solids, very high surface area can be achieved in bulk and also, new capabilities can be gained such as gas/liquid adsorption, storage and filtration based on the pore characteristics of the materials. Porosity in solid materials is crucial for all gas/liquid sensing, adsorption, storage, filtration and catalysis related applications as the interaction between the liquid/gas and the solid occurs on the surface.

Pores in a solid can be created in different ways using top-down, bottom-up or both approaches. The science and engineering of porous materials is a wide field that deals with the development, production, characterization and the application of these materials. The general properties that are considered in a porous material are the pore size, pore size distribution, pore orientation, accessible surface area, crystallinity of the pore walls, among many others. Countless techniques have been developed so far to create porosity in materials however, converting a bulk material into a porous material has not been always easy. As in most cases in science, the first materials were already existent in the nature or somehow had a natural source.

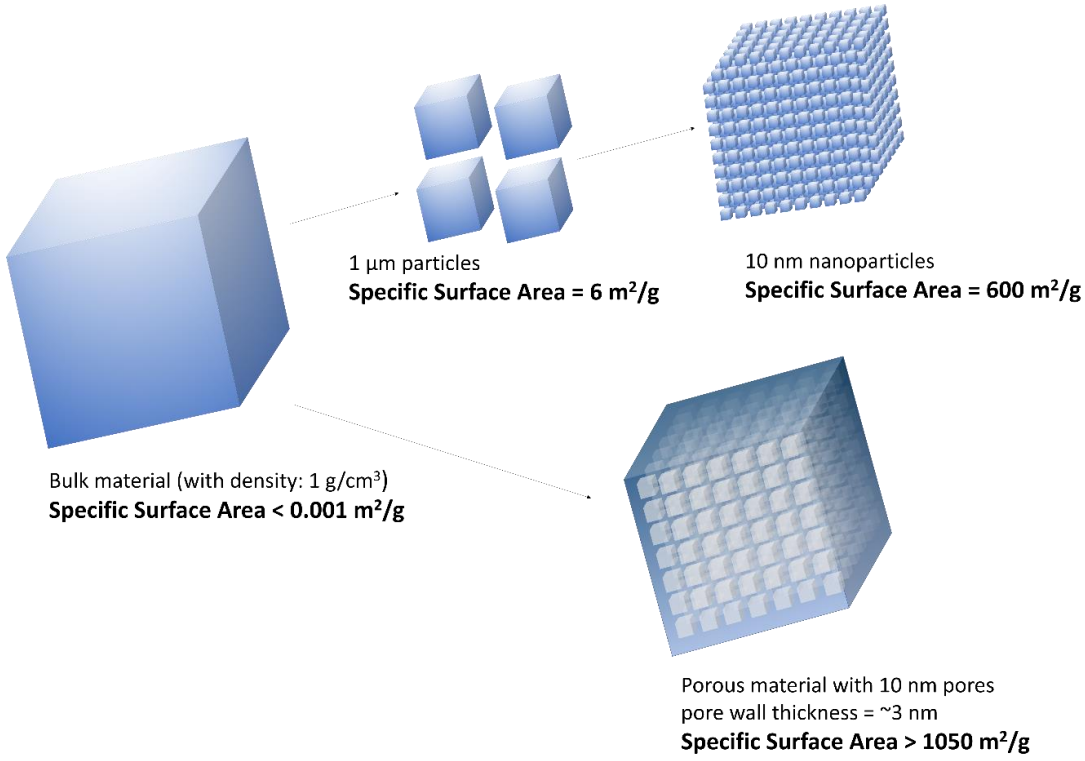


**Figure 1.** Schematic illustration showing how the specific surface area of a bulk material can be increased.

For instance, activated carbon is a highly porous material that is somewhat originated from nature. Historically, people produced charcoal, which is basically a less porous activated carbon, by slowly burning woods and bones. They realized that the black powder obtained from this process, could be used as an adsorbent to eliminate odorous vapors, to ease the symptoms of food poisoning and even, to purify drinkable water. For example, seamen charred the internal parts of their drinking water barrels since they realized that water maintained its freshness for longer times. The earlier versions of activated carbons were obviously not as porous as nowadays products, since the carbonization and pore development of the material were poor. Higher porosities were achieved when the pyrolysis was carried in the absence of oxygen and a second treatment called "activation" was applied. Typically physical (hot steam) or chemical (acidic washing) activation is today done in order to enlarge the pores (that are initially too small) of activated carbon, and thus to make them accessible to bigger molecules. Using this latest technology, activated carbon can reach a tremendous specific surface area of 3000 $m^2/g$.[3] This material is still being used for gas and vapor filtration in several applications, such as in the industrial, medical, agricultural and environmental applications.[4]

The production of activated carbon is a good example to top-down approach to grant porosity to an initially non-porous material. However, Nature also uses the bottom-up approach to produce highly porous materials. For instance, zeolites are highly porous materials found in nature (in zeolite deposits), readily formed as aluminasilicate minerals that can accommodate a wide variety of cations and high amount of water.[5] Provided with very tiny interconnected pore channels that continues along the material, their specific surface area can be higher than 750 $m^2/g$ and they are reasonably abundant in nature. The formation of zeolites is upon volcanic eruptions, from which the spread airborne volcanic ashes land on a nearby lake, where the alumina- and silica-rich raw material meets saline water to initiate the zeolite formation or the zeolitization.[6] In 1756, the Swedish mineralogist Axel Fredrik Cronstedt called this material zeolite ("boiling rock" in Greek) because of the high amount of steam generated upon rapidly heating the material.[7] Since more than a century, this "boiling rock" has been employed in many applications, such as highly selective molecular sieves,[8] separation of different isomers and gas mixtures,[9] ion exchanging, catalysis[10] and cleaning up of radioactive wastes.[11] Today, natural and synthetic zeolites with 300 varieties are known, and many of them are standard materials of some industries since decades.

## 1.2. Definition, Classification and Important Parameters of Porous Materials

### 1.2.1. Standard Definition of Porous Materials

In 1994, a technical report acknowledged from the International Union of Pure and Applied Chemistry (IUPAC) entitled "Recommendations for the Characterization of Porous Solids" was published.[12] Contributed from many scientists around the world, the report contains some of the ground concepts and definitions about porous materials. According to this report, porous solids (or materials) are solids with pores, i.e. cavities, channels or interstices, which are deeper than they are wide. They are divided into three subclasses by means of their pore size ($r_p$):

-- Micropores have widths smaller than 2 nm.

-- Mesopores have widths between 2 and 50 nm.

-- Macropores have widths larger than 50 nm.

One should not be in confusion with the term micro- and nanopores because materials having nano-sized or even subnano-sized pores are sometimes called "nanoporous materials".[13] This term is often used for materials having pores with size less than 100 nm. This statement is not totally wrong, but IUPAC notations[14] clearly state that those materials are classified as microporous, mesoporous and macroporous materials.

### 1.2.2. Specific Surface Area

The porosity of a material is measured with its specific surface area (S) which is an extent of the surface area per 1 g of the porous material with a unit of $m^2/g$. The specific surface area of porous materials is often measured with $N_2$ adsorption/desorption (shortly, sorption) isotherms taken at 77 K. The shapes of the isotherms are the fingerprint of the porous materials. The isotherms are classified as type I, II, III, IV and V according to their shapes, indicating different gas sorption behaviors for different materials (**Figure 2**). Among

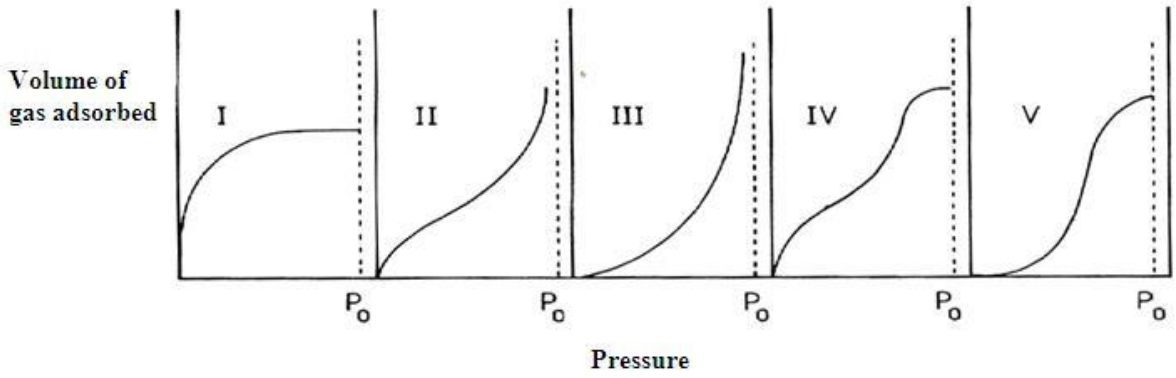


**Figure 2.** Typical type I, II, III, IV and V gas sorption isotherms of materials.

these, generically, type I isotherms are associated with microporous materials. Meanwhile type II, III, IV and V are associated with macroporous and mesoporous materials, respectively. For the surface area measurement, some of the points from the isotherm (generally 1, 3 or 5 isothermal points) are interpreted for Brunauer-Emmett-Teller (BET) calculation, a method that relates the amount of adsorbed $N_2$ molecules to the accessible surface area of the material. The output data of this measurement is named as the BET surface area or $S_{BET.}$ Also, another way to express the porosity is the Langmuir surface area ($S_{Langmuir}$), which is a calculation that assumes that all $N_2$ molecules adsorbed by the material form a monolayer on the pore surfaces. Meanwhile, BET calculation takes into account a random multilayer adsorption. For that reason, the Langmuir calculation leads to a higher surface area compared to BET. The scientific community mostly adopted the BET calculation as a reference in their articles due to its more realistic approach considering that porous materials can host more than a monolayer inside the pores.[15]

### 1.2.3. Pore Volume and Pore Size Distribution

Another important parameter of a porous material is the pore volume ($V_p$), which is the total volume of the pores in 1 g of material and has a unit of $cm^3/g$. In order to derive a pore size distribution graph, one should know the volume occupied by each pore system with respect to all the pores in the material. For most porous materials, this parameter is calculated with the Barrett-Joyner-Halenda (BJH) method that is based on the Kelvin equation.[16] The aim of that equation is to predict the vapor pressure change in the curved liquid/vapor interfaces such as droplets or pores filled with liquid. Accordingly, small pores providing higher curvatures are the first ones to be filled by the adsorbent and the last ones to be emptied during desorption.

Therefore, an isotherm with sufficient data collected from a range of $P/P_0$, where $P_0$ = 760 mmHg, can be used to draw a pore size distribution plot. This method works best for the materials with rigid pore walls (such as mesoporous materials) with less varying chemistry. However, more sophisticated considerations have to be taken into account in microporous materials. Once the pore size distribution is obtained, the total pore volume of the materials is the area below this plot ($dV_p/dr_p$).

When two materials have the same $S_{BET}$ but very different pore size plots, the narrowness of the pore size distributions becomes relevant. Therefore, it is essential to notify all the parameters while describing a porous material. For instance, a typical microporous material will usually have a higher specific surface area in comparison to mesoporous or macroporous materials. However, in some cases, a mesoporous material with thinner pore walls might have a larger $V_p$ and consequently, higher $S_{BET}$ than some microporous materials.

# 2. Metal-Organic Frameworks (MOFs)

## 2.1. Definition

Only 3 years after of the abovementioned technical publication of the IUPAC, a new era in the porous materials was about to begin when Kitagawa et al. reported a synthetic coordination polymer that exhibited microporous features.[17] This molecular material built up from metal ions and organic linkers was apt to gas adsorption at high quantities at elevated pressures. Only a year later, the developments pursued when Yaghi et al. reported the first molecular material that showed gas adsorption at low pressures.[18] However, the real breakthrough was achieved in 1999 when the same group published another porous coordination polymer that exhibited permanent porosity and a very high $N_2$ uptake, with the potential of competing with microporous materials known so far.[19] Due to the metal ions and the organic ligands that are coordinated to them forming a crystalline framework, these new porous materials were named as metal-organic frameworks (MOFs).

As an emerging new class of synthetic materials, MOFs have marked an era in the field of porous materials. The highly versatile underlying coordination chemistry, brought the organic

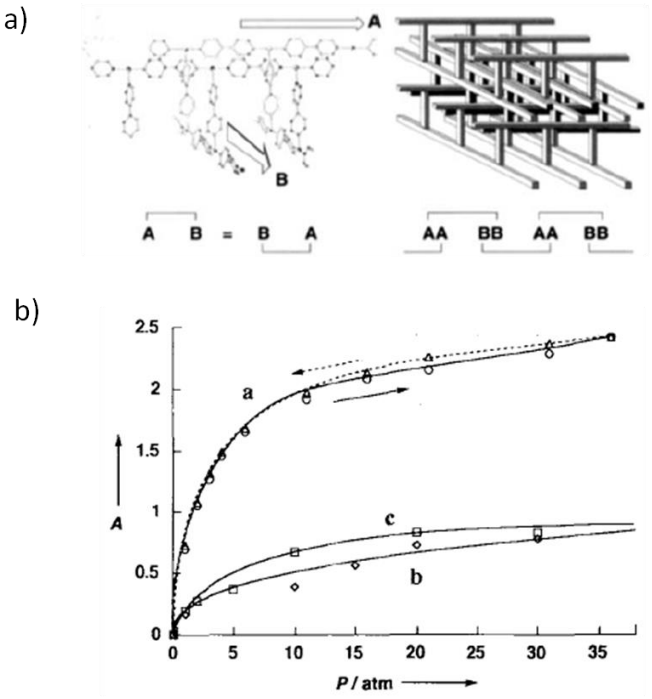


**Figure 3.** First MOF with stable porosity. a) Schematic of the crystal structure. b) Gas sorption isotherms taken at high pressures (a = $CH_4$, b = $N_2$ and c = $O_2$). (Adapted from ref. 17).

and inorganic communities together to yield a tremendous number of ~20000 different MOFs reported so far in less than 20 years, dwarfing the number of > ~300 zeolites ever produced since decades.[20] MOFs are defined as highly porous hybrid molecular crystals made of metal ions (or clusters) and organic linkers that form a 2D or 3D network throughout the crystal.[21] They are also considered as a subclass of crystalline coordination polymers having stable micropores that originate from the voids in the hybrid crystalline lattice. The versatility of the crystal structure of MOFs comes from the infinite types of organic ligands having different topologies and coordination sites, combined with the numerous metal ions having different coordination numbers and geometries (**Figure 3**). In a classical point of view, the structure of MOFs is described as the combination of organic linkers with 0D metallic nodes.[22] This approach has been helpful to understand the rational design of MOFs and their potential gas adsorption/filtration properties. Then, Yaghi et al. described the term Secondary Building Unit (SBU) as the moiety that included the metal cluster and the coordination sites of the linker.[23] This model replaced the metallic 0D node with the SBU that contains more than one metal ion; and somehow highlighted the importance of the metal cluster that can be designed in different geometries and the length of the organic linkers that is an independent variable.[24] According to this, MOFs are composed of SBUs and spacers that can also be long molecular

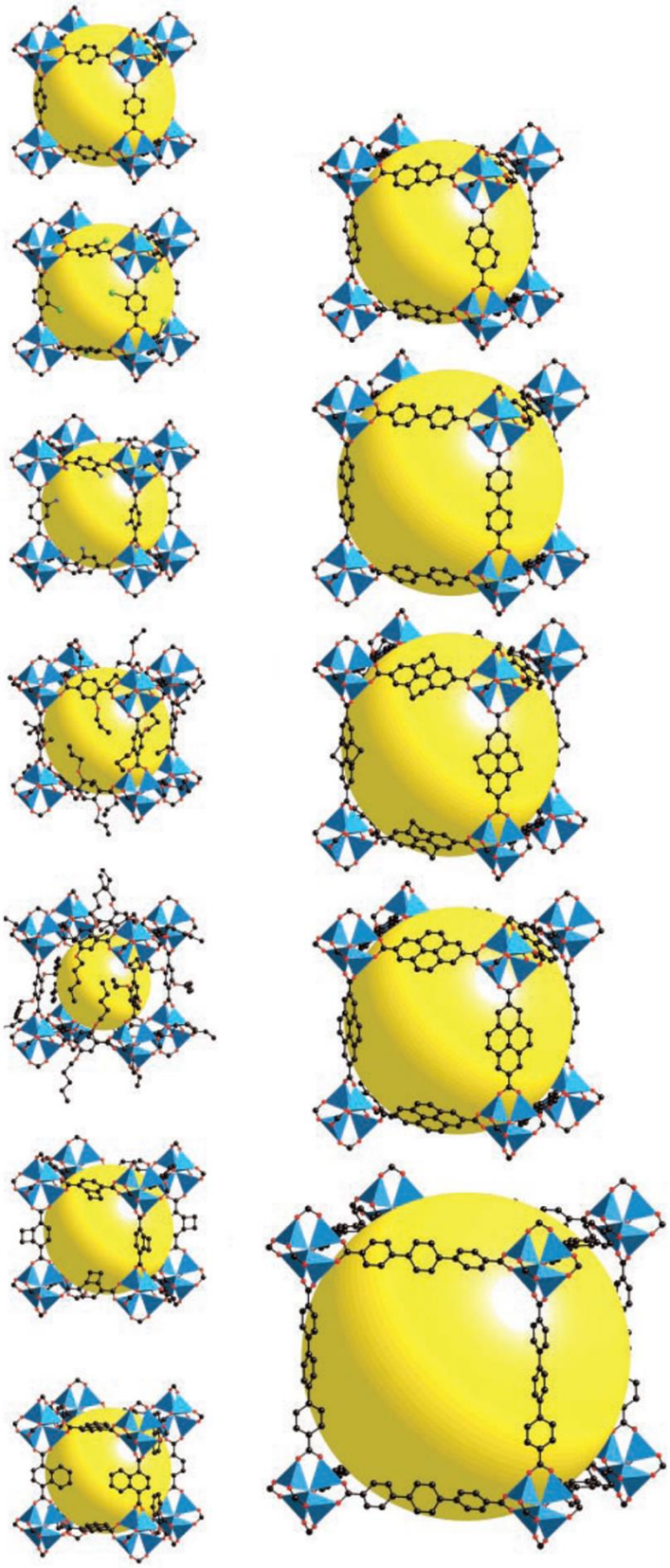

**Figure 4.** The iso-reticular MOF series (IRMOFs) designed by keeping a constant SBU and changing the length of the carboxylate ligands. (Adapted from ref. 24).

"struts" with different chain lengths of, for example, phenyl rings. This approach provides three parameters to rationally design a MOF: i) the coordination number of the metallic node; ii) the coordination sites of the organic linker; and iii) the length of the organic linker. The combination of these three variants gave rise to a new field of research that is called reticular chemistry.[25] Today, one can reach extraordinarily porous and crystalline materials by doing the proper molecular engineering using the ingredients of the reticular chemistry.

## 2.2. Properties of MOFs: Highly Porous, Lightweight and Stable Crystals

### 2.2.1. Porosity of MOFs

The majority of MOFs are microporous materials with a pore size less than 2 nm, that exhibit type I isotherm, a $S_{BET}$ typically larger than 1000 $m^2/g$ and an ultra-narrow pore size distribution. The type I isotherm is known for its high adsorption in the low $P/P_0$ regime, quickly reaching a plateau that is not disrupted until the end of the isotherm. As mentioned before, BJH method does not work on MOFs due to the wide variety of their pore structures, which can be sometimes flexible, and their sophisticated chemistry. There are currently no single model that responds to the need of MOFs. Non-linear Density Functional Theory (DFT),[26] Grand Canonical Monte Carlo simulation[27] and Howard Kawazoe Model[28] (that is somehow similar to BJH) are some of the calculation methods used by the community to determine the pore size distribution of MOFs. Here, the exhaustive study of the crystal structure determination by single crystal X-Ray diffraction (XRD) is also used to deduce the pore size of a MOF. For this, the experimental pore volume is measured from the plateau region of the isotherm assuming that all pore volume comes from the micropores. Then, this pore volume is compared with the single crystal XRD data by calculating the pore volume of one unit cell. However, this method is also not quite definitive since the Van der Waals (vdW) radius of the pore opening of MOFs can sometimes change upon gas adsorption, at high pressures or at different pHs.

The surface area of MOFs can range from 1000 to 10000 $m^2/g$ (**Figure 5**), equivalent to a soccer field, thus exceeding all the known zeolites and carbons. Hupp et al. run some simulations to predict the theoretical highest surface area achievable with MOFs. They constructed hypothetical structures by incrementally adding phenyl, phenylethynyl, or ethynyl

groups to the $Cu_2^{II}$-paddlewheel clusters until their unit-cell edge lengths reached at least 30 nm. The theoretical limits have been found to be 9950 $m^2/g$, 12250 $m^2/g$ and 14600 $m^2/g$ for MOFs built from phenyl, phenylethynyl and ethynyl derived linkers, respectively.[29] Also a previous study by Matzger et al. showed that 10500 $m^2/g$ is the upper limit that can be reached using benzene derived linkers.[30] The same group reported a MOF named UMCM-2 with $S_{BET}$ of 5200 $m^2/g$ (Langmuir surface area: 6060 $m^2/g$), ranking in the top 5 high-surface area MOFs in the literature.[31] On the other hand, the MOF-210 reported by Yaghi et al. and the NU-110 reported by Hupp et al. are so far the most porous crystals ever produced with tremendous $S_{BET}$ of 6240 $m^2/g$ and 7140 $m^2/g$, respectively.[32,33] Having already at least doubled their zeolite and carbon-based opponents, the race of achieving higher surface area-MOFs is still excitingly ongoing. The crystal structure of some prototypical MOFs are depicted in **Figure 6**.

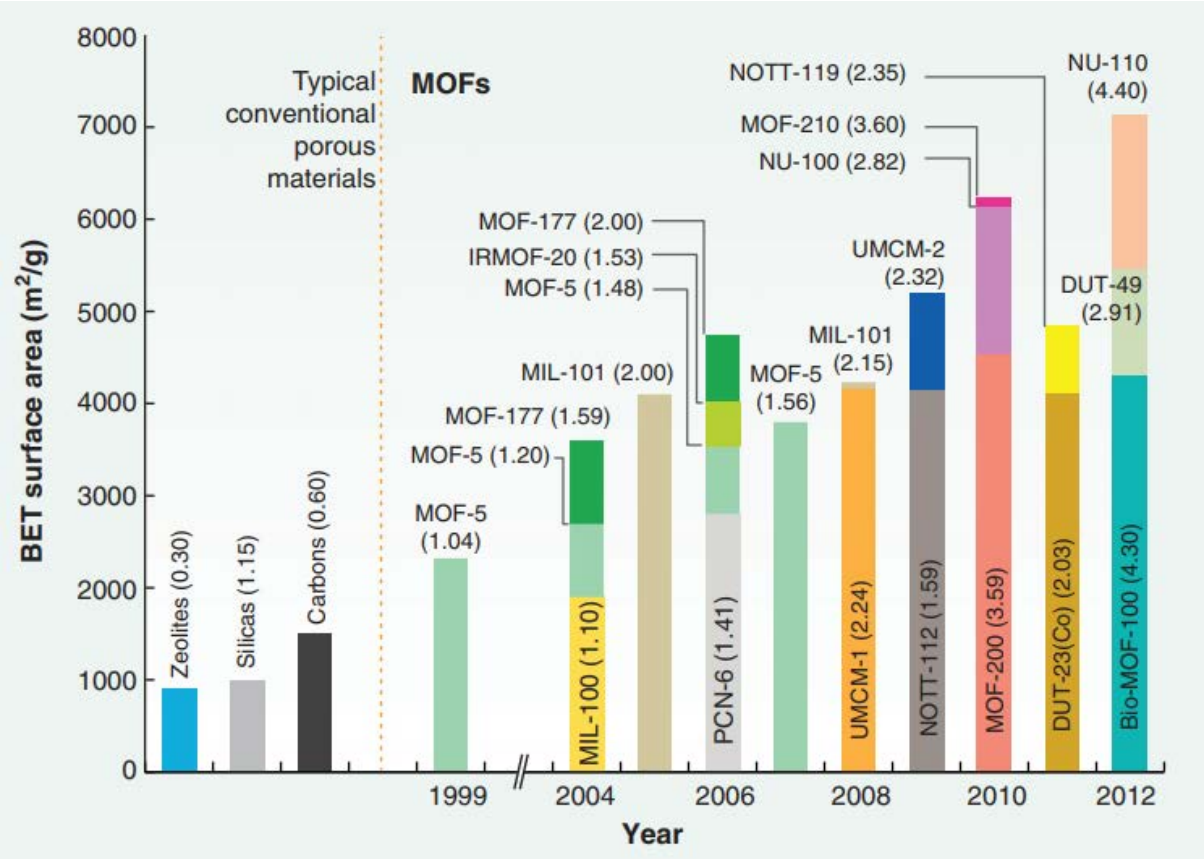


**Figure 5.** Chart of MOFs with the highest $S_{BET}$ and $V_p$ reported until 2012. (Adapted from ref. 33).

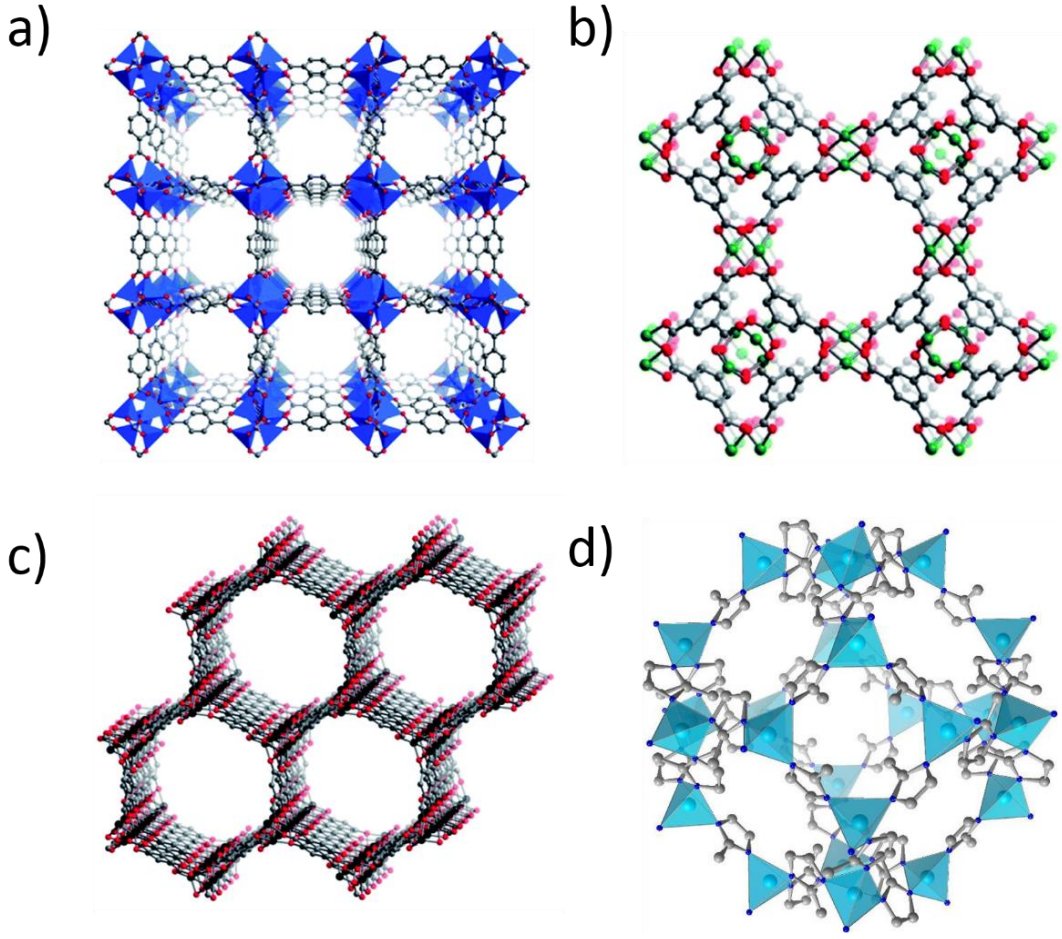


**Figure 6.** Crystal structures of some prototypical MOFs for gas adsorption applications: a) MOF-5, b) HKUST-1, c) M-MOF-74, and d) ZIF-8.

### 2.2.2. Density of MOFs

MOFs can be considered as the lightest crystalline solids ever produced in laboratories. After having reported the first stable MOFs named "MOF-2" in 1998[18] and the more famous MOF-5 in 1999,[19] Yaghi et al. also reported the lightest crystalline material ever existed until then (0.21 g/cm$^3$). This material was an iso-reticular version of MOF-5 composed of 91 % of empty space having a pore size of nearly 3 nm.[24] Later in 2012, they improved this value with another MOF named IRMOF-74 having 0.19 g/cm$^3$ of density with a giant pore size of 9.8 nm (bigger than mesoporous silica), again using the same iso-reticular strategy (**Figure-4**, IRMOFs).[34] The latest record is held by Farha et al., who reported a uranium based MOF named NU-1301 having 0.12 g/cm$^3$ of density with pore size of 5.0 and 6.2 nm.[35] These successful

examples showed that materials can simultaneously be crystalline, ultra-lightweight and with a very high porosity.

### 2.2.3. Stability of MOFs

Especially during its embryonic years, MOFs have been widely criticized for being unstable in contact with water. This was mainly because the first successfully synthesized MOF (MOF-5) that exhibited a $N_2$ sorption behavior ($S_{BET}$ = 2700 $m^2/g$) comparable to its theoretical expectations was unstable in water. MOF-5 and its analogues (IRMOFs) suffered from hydrolysis, in which their Zn-O bonds supporting the framework were broken under humid conditions.[24] More recently, several solutions and the discovery of new MOFs have allowed improving the hydrolytic stability of these MOFs. In 2012, it was found that the water stability of these MOF-n series can be improved by shielding the Zn-O bond with functional groups of the ligand.[36] Also, the invention of zeolitic imidazolate frameworks (ZIFs),[37,38] which are highly stable MOFs in hydrothermal conditions, solidified the armor of MOFs in terms of hydrothermal stability.[39] Similarly, carboxylate MOFs with high-valent cations ($Zr^{+4}$, $Cr^{+3}$ and $Fe^{+3}$) such as the well-known UiO (Universitetet i Oslo),[40] and MIL (Matérial Institut Lavoisier)[41] families, exhibit high thermal and water stability. However, some harsher conditions such as long term humidity and/or exposure to acidic gases $SO_x$, $NO_x$ and $H_2S$ at elevated temperatures still need to be considered when MOFs are evaluated for applications such as pre- or post-combustion $CO_2$ capture or natural gas sweetening.[42,43] Some of the applications and potential capabilities of MOFs are covered in the next section.

## 2.3. Applications of MOFs

### 2.3.1. $H_2$ and $CH_4$ Storage for Fuel Applications

As a potentially renewable and clean burning energy source, $H_2$ can someday replace carbon-based fuels.[44] However, as $H_2$ is an exceptionally difficult gas to store, current technologies that are being investigated, such as metal hydrides, cryogenic storage, and ultra-high pressure storage do not offer economical and practical advantages over fossil fuels.[45] The U.S. Department of Energy (DOE) put a target to be achieved by the year 2020: the

development of a system of a 4.5 wt % $H_2$ gravimetric capacity and a volumetric capacity of 30 g of $H_2$/L that must function at −40 to 60 °C with a maximum pressure of 100 bar. This is the target that will compete and one day replace the fossil fuels offering an appreciable driving distance of 300 miles with a regular 4-wheels vehicle.[46] This goal has not been achieved yet with any material. However, with their exceptional surface area and versatile surface chemistry, MOFs are considered to be the strongest candidates to fulfill these requirements. With a kinetic diameter of 2.89 Å, $H_2$ is a very small molecule that can penetrate in almost every pore. Therefore, the kinetic restriction due to the pore size is not a limiting factor. Also, an ultra large surface area is desired to enhance the volumetric capacity but it is not the only property sought for $H_2$ storage. For cost-effectiveness, a significant adsorption should take place at room temperature under relatively low pressures (≤ 100 bars). The key to obtain this adsorption is to have a $H_2$ binding enthalpy < -20 kJ/mol, which is possible by having active open metal sites that polarize the $H_2$ molecules in the structure of the MOF. Preferably, MOFs containing open M(II) or M(III) cations that can accommodate at least four or five $H_2$ molecules each, are potentially good $H_2$ adsorbents.[47] As a well-studied MOF with its high surface area, MOF-5 was considered as a potential material for $H_2$ storage. However, no significant gain was achieved at 100 bar and 25 $^oC$ compared to the compressed pure $H_2$ in the same conditions. However, MOF-74 and its isostructural M-MOF-74 series (where M = Mg, Mn, Fe, Co, Ni, Cu, Zn) providing denser open metal sites yielded higher values. Among these, Ni-MOF-74 [also known as $Ni_2$(*m*-dobdc)] showed a promising volumetric capacity of 12.1 g/L at 25 $^oC$ and 22.3 g/L at -75 $^oC$; both at 100 bar.[48] A recent study showed that, among more than 13000 screened MOFs that have been virtually created and tested for $H_2$ storage, some of the –hypothetical- MOFs can actually fulfill the requirements for this application. After having run an exhaustive screening, Snurr et al. synthesized two MOF families (she-MOF-x and NU-x) to be evaluated experimentally. Surprisingly, the NU-1103 had an experimental volumetric capacity of 43.2 g/L at 100 bar at 77 K. This result improved the current technology of compressed $H_2$ in a tank, which can offer 37 g/L at 700 bar at ambient temperature.[49] To date, even though the requirements of the DOE have not been satisfied yet, MOFs have proved themselves as one the strongest candidates for this near-future technology.

The storage of natural gas in MOFs showed more promising results compared to $H_2$ storage. The natural gas that is mainly composed of $CH_4$ is also an attractive alternative to the current fuels due to its abundance and lighter $CO_2$ emission compared to coal and petroleum. However, very much like $H_2$, $CH_4$ storage requires pressurized tanks, typically at 250 bars; a

feature that boosts the cost of this technology. The DOE targets for $CH_4$ storage are 0.5 g($CH_4$)/g of gravimetric and 263 $cm^3$(STP)/$cm^3$ of volumetric uptake at room temperature and 65 bar. Conventional zeolites typically exhibit $CH_4$ uptakes below 100 $cm^3$(STP)/$cm^3$, whereas most porous carbons show uptakes in the range of ~50–160 $cm^3$(STP)/$cm^3$.[50] In the meantime, MOFs exhibited superior storage capacities compared to other materials, although the DOE targets have not been reached. The strategy to enhance the $CH_4$ adsorption of MOFs is similar to that of $H_2$ because both molecules are non-polar and have very high binding enthalpies. For this, similar MOFs with open metal sites employed for $H_2$ adsorption have also been employed for $CH_4$ storage.

M-MOF-74 series, especially Ni-MOF-74, is in the highlight due the strong polarizing ability of $Ni^{2+}$ cationic sites. According to the most recent reports, Ni-MOF-74 has a volumetric capacity of 230 $cm^3$(STP)/$cm^3$ at 35 bar and 260 $cm^3$(STP)/$cm^3$ at 65 bar and at room temperature.[51] Similarly, Co-MOF-74 and Mg-MOF-74 also have promising values of 221 and 200 $cm^3$(STP)/$cm^3$, respectively, at 35 bar and atroom temperature.[51] HKUST-1, as a benchmark Cu-based carboxylate MOF first synthesized right after the MOF-5 in 1999,[52] also exhibits a high value of 267 $cm^3$(STP)/$cm^3$;[53] very much like the open metal site-free MAF-38, a Zn-based mixed ligand MOF that exhibits 263 $cm^3$(STP)/$cm^3$ at 65 bar and at room temperature.[54]

Although it seems that the DOE target has already been achieved, these values do not represent the real life application capacities of these MOFs. The reported volumetric capacities are calculated with the theoretical crystal densities of these MOF structures, neglecting the voids between the particles. Like any materials, MOFs also suffer from an at least 25% of volumetric loss upon packaging the powder into containers/tanks. The voids between the powder leads to a drastic decrease in the real $CH_4$ uptake and compressing the MOF particle into pellets often leads to pore collapse of the framework during compaction. Therefore, it is necessary to normalize the DOE target to 350 $cm^3$(STP)/$cm^3$ in terms of volumetric capacity or, to use directly the working capacity as a reference, which is the real value obtained after packaging the MOF particles for application. Optimistically speaking, a MOF with at least 350 $cm^3$(STP)/$cm^3$ volumetric capacity will exceed the DOE target of 263 $cm^3$(STP)/$cm^3$ due to the 25 % of loss caused by the bulk density of the MOF powder. For instance, the volumetric capacities of HKUST-1 and MAF-38 decrease from ~260 to ~190 $cm^3$(STP)/$cm^3$, at 65 bar room temperature, upon calculating the bulk density of the powders. Recently, MOFs such as NU-111 and MOF-177 have approached the DOE target with exceptional working capacities

of 239 and 230 $cm^3$(STP)/$cm^3$, respectively, shown at 270 K and 65 bar.[55] Note that the latter two examples are demonstrated at 270 K, which can be also speculated as a feasible temperature for this application.

Nevertheless, while the race for improved $CH_4$ working capacity is still going on, a different approach was reported by Jimenez et al., whose group successfully synthesized HKUST-1 monoliths in ~1 $cm^3$ size, having a record $CH_4$ working capacity of 259 $cm^3$(STP)/$cm^3$ at 65 bar and at room temperature. These monoliths were fabricated by a sol-gel method (**Figure 7**) that enabled cm-sized continuous MOF materials, eliminating the volumetric drawback caused by the powder packaging.[56] This result is so far the closest achieved value to the DOE target. However, another challenge will be to fill a car's $CH_4$ tank of tens of liters with HKUST-1 monoliths. Even though the real expectations have not been totally achieved yet, as in the $H_2$ storage, it has been demonstrated with numerous examples that the strongest candidates for $CH_4$ storage are the MOFs. On the other hand, a recent study showed that some of the MOFs that are popularly studied for methane storage, such as HKUST-1, are actually not very suitable for real natural gas storage mainly because the natural gas is composed of 95 % of $CH_4$ and the other 5 % is composed of $H_2S$, $H_2O$, $CO_2$ and heavier hydrocarbons. It is expected that these hydrocarbons, which are harder to desorb, will accumulate in the pores upon storing cycles and eventually decrease the working capacity of the MOF.[57] Therefore, either a system that traps the poisonous gases should be engineered or the natural has to be purified to $CH_4$. Interestingly, this latter option is also in the job description of MOFs. In the next section, the gas purification abilities of MOFs are discussed.

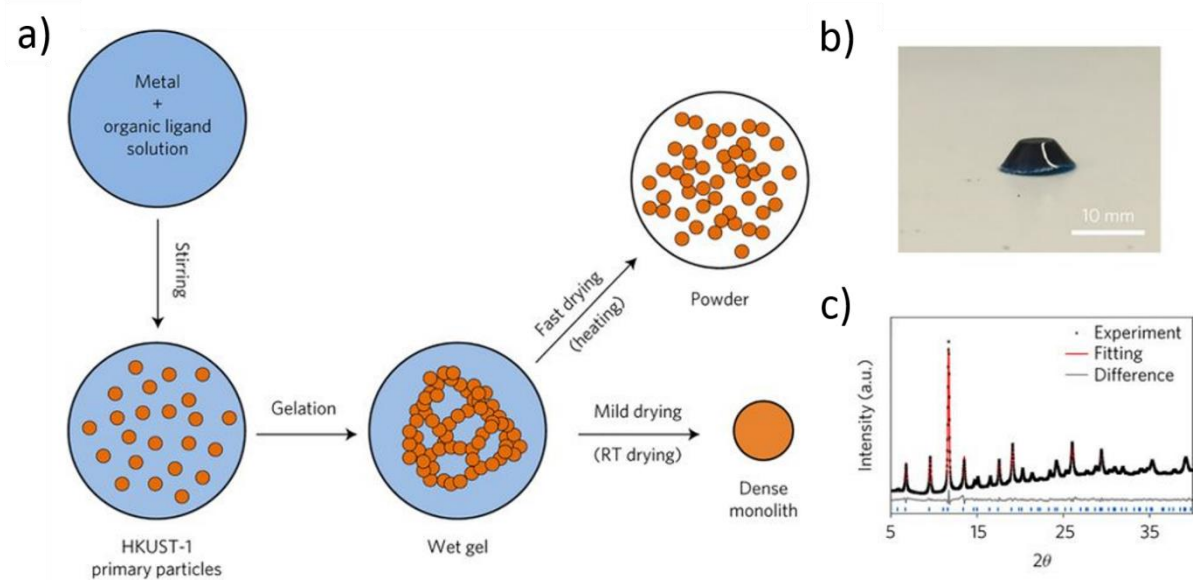


**Figure 7.** Schematic of the formation of HKUST-1 monoliths exhibiting record $CH_4$ uptake (Adapted from ref. 56).

### 2.3.2. $CO_2$ Capturing and Sequestration

Undoubtedly, $CO_2$ is the primary harmful gas to human and other livings by threatening the future of our planet. The escalating energy consumption based on carbon fuels is dangerously increasing the level of $CO_2$ concentration in the atmosphere and contributing to the global warming.[58] Anthropological studies show that this level of $CO_2$ has never been achieved since 400 000 years. Along with the continuous development of non-$CO_2$ emitting generation of energy from wind, solar or hydro and geothermal sources, the capture and sequestration of $CO_2$, the predominant greenhouse gas, has become a central strategy for short- and medium-term clean energy plans.[59] Although the transition of the existing infrastructure from carbon-based sources to cleaner alternatives would be ideal in this regard, such a change requires considerable modifications to the current energy framework, and many of the proposed technologies are not yet sufficiently developed to facilitate large-scale industrial implementation. Thus, carbon capture and sequestration technologies that efficiently capture $CO_2$ from existing emission sources is expected to play an important role until more significant modifications to the energy infrastructure can be realized.[60]

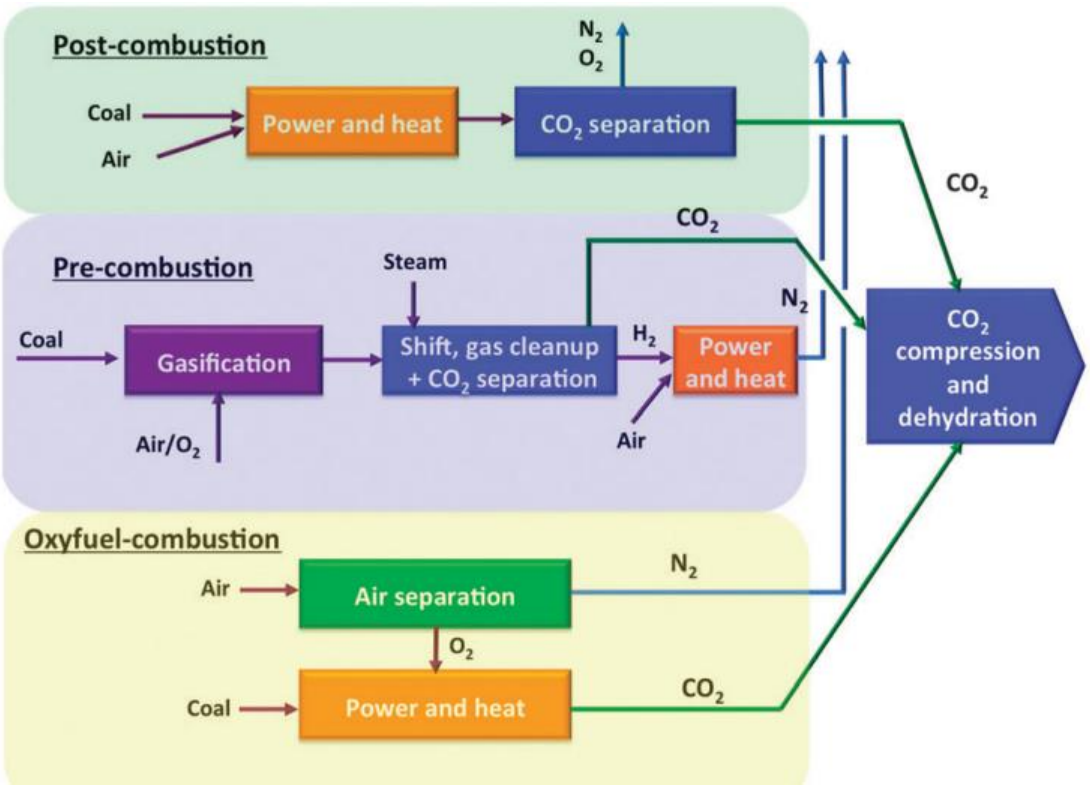


**Figure 8.** Typical schematic for $CO_2$ capture options in a coal power plant. (Adapted from ref. 59).

Unlike $H_2$ and $CH_4$, $CO_2$ is an easily polarizable molecule that, in principle, is not very difficult to store even at elevated temperatures and low pressures. However, in real applications, the impure composition of the hot post-combustion gas flue of the power plants complicates $CO_2$ capturing and sequestration. For instance, the post-combustion flue gas of a coal-fired power plant has a temperature of 40-60 $^oC$ and often contains 73-77% $N_2$, 15-16% $CO_2$, 5-7% $H_2O$, 3-4% $O_2$ and some $SO_x/NO_x$ gases at some hundreds of ppm levels.[61] The selective gas separation primarily includes $CO_2/N_2$ separation in post-combustion capture, $CO_2/H_2$ separation in pre-combustion capture, air ($O_2/N_2$) and $CO_2/CO$ separation in oxy-combustion, and $CO_2/CH_4$ separation in the purification of natural gas. A schematic of $CO_2$ capture options in a coal power plant is depicted in **Figure 8.** Also, $CO_2$ capturing in power plants requires good water stability and high $CO_2$ uptake at 40-60 $^oC$, good selectivity, especially for $N_2/CO_2$ mixtures, and mild adsorption enthalpy. The latter parameter has a high significance since it can directly affect the cost of the $CO_2$ sequestration process. The term energy penalty (for $CO_2$ capture) refers to the energy loss of a power plant, as a result of the energy that is consumed to desorb the $CO_2$ from the adsorbent for its recycling. This energy penalty -that is related to the adsorption enthalpy of $CO_2$- is directly reflected on the electricity

price by an increase of 10-20%.[62] Therefore, the adsorption enthalpy should be optimized to have the maximum $CO_2$ uptake with the minimum energy loss possible.

The current $CO_2$ capturing technology is mainly centered on the aqueous alkanolamines and some porous solids, such as the zeolites and activated carbons. However, bot types of technologies have their advantages and drawbacks. For instance, the aqueous alkanolamines are chemical solutions that have been used for decades and have proven to be very effective for $CO_2$ capturing due to the high affinity of the amine functionalities to the carbon atom of $CO_2$, forming C-N bonds, and thus, having a strong adsorption of $CO_2$. However, the high enthalpy of adsorption that lies between -50 to -100 kJ/mol at 298 K and that falls into the chemisorptive regime makes a very costly recuperation of the adsorbent solution.[63] In contrast, zeolites with their low heat capacities compared to alkanolamines provide a more economical recovery. Zeolites are known to be hydrothermally stable and to have a fair $CO_2$ uptake, making them good target materials for $CO_2$ capture. Especially the cationic sites that the zeolite hosts play an important role in the increment of $CO_2$ capture by increasing the enthalpy of adsorption.[64,65] However, zeolites often suffer from the saturation of the pores with water, which is impractical to remove. Alternatively, activated carbon is another porous solid considered for $CO_2$ capture due to its higher specific surface area than zeolites. However, the neutrally charged network of this material does not offer the necessary enthalpy of adsorption for room temperature $CO_2$ uptake at low pressures. On the other hand, activated carbon can be very useful in high pressure adsorption of $CO_2$, such as the natural gas sweetening, also known as the pre-combustion capture of $CO_2$. Indeed, one study has shown that the upper limit for the $CO_2$ adsorption capacity within activated carbon materials is approximately 10-11 wt % under post-combustion $CO_2$ capture conditions, whereas it reaches 60-70 wt % under pre-combustion $CO_2$ capture conditions.[66]

Considering their higher surface area and lower density compared to the aforementioned materials, MOFs have the potential to overcome current challenges in $CO_2$ sequestration. The tunable chemistry of MOFs allows the rational design of an adsorbent for the specific purpose. For instance, the adsorbent that is to be used in $CO_2$ sequestration should exhibit selectivity to $CO_2$ over the other components including $N_2$, $H_2$ and $CH_4$. This selectivity can be achieved mainly with two mechanisms: kinetic and thermodynamic separation. The kinetic separation is the size-based separation that is engineered using an adsorbent with a pore size in the regime of the adsorption of concern. In this case, one molecule can diffuse easily while the others are kinetically arrested due to their molecular size. For this, MOFs are excellent target materials

due to their pore size being very close to the kinetic diameter of the gas molecules, such as $CO_2$, $N_2$, $CH_4$, etc. (**Table 1**). However, the components of the pre- or post-combustion gases having very similar kinetic diameters, making their kinetic separation impractical.

**Table 1:** Physical parameters of relevant gases for $CO_2$ capture (Adapted from ref. 60).

| molecule | kinetic diameter (Å) | polarizability ($10^{-25}$ cm$^{-3}$) | dipole moment ($10^{-19}$ esu$^{-1}$ cm$^{-1}$) | quadrupole moment ($10^{-27}$ esu$^{-1}$ cm$^{-1}$) |
|---|---|---|---|---|
| $H_2$ | 2.89 | 8.04 | 0 | 6.62 |
| $N_2$ | 3.64 | 17.4 | 0 | 15.2 |
| $O_2$ | 3.46 | 15.8 | 0 | 3.9 |
| CO | 3.76 | 19.5 | 1.10 | 25.0 |
| NO | 3.49 | 17.0 | 1.59 | |
| $H_2O$ | 2.65 | 14.5 | 18.5 | |
| $H_2S$ | 3.60 | 37.8 | 9.78 | |
| $CO_2$ | 3.30 | 29.1 | 0 | 43.0 |
| $NO_2$ | | 30.2 | 0 | |

In the thermodynamic separation, the adsorption is selective to the bonding enthalpy of the gas to the adsorbent. This is important when considering the case of $CO_2$ capture from flue gas: the larger quadrupole moment and greater polarizability of $CO_2$ compared with, for example, $N_2$ leads to a stronger electrostatic interaction with an exposed metal site.[67] MOFs with coordinatively unsaturated metals exhibit Lewis acidity, which is afforded by partial positive charges on open metal sites. These open metal sites in MOFs are generally occupied by some coordinated solvent molecules that can be removed by applying vacuum and/or heat after the synthesis of the MOF in a process called "activation." MOFs with these sites exhibit relatively high heats of $CO_2$ adsorption (Qst) at low pressures, thus leading to substantial selectivity and $CO_2$ uptake. The coordinately open metal centers act as binding sites where $CO_2$ molecules can attach and bind to the pore surface by the induction of dipole–quadrupole interactions. Accordingly, among the well studied M-MOF-74 series (where M = Mg, Mn, Fe, Ni, Zn),[67] the famous Mg-MOF-74 has the highest uptake capacity (27.5 wt%) ever reported under standard conditions (298 K and 1 bar) (**Table 2**).[68]

**Table 2:** Representative MOFs with high $CO_2$ capacity under standard conditions. (Adapted from ref. 60).

| chemical formula[a] | common name | surface area ($m^2/g$) | | capacity[b] (wt %) | pressure (bar) | temp (K) |
|---|---|---|---|---|---|---|
| | | BET | Langmuir | | | |
| $Mg_2$(dobdc) | Mg-MOF-74, CPO-27-Mg | 1174 | 1733 | 27.5 | 1 | 298 |
| | | | | 27.2 | 1 | 298 |
| | | 1800 | 2060 | 26.7 | 1 | 298 |
| | | | | 26 | 1.1 | 298 |
| | | 1495 | 1905 | 26 | 1 | 296 |
| $Cu_3(BTC)_2(H_2O)_{1.5}$ | HKUST-1, (4 wt % $H_2O$) | | | 27 | 1 | 298 |
| $Co_2$(dobdc) | Co-MOF-74 | 957 | 1388 | 24.9 | 1 | 298 |
| | CPO-27-Co | | | | | |
| | | 1080 | | 23.4 | 1 | 296 |
| $Ni_2$(dobdc) | Ni-MOF-74 | 936 | 1356 | 23.9 | 1 | 298 |
| | CPO-27-Ni | | | | | |
| | | 639 | | 22.7 | 1 | 298 |
| | | 1083 | 1312 | 22.6 | 1 | 303 |
| | | 1070 | | 20.4 | 1 | 296 |
| $Zn_2$(dobdc) | Zn-MOF-74 | | | 19.8 | 1 | 296 |
| | CPO-27-Zn | | | | | |
| | | | | 19.6 | 1 | 296 |
| | | 816 | | 17.6 | 1.1 | 298 |
| $Cu_3(BTC)_2$ | HKUST-1 | 1400 | | 19.8 | 1 | 293 |
| | | | 1492 | 18.4 | 1 | 298 |
| | | | | 18.3 | 1 | 295 |
| | | 1781 | | 15.2 | 1 | 298 |
| | | 1482 | | 15 | 1 | 295 |
| | | | | 10.6 | 0.8 | 298 |
| | | | | 6.2 | 1 | 313 |
| | | 857 | | 6.2 | 1 | 295 |

In this context, in 2012, Gagliardi et al. developed a systematic procedure to precisely understand the interactions between the $CO_2$ molecule and the force field generated by the open metal sites in MOF-74.[69] This developed method allowed for accurate estimation of adsorption isotherms using computational approach, enabling the evaluation of different hypothetical open metal sites. These observations were further confirmed with the findings of Smit et al. on understanding $CO_2$ dynamics in MOFs with open metal centers.[70] Here, other MOFs such as HKUST-1, M-MIL-100, M-MIL-101 have also been studied. For instance, Dincă et al. studied the isostructural series of HKUST-1 with different metal centers (Mo, Ru, Ni, Fe, Cu, and Cr).[71] They found that Ni and Ru significantly increased $CO_2$ binding strength and resulted in higher selectivity toward $CO_2$. Palomino et al.[72] investigated the interaction between $CO_2$ and the unsaturated Cr(III), V(III), and Sc(III) metal sites in MIL-100 and found that the enthalpies of adsorption for Cr(III), V(III), and Sc(III) are −63, −54, and −48 kJ/mol, respectively. These

values are considered among the highest values for $CO_2$ adsorption on MOFs with open metal centers to date. Li et al. reported an M-DABCO series (M = Ni, Co, Cu, Zn) and concluded that Ni-DABCO has shown the highest pore volume and $S_{BET}$ due to the high charge density present at the metal center. This material with a $CO_2$ uptake of 180 $cm^3/g$ at 1 bar and 298 K, surpassed the activated carbon (30 $cm^3/g$) and MIL-100(Cr) (60 $cm^3/g$).[73] It was also found that the activation method has a significant impact on the $CO_2$ uptake and heat of adsorption. Hwang et al. studied MIL-100 and MIL-101, where various activation methods resulted in different $CO_2$ loadings and heat of adsorption.[74]

### 2.3.3. Other Adsorption and Controlled Release Applications

MOFs are also good candidate materials for vapor adsorption, filtration and purifying applications. For instance, Behrens et al. reported a Zr-based MOF (MOF-801)[75] that has shown an excellent water uptake and Yaghi et al. designed a real-life device made of this MOF. This device captures water from the air during the night and releases it during the day using sunlight, providing drinking water in harsh environments such as deserts.[76] In principle, any dehumidifier can capture the atmospheric water. However, it requires a lot of time and energy to recover it back. In MOFs, due to their porous nature and rationally designed surface that has low binding energy; the recovery of water is easier and can be done using only sunlight. Other studies have also suggested that MOFs can be used to purify water from hazardous materials such as PPCPs (pharmaceuticals and personal care products),[77] dye materials,[78] oil spills,[79] sulphur containing compounds,[80] heavy metal ions,[81] bisphenol-A,[82] volatile iodine,[83] and microcystin[84] due their selective adsorption sites.

Alternative uses of MOFs such as storage and controlled release of molecules have been reported and some of them are already in application. For instance, Morris et al. proposed the usage of MOFs as smart antimicrobial coatings for healthcare products. In this case, the MOF is loaded with biologically active gases, therapeutic agents or metal ions where the release gets triggered with the contact of water.[85] In the same line of encapsulation and controlled release of substances, a commercial MOF product namely Trupick[86] developed by the spin-off company MOF Technologies, is loaded with 1-methylcyclopropene (1-MCP), a molecule that retards the fruit ripening during storage. This MOF-based product is already in use in the US and Turkey markets as disposable sachets, which release slowly the 1-MCP gas into the air when put in water.[87]

Undoubtedly, the encapsulation and controlled release capabilities made MOFs target materials for drug delivery systems as well. Latest studies showed that MOFs such as UiO-66, MIL-100, MIL-88-Fe and $Zn(BDC)(H_2O)_n$ can be used to encapsulate and release caffeine,[88] ibuprofen,[89] methylene blue, amoxicillin, and gentamicin.[90] Anti-cancer drug delivery using MOFs have also been reported.[91] It has been shown that MOFs can also perform exceptionally well for gaseous therapeutics such as nitric oxide (NO) exhibiting good storage and a smart release when triggered with water.[92]

### 2.3.4. MOFs as Nanomaterials

Beyond the classical applications that are centered mainly to the bulk porosity, the advent of nanoscale MOFs has recently opened new avenues for this type of materials. In almost all applications demonstrated so far, MOFs have been identified with their average bulk properties, regardless to their nanostructures. Recently, MOFs have been shaped as thin films and produced as size- and shape- selective colloidal particles by well controlled nanoscale engineering. It had been already mentioned in the previous sections that MOFs are typically identified with their ligands, SBUs, unsaturated metal centers, etc. Here, in addition to these parameters, it is worthwhile to introduce a new variant: the nanostructure. Having sub-nanometric pores makes MOFs to be considered as nanomaterials. However, even new functions can be exploited through tailoring the morphology of the MOF crystals at the nanoscale.

For instance, latest studies showed that MOF thin films can be used as low-κ materials showing potential to replace one day the current $SiO_2$-based microelectronic technology. Typically in microelectronics, a thin layer of $SiO_2$ that has a κ value of 3.9 is used to insulate two conductive parts from each other. However, the issue arises when the thickness of $SiO_2$ layer is decreased to a certain level as the dielectric barrier becomes ineffective, thus making the further miniaturization of the microcircuits impossible. In this case, it is necessary to use a material with a lower κ value. For instance, an ideal insulating barrier would be vacuum (or air) that has a κ of 1. In this sense, materials that have some certain robustness and a lot of empty spaces inside are ideal low- κ materials. MOFs that constitute of > 50% of empty space are perfect materials for this purpose, having κ values typically below 3. For instance, Saiz et al. were able to produce ZIF-8 films on semiconductor substrates with various thicknesses

(**Figure 9**) and proposed its use as a low-κ layer. For ZIF-8, they found a κ value of 2.33.[93] Also, Lu et al. reported a Sr-based MOF that has excellent thermal stability (up to 420 $^{o}$C), having a κ value of 2.40.[94] In addition to the low-κ barrier applications, it has been proposed that some MOFs can also be used as heat pumps in microelectronics due their high water adsorption regimes at room temperatures. MOF Technologies initiated collaboration with IBM to develop new generation heat pumps using MOFs that are capable of cooling down microprocessors.

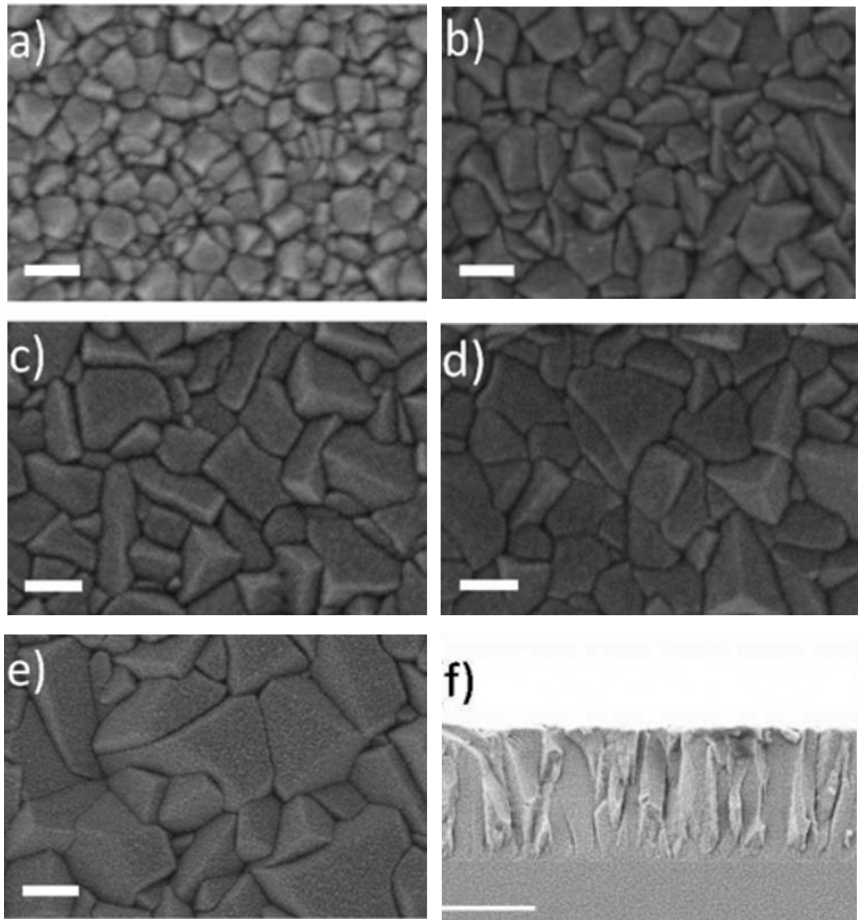


**Figure 9**. Representative SEM images of ZIF-8 films deposited on silicon wafer after different number of cycles: a) 1 cycle, 100 nm; b) 4 cycles, 400 nm; c) 7 cycles, 710 nm; d) 10 cycles, 1090 nm; and e) 12 cycles, 1440 nm. Scale bar for top view a−e): 200 nm. Scale bar for cross section f): 1 μm (Adapted from ref. 93).

As a smart design, Lu and Hupp reported a Fabry-Pérot device comprising of a ZIF-8 thin film with controlled thickness deposited on Si substrate. This device showed to be a selective sensor for chemical vapors. It is known that monolayers with certain thicknesses, close to the wavelength of the incident light, create interferometric reflections of light called Fabry-Pérot reflections or fringes. These reflections depend on the thickness and the refractive index (n) of

the monolayer, and this n can be changed upon an adsorbed chemical species in the monolayer. Since ZIF-8 is highly porous and apt to high adsorption, the shift in the Fabry-Pérot reflections upon adsorption can be significant. In this study, a thin ZIF-8 film was deposited on a solid substrate and was exposed to different alcohols and alcohol/water mixtures. It was found that the different alcohols could be differentiated using the optical shift in the Fabry-Pérot fringes. Water was not adsorbed due to the hydrophobicity of the ZIF-8 film, and the alcohol concentration of alcohol/water mixtures could be detected. Also, size selectivity among vapors was achieved since ZIF-8 did not adsorb, for example, the cyclohexane, a sterically large molecule.[95]

ZIF-8 is a wide band gap material that is transparent to the visible spectrum of light. Lechuga et al. reported a $CO_2$ gas sensor based on an optically transparent ZIF-8 film that comprised of 32 nm sized nanoparticles deposited on a bimodal waveguide (BiMW) nanointerferometer chip. In this study, the optical transparency of the ZIF-8 film was the key since the laser had to travel through the film. This transparency was achieved due to the miniaturization of the monodisperse ZIF-8 particles below 50 nm since bigger particles yielded opaque films. The adsorption of $CO_2$ in the ZIF-8 particles caused a small shift in the refractive index of ZIF-8 film that could be detected by a two-section photodetector with an upper and lower section to generate $I_{up}$ and $I_{down}$ currents, respectively. Using this setup, they were able to detect $CO_2$ in various gas mixtures with concentrations as low as 3130 ppm at room temperature and 774 ppm at 278 K (**Figure 10**).[96]

MOFs can also be produced in colloidal form, with high colloidal quality, which means with good size and shape monodispersity. In the classical approach, the properties of MOFs are assumed to be isotropic. However, by their nature, MOFs crystallize in anisotropic polyhedral shapes with well-defined facets that are distinct in chemical and physical properties. Topologically identical MOFs with different morphologies can also show different properties through the amplification of the chemical and physical discrepancies between different growth orientations. For instance, the size of the pore opening of a MOF particle may vary deeply on the crystal orientation. Or, the chemical stability of the MOFs particles may change drastically upon the functional groups that are orientated in a certain facet. To realize this, a precise control on the particle morphology, reaching size and shape monodispersity is necessary.

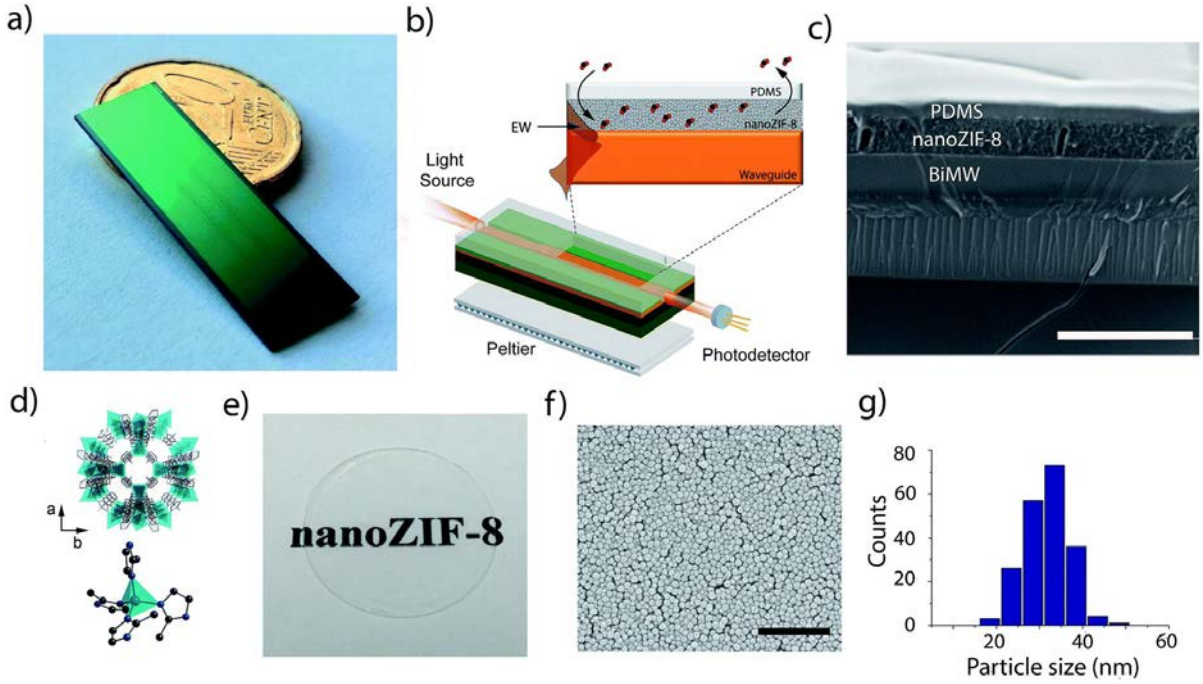


**Figure 10.** a) Photo of a chip containing 20 BiMW sensors. b) Schematic of the ZIF-8-based BiMW sensor. c) FESEM image (side view) of the ZIF-8-based BiMW sensor, showing the layers of ZIF-8 and PDMS built on top of the waveguide. Scale bar: 5 μm. d) Representation of the structure of ZIF-8. e) Photo of the transparent film of self-assembled ZIF-8 nanoparticles. f) Representative FESEM images of a self-assembled nanosized ZIF-8 film. Scale bar: 500 nm. g) Size-distribution histogram of the ZIF-8 nanoparticles (32 nm ± 5 nm). (Adapted from ref. 96).

Despite the gigantic number of MOF publications reported so far, only a handful of studies exist regarding the controlled production of MOF colloidal particles with good size and shape monodispersity. The first example was reported in 2008 by Oh et al. regarding the synthesis of $In_2(bdc)_3$ MOF in hexagonal prismatic shape with tunable lengths using pyridine as blocking agent. The polydispersity (PD) was ~ 10 - 15 % in all cases. This work was a successful example to controllably change the areal ratio of the exposed facets of a polyhedral MOF.[97] In 2009, Kitagawa et al. demonstrated the modulated anisotropic growth of $Cu_2(ndc)_2(dabco)$ nanocrystals in the shapes of nanocubes, nanorods and nanosheets by using acetic acid as modulator. Although the authors did not claim that they aimed a certain monodispersity (since the study was more conceptual), the PD they reported for their particles was ~ 15 - 20 %.[98] Later in 2011, the same group reported the shape control of HKUST-1 particles (**Figure 11**). They used *n*-dodecanoic acid or lauric acid to hinder the growth in <100> direction and to monitor a morphological transition from octahedron to cuboctahedron and finally, to cube with increased modulator concentration.[99] In 2012, Eddaoudi et al. reported some cubic and truncated rhombic dodecahedral In- and Ga-soc-MOF particles that they produced using

various surfactants. Although a fairly good monodispersity is visible from the SEM images, the PD they reported for In-soc-MOF (~ 1.3 – 3.5 %) and Ga-soc-MOF (~ 6.2 %) particles is questionable since the authors did not provide the methodology or the source of this data.[100] In 2013, Granick et al. reported the controlled synthesis of monodisperse MIL-96(Al) colloidal particles in four different shapes: regular, truncated, rounded and elongated variations of hexagonal bipyramidal morphology. In their aqueous syntheses, the shape control and the PD of ~ 3.5 % of the particles were achieved using acetic acid and co-solvents such as THF, DMF and toluene.[101]

There are also few but nice examples of controllably produced MOF particles with good size and shape monodispersity as building blocks for colloidal applications. For instance, Granick et al. reported the synthesis of rhombic dodecahedral (RD) ZIF-8 particles with a PD of 9 % and used them to make superstructures via the self-assembly of these RD ZIF-8 particles into fairly ordered monolayers with two different facet orientations (**Figure 12**).[102] In another study (published from the same group), they demonstrated the electric field-induced self-assembly of RD or cubic ZIF-8 particles into 1D chains. The cubic and RD particles were locked through their (100) or (110) facets, respectively, to form some 1D chains.[103] Eddaoudi et al. reported the formation of colloidosomes (hollow superstructures) using their Fe-soc-MOF particles in 2013, and Ga-soc-MOF particles in 2016,[104,105] via an emulsion-based method. Huo et al. reported the synthesis of monodisperse octahedral UiO-66 particles (PD = ~ % 7.1) using acetic acid as modulator and the self-assembly of these particles into large, multilayered superstructures via Langmuir-Blodgett and sedimentation methods.[106] They also employed these superstructures in photonic sensing of chemical vapors using the shifts of the Fabry-Pérot reflections.[107]

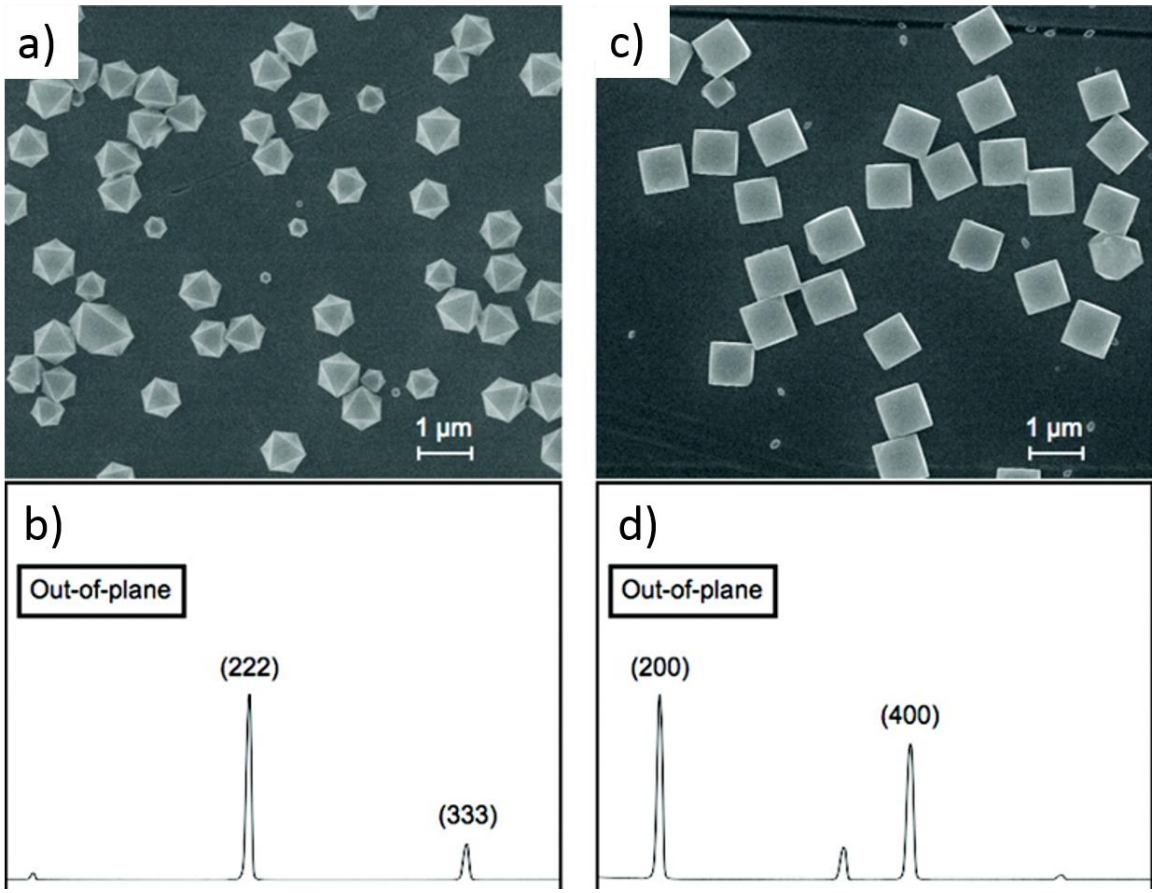


**Figure 11.** HKUST-1 particles grown on bare-gold-coated quartz substrates without function termini. a) FESEM image of octahedral crystals and (b) corresponding X-ray diffraction pattern. c) FESEM image of cubic crystals and (d) corresponding X-ray diffraction patterns. (Adapted from ref. 99).

Photonic crystals are interesting materials that comprise of periodically repeating dielectric materials.[108] They exhibit yielding a structural color that is originated from the photonic band gap. 1D, 2D or 3D photonic crystals are classified after the periodicity of the dielectrics that can repeat themselves in 1, 2 or 3 dimensions. The adsorbed molecules in a photonic crystal result in a shift in the effective refractive index of the superstructure that can be visualized by the naked eye. Therefore, MOF-based photonic crystals stand as highly promising materials for chemical sensing since they -intrinsically- provide a selective adsorption of molecules.

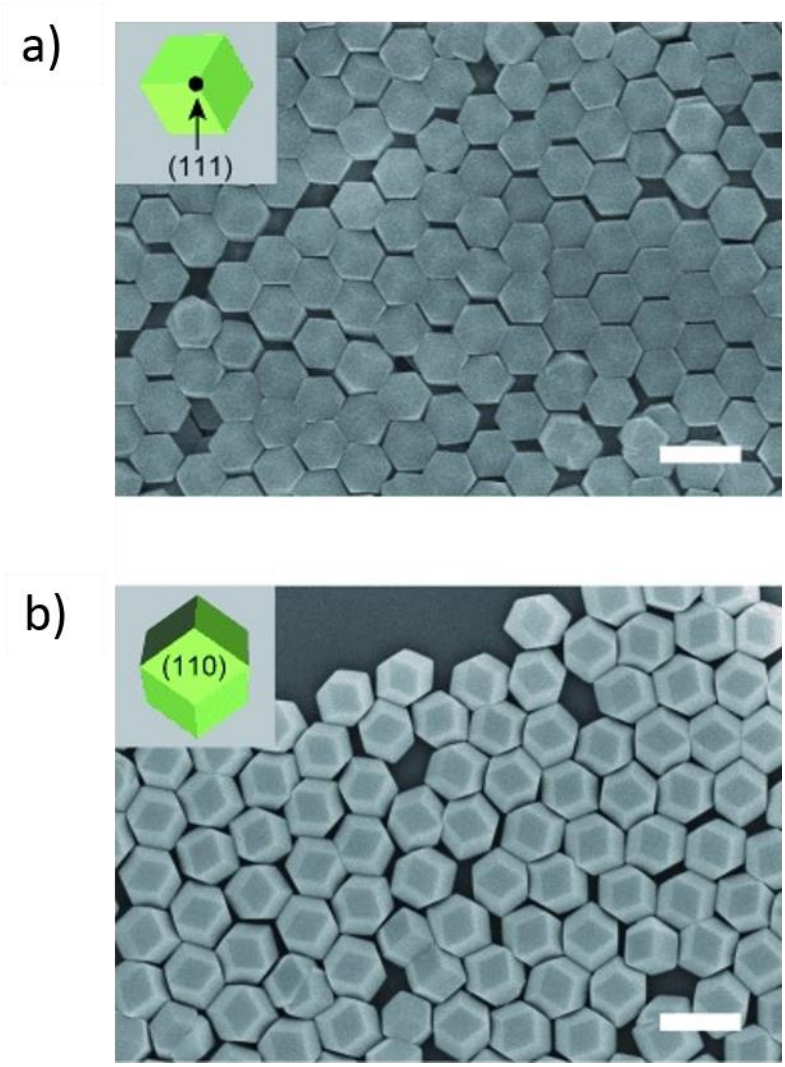


**Figure 12.** Self-assembled ZIF-8 monolayer oriented through their a) (111) facets and b) (100) facets. Scale bar: 1 μm. (Adapted from ref. 102).

Thus far, very few examples have been demonstrated regarding 1D, 2D or 3D MOF-based photonic crystals. Lotsch et al. reported a 1D photonic crystal using 2D layers of ZIF-8 and $TiO_2$ films that were made of nanoparticles. The alternating sequence of ZIF-8 and $TiO_2$ films in different thicknesses created 1D photonic materials with a range of photonic band gap, which is susceptible to vapor adsorption.[109] As for 2D MOF-based photonic crystals, Faustini et al. used a soft-lithographic method to deposit patterned ZIF-8 nanoparticles on various substrates. They were able to detect the styrene as a relevant environmental contaminant system in humid environment.[110] Li et al. reported a 3D photonic crystal based on HKUST-1 using a template-assisted method (**Figure 13**). The ingredients of HKUST-1 were infiltrated in an opalline polystyrene (PS) template, so that HKUST-1 was crystallized in-situ and formed a 3D macro-

network. Then, the PS beads were selectively etched to yield an inverse opal structure made of HKUST-1 that was also used as a vapor sensing platform.[110]

There have been a couple of examples to the usage of MOF films as vapor sensing Fabry-Pérot devices. These structures are similar to 1D photonic crystals, exhibiting colors in the visible range if the film thickness is properly adjusted; but they comprise of only one layer of MOF, without using a secondary dielectric. These MOF-based Fabry-Pérot sensors have been built using ZIF-8,[95] UiO-66[106] and MIL-88B.[112]

As seen from the aforementioned examples, there is an emerging field for the MOFs regarding their design and control in the nano-scale. In this way, new usages should be exploited along with new properties that will be unique for nano-controlled MOFs. As a prototypical MOF, ZIF-8 is a good candidate for the nano-scale engineering prone to many applications due to its high-surface area, relatively more robust structure and the abundant literature that exists regarding its well-established synthesis and growing conditions. In order to understand the nano-scale control of ZIF-8, an introduction to ZIFs in general and a detailed introduction to ZIF-8 in special is given in the next sections.

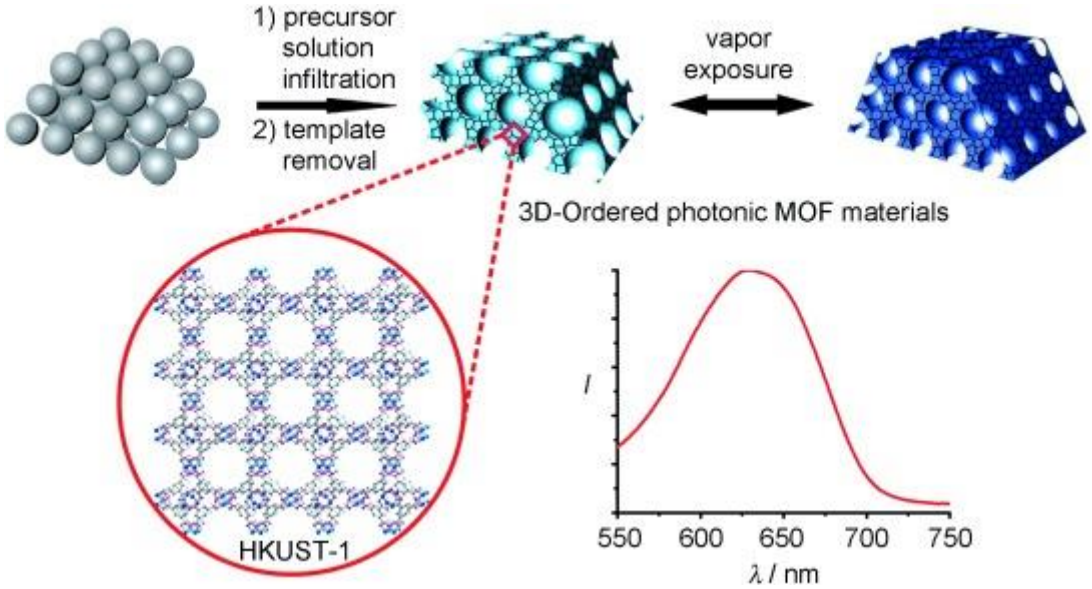


**Figure 13**. Schematic illustration of the preparation of HKUST-1 with a three-dimensional ordered macroporous structure serving as a dynamic photonic material. (Adapted from ref. 111).

# 3. Zeolitic Imidazolate Frameworks (ZIFs)

## 3.1. Description

Zeolitic Imidazolate Frameworks (ZIFs) are a sub-class of MOFs that consist of M-Im-M moieties where M stands for Zn (II) or Co (II) cations and Im stands for imidazolate linker.[37,38] The term zeolitic refers to the zeolite-like structure in which the Zn (II) or Co (II) cations act like Si and the imidazolate anions form bridges that mimic the role of oxygen in zeolites. Typically, most initial MOF structures contained the linear benzenedicarboxylate (BDC) or benzenetricarboxylate (BTC; providing 120° bonding angles) ligands (**Figure 14**).[19] However, the M-Im-M bond forms an angle of 145°, very similar to that of Si-O-Si bonds[113,114] (**Figure 15**), resulting in a crystalline topology similar to zeolites.[115] These topologies are usually named after the zeolites such as sodalite (SOD), zeolite rho (RHO), analcime (ANA), Linde Type A (LTA), Gmelinite (GME), etc. (**Figure 16**). The discovery of the ZIFs was a breakthrough in MOF-related materials due to their high thermal, chemical and water stability.

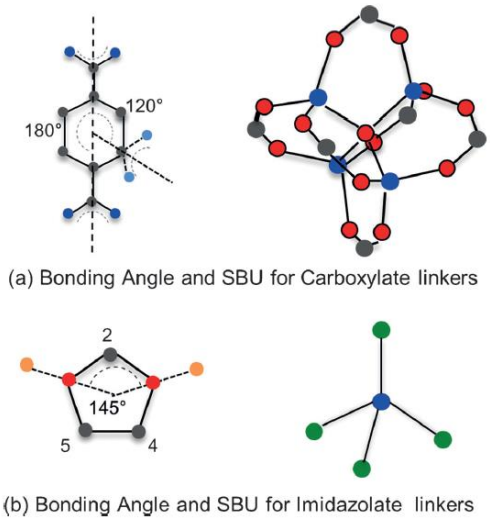


**Figure 14**. a) The bonding angle and SBU for carboxylate linkers. b) The bonding angle and SBU for imidazolate linkers. (Adapted from ref. 115)

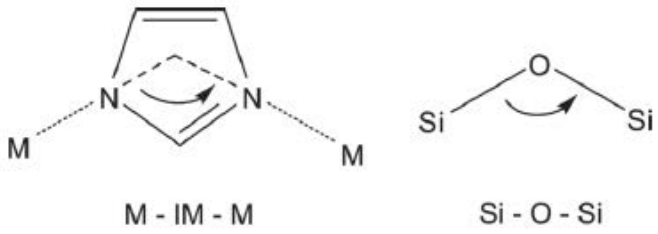


**Figure 15**. The similarity between the M-Im-M bond in ZIFs and the Si-O-Si bond in zeolites. (Adapted from ref. 38).

## 3.2. Discovery and Properties

In the early 2000s, MOFs were heavily criticized for being chemically and thermally unstable and especially, for showing vulnerability to water exposure, which was considered to be very important for their applications. It was a challenge for earlier groups to demonstrate some robustness in MOFs that could compete with its inorganic opponents including zeolites and silicas. In 2002, the first zeolite-like MOF was synthesized with this motivation by Lee et al.,[116] using an imidazole (im) type ligand and Co(II) ions that formed a robust structure like in zeolites, proving that MOFs could also have a certain thermal and chemical robustness. In fact, this reported MOF exhibited the best thermal and chemical stabilities so far, surpassing the famous MOF-5 and its isoreticular series.[24] The formula of this zeolite-like MOF was $[Co_5(im)_{10}]\cdot 2(MB)$ (where Him is imidazole and MB is 3-methyl-1-butanol) and the framework had various 5-, 6- and 8-ring pore openings that formed tubular pores with sizes of 16.9 and 11.7 Å in diameter. For some reasonable causes, MOFs were also criticized for having pore openings too small to do host-guest chemistry. By that time, this $[Co_5(im)_{10}]\cdot 2(MB)$ was considered to be a metal-organic "zeotype" material, specifically designed to have large pores, which could potentially be even larger (to fall in the mesoporous regime) by increasing the number of the rings of the pore openings (e.g. up to 10). Also, this zeolite-like MOF was stable up to 430 $^{o}$C without decomposition and exhibited solvent exchange of 3-methyl-1-butanol with ethanol, xylene and toluene without structural collapse. A year later, Chen et al. reported another thermally and chemically stable zeolite-like MOF with the formula $[Zn(bim)_2]$ (where Hbim is benzimidazole) which was the first ZIF ever produced that exhibited the well-known sodalite (SOD) topology.[118] Later, according to the nomenclature proposed by Yaghi et al., this MOF was going to be recognized as ZIF-7.

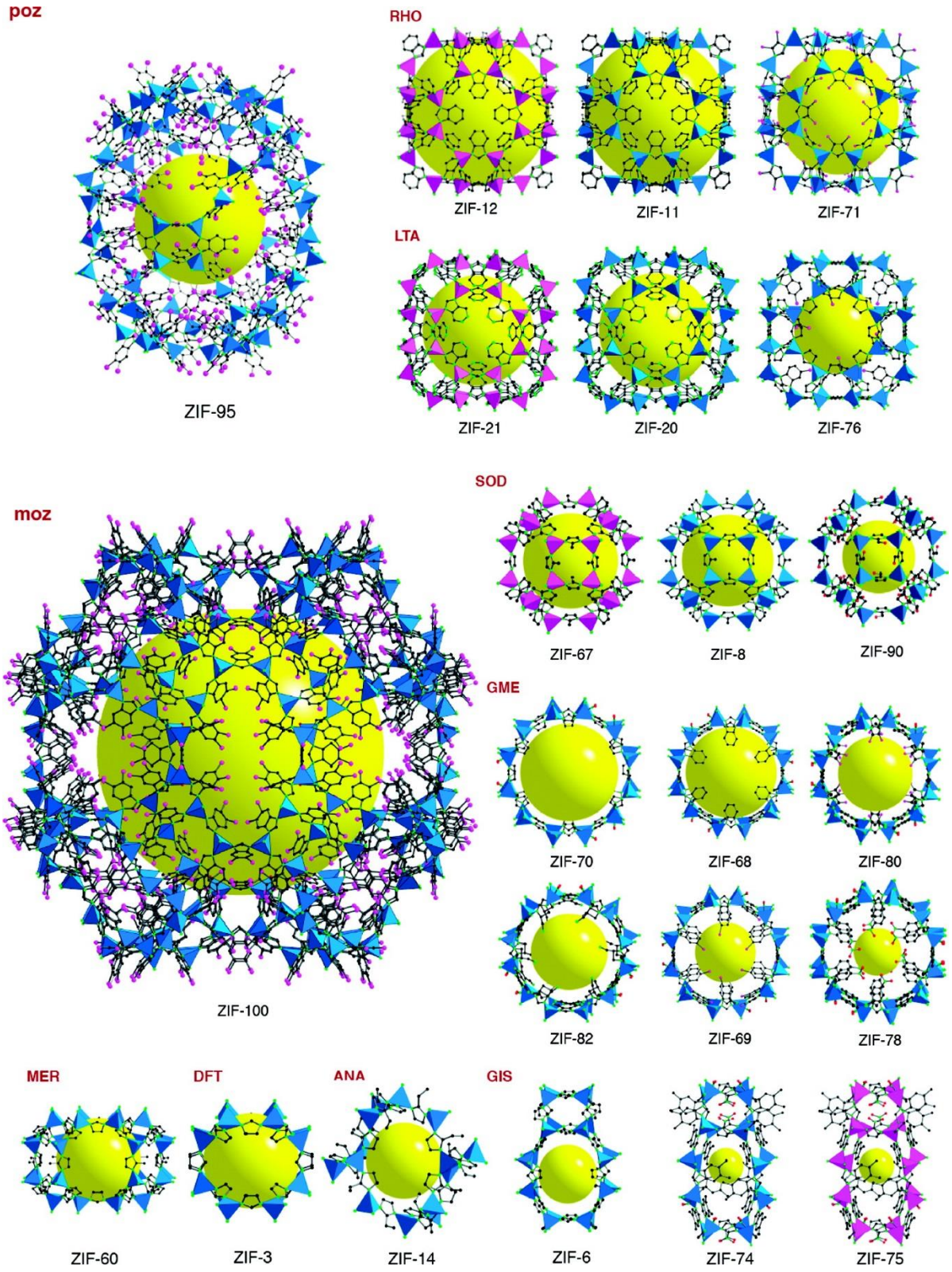


**Figure 16**. Some crystal structures of ZIFs grouped according to their topology (three-letter symbol). (Adapted from ref. 116).

After these earlier studies, the real breakthrough of ZIFs was in 2006 when Chen et al. and Yaghi et al. reported almost simultaneously a series of stable ZIFs with full identification and structural characterization. In these studies, these zeolite-like MOFs were named as ZIFs and got recognition as a subfamily of MOFs. First, Chen et al. reported three new Zn-based ZIFs with formula $[Zn(mim)_2]$, $[Zn(eim)_2]$ and $[Zn(eim/mim)_2]$ (where Hmim is 2-methylimidazole and Heim is 2-ethylimidazole) which showed SOD, analcime (ANA) and zeolite rho (RHO) topologies, respectively. Among these, $[Zn(mim)_2]$ and $[Zn(eim)_2]$ were properly characterized, exhibiting similar thermal stabilities to that of previously reported $[Zn(bim)_2]$. Furthermore, $[Zn(mim)_2]$ exhibited a stable microporosity with a $S_{BET}$ of 1030 $m^2/g$. Meanwhile, $[Zn(eim)_2]$ was almost nonporous to $N_2$ with a $S_{BET}$ of 28 $m^2/g$. This work pioneered the idea of changing the coordinatively unimportant 2-position of the imidazolates with methyl or ethyl groups to get different zeolite-like crystal structures with complete different topologies.[37]

Only 6 months later, Yaghi et al. reported twelve zeolite-like MOFs (**Figure 17**) (from which 10 of them were new) that were named as ZIF-1, ZIF-2, …, and ZIF-12. Although, they acknowledged that ZIF-7 and ZIF-8 were already reported by Chen et al. as $[Zn(bim)_2]$ and $[Zn(mim)_2]$, respectively, they claimed that they were able to produce these ZIFs in much shorter times, by reducing the previously reported 1-month syntheses to 1 day. In this ZIF-n series, ZIF-1 to -4, ZIF-6, and ZIF-10 were $[Zn(im)_2]$ polymorphs with different topologies; ZIF-7 and ZIF-11 were $[Zn(bim)_2]$ polymorphs with SOD and RHO topologies, respectively; ZIF-9 and ZIF-12 were $[Co(bim)_2]$ polymorphs that were isostructural to ZIF-7 and ZIF-11; ZIF-5 was $[In_2Zn_3(im)_{12}]$ having a topology unseen in zeolites; and ZIF-8 was $[Zn(mim)_2]$ with SOD topology. Among all these ZIFs, both ZIF-8 and ZIF-11 were highlighted due to their large pores (11.6 and 14.6 Å in diameter for ZIF-8 and ZIF-11, respectively) connected through small pore openings (3.4 and 3.0 Å across for ZIF-8 and ZIF-11, respectively), which made these MOFs apt to molecular sieving. Based on $N_2$ sorption isotherms, ZIF-8 yielded a tremendous $S_{BET}$ of 1630 $m^2/g$, whereas ZIF-11 was found to be nonporous to $N_2$ due its smaller pore openings. Both ZIFs exhibited an excellent thermal stability up to 550 $^oC$ under $N_2$ atmosphere, surpassing all the MOFs reported by then. They also exhibited no structural disintegration in boiling organic solvents and water at 50 $^oC$ for 7 days. In terms of hydrothermal stability, especially ZIF-8 was rivaling with most of the mesoporous silicas published by then by being stable in boiling water for 7 days and in boiling alkaline water (pH

= 8.0) for 24 hours.[38] These developments proved that MOFs could attain and even outperform the physical and chemical properties of some purely inorganic covalent solids.

As for the nomenclature, Chen et al. proposed the name metal-azolate framework (MAF) in which, for example, MAF-3 is ZIF-7, MAF-4 is ZIF-8, MAF-5 and -6 are RHO and ANA [$Zn(eim)_2$], respectively. The latter two MAFs did not make the "ZIF list" firstly because they were not in the study of Yaghi et al., and secondly, because they did not attract very much attention due to their nonporous structure to $N_2$. In time, the ZIF terminology of Yaghi et al. was adopted and preferred over the MAF terminology of Chen et al. Up to now, some 150 ZIFs have been reported. Among them, very important ZIFs such as ZIF-67 that is the Co isomorph of ZIF-8, ZIF-90 that has the formula [$Zn(ICA)_2$] (zinc imidazolate-2-carboxyaldehyde)[119] and ZIF-8 have been broadly studied due to their large pore size and easy synthesis.

In the recent years, ZIFs have become a trending-topic by being the mostly published MOFs in the literature. For instance, in the last year, 30 % of the publications about MOFs involved at least one member of the ZIF family. This impact can be better conceived considering that there are only ~150 ZIFs with respect to 20000 MOFs known in the literature. Furthermore, among these ZIFs, and even all the MOFs in general, ZIF-8 has a privileged position in terms of number of publications. Based on the review article of Koros et al., ZIF-8 has been the most prevalent ZIF studied that accounted for over 70% of the ZIF literature citations by 2015.[120] According to the statistics of the past year,[121] publications about ZIF-8 itself constituted the 15 % of all publications about MOFs, edging the MIL family combined and far outnumbering all the other famous MOFs such as the UiO family, HKUST-1, MOF-5, MOF-74, etc. This is mainly due to the easy handling, synthesis, control and potential applications of ZIF-8. For this, and within the scope of this Thesis, we will focus on ZIF-8, its properties, applications, synthesis, effecting parameters of the synthesis, control of the crystal morphology and the latest achievements of the nano-engineering made with ZIF-8 crystals.

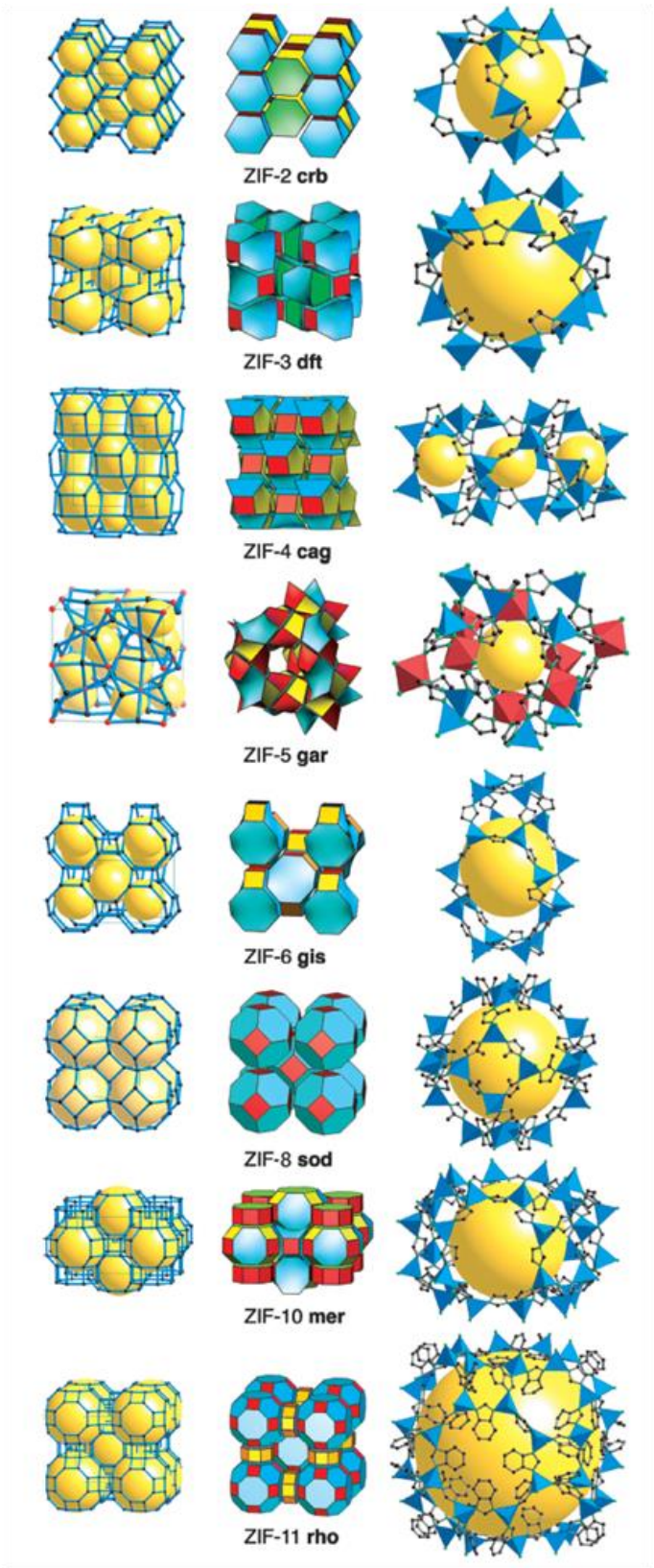


**Figure 17**. Single crystal X-Ray structures of ZIFs published by Yaghi et al. in 2006. (Adapted from ref. 38).

# 4. ZIF-8

## 4.1. Structural Properties

ZIF-8 has the chemical formula of $[Zn(mim)_2]_\infty$ and is formed of Zn (II) cations and 2-metyhlimidazole (2-mim) linkers that crystallize in the SOD topology, having a cubic lattice in the noncentrosymmetric space group $I\bar{4}3m$. The Zn (II) cation coordinates to four 2-mim linkers forming $ZnN_4$ clusters as SBUs. These SBUs are then bridged via imidazolate rings to form the sodalite structure with a pore size of 11.6 Å and a pore opening of 3.4 Å (**Figure 18**). This 3.4 Å opening is the hexagonal 6-membered ring situated in the <111> direction of the cubic unit cell of ZIF-8. Meanwhile, a 4-membered square opening of 1.7 Å in the <100> is also present, however, is not considered as a pore opening due its small size.

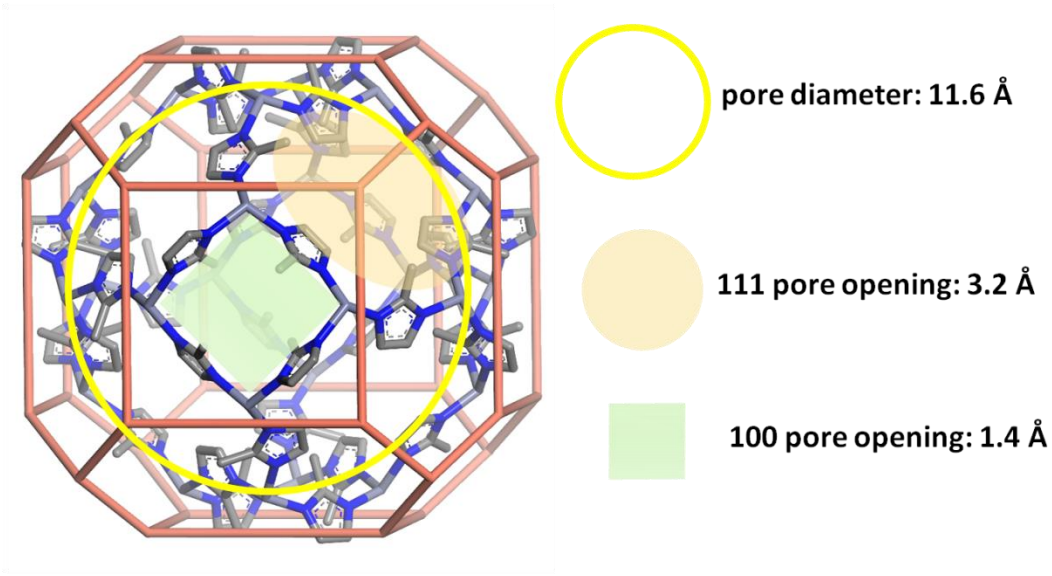


**Figure 18.** The pore structure of ZIF-8.

In principle, deprotonating the imidazolate ligand enables the bi-dentate coordination required to create 3D frameworks. The imidazolate ligand has three positions that can be independently functionalized with different groups, leading to various porous and nonporous ZIF structures. Some of relevant imidazole structures are given in **Figure 19** for a better understanding. Chen et al. [37] proposed that the type and position of these substitutions play an important role in determining the final structure of ZIFs. In the ZIF-8 case, the imidazolate ligand is decorated with a methyl group in the 2- position (**Figure 19**). This coordinated methyl group plays a crucial role in the formation of the open porous framework (since bare zinc imidazolates are nonporous) and is responsible for the excellent water stability of ZIF-8 due to

its hydrophobic character. Although ZIF-8 structurally resembles very much to zeolites, its surface chemistry is completely different. In contrast to zeolites that are known for their water affinity due to their open cationic sites, ZIF-8 does not show affinity to water, mainly owing to its structure decorated with hydrophobic methyl groups. In fact, unlike other MOFs such as MOF-5, the adsorption of ZIF-8 exhibits very low dependence on metal-adsorbate interaction.[122-124] This low dependence has been demonstrated by DFT calculations of $H_2$ adsorption and reasoned to the $ZnN_4$ clusters having insufficient free space near the zinc metal centers to guest molecules that led to poor electrostatic attraction.[125] However, studies show that ZIF-8 does not have a completely neutral network either. Simulations have been evaluated in order to determine the interaction type between the ZIF-8 pores and adsorbates such as $CO_2$ and $CH_4$. It has been found that the vdW interactions get maximized near the rings of the 2-mim linkers within the cage and the sides of the six-membered pore openings, near the methyl groups.[126] Nevertheless, its hydrophobic structure makes ZIF-8 a great candidate for gas separation membranes; a topic that we will discuss later in the applications section.

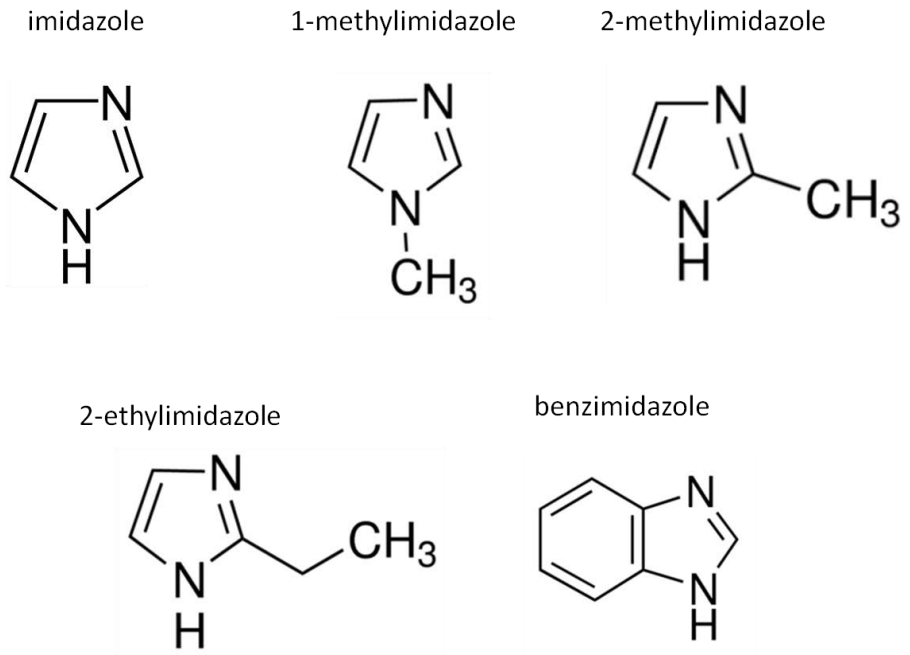


**Figure 19.** Representation of some imidazole derivatives used as linkers.

## 4.2. Thermal Properties

Upon its discovery, ZIF-8 was reported to be thermally stable up to 550 ºC under inert atmosphere according to thermogravimetric analysis (TGA).[38] This was an initial data to provide a comparison between the thermal stability of ZIF-8 and other MOFs and silicas. However, soon was realized that these TGA values were misleading for industrial applications since they represent an "instantaneous-like" thermal endurance rather than long term stability (e.g. stability at 300 ºC for 12h). In a typical TGA measurement, a fast temperature ramp is applied to heat the material and the mass change is monitored with respect to temperature. This technique is useful to track, for example, the solvent desorption from the MOF. However, it does not provide an insightful data about the kinetics of the thermal decomposition. For industrial applications, isothermal TGA tests under static temperature conditions are more relevant for material valuation.[127]

ZIF-8 is a promising material for applications that requires continuous operation at high temperatures. For instance, a ZIF-8 catalytic membrane reactor for paraffin dehydrogenation would need to be operated continuously at temperatures greater than 300 °C.[128,129] However, studies suggest that above 300 °C, ZIF-8 undergoes partial carbonization in inert, oxidizing and reducing atmospheres to form an imidazole-Zn-azirine structure, as postulated through evidence obtained from multiple characterization techniques.[130,131] Yip et al. systematically studied the thermal decomposition of ZIF-8 with static isothermal TGA under inert, air and steam atmospheres. Significant degradation was observed when holding ZIF-8 in the presence of air or steam environments at temperatures greater than 300 °C for 24 hours. ZIF-8 was also extensively depleted when held in inert environments at temperatures above 400 °C.[131] In general, when combined all the studies up to now, 200 °C is considered to be a safe operating temperature for ZIF-8 regardless the atmospheric conditions.[130,132]

It has been reported that the thermal stability of ZIF-8 also depends on the synthesis conditions and particle size. Usually, rapid syntheses at low temperatures lead to defective crystallization that alters the thermal stability, whereas solvothermal syntheses yield particles with better thermal stability. Also, smaller particles (e.g. 40 nm) were found to be less stable than micron-sized particles.[133] Similarly, ZIF-8 particles produced in methanol or DMF exhibit less stability than the ones produced in water.[131]

## 4.3. Mechanical Properties

The mechanical properties of MOFs are of great importance when considering applications such as gas sorption/breakthrough, filtering, molecular sensing and heterogeneous catalysis. For instance, MOF need to exhibit good stiffness, rigidity, and robustness to retain their structural integrity under high-pressure environments, as encountered in sorption applications. Another example lies in the usage of MOF-type materials for sensing applications,[134] where a sufficiently high elastic modulus (stiffness) is required to induce high responsiveness, in addition to the need for minimizing elastic hysteresis. Interestingly, there exist few studies about the mechanical properties of not only ZIF-8 but MOFs in general. Tan et al. conducted some systematic experiments on some ZIFs by measuring their elastic modulus (E) and hardness (H) properties along specific crystallographic orientations, using the nano-indentation method. The E is a measure of the intrinsic stiffness of the material under an elastic strain, whereas H, in general, indicates its resistance toward plastic deformation. They reported an E of ~ 3 GPa and an H of ~ 0.5 GPa for the <110> orientated facets of the ZIF-8 crystal. They also found that activated (solvent-free) crystals exhibit some ~ 6-7 % lower modulus and hardness values.[135] In another study of the same group, the shear modulus of ZIF-8 was found to be ~ 1 GPa,[136] which was considered anomalously low. However, latest studies showed that these values were not anomalies but actually the norms for highly porous materials since they mostly constitute of empty space. There also exist -in minority- some highly flexible MOFs that are superior in mechanical properties. In this context, studies suggest that ZIF-8 is a mildly "brittle MOF" compared to other flexible MOFs (e.g. MIL-53 series, MIL-47 and NOTT-300) that exhibit crystal-to-crystal phase transition (breathing behavior) under different pressures.[137] Compression tests run by Chupas et al. showed that ZIF-8 undergoes an irreversible phase amorphization at a pressure of 0.3 GPa[138] and mild ball-milling conditions.[139] However, it should be noted that there is a controversy among the results published since Düren et al. claimed that ZIF-8 shows a gate opening effect at a compression of 1.47 GPa,[114] which is a much higher pressure than the previously reported 0.3 GPa. This gate opening effect is interesting because it credits ZIF-8 for having a certain structural flexibility. It was first hypothesized with the observation of the steps that appear in the $N_2$ sorption isotherms of ZIF-8. Although, not everyone is convinced about the flexibility of ZIF-8; Silvestre-Albero et al. reported some experimental inelastic neutron scattering (INS) data, which apparently reveals the swinging of methyl groups to open the pore and allow larger molecules to enter. [140] This effect is illustrated in **Figure 20**.

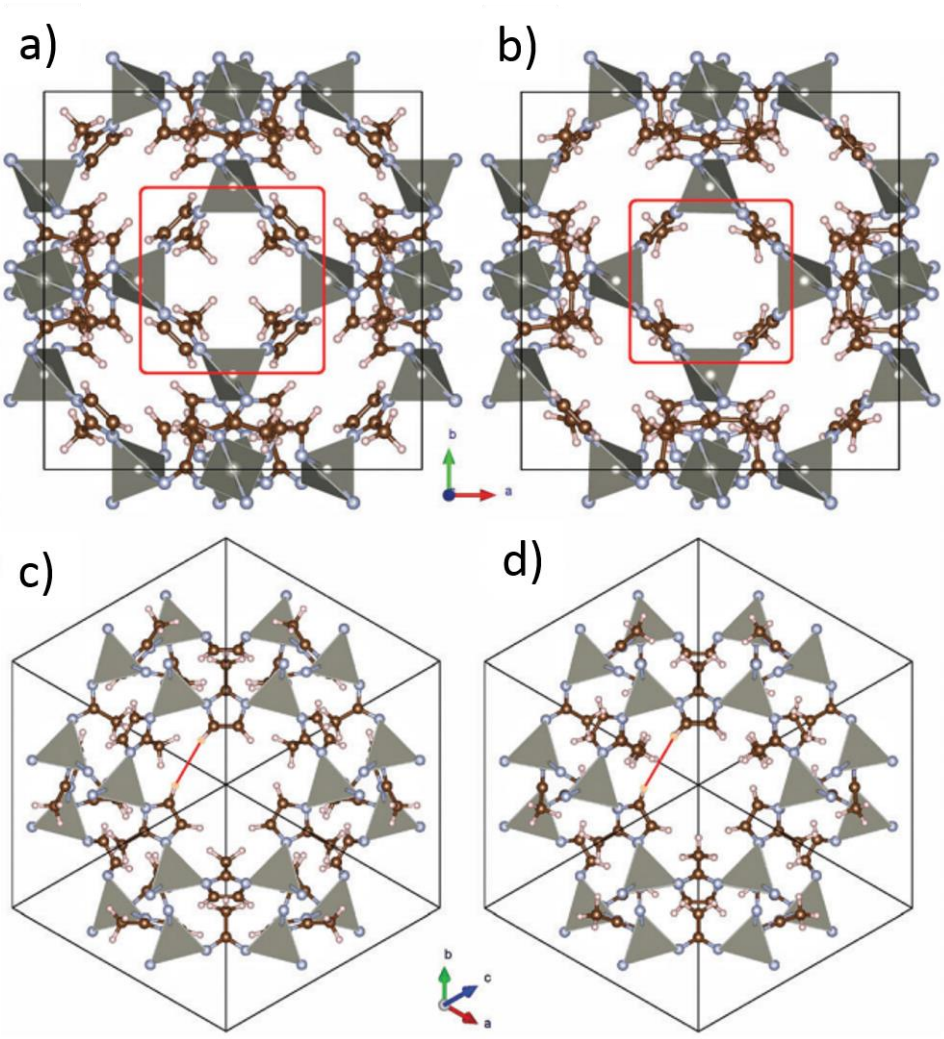


**Figure 20**. ZIF-8 structure from **a)** 100 and **c)** 111 directions. ZIF-8 with open gate structure from **b)** 100 and **d)** 111 directions. (Adapted from ref. 140).

## 4.4. Applications

Today, ZIF-8 is a commercial MOF that hit the shelves with the name Basolite® Z1200; a product manufactured by BASF and distributed by the well-known Sigma Aldrich.[141] ZIF-8 is not the most porous MOF. However, its structural robustness (hydrothermal and chemical stability) and rigid pore structure with a narrow opening make ZIF-8 a great candidate for diverse applications including molecular sieving, sensing, catalysis and drug delivery.

### 4.4.1. Molecular Sieving

Ideally, a ZIF-8 material to be used in gas separation would be a ZIF-8 membrane consisting of a thin film of continuously self-supporting material. However, real ZIF-8 is not mechanically stable enough to be a self-supporting material due to the reasons that are mentioned in **section 4.3**. To overcome this, ZIF-8 has been synthesized on different supports, including common inorganic and organic supports that are porous to provide mechanical stability. Moreover, real ZIF-8 thin films also have grain boundaries that serve as defects and provide non-selective gas transport. Defects can be limited through increasing the membrane layer thickness, but this simultaneously decreases the productivity of the membrane unit. Lately, a popular approach has been mixing the ZIF-8 particles with polymeric resins to make mechanically robust self-standing mixed matrix membranes (MMMs). Unlike zeolites, ZIF-8 can be easily mixed with polymeric resins owing to its organic structure that allows good cohesion between the particles and the polymeric matrix. Up to date, several studies have been reported on the successful application of ZIF-8 MMMs in gas separations, including $H_2$ purification that involves selective permeation of $H_2$ in $H_2/CO_2$, $H_2/N_2$ and $H_2/CH_4$ gas mixtures, natural gas sweetening by $CO_2$ removal in $CO_2/CH_4$ mixtures, post-combustion $CO_2$ capture in $CO_2/N_2$ mixtures and $O_2$ enrichment by $N_2$ removal in $O_2/N_2$ mixtures.[115]

The hydrophobic nature of ZIF-8 makes it a good target material for bio-fuel recovery. The production of bio-fuels usually results in a dilute solution having large quantities of water and short chain alcohols that can be selectively adsorbed by ZIF-8.[140,141] Various ZIF-8 materials, such as virgin or binder-added pellets, and MMMs have been successfully applied to recover mainly bio-buthanol[144,145] and other bio-alcohols[146] from aqueous solutions. In the same line, capture of other liquids that are immiscible with water can also be done.[147] ZIF-8 can also be used in the thermodynamic separation of olefin/paraffin mixtures,[148] including the separation of propane/propylene.[149-151] Given their strong diffusive selectivity towards the olefin, ZIF-8 membranes show selectivity toward the olefin greater than 30 with permeabilities beyond 100 Barrer.[150]

It should be noted that the molecular sieving studies do not represent the intrinsic capabilities of ZIF-8 since the values are highly depending on the quality of the prepared pellet or membrane. It has been found that the size of the ZIF-8 crystals can also affect the properties of a ZIF-8 membrane. For instance, nanometer-sized ZIF-8 particles are preferred to micron-sized particles in asymmetric membranes since they provide a thinner and denser selective

layer.[152] This dependence highlights the importance of the development of size/shape controlled synthesis of ZIF-8 to reach better quality membranes. Also, understanding the synthetic characters of ZIF-8 crystals can be promising for the production of high-performance and/or pore-oriented membranes that boost the separation yield. [115,153,154]

### 4.4.2. Sensing

The selective adsorption properties of ZIF-8 also make it a good candidate material for chemical and vapor sensing. Although a significantly large literature exist on the sensing applications of ZIF-8, some representative examples related to the scope of this Thesis are shared here.

The exploited photonic sensing capabilities of ZIF-8 had been exemplified in **section 2.3.4.** It is worthwhile to mention some other few but good examples to ZIF-8-based molecular sensing. For instance, electrochemical sensing has also been employed to selectively detect species in solutions and in gas mixtures.[155] Typically, ZIF-8 is coupled with a semiconductor material to gain conductivity and, the change in the electrical output upon the selective adsorption of ZIF-8 is monitored. For instance, Wang et al. reported a hybrid reduced graphene oxide/ZIF-8 material that was used to determine dopamine concentrations.[156] Zhang et al developed ZnO@ZIF-8 core-shell materials to detect $H_2O_2$ in the presence of a series of buffer solutions.[157] Similarly Ma et al. used ZnO@ZIF-8 nanorods to detect formaldehyde.[158] Luminescence has also been used as a probe to have selective detection of metal ions and small molecules using ZIF-8. Cao et al. used the difference in the luminescence intensity of ZIF-8 to selectively detect Cu(II) and Cd(II) ions and acetone in solutions.[159]

### 4.4.3. Heterogeneous Catalysis

Today, the most common heterogeneous catalysis is the case where the reactants are liquids and/or gases and the catalyst is a solid. As the catalytic reaction occurs on the surface of the solid, the surface area and the surface activity become critical. For this, the known catalyst materials are typically nanoparticles of noble metals with late transition states (Au, Pd, Pt and etc.), highly porous materials with active sites (zeolites, carbons, MOFs), oxide quantum dots, etc. Porous catalysts are identified with their active sites having moieties with

Lewis/Brønsted acidic/basic characters. Despite its excellent porosity, an ideal ZIF-8 structure is considered catalytically inactive due its inaccessible metal centers and coordinated ligands. However, in the non-ideal cases, the non-terminated surfaces and the imperfect, defect-rich areas of the crystal (resulted from fast synthesis) provide the necessary open sites for catalysis. In fact, only in the last year, there have been more than 5000 publications regarding the catalytic applications of ZIF-8 or its related composites.[121]

In 2010, as a fundamental study, Bats et al. identified the acido-basic sites of pristine ZIF-8 using CO sorption as a probe that they monitored by FTIR and DFT calculations. They found that the acido-basic sites are located at the external surface of the material or at defects, but not in the micropores of ZIF-8. These acido-basic sites were characterized as OH and NH groups, hydrogenocarbonates, low-coordinated Zn atoms, and free $N^-$ moieties belonging to linkers.[159] Reported examples confirm that ZIF-8 can catalyze both acid-, base- and acido-base-catalyzed reactions. For instance, several studies showed that ZIF-8 can catalyze the Knoevenagel condensation reaction as a base-catalyzed model reaction with high conversion factors.[161-165] For instance, Phan et al. reported a 100 % conversion for the condensation of benzaldehyde and malononitrile using ZIF-8 at room temperature. As for acid-catalyzed reactions, it has been demonstrated that ZIF-8 can catalyze Friedel-Craft acylation of anisole and benzoyl and esterification of glycerol and oleic acid.[166,167] Also, Bats et al. showed that ZIF-8 can catalyze the transesterification of vegetable oils as an example to acido-base-catalyzed reactions.[160] Some other catalytic reactions such as the synthesis of carbonates,[168,169] oxidation and epoxidation,[170,171] and the hydrogen production[172,173] could also be conducted using pristine ZIF-8.

ZIF-8 is also an excellent support material for other catalysts such as inorganic nanoparticles (InNPs) that can be incorporated to ZIF-8 to form InNP@ZIF-8 via encapsulation,[174] post-synthetic attachment or growth.[175] Noble metal nanoparticle@ZIF-8 materials were the most explored for catalytic applications, such as Au@ZIF-8 for the oxidation of CO[176] and alcohols,[177] reduction of 4-nitrophenol[177] and cyclization reactions.[179] Also, examples of Pt@ZIF-8 were reported to catalyze the reduction of 1-hexene[180] and 1-hexyne,[181] oxidation of ethylene[182] and hydrogen generation.[183] Oxidation of 1,4-butynediol[184] and aminocarbonylation[185] have been catalyzed using Pd@ZIF-8 materials.

Otherwise $Fe_3O_4$@ZIF-8 material has been used to catalyze the Knoevenagel condensation reaction with 99% conversion. The Ir, Pd, Pt, and Ru nanoparticles incorporated on ZIF-8 were

applied to the hydrogenation reaction using molecular $H_2$.[174,186-189] An interesting $Zn_2GeO_4$@ZIF-8 material (ZIF-8 nanoparticles onto $Zn_2GeO_4$ nanorods) was also used as a photocatalyst for the reduction of $CO_2$ in an aqueous solution to form methanol.[190]

### 4.4.4. Drug delivery

Several studies have shown that ZIF-8 can be used as a therapeutic agent due to its high encapsulation capabilities of bio-macromolecules. Typically, anti-cancer drugs (e.g. doxorubicin, 5-fluorouracil, etc.),[191,192] proteins,[193] insulin[194] and many others have been encapsulated by synthesizing ZIF-8 crystals in the presence of these large molecules in solution. The new generation drugs are desired to have a drug carrier that provides either an externally stimulated (targeted) or a controlled (slow) release of the drug molecules. The fair stability of ZIF-8 in basic conditions[38] and its instability in acidic conditions[195] make ZIF-8 a potential pH sensitive drug carrier that releases its content upon decomposition. Wang et al. demonstrated that 5-fluorouracil loaded ZIF-8 particles can exhibit a slow drug release (in 7 days) at pH 7.4 and fast release at pH 5.0 upon the dissolution of ZIF-8 particles.[191]A similar study was reported by Su et al. for doxorubicin as the encapsulated drug and polyacrylic acid@ZIF-8 nanoparticles as carriers.[196] Coronas et al. encapsulated caffeine in ZIF-8 and reported its controlled release in 27 days. They also commented that ZIF-8 can provide a thermal protection to caffeine since the loaded particles (and the caffeine molecules) withstood 300 $^oC$ without significant decomposition.[197] Kim et al. proposed the usage of ZIF-8 as a storage material for proteins and demonstrated that bovine serum albumin (BSA) can be totally encapsulated in ZIF-8 with a mass ratio of BSA:ZIF-8 = 1:3.[193] For diabetes diseases, the controlled release of insulin is desired for the homeostasis of glucose. Despite these many examples of ZIF-8 based drug carriers, studies on the biocompatibility of ZIF-8 are only at an embryonic stage. Recently, Pané et al. reported an extensive study on the biocompatibility of ZIF-8 and the encapsulation of the insulin hormone. They conducted some *in vitro* experiments to explore the cytotoxicity of ZIF-8 on various types of human cells. Based on their findings, they claimed that ZIF-8 is biocompatible when used below the threshold concentration of 30μm/ml in the human body. This result was also evaluated with the insulin encapsulation experiments. It has been found that, an insulin@ZIF-8 dose of only 1.2 μm/ml is sufficient to provide the daily dose of insulin necessary in a conventional therapy of type I or II diabetes.[194] It is remarkable that this dose is way below the biocompatibility threshold that they reported

and the results are promising. However, this threshold, for now, cannot be universal for some reasons that are discussed below.

Zn(II) ions leaching from ZIF-8 particles is one of the main reason of the cytotoxicity and is a consequence of the instability of ZIF-8 in the solvent medium. It has been already covered that the thermal stability of ZIF-8 crystals might vary upon many factors such as the solvent used in the synthesis, the particle size, etc. Reasonably, one can expect similar trends for the water stability as well. In their study, Pané et al. did their cytotoxicity experiments using one single type of ZIF-8 particle, micron-sized ZIF-8 crystals that they synthesized in water following a protocol adopted from the work of Maspoch et al.[195] Also recently, Sumby et al. reported an extensive study on the influence of the crystal morphology on the catalytic activity of ZIF-8. Coherent with previous studies,[169] they found that smaller particles (e.g. 50 nm) with higher surface-to-volume ratio exhibited better catalytic activity. In the mean time, they also monitored the leaching of Zn(II) ions in the reaction solutions for different sizes of ZIF-8, and found that this Zn(II) leaching is maximum for the smallest particles, being mainly responsible for the increase of the catalytic activity.[198] This finding is somehow coherent with the finding of Wiebcke et al., who had claimed that small (40 nm) nanoparticles were thermally less stable[133] compared to microcrystals. Interestingly, in their systematic comparison, Sumby et al. also employed the protocol of Maspoch et al. to produce ZIF-8 microcrystals and found that they had less Zn(II) leaching compared to 50 nm particles. These results suggest that the generality of the 30 µg/ml threshold reported by Pané et al. is questionable since, as demonstrated by Sumby et al., smaller crystals will have more leaching of Zn(II) and hence, will be more cytotoxic.[198]

In the light of these experiences and future expectations, high importance should be given to understand the synthesis and crystallization behaviors of ZIF-8 and, with this learning, to rationally control the morphology of ZIF-8 crystals with nanometric precisions and preferred orientations.

## 4.5. Crystallization and Morphology

Typically, ZIF-8 crystals are recognized by their rhombic dodecahedral (RD) or truncated rhombic dodecahedral (TRD) shapes. The term RD means literally a polyhedral shape with 12 rhombus-shaped facets, and the term truncated is used to determine polyhedrons with cut vertices. For ZIF-8 having SOD topology, the RD shape constitutes of 12 equivalent rhombus-shaped (or tetragonal) facets that are all <110> oriented. On the other hand, the TRD shape is an RD shape with square cuts (or truncations) in the 6 {100} vertices. The TRD shape constitutes of 12 irregular hexagonal facets that are <110> oriented and 6 square facets that are <100> oriented (**Figure 21**). This final RD shape of ZIF-8 is the consequence of the Wulff's rule, where the slowest growing direction (which is the <110> for ZIF-8) determines the final shape and thermodynamically most stable facet orientation. The crystal growth of a ZIF-8 particle starts from an all <100> oriented cube that gradually evolves first into TRD and finally to RD shape (ref. 196). Therefore, the TRD shape of ZIF-8 can be considered as the product of some "unfinished" crystal growth process. In some cases, this crystal growth habit is intentionally hindered by using capping agents to obtain well-defined cubic crystals in different sizes[199] or TRD crystals with known truncations to do shape-engineering in the colloidal particles.[200] This will be covered in detail in the following sections after being familiarized with the synthesis of ZIF-8.

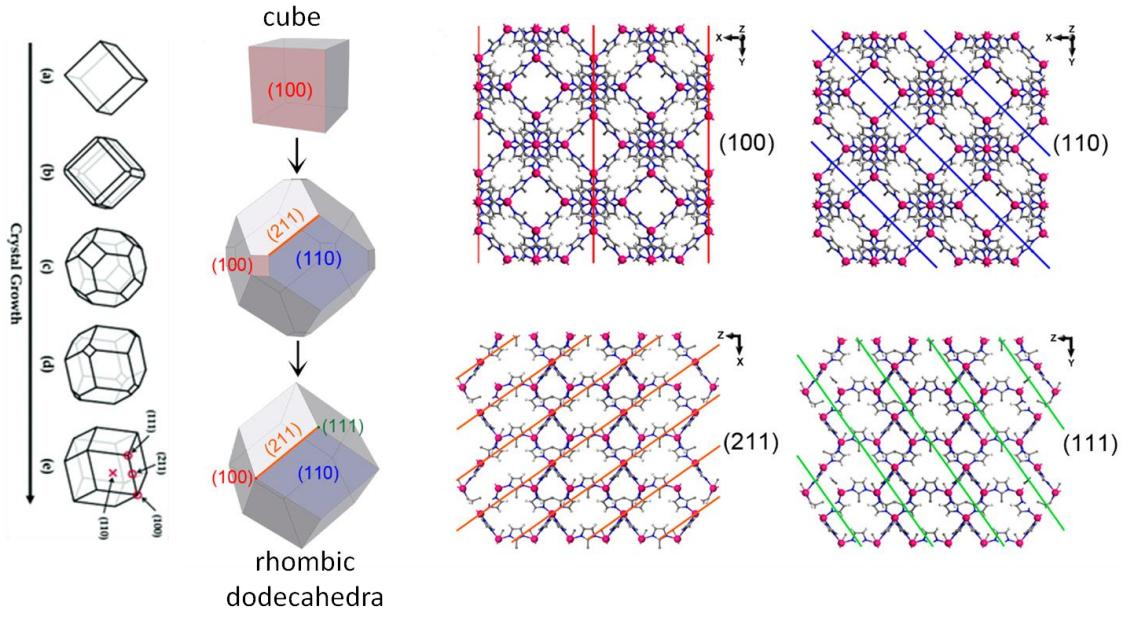


**Figure 21** Morphological evolution of ZIF-8 crystal and the crystallographic view of different facet orientations.

## 4.6. Synthesis

Among others, one of the aspects that brought fame to ZIF-8 is the simplicity of its synthesis. Typically, a 2-mim solution is mixed with a Zn (II) solution under certain circumstances that can vary deeply. In the first reported protocol, Chen et al. carefully layered a methanolic 2-mim solution over an aqueous $Zn(OH)_2$ and ammonia solution in a crystallization tube to get colorless ZIF-8 crystals after a month.[37] Since then, the synthesis of ZIF-8 has rapidly evolved to be easier, faster, greener and to get higher yields. Today, it is known that the type of solvent, metal source, metal-to-ligand ratio, capping agent and the addition of base have an effect on the synthesis and the morphology of ZIF-8 crystals. In this Thesis, the solvothermal (typically in DMF at high temperatures) and others, either aqueous or methanolic room temperature syntheses will be covered along with the aforementioned synthesis variables that enable morphology control. The alternative methods such as microwave-assisted, sonochemical, mechanochemical, microfluidic and continuous flow syntheses are not included here since they are mainly developed to improve yield and to reduce cost, which are some valuable concerns but out of the scope of this Thesis.

### 4.6.1. Evolution of the Synthesis of ZIF-8

In the first ZIF-8 synthesis of Chen et al., the Zn (II) and 2-mim were mixed with the stoichiometric ratio of ZIF-8; that was 1:2. Since the formation of ZIF-8 relies on the deprotonation of 2-mim, the synthesis was realized in the presence of ammonium to help the deprotonation. However, the process was very slow due to the lack of available deprotonated 2-mim in the medium.[37] Then, Yaghi et al. reported a faster protocol based on a solvothermal method using DMF as the solvent at 140 $^{o}$C in an autoclave. This protocol seemed to be robust and yielded good quality large ZIF-8 microcrystals within a day. This ZIF-8 showed excellent porosity close to the theoretical approximation. This relatively faster crystallization can be attributed to the high temperature and the decomposition of DMF into basic species that help the deprotonation of the 2-mim. However, as a drawback, DMF was trapped in the pores of ZIF-8 due its large size. Thus, these DMF molecules could not be completely removed by evacuation (activation) even at high temperatures. It required a process called solvent exchange, in which the DMF molecules were first replaced with methanol (that has a smaller kinetic diameter than DMF) to get properly activated porous crystals.[38] Nevertheless, these

crystals were produced as a proof of concept and designed to be very large (distinguishable by naked eye) on purpose for synchrotron X-ray analysis. In 2009, Wiebcke et al. reported the synthesis of colloidal nano-sized ZIF-8 in methanol at room temperature by using an excess amount of ligand (Zn:2-mim = 1:8). They claimed that the ligand could act both as a linker unit in its deprotonated form and as a stabilizing unit in its neutral form. Considering the $pK_{a1}$ (7.1) and $pK_{a2}$ (14.2) values for imidazole as a rough estimate for the acid-base properties of 2-mim in methanol, one would expect that an equilibrium of the cationic (protonated) and neutral forms exists in solution and deprotonation of 2-mim is only driven by the crystallization of ZIF-8 (gain of lattice energy). Enough neutral 2-mim should then be available in solution for terminating the growth and stabilizing the positively charged nanocrystals.[132] This study of Wiebcke et al. was credited for replacing the environmentally malign DMF with a relatively less malign methanol that can easily be removed from the structure by simple activation. Also, the trick of using an excess amount of ligand paved the way of the facile room temperature synthesis of ZIF-8 in the future. In 2011, Lai et al. were the firsts to produce ZIF-8 in water at room temperature. Switching from methanol to water in the synthesis of any product is of extreme importance for the economical and environmental aspects. However, in the work of Lai et al., the fast synthesis that took only a few minutes led to poorly crystalline ZIF-8. This was confirmed with a pore volume of 0.32 $cm^3/g$, which is a value almost the half of the theoretical prediction.[132] A year later, Vajo et al. also produced ZIF-8 in water at room temperature with the addition of triethylamine as a pH adjuster however, similarly low porous crystals ($V_p$ = 0.32 $cm^3/g$) were obtained. In addition, there was also clear evidence of existence some by-products or amorphous phases.[201] The relatively more successful aqueous room temperature synthesis of ZIF-8 was reported by Miyake et al. in 2013. Although they reported similarly low porosity values at fast synthesis conditions (5 min), the porosity of their ZIF-8 crystals approached to the theoretical values with an $S_{BET}$ of 1550 $m^2/g$ and a $V_p$ of 0.65 $cm^3/g$ when synthesized in one hour using Zn:2-mim in the 1:60 ratio. They also systematically investigated the role of the Zn:2-mim ratio on the crystal size of ZIF-8, and they found that increasing the ligand decreases the size of ZIF-8. [202] In fact, all the ZIF-8 crystals produced by then at room temperature were not bigger than ~250 nm. In 2013, Yamauchi et al. reported a synthetic procedure to get bigger ZIF-8 crystals (up to 1 μm) by using $Zn(OAc)_2$ instead of the commonly used $Zn(NO_3)_2$.[203] By 2013, the synthesis of ZIF-8 was fairly understood and began the era of controlling the morphology with different synthetic ingredients (e.g. solvent, metal source, ligand, capping agent, etc.) in order to get ZIF-8 crystals with different size, shape and good monodispersity.

### 4.6.2. Effect of the Solvent

In every particle synthesis in solution chemistry, the particle size is determined by the nucleation and growth rates. Increasing the nucleation rate always leads to smaller particles since the growth will slow down very early and eventually stop due to the lack of nutrients. For ZIF-8, a critical step in controlling the nucleation process is the deprotonation of 2-mim ligand and the amount of deprotonated ligand controls the amount of particle nucleation.[114] In this sense, the solvent can have an effect in the deprotonation process and therefore on the final particle size. For instance, the firstly synthesized ZIF-8 particles were as big as 200 μm as a result of the slow nucleation and growth. In the solvothermal process, the DMF was heated until it got slightly decomposed to some basic species, which slowly deprotonated the imidazolate ligand, leading to large crystals.[37] Later, methanol was used in the synthesis of ZIF-8 with high Zn:2-mim ratios, yielding crystals as small as 40 nm. It has been reported that, when repeated the same procedures with the same concentration and metal sources; syntheses in water yielded bigger crystals than methanol. The method of crystal nucleation through creating an environment where the reactants are less soluble is known.[204] In this scenario, the reactants of ZIF-8 are less soluble in methanol than water and therefore, the almost instantaneous precipitation in methanol leads to small nanocrystals compared to larger microcrystals that are produced in water.

### 4.6.3. Effect of the Metal Source

Many sources of zinc can be utilized in ZIF-8 synthesis, including nitrate, chloride, carbonate, and acetate salts and zinc oxide. These different metal sources have been shown to affect the particle size. The counterion of the zinc source serves as a coordination modulator, where the difference in acidity of conjugate acids can affect the population of the species present in the growth solution. For instance, utilizing identical synthesis conditions produced 50 nm nanoparticles when using $Zn(NO_3)_2$ and 2 μm-sized particles when using $Zn(OAc)_2$; presumably because the acetate counterions suppress nucleation.[115] In 2014, Schneider et al. reported a systematic study about the effect of the different zinc salts on the morphology and size of ZIF-8 crystals (**Figure 22)**.[205] They synthesized ZIF-8 in methanol using $Zn(NO_3)_2$, $Zn(acac)_2$, $Zn(ClO_4)_2$, $ZnSO_4$, $Zn(OAc)_2$, $ZnCl_2$, $ZnBr_2$ and $ZnI_2$. They found that small ZIF-8 nanocrystals with diameters varying between 50 and 200 nm were obtained with reactive zinc

salts like $Zn(acac)_2$, $Zn(NO_3)_2$, $ZnSO_4$ and $Zn(ClO_4)_2$. However, the use of $ZnCl_2$, $Zn(OAc)_2$ and $ZnI_2$ yielded ZIF-8 crystals with sizes varying between 350 and 650 nm. Finally, the low reactive $ZnBr_2$ was found to generate the largest microsized crystals. They also demonstrated that ZIF-8 crystals produced with different zinc salts having different size and morphology have different porosities and catalytic activities. In this study, the crystals produced with the nitrate salt exhibited the highest $S_{BET}$ of 1700 $m^2/g$ and the highest catalytic activity when used for Knoevenagel or Friedländer condensations, potentially because of its nano-sized morphology and highly porous structure.

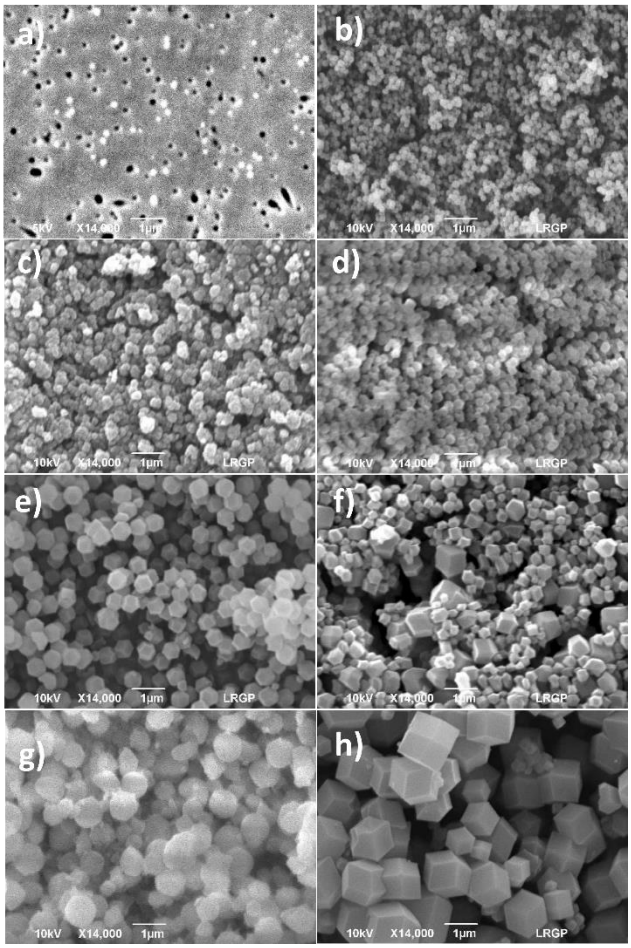


**Figure 22**. SEM images of ZIF-8 crystals obtained from a) $Zn(acac)_2$, b) $Zn(NO_3)_2$, c) $ZnSO_4$, d) $Zn(ClO_4)_2$, e) $Zn(OAc)_2$, f) $ZnCl_2$, g) $ZnI_2$, and h) $ZnBr_2$. (Adapted from ref. 205).

### 4.6.4. Effect of the Added Base

The popular usage of large excesses of ligand (up to Zn:Hmim = 1:100) in the synthesis of ZIF-8 set a significant scale-up limitation since a great majority of the ligand remains

unreacted. This issue was overcome through the addition of basic species in the synthesis.[206-208] For instance, incorporating triethylamine (TEA) into the synthesis enabled good crystallization of ZIF-8 in water at a Zn:Hmim ratio of 1:8 (ref. 201) and the addition of *n*-butylamine as the growth modulator resulted in smaller ZIF-8 particles with diameter of 18 nm.[206] The concentration of *n*-butylamine affected the final particle size, with lower concentrations producing smaller particles. This observation points to the complex speciation present in these growth solutions. The basic species can deprotonate the ligand and also coordinate with the metal center as well. These two phenomena can compete with each other, and the addition of base can have different trends. For instance, it has been reported that, at room temperature, formate ion and 1-methylimidazole can act as coordination modulators to suppress nucleation and to have larger ZIF-8 crystals.[206] On the other hand, at higher temperatures, the formate ion does not coordinate to the growing ZIF-8 structure and only serves to deprotonate the 2-mim, which results in a larger concentration of small particles.[208] The role of the base has been majorly increasing the yield of the synthesis rather than size and shape control. In this latter case the real shape modulators as additives have been the surfactants.

### 4.6.5. Effect of the Added Surfactant

The word surfactant is the blend of surface active agent, which is typically a molecule that modifies the interface properties between two substances. They have been widely used in nanoparticle synthesis since the attachment of the surfactant to the surface of the nanoparticle provides a controlled growth and an electrostatic or steric shield that prevents the aggregation. It has been also found that surfactants can modulate the nanoparticle size and shape by getting involved in the synthesis; typically as growth inhibitors.[210] The first study on the effect of the surfactants on the size and shape of ZIF-8 was done by Lai et al. in 2011, which was also the first example for MOFs in general.[199] In their work, they systematically studied the effect of cetyltrimethylammonium bromide (CTAB) concentration (lower than the critical micellar concentration) on the morphology of the ZIF-8 particles in aqueous synthesis (**Figure 23**). They found that increasing the CTAB concentration suppressed the <100> growth of ZIF-8, leading to the formation of smaller and cubic-shaped crystals. This was explained with the selective attachment of the hydrophobic tail of the CTAB molecules on the energetically favorable {100} facets. Therefore, the growth of ZIF-8 was drastically slowed down since the

fastest growth of ZIF-8 occurs in the <100> direction. As the hydrophobic tail of CTAB was responsible for the growth modulation, similar results were obtained using cetyltrimethylammonium chloride (CTAC) and trimethylstearylammonium chloride (STAC), which are some analogous surfactants having a similar hydrocarbon tail. However tetrapropylammonium bromide (TPABr) seemed to have no significant effect due its shorter hydrocarbon tail. Also, no modulation occurred when using methanol as the solvent, probably due to the higher solubility of the surfactant in methanol.

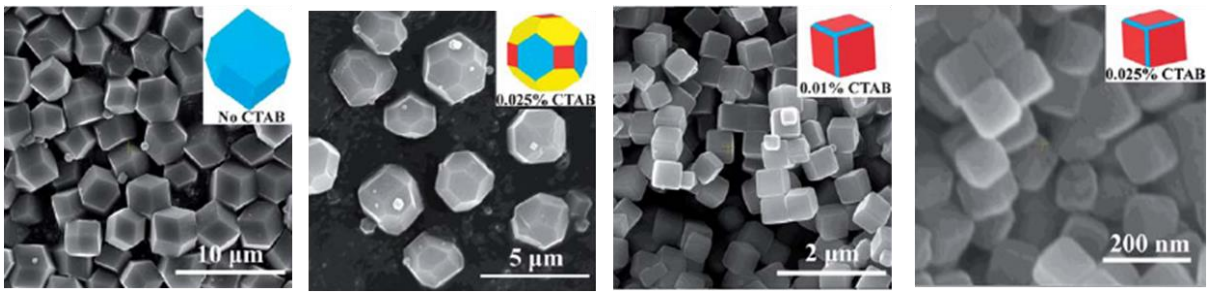


**Figure 23.** SEM images of ZIF-8 particles produced with different amounts of CTAB. (Adapted from ref. 199).

Sodium dodecyl sulphate was also found to have similar modulating effects as CTAB, proving further that the type of the counterion does not have much effect on the modulation. Later, nonionic surfactants such as Pluronics P123 and F127,[211] Tween 80, Span 80[212] and Brij 78[213] were employed for the modulation of ZIF-8 crystals and smaller nanocrystals with irregular shapes were obtained. In 2017, Hong et al. reported some unprecented shapes of ZIF-8 crystals including octahedra, hexapods and burr puzzles using ony tris(hydroxymetyl)aminomethane (TRIS) or a combination of TRIS with CTAB. They found that, similar to the adsorption affinity of CTAB molecules to the {100} facets, TRIS molecules preferentially stabilize the {111} facets and lead to the formation of octahedral ZIF-8 crystals.[214] In 2018, Maspoch et al. reported some highly monodisperse TRD ZIF-8 crystals (polydispersity < 5 %) with different truncations, produced with CTAB via an aqueous synthesis. Different from the work of Lai et al., instead of the nitrate salt, they used the acetate that is known to yield bigger and more monodisperse crystals compared to the ones produced with the nitrate salt. They were able modulate the truncation of the TRD particles with a precision of ~5-10 nm, by combining both the CTAB and ligand concentration as modulating agents (Figure X phase diagram of particles with different truncations).[200] Very recently, Pan et al. published a work in which they extensively screened the effect of the CTAB and ligand concentration on the final morphology of ZIF-8 crystals (**Figure 24**). In this study, the authors

reported three unprecedented shapes for ZIF-8, namely octagonal plates, interpenetration twins and nanorods.[215]

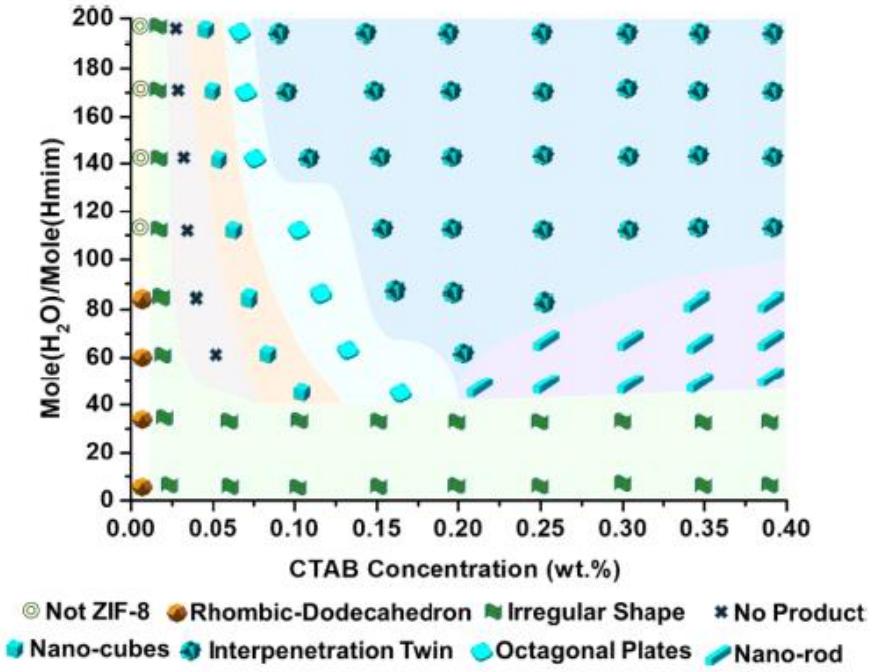


**Figure 24**. Map of ZIF-8 morphologies with respect to 2-mim and CTAB concentration. (Adapted from ref. 215).

This synthetic and morphological control using synthetic ingredients enabled different morphologies of ZIF-8 that promise different potential applications, such as improved catalytic activity, molecular sieving, photonic properties, etc. There also exists a large literature on the post-synthetic engineering of ZIF-8 to obtain different morphologies (e.g. hollow shapes) unachievable with conventional synthetic methods, carbon materials using ZIF-8 as a sacrificial agent, and some functional composites with other ZIFs, MOFs and inorganic nanoparticles (InNPs) to impart new functions to ZIF-8 (e.g. catalytic activity).

## 4.7. Post-Synthetic Modification and Engineering of ZIF-8

In this section, the alteration of the morphology of ZIF-8 using post-synthetic treatments is covered. For a better conception, these shaping treatments are grouped into top-down and bottom-up shaping approaches, depending on the followed post-synthetic route to make the ZIF-8-based material. Also, it should be noted that ZIF-67 (as the cobalt version of ZIF-8) will appear in some examples mainly because the works on these two ZIFs are majorly

interconnected (e.g. ZIF-8@ZIF-67 materials). Since ZIF-67 shares identical SOD topology, RD morphology and synthetic/crystallization behaviors with ZIF-8, another introduction regarding this MOF was not considered necessary in this text.

### 4.7.1. Top-down Shaping of ZIF-8

In the recent years, it has been possible to post-synthetically change the morphology of ZIF-8 by top-down approaches that controllably deconstruct the material to yield the desired morphologies. Typically, some unprecedentedly shaped, hierarchically porous or simply hollow ZIF-8 crystals have been obtained using wet-chemical etching, template removal and solvothermal treatment. The key of this top-down shaping is finding a mechanism that selectively and controllably sculpts the crystals. In 2012, Oh et al. obtained some spherical hollow ZIF-8 particles by a template-assisted method using polystyrene (PS) spheres as template. These polystyrene spheres with a carboxylate terminal were added to the reaction precursors containing Zn(II) ions and 2-mim and initiated the crystallization of ZIF-8 on their surface, yielding a core-shell type PS@ZIF-8 material. Finally, hollow ZIF-8 microspheres were obtained by treating this PS@ZIF-8 with DMF, which selectively removed the PS polymer (**Figure 25**).[216]

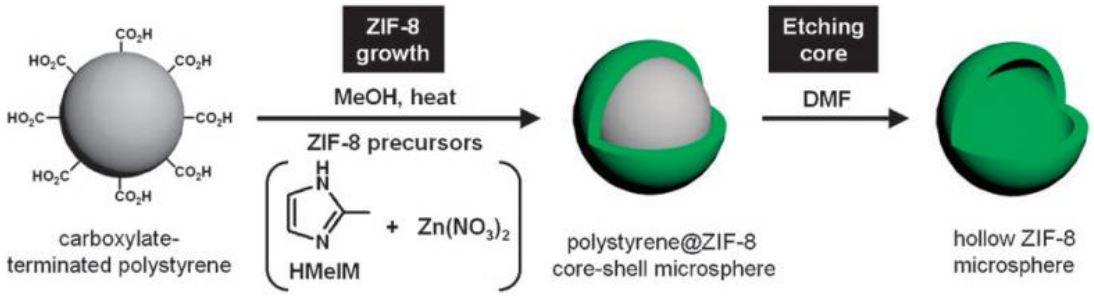


**Figure 25**. Schematic illustration of obtaining hollow ZIF-8 microspheres by using PS template. (Adapted from ref. 216).

In 2015, Maspoch et al. followed a template-free, wet-chemical selective etching process to obtain cubic, tetrahedral and hollow-box-shaped ZIF-8/67 crystals. In this work, they used an acidified/basified xylenol orange (XO) solution as etchant and chelating agent. The XO

solution sequentially protonated the imidazolate ligands, broke the metal-ligand coordination bonds and sequestered the liberated Zn(II)/Co(II) ions to form water soluble metal-XO complexes. Different morphologies were obtained by simple adjustment of the pH of the etchant solution, from which any significant loss in surface area/porosity was observed. The acidic/basic etching of the ZIF-8 was surface-selective and preferentially favored the directions of metal-ligand bond and the crystal facets with higher dimensionalities.[195] Later, the same hollow-box-shaped ZIF-8 particles were produced by Moon et al. with slight improvements. In their study, they finely adjusted the pH of the acidic XO solution to tune the size of the macropores and the wall thickness of the ZIF-8 hollow-boxes from ~100 nm to ~200 nm. They also demonstrated that these hierarchically macro- and microporous ZIF-8 hollow-boxes can be used as sacrificial templates to obtain N-doped porous carbon materials by pyrolysis, maintaining their initial shapes. These hierarchical ZIF-8 derived carbon materials exhibited superior performance as adsorbents for large dye molecules and as catalysts for the oxygen reduction relative to macropore-free N-doped carbons obtained from the parent non-etched ZIF-8 crystals.[217] As another example to chemical etching, Caruso et al. reported in 2016 some hollow ZIF-8 structures along with some other MOFs, obtained via post-synthetic acidic etching with tannic and gallic acids. In their proposed mechanism, the H+ ions generated by the tannic/gallic acid protonated the 2-mim and destroyed the MOF from inside, whereas the shell remained untouched as the large tannic and gallic acid molecules blocked the pores of the ZIF-8, providing a surface protection against etching. They reported an $S_{BET}$ value ~30 % lower than the parent ZIF-8 crystals, indicating a partial amorphization in the crystals due to the etching treatment.[218]

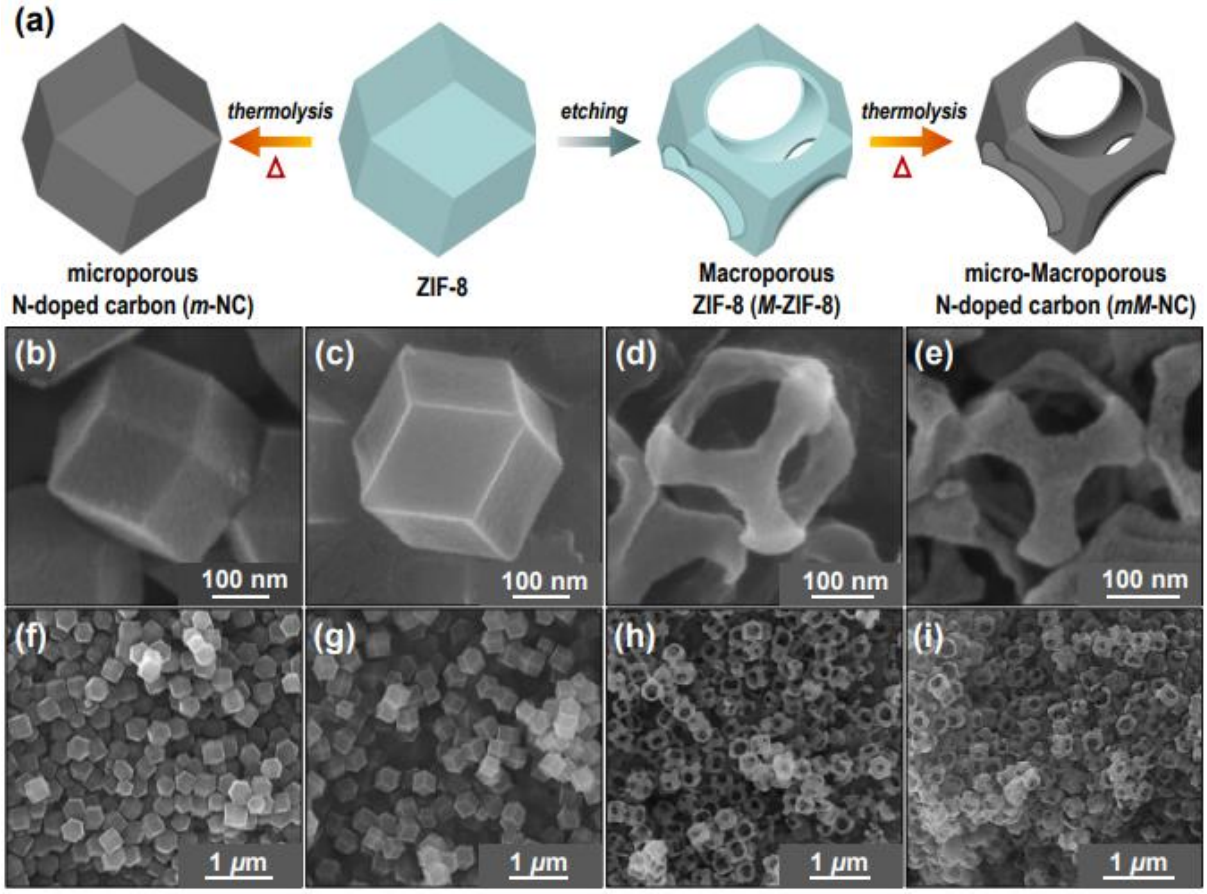


**Figure 26.** a) Schematic illustration of the preparation of hollow-box ZIF-8, carbonized hollow-box ZIF-8, and carbonized regular ZIF-8. High and low magnification SEM images of b) and f) carbonized regular ZIF-8, c) and g) ZIF-8, d) and h) hollow-box ZIF-8, and e) and i) carbonized hollow-box ZIF-8. (Adapted from ref. 217).

The chemical etching with tannic acid was later employed by Lou et al. to produce some yolk-shelled bimetallic Zn/Co-ZIF particles that were then subjected to a sulphurization process to yield a Zn-Co-S material having the same yolk-shelled RD morphology as their parent Zn/Co-ZIF particles. This Zn-Co-S material was used as battery-type electrode material for hybrid supercapacitors, exhibiting enhanced specific capacitance and improved cycling stability compared with its single-shelled versions. This example proved that the complexity in the morphology can be beneficial for application purposes.[219] Very recently, the same group published another work on the chemical etching of ZIF-8 particles with tannic acid to obtain multi-shelled (up to 5-shelled) particles in the yolk-shell design. In this work, the number of the shells was correlated with the initial particle size of the parent ZIF-8 where ~4 μm crystals yielded 5-shelled RD particles and ~3 μm crystals yielded 4-shelled RD particles. Then, similarly to the previous work, the shelled particles were converted into zinc sulphide and a cation exchange was applied to partially replace the Zn with Cd to have a ZnS/CdS material in

RD shape. They found that the 3-shelled ZnS/CdS material exhibited the best photocatalytic activity among others.[220] Their work is illustrated in **Figure 27**.

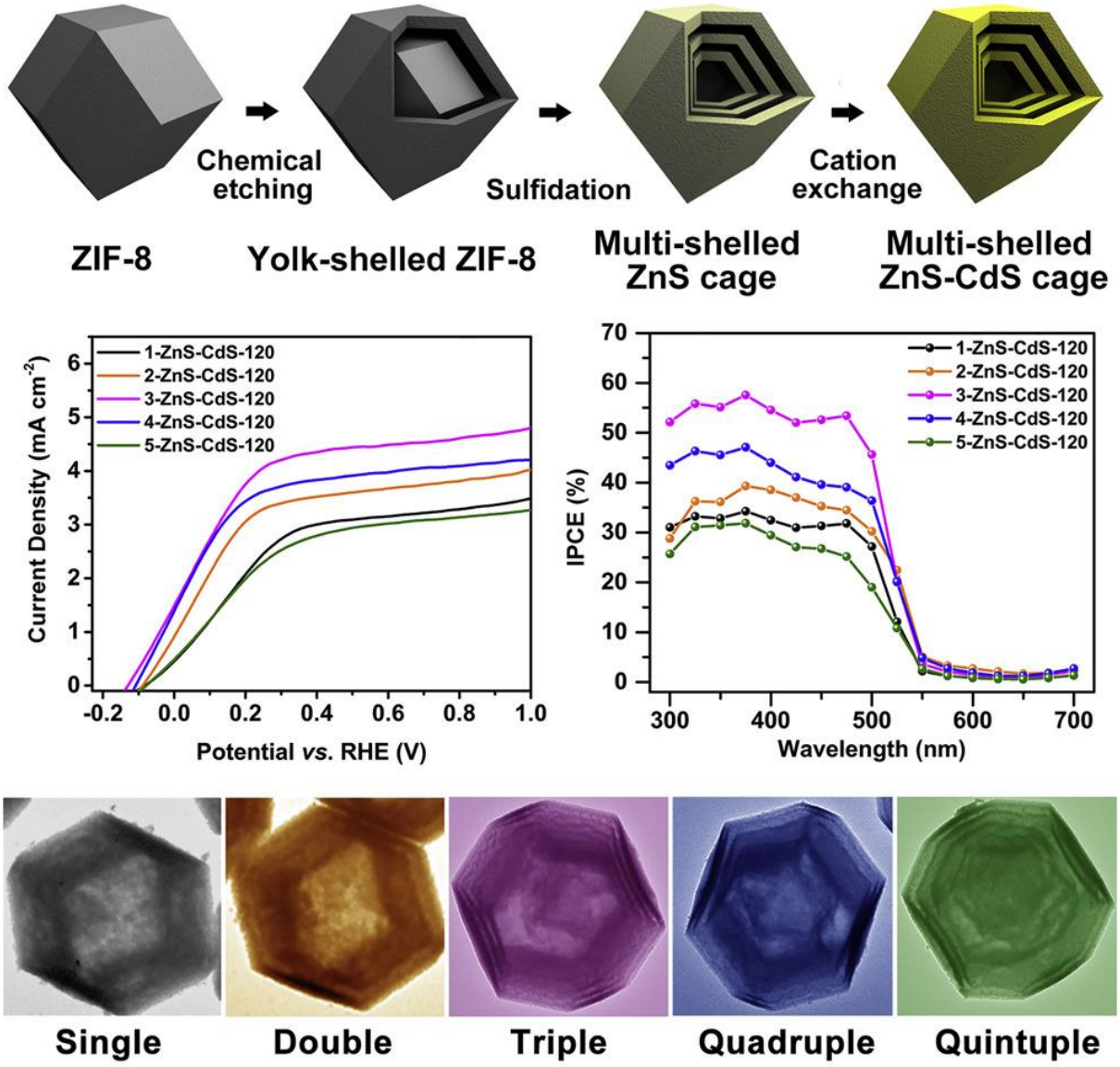


**Figure 27.** Multi-shelled (up to 5-shelled) ZIF-8 derived ZnS/CdS particles in the yolk-shell design. (Adapted from ref. 220).

Tsung et al. produced some hollow ZIF-8 particles via a process called double-solvent mediated overgrowth. Pristine ZIF-8 particles produced in water were used as seeds to grow a ZIF-8 on these crystals in methanol. They realized that the inner cores that were water-loaded ZIF-8 particles got disassociated and dissolved after a certain ageing in methanol leaving behind well shaped hollow ZIF-8 particles. They proposed that, during the formation of the ZIF-8 shell under the water–methanol double-solvent overgrowth, the pH of the internal water

environment drops due to the deprotonation of the 2-mim in the external methanol environment. Since ZIF-8 is not stable under this condition in water, it dissociates and forms a hollow cavity.[221] A similar example was demonstrated by Li (Y. D.) et al., who conducted a seed-mediated synthesis of core-shell ZIF-67@ZIF-8 to produce hollow ZIF-8 crystals. They used the solubility difference between these two isostructural ZIFs to selectively dissolve the ZIF-67 core in hot methanol to obtain hollow ZIF-8 crystals with some residual Zn-Co species trapped inside the hollow cavity.[222] Li (Y.) et al. employed a method to obtain several materials called hollow Zn-Co-ZIFs following a similar approach to the one reported from Li (Y. D.) et al. In their study, they first produced the ZIF-67@ZIF-8 core-shell material by a sequential addition of Co (II) and Zn (II) solutions into the 2-mim solution. Then, the obtained crystals were incubated in hot methanol in the presence of Co (II) ions to selectively etch the ZIF-67 core and to yield hollow ZIF-8 crystals with residual Zn-Co species trapped inside the hollow cavity.[223]

Very recently, an interesting ZIF-8 material consisting of ~ 1 to ~4 µm sized crystals with ordered internal macropores has been reported by Chen et al. In their work, they followed a strategy (known to produce inverse opals) of soaking the ZIF-8 ingredients in an ordered monolithic superstructure made of PS spheres. They induced the in-situ crystallization of ZIF-8 inside the superstructure by adding a mixture of ammonia/methanol. Interestingly, instead of the expectedly continuous monolithic PS@ZIF-8 structures, some polyhedral crystals with exposed {111}, {100} and {110} facets were formed. Finally, these microparticles were exposed to THF to remove the PS template and to yield some hierarchically porous ZIF-8 materials with ordered ~270 nm sized macropores (**Figure 28**).[224]

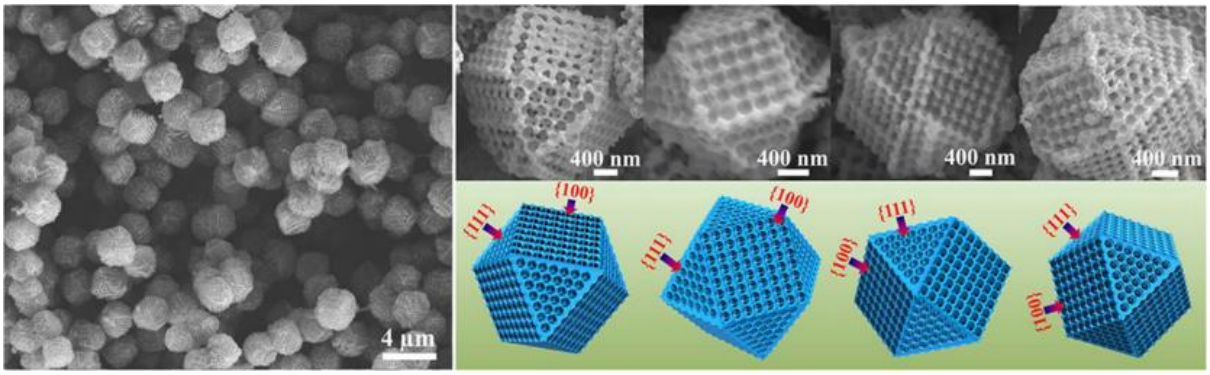


**Figure 28.** Hierarchically porous ZIF-8 particles with ordered ~270 nm sized macropores prepared by removal of an ordered PS template. (Adapted from ref. 224).

### 4.7.2. Bottom-up Shaping of ZIF-8

The post-synthetic bottom-up shaping has been used as a constructive strategy to obtain new morphologies or complex structures of ZIF-8/67 crystals. Generally, some as-synthesized crystals were taken as seeds and subjected to one or more growing steps to yield layered ZIF-8/67 crystals. The first examples of post-synthetic manipulations of MOF crystals to built complex morphologies were reported by Kitagawa et al.[225] and Matzger et al.[226] in 2009. In their study, Matzger et al. nicely demonstrated some optical micrographs of IRMOF-3 grown over cubic-shaped MOF-5 and vice versa. Even a second MOF layer (with alternating sequence) was grown over the first composite crystals to yield some nearly millimetric three-layered crystals made of two different MOFs in a core-shell or in a Matryoshka doll-like (or onion-like) design (**Figure 29**).[226] In 2013, this approach was adopted by Li and Zeng to ZIFs producing some interesting core-shell ZIF-8@ZIF-67 (and vice versa) particles by immersing the as-synthesized ZIF seeds in a methanolic Zn(II)/Co(II) and 2-mim solution at room temperature. They were able to obtain particles with RD@RD, RD@cubic, cubic@RD and cubic@cubic as core@shell designs. By then, the modulation capability of CTAB for ZIF-8 was known and the growth was modulated with CTAB in order to obtain cubic morphologies. Furthermore, the interface of the two ZIF layers was decorated with a thin Au layer composed of homogeneously distributed small Au nanoparticles (2-3 nm in size). This Au layer was deposited with a special method ZIF crystals were first functionalized with as-prepared 3-mercaptopropionic acid (MPA)-Au(I) complex that forms an intermediate layer on the particle surface. Then, tertrabutylammonium borohydride (R-$NBH_4$) was used to reduce the Au(I) to yield the final ZIF@Au composite material. Finally, another ZIF layer was deposited to yield ZIF@Au@ZIF materials in different morphologies (**Figure 30**). They also applied this latter procedure one more time, using ZIF@Au@ZIF as seeds, to obtain multilayered composites. However, some intergrowth between crystals was observed. The versatility of the method was checked by replacing Ag(I) with Au(I) to obtain ZIF@Ag@ZIF materials. However; this resulted in a non-homogeneous covering of Ag nanoparticles that exhibited high polydispersity in size and aggregation on the surface. [227]

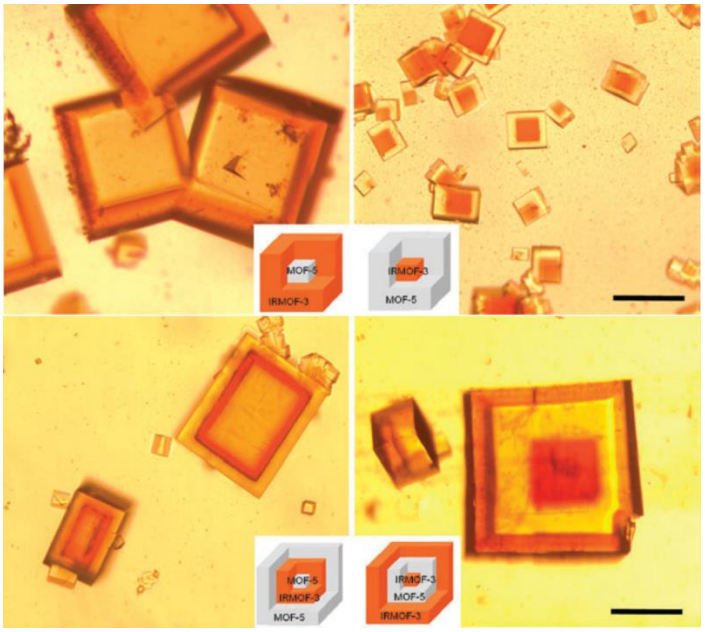


**Figure 29.** MOF-5@IRMOF-3 and IRMOF-3@MOF-5 multilayered particles. Scale bar: 200 μm. (Adapted from ref. 226).

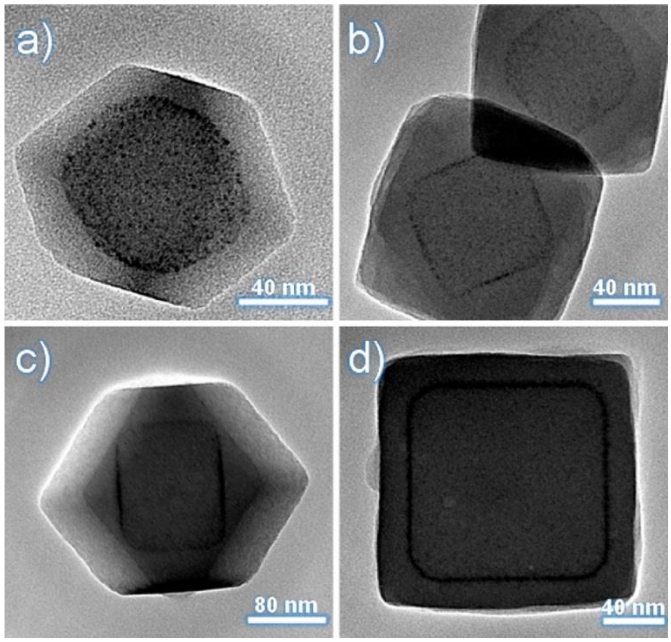


**Figure 30.** TEM images of gold–ZIF-8 hybrid nanocomposites with various geometric combinations: a) RD@Au@RD, b) RD@Au@cubic, c) cubic@Au@RD, and d) cubic@Au@ NC. (Adapted from ref. 227).

Two years later, Yamauchi et al. adopted this method to produce some ZIF-8@ZIF-67 particles in a RD@RD morphology. Although the report did not involve very much complexity in terms of morphology control, the ZIF-8@ZIF-67 particles were then pyrolized to form some

interesting porous carbon materials maintaining the RD@RD morphology (**Figure 31**). They realized that, under the same pyrolysis (at 800 $^{o}$C in $N_2$ atmosphere for 3 hours), ZIF-8 transformed into highly porous N-doped amorphous carbon (NC) while ZIF-67 formed less porous but highly crystalline graphitic carbon (GC). The optimized NC@GC material with RD@RD morphology exhibited a distinguished electrochemical performance as an electrode in supercapacitors.[228] Two years later, a very similar strategy was adopted by Wang et al. to produce some Co- and N- co-doped carbon materials using ZIF-8@ZIF-67 particles as templates. This reported material promised good electrocatalytic activity for oxygen reduction reactions.[229]

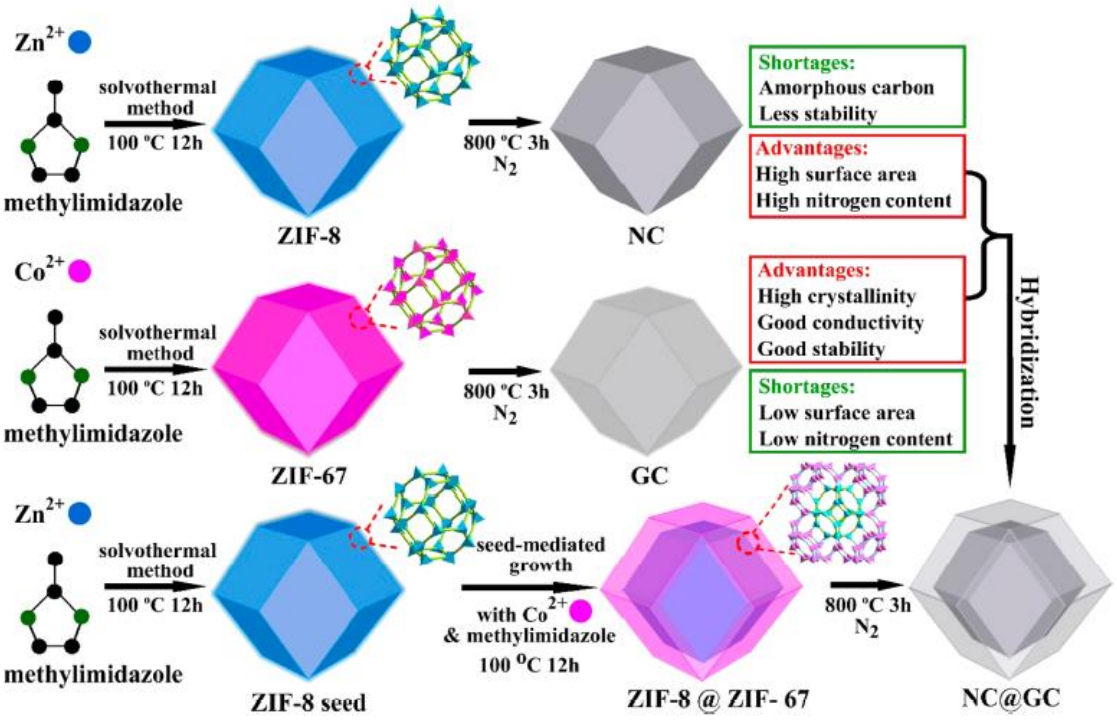


**Figure 31.** Schematic illustration of building ZIF-8@ZIF-67 particles and NC@GC materials (Adapted from ref. 228).

Among others, Feng et al. were the firsts to achieve some control in the shell thickness of ZIF@ZIF materials in 2016. They systematically studied the effect of the metal to ligand ratio and the type of metal source (nitrate or acetate salt) used in the growth of the shell thickness. They found that, at a fixed time and 2-mim concentration, using the acetate salt at lower concentrations leads to thinner shell formation. However, the use of the nitrate salt with higher concentration yielded ZIF@ZIF particles with the thickest shells.[230] These findings were consistent with the previously reported results on the nucleation and growth rates of ZIF-8 covered in **section 4.6**. Later, Maspoch et al. reported some core-shell ZIF-67@ZIF-8 particles

having ZIF-67 cores in cubic, tetrahedral and hollow-box morphologies. The cores with different morphologies were obtained by selective chemical etching with a procedure that is mentioned before in this text.[194] These etched ZIF-67 crystals were used as seeds and the growth was optimized by varying the Zn(II)/2-mim concentrations and reaction time for each core morphology. Interestingly, all the morphologies (even the hollow-box) ended up with the TRD or the RD shape, like a reverse process of the etching, to form cubic@TRD, cubic@RD, tetrahedral@TRD, tetrahedral@RD and hollow-box@RD morphologies. Also, multi-shelled particles were obtained via the repetition of the ZIF growths. Also, the incorporation of different metallic nanoparticles in between each ZIF layers was achieved by sequential post-synthetic attachment to synthesize materials like ZIF@NP1@ZIF@NP2@ZIF, where NP1 and NP2 are a combination of five different nanoparticles (e.g. Au nanoparticles with two different sizes, Pd particles with two different shapes (cubic and icosahedral) and CuPd nanoparticles). As a proof of concept, they employed one of these multi-shelled ZIF@NP1@ZIF@NP2@ZIF composites as a catalyst for a two-step cascade reaction, where each of the two different nanoparticles (located in different layers) is responsible for one of the steps. They demonstrated that the maximum yield of this catalytic reaction was achieved by using the proper nanoparticle sequence. To facilitate the diffusion of the reaction species, the two types of nanoparticles were separated by a very thin (20 nm) layer of ZIF-8. This work proved the importance of not only the morphological control of ZIF-8/67 but also the control on the incorporation (by composition and positioning) of the functional additives to ZIF-8/67.[179]

All of these examples are without doubt the beautiful products of the accumulated knowledge on the nucleation and growth mechanisms of ZIF-8 since its discovery. These will be the developments that will help ZIF-8 to approach more to the real-life applications.

# 5. References


1- Robert H. Notter, Lung Surfactants: Basic Science and Clinical Applications, *CRC Press* **2000**

2- M. Faraday, *Philos. Trans. R. Soc. London*, **1857**, 147, 145

3- Activated Charcoal Review Sheet, *USDA Organic Materials Review*, **2002**

4- H. Marsh, F. Rodríguez Reinoso, Activated Carbon, Elsevier Science, **2006**

5- D. W. Breck, Zeolite molecular sieves: structure, chemistry, and use, *Wiley*, **1973**

6- R. Tschernich, Zeolites of the World, *Harbinger House*, **1994**

7- A.F. Cronstedt, *Kongl Vetenskaps Academiens Handlingar Stockholm*, **1756**, 17, 120

8- M. W. Meier, "Molecular Sieves," in *1st International Zeolite Conference*, London, **1967**

9- R. M. Dessau, G. T. Kerr, *Zeolites* **1984**, 4, 315

10- M. E. Davis, *Ind. Eng. Chem. Res*. **1991**, 30, 1675

11- J. Weitkamp, *Solid State Ion* **2001**, 131, 175

12- J. Rouquerol, D. Avnir, C. W. Fairbridge, D. H. Everett, J. M. Haynes, N. Pernicone, J. D. F. Ramsay, K. S. W. Sing, K. K. Unger, *Pure & Appl. Chem*., **1994**, 66, 1739

13- P. Holister, C. Roman, T. Harper, "Nanoporous Materials", *Cientifica* **2003**

14- J. Haber, *Pure & Appl. Chem.*, **1991**, 63, 1227

15- A. G. Keenan, *J. Chem. Educ.* **1948**, 25, 666

16- E. P. Barrett, L. G. Joyner, P. P. Halenda, *J. Am. Chem. Soc.* **1951**, 73, 373

17- M. Kondo, T. Yoshitomi, K. Seki, H. Matsuzaka, S. Kitagawa, *Angew, Chem*. **1997**, 36, 1725

18- H. Li, M. Eddaoudi, T. L. Groy, O. M. Yaghi, *J. Am. Chem. Soc*. **1998**, 120, 8571

19- H. Li, M. Eddaoudi, M. O'Keeffe, O. M. Yaghi, *Nature* **1999**, 402, 276

20- C. J. Sumby, *Nat. Chem.* **2016**, 8, 294

21- J. L. C. Rowsell, O. M. Yaghi, *Microporous and Mesoporous Mater*. **2004**, 73, 3

22- B. F. Hoskins, R. Robson, *J. Am. Chem. Soc*. **1989**, 11, 5964

23- O. M. Yaghi, H. Li, *J. Am. Chem. Soc*. **1995**, 117, 10401

34- M. Eddaoudi, J. Kim, N. Rosi, D. Vodak, J. Wachter, M. O'Keeffe, O. M. Yaghi, *Science* **2002**, 295, 469

25- O. M. Yaghi, *J. Am. Chem. Soc*. **2016**, 138, 15507

26- P. I. Ravikovitcha, G. L. Haller, A. V. Neimark, *Colloid Interface Sci*. **1998**, 76-77, 203

27- F.-X. Coudert, A. H. Fuchs, *Coord. Chem. Rev*. **2016**, 307, 211

28- G. Horvath, K. Kawazoe, *J. Chem. Eng. Japan* **1983**, 16, 470

29- O. K. Farha, I. Eryazici, N. C. Jeong, B. G. Hauser, C. E. Wilmer, A. A. Sarjeant, R. Q. Snurr, S. T. Nguyen, A. Ö. Yazaydın, J. T. Hupp, *J. Am. Chem. Soc*. **2012**, 134, 15016

30- J. K. Schnobrich, K. Koh, K. N. Sura, A. J. Matzger, *Langmuir* **2010**, 26, 5808

31- K. Koh, A. G. Wong-Foy, A. J. Matzger, *J. Am. Chem. Soc.* **2009**, 131, 41

32- H. Furukawa, N. Ko, Y. B. Go, N. Aratani, S. B. Choi, E. Choi, A. Ö. Yazaydin, R. Q. Snurr, M. O'Keeffe, J. Kim, O. M. Yaghi, *Science* **2010**, 329, 424

33- H. Furukawa, K. E. Cordova, M. O'Keeffe, O. M. Yaghi, *Science* **2013**, 341, 974

34- H Deng, S. Grunder, K. E. Cordova, C. Valente, H. Furukawa, M. Hmadeh, F. Gándara, A. C. Whalley, Z. Liu, S. Asahina, H. Kazumori, M. O'Keeffe, O. Terasaki, J. F. Stoddart, O. M. Yaghi, *Science* **2012**, 336, 1018

35- P. Li, N. A. Vermeulen, C. D. Malliakas, D. A. Gómez-Gualdrón, A. J. Howarth, B. L. Mehdi, A. Dohnalkova, N. D. Browning, M. O'Keeffe, O. K. Farha, *Science* **2017**, 356, 624

36- G. E. Cmarik, M. Kim, S. M. Cohen, K. S. Walton, *Langmuir* **2012**, 28, 15606

37- X.-C. Huang, Y.-Y. Lin, J.-P. Zhang, X.-M. Chen, *Angew. Chem. Int. Ed*. **2006**, 45, 15

38- K. S. Park, Z. Ni, A. P. Côté, J. Y. Choi, R. Huang, F. J. Uribe-Romo, H. K. Chae, M. O'Keeffe, O. M. Yaghi, *Proc. Natl. Acad. Sci.* **2006**, 103, 10186

39- N. Rangnekar, N. Mittal, B. Elyassi, J. Caro, M. Tsapatsis, *Chem. Soc. Rev*. **2015**, 44, 7128

40- J. H.c Cavka, S. Jakobsen, U. Olsbye, N. Guillou, C. Lamberti, S. Bordiga, K. Petter Lillerud, *J. Am. Chem. Soc.* **2008**, 130, 13850

41- F. Millange, C. Serre, G. Férey, *Chem. Commun*. **2002**, 0, 822

42- N. C. Burtch, H. Jasuja, K. S. Walton, *Chem. Rev*. **2014**, 114, 20, 1057

43- J. B. DeCoste, G. W. Peterson, H. Jasuja, T. G. Glover, Y.-g. Huang, K. S. Walton, *J. Mater. Chem. A* **2013**, 1, 5642

44- J. M. Ogden, M. M. Steinbugler, T. G. Kreutz, *J. Power Sources* **1999**, 79, 143

45- D. Gygi, E. D. Bloch, J. A. Mason, M. R. Hudson, M. I. Gonzalez, R. L. Siegelman, T. A. Darwish, W. L. Queen, C. M. Brown, J. R. Long, *Chem. Mater*. **2016**, 28, 1128

46- https://www.energy.gov/eere/fuelcells/hydrogen-storage

47- M. P. Suh, H. J. Park, T. K. Prasad, D.-W. Lim, *Chem. Rev*. **2012**, 112, 782

48- E.D. Bloch, M. R. Hudson, J. A. Mason, S. Chavan, V. Crocellà, J. D. Howe, K. Lee, A. L. Dzubak, W. L. Queen, J. M. Zadrozny, S. J. Geier, L.-C. Lin, L. Gagliardi, B. Smit, J. B. Neaton, S. Bordiga, C. M. Brown, J. R. Long, *J. Am. Chem. Soc*. **2014**, 136, 10752

49- S. Li, Y. G. Chung, R. Q. Snurr, *Langmuir* **2016**, 32, 10368

50- Y. He, W. Zhou, G. Qiand, B. Chen, *Chem. Soc. Rev*. **2014**, 43, 5657

51- J. A. Mason, M. Veenstra, J. R. Long, *Chem. Sci.* **2014**, 5, 32

52- S. S.-Y. Chui, S. M.-F. Lo, J. P. H. Charmant, A. G. Orpen, I. D. Williams, *Science* **1999**, 283, 1148

53- Y. Peng, V. Krungleviciute, I. Eryazici, J. T. Hupp, O. K. Farha, T.Yildirim, *J. Am. Chem. Soc.* **2013**, 135, 11887

54- J.-M. Lin, C.-T. He, Y. Liu, P.-Q. Liao, D.-D. Zhou, J.-P. Zhang, X.-M. Chen, *Angew. Chem. Int. Ed.* **2016**, 55, 4674

55- B. Li, H.-M. Wen, W. Zhou, J. Q. Xu, B. Chen, *Chem.* **2006**, 1, 557

56- T. Tian, Z. Zeng, D. Vulpe, M. E. Casco, G. Divitini, P. A. Midgley, J. Silvestre-Albero, J.-C. Tan, P. Z. Moghadam, D. Fairen-Jimenez, *Nature Materials* **2018**, 17, 174

57- H. Zhang, P. Deria, O. K. Farha, J. T. Hupp and R. Q. Snurr, *Energy Environ. Sci.*, **2015**, 8, 1501

58- http://www.esrl.noaa.gov/

59- B. Seoane, J. Coronas, I. Gascon, M. E. Benavides, O. Karvan, J. Caro, F. Kapteijn and J. Gascon, *Chem. Soc. Rev.*, **2015**, 44, 2421

60- K. Sumida, D. L. Rogow, J. A. Mason, T. M. McDonald, E. D. Bloch, Z. R. Herm, T.-H. Bae, J. R. Long, *Chemical Reviews*, **2012**, 112, 724

61- E. J. Granite, H. W. Pennline, *Ind. Eng. Chem. Res.*, **2002**, 41, 5470

62- S. Vasudevan, S. Farooq, I. A. Karimi, M. Saeys, M.C.G. Quah, R. Agrawal, *Energy* **2016**, 103, 709

63- E. B. le Bouhelec, P. Mougin, A. Barreau, R. Solimando, *Energy & Fuels*, **2007**, 21, 2044

64- M. Palomino, A. Corma, F. Rey, S. Valencia, *Langmuir*, **2010**, 26, 1910

65- J. Zhang, R. Singh, P. A. Webley, *Microporous Mesoporous Mater.*, **2008**, 111, 478

66- C.F. Martin, M. G. Plaza, J. J. Pis, F. Rubiera, C. Pevida, T. A. Centeno, *Sep. Purif. Technol*., **2010**, 74, 225

67- C. A. Trickett, A. Helal, B. A. Al-Maythalony, Z. H. Yamani, K. E. Cordova, O. M. Yaghi, *Nat. Rev. Mater*., **2017**, 2, 8

68- Z. Bao, L. Yu, Q. Ren, X. Lu, S. Deng, *J. Colloid Interface Sci*., **2011**, 353, 549

69- A. L. Dzubak, L.-C. Lin, J. K., J. A. Swisher, R. Poloni, S. N. Maximoff, B. Smit, L. Gagliardi, *Nature Chemistry*, **2012**, 4, 810

70- Lin, L. , Kim, J. , Kong, X. , Scott, E. , McDonald, T. M., Long, J. R., Reimer, J. A. and Smit, B., *Angew. Chem. Int. Ed.*, **2013**, 125, 4506

71- C. R. Wade, M. Dincă, *Dalton Trans*., **2012**, 41, 7931

72- C. P. Cabello, P. Rumori and G. T. Palomino, *Microporous Mesoporous Mater.*, **2014**, 190, 234

73- L. Li, J. Yang, J. Li, Y. Chen and J. Li, *Microporous Mesoporous Mater.*, **2014**, 198, 236

74- P. L. Llewellyn, S. Bourrelly, C. Serre, A. Vimont, M. Daturi, L. Hamon, G. De Weireld, J.-S. Chang, D.-Y. Hong and Y. Kyu Hwang, *Langmuir*, **2008**, 24, 7245

75- G. Wißmann, A. Schaate, S. Lilienthal, I. Bremer, A. M. Schneider, P. Behrens, *Microporous Mesoporous Mater.*, **2012**, 152, 64

76- H. Kim, S. Yang, S. R. Rao1, S. Narayanan, E. A. Kapustin, H. Furukawa, A. S. Umans, O. M. Yaghi, E. N. Wang, *Science*, **2017**, 356, 430

77- Z. Hasan, J. Jeon, S. H. Jhung, *J. Hazard Mater*., **2012**, 209–210, 151

78- A. A. Adeyemo, I. O. Adeoye, O. S. Bello: *Toxicol. Environ. Chem*., **2012**, 94, 1846

79- C. Yang, U. Kaipa, Q. Z. Mather, X. Wang, V. Nesterov, A. F. Venero, M. A. Omary, *J. Am. Chem. Soc.*, **2011**, 133, 18094

80- L. Hamon, C. Serre, T. Devic, T. Loiseau, F. Millange, G. Ferey, G. De Weireld, *J. Am. Chem. Soc.*, **2009**, 131, 8775

81- F. Ke, L. G. Qiu, Y. P. Yuan, F. M. Peng, X. Jiang, A. J. Xie, Y. H. Shen, J. F. Zhu: *J. Hazard Mater.*, **2011**, 196, 36

82- E. Y. Park, Z. Hasan, N. A. Khan, S. H. Jhung, *J. Nanosci. Nanotechnol*., **2013**, 13, 2789

83- D. F. Sava, M. A. Rodriguez, K. W. Chapman, P. J. Chupas, J. A. Greathouse, P. S. Crozier, T. M. Nenoff, *J. Am. Chem. Soc*., **2011**, 133, 12398

84- W. Xia, X. Zhang, L. Xu, Y.Wang, J. Lin, R. Zou: *RSC Adv*., **2013**, 3, 11007

85- http://www.mofgen.com/

86- http://www.moftechnologies.com

87- http://connect.catalyst-inc.org/techwatch/mof

88- H. Jiang, T. Wang, L. Wang, C. Sun, T. Jiang, G. Cheng, S. Wang: *Microporous Mesoporous Mater*, **2012**, 153, 124

89- D. Cunha, C. Gaudin, I. Colinet, P. Horcajada, G. Maurin, C. Serre, *J. Mater. Chem.* B, **2013**, 1B, 1101

90- M. O. Rodrigues, M. V. de Paula, K. A. Wanderley, I. B. Vasconcelos, S. Alves, Jr, T. A. Soares, *Int. J. Quantum Chem*., **2012**, 112, 3346

91- M. Ibrahim, R. Sabouni, G. A. Husseini, *Curr Med Chem*., **2017**, 24, 193

92- M. J. Neufeld, A. Lutzke, W. M. Jones, M M. Reynolds, *ACS Appl. Mater. Interfaces*, **2017**, 9, 35628

93- S. Eslava, L. Zhang, S. Esconjauregui, J. Yang, K. Vanstreels, M. R. Baklanov, E. Saiz, *Chem. Mater*., **2013**, 25, 1, 27

94- M. Usman, C.-H. Lee, D.-S. Hung, S.-F. Lee, C.-C. Wang, T.-T. Luo, L. Zhao, M.-K. Wueg, K.-L. Lu, *J. Mater. Chem. C*, **2014**, 2, 3762

95- G. Lu, J. T. Hupp, *J. Am. Chem. Soc*. **2010**, 132, 7832

96- B. Chocarro-Ruiz, J. Pérez-Carvajal, C. Avci, O. Calvo-Lozano, M. Isabel Alonso, D. Maspoch, L. M. Lechuga, *J. Mater. Chem. A*, **2018**, 6, 13171

97- W. Cho, H. J. Lee, M. Oh, *J. Am. Chem. Soc*., **2008**, 130, 16943

98- T. Tsuruoka, S. Furukawa, Y. Takashima, K. Yoshida, S. Isoda, S. Kitagawa, *Angew. Chem. Int. Ed*., **2009**, 48, 4739

99- A. Umemura, S. Diring, S. Furukawa, H. Uehara, T. Tsuruoka, S. Kitagawa, *J. Am. Chem. Soc.*, **2011**, 133, 15506

100- M. Pang, A. J. Cairns, Y. Liu, Y. Belmabkhout, H. C. Zeng, M. Eddaoudi, *J. Am. Chem. Soc.*, **2012**, 134, 13176

101- M. Sindoro, A.-Y. Jeeb, S. Granick, *Chem. Commun*., **2013**, 49, 9576

102- N. Yanai, S. Granick, *Angew. Chem. Int. Ed*., **2012**, 51, 5638

103- N. Yanai, M. Sindoro, J. Yan, S. Granick, *J. Am. Chem. Soc.*, **2013**, 135, 34

104- M. Pang, A. J. Cairns, Y. Liu, Y. Belmabkhout, H. C. Zeng, M. Eddaoudi, *J. Am. Chem. Soc*., **2013**, 135, 10234

105- X. Cai, X. Deng, Z. Xie, S. Bao, Y. Shi, J. Lin, M. Pang, M. Eddaoudi, *Chem. Commun*., **2016**, 52, 9901

106- G. Lu, C. Cui, W. Zhang, Y. Liu, F. Huo, *Chem. Asian J*. **2013**, 8, 69

107- C. Cui, Y. Liu, H. Xu, S. Li, W. Zhang, P. Cui, F. Huo, *Small*, **2014**, 10, 3672

108- J. D. Joannopoulos, S. G. Johnson, J. N. Winn, R. D. Meade, Photonic Crystals: Molding the Flow of Light - Second Edition, *Princeton University Press* **2011**

109- F. M. Hinterholzinger, A. Ranft, J. M. Feckl, B. Rühle, T. Bein, Bettina V. Lotsch, *J. Mater. Chem.*, **2012**, 22, 10356

110- O. Dalstein, D. R. Ceratti, C. Boissière, D. Grosso, A. Cattoni, M. Faustini, *Adv. Funct. Mater.*, **2016**, 26, 81

111- Y. Wu, F. Li, W. Zhu, J. Cui, C. Tao, C. Lin, P. M. Hannam, G. Li, *Angew. Chem. Int. Ed.*, **2011**, 50, 12518

112- Z. Hu, C. Tao, H. Liu, X. Zou, H. Zhua, J. Wang, *J. Mater. Chem. A*, **2014**, 2, 14222

113- S. A. Moggach, T. D. Bennett and A. K. Cheetham, *Angew. Chem*., **2009**, 121, 7221

114- D. Fairen-Jimenez, S. A. Moggach, M. T. Wharmby, P. A. Wright, S. Parsons and T. Düren, *J. Am. Chem. Soc.*, **2011**, 133, 8900

115- B. R. Pimentel, A. Parulkar, E. Zhou, N. A. Brunelli, R. P. Lively, *ChemSusChem*, **2014**, 7, 3202

116- A. Phan, C. J. Doonan, F. J. Uribe-Romo, C. B. Knobler, M. O'Keeffe, O. M. Yaghi, *Acc. Chem. Res*., **2010**, 43, 58

117- Y.-Q. Tian, C.-X. Cai, Y. Ji, X.-Z. You, S.-M. Peng, G.-H. Lee, *Angew. Chem. Int. Ed*., **2002**, 41, 1384

118- H. Xiaochun, Z. Jiepeng, C. Xiaoming, *Chin. Sci. Bull*., **2003**, 48, 1531

119- W. Morris, C. J. Doonan, H. Furukawa, R. Banerjee, O. M. Yaghi, *J. Am. Chem. Soc*., **2008**, 130, 12626

120- C. Zhang, W.J. Koros, *J. Phys. Chem. Lett*., **2015**, 6, 3841

121- Based on searching results from https://scholar.google.com/

122- J. Perez-Pellitero, H. Amrouche, F. R. Siperstein, G. Pirngruber, C. Nieto-Draghi, G. Chaplais, A. Simon-Masseron, D. Bazer-Bachi, D. Peralta, N. Bats, *Chem. Eur. J.*, **2010**, 16, 1560

123- H.-c. Guo, F. Shi, Z.-f. Ma, X.-q. Liu, J., *Phys. Chem. C*, **2010**, 114, 12158

124- A. Battisti, S. Taioli, G. Garberoglio, *Microporous Mesoporous Mater*., **2011**, 143, 46

125- M. Zhou, Q. Wang, L. Zhang, Y.-C. Liu, Y. Kang, *J. Phys. Chem. B*, **2009**, 113, 11049

126- H. Wu, W. Zhou, T. Yildirim, *J. Phys. Chem. C*, **2009**, 113, 3029

127- J. B. James, Y. S. Lin, *J. Phys. Chem. C*, **2016**, 120, 14015

128- A. M. Champagnie, T. T. Tsotsis, R. G. Minet, E. Wagner, *J. Catal.*, **1992**, 134, 713

129- Z. D. Ziaka, R. G. Minet, T. T. Tsotsis, *J. Membr. Sci*., **1993**, 77, 221

130- J. B. James, Y. S. Lin, *J. Phys. Chem. C*, **2016**, 120, 14015

131- H. Yin, H. Kim, J. Choi, A. C. K. Yip, *Chem. Eng. Sci*., **2015**, 273, 293

132- Y. Pan, Y. Liu, G. Zeng, L. Zhao, Z. Lai, *Chem. Commun*., **2011**, 47, 2071

133- J. Cravillon, S. Münzer, S.-J. Lohmeier, A. Feldhoff, K. Huber, M. Wiebcke, *Chem. Mater*., **2009**, 21, 1410

134- M. D. Allendorf, R. J. T. Houk, L. Andruszkiewicz, A. A. Talin, J. Pikarsky, A. Choudhury, K. A. Gall, P. J. Hesketh, *J. Am. Chem. Soc.* **2008**, 130, 14404

135- Jin Chong Tan, Thomas D. Bennett, Anthony K. Cheetham, *Proc. Natl. Acad. Sci.* **2010**, 107, 9938

136- J.-C. Tan, B. Civalleri, C.-C. Lin, L. Valenzano, R. Galvelis, P.-F. Chen, T. D. Bennett, C. Mellot-Draznieks, C. M. Zicovich-Wilson, A. K. Cheetham, *Phys. Rev. Lett*. **2012**, 108, 095502

137- F. X. Coudert, *Chem. Mater*. **2015**, 27, 1905

138- K. W. Chapman, G. J. Halder, P. J. Chupas, *J. Am. Chem. Soc.* **2009**, 131, 17546

139- S. Cao, T. D. Bennett, D. A. Keen, A. L. Goodwind, A. K. Cheetham, *Chem. Commun*. **2012**, 48, 7805

140- M. E. Casco, Y. Q. Cheng, L. L. Daemen, D. Fairen-Jimenez, E. V. Ramos-Fernández, A. J. Ramirez-Cuesta, J. Silvestre-Albero, *Chem. Commun*. **2016**, 52, 3639

141- https://www.sigmaaldrich.com

142- K. Zhang, R. P. Lively, M. E. Dose, A. J. Brown, C. Zhang, J. Chung, S. Nair, W. J. Koros, R. R. Chance, *Chem. Commun*. **2013**, 49, 3245

143- K. Zhang, R. P. Lively, C. Zhang, W. J. Koros, R. R. Chance, *J. Phys. Chem. C* **2013**, 117, 7214

144- J. Cousin Saint Remi, T. Rémy, V. Van Hunskerken, S. van de Perre, T. Duerinck, M. Maes, D. De Vos, E. Gobechiya, C. E. A. Kirschhock, G. V. Baron, J. F. M. Denayer, *ChemSusChem* **2011**, 4, 1074

145- Y. Bai, L. Dong, C. Zhang, J. Gu, Y. Sun, L. Zhang, H. Chen, *Sep. Sci. Technol.* **2013**, 48, 2531

146- X. Liu, Y. Li, G. Zhu, Y. Ban, L. Xu, W. Yang, *Angew. Chem. Int. Ed*. **2011**, 50, 10734

147- E. E. Sann,Y. Pan, Z. Gao, S. Zhan, F. Xia, *Sep. Purif. Technol*. **2018**, 206, 186

148- D. Peralta, G. Chaplais, A. Simon-Masseron, K. Barthelet, C. Chizallet, A.-A. Quoineaud, G. D. Pirngruber, *J. Am. Chem. Soc*. **2012**, 134, 8115

149- H. T. Kwon, H.-K. Jeong, *J. Am. Chem. Soc.* **2013**, 135, 10763

150- Y. Pan, T. Li, G. Lestari, Z. Lai, *J. Membr. Sci.* **2012**, 390, 93

151- H. T. Kwon, H.-K. Jeong, *Chem. Commun*. **2013**, 49, 3854

152- C. Zhang, K. Zhang, L. Xu, Y. Labreche, B. Kraftschik, W. J. Koros, *Angew. Chem. Int. Ed*. **2014**, 60, 2625

153- W. Li, P. Su, Z. Li, Z. Xu, F. Wang, H. Ou, J. Zhang, G. Zhang, E. Zeng, *Nat. Commun.* **2017**, 8, 406

154- P. Falcaro, K. Okada, T. Hara, K. Ikigaki, Y. Tokudome, A. W. Thornton, A. J. Hill, T. Williams, C. Doonan, M. Takahashi, *Nat. Mater*. **2017**, 16, 342

155- L. Liu, Y. Zhou, S. Liu, M. Xu, *ChemElectroChem* **2017**, 5, 6

156- G. G. Yu, J. F. Xia, F. F. Zhang, Z. H. Wang, *J. Electroanal. Chem.* **2017**, 801, 496

157- W. Zhan, Q. Kuang, J. Zhou, X. Kong, Z. Xie and L. Zheng, *J. Am. Chem. Soc.* **2013**, 135, 1926

158- H. Tian, H. Fan, M. Li, L. Ma, *ACS Sens*. **2016**, 1, 243

159- S. Liu, Zhonghua Xiang, Z. Hu, X. Zheng, D. Cao, *J. Mater. Chem*. **2011**, 21, 6649

160- C. Chizallet, S. Lazare, D. Bazer-Bachi, F. Bonnier, V. Lecocq, E. Soyer, A. A. Quoineaud, N. Bats, *J. Am. Chem. Soc.* **2010,** 132, 12365

161- H. Y. Cho, J. Kim, S. N. Kim, W. S. Ahn, *Microporous Mesoporous Mater*. **2013,** 169, 180

162- T. Zhang, X. Zhang, X. Yan, L. Kong, G. Zhang, H. Liu, J. Qiu, K. L. Yeung, *Chem. Eng. J.* **2013**, 228, 398

163- R. Jin, Z. Bian, J. Li, M. Ding, L. Gao, *Dalton Trans* **2013**, 42, 3936

164- U. P. N. Tran, K. K. A. Le, N. T. S. Phan, *ACS Catal.* **2011**, 1, 120

165- L. T. L. Nguyen, K. K. A. Le, H. X. Truong, N. T. S. Phan, *Catal. Sci. Technol.* **2012**, 2, 521

166- L. T. L. Nguyen, K. K. A. Le, N. T. S. Phan, *Chin. J. Catal*. **2012**, 33, 688

167- L. H. Wee, T. Lescouet, J. Ethiraj, F. Bonino, R. Vidruk, E. Garrier, D. Packet, S. Bordiga, D. Farrusseng, M. Herskowitz, J. A. Martens, *ChemCatChem* **2013,** 5, 3562

168- X. Zhou, H. P. Zhang, G. Y. Wang, Z. G. Yao, Y. R. Tang, S. S. Zheng, *J. Mol. Catal. A: Chem*. **2013**, 366, 43

169- C. M. Miralda, E. E. Macias, M. Zhu, P. Ratnasamy, M. A. Carreon, *ACS Catal*. **2011**, 2, 180

170- J. Zakzeski, A. Dębczak, P. C. A. Bruijnincx, B. M. Weckhuysen, *Appl. Catal., A* **2011**, 394, 79

171- A. Zhang, L. Li, J. Li, Y. Zhang, S. Gao, *Catal. Commun*. **2011**, 12, 1183

172- S. B. Kalidindi, D. Esken, R. A. Fischer, *Chem. Eur. J.* **2011**, 17, 6594

173- Q. Li, H. Kim, *Fuel Process. Technol*. **2012**, 100, 43

174- G. Lu, S Li, Z. Guo, O. K. Farha, B. G. Hauser, X. Qi, Y. Wang, X. Wang, S. Han, X. Liu, J. S. DuChene, H. Zhang, Q. Zhang, X. Chen, J. Ma, S. C. J. Loo, W. D. Wei, Y. Yang, J. T. Hupp, F. Huo, *Nat. Chem*. **2012**, 4, 310

175- P. Falcaro, R. Ricco, A. Yazdi, I. Imaz, S. Furukawa, D. Maspoch, R. Ameloot, J. D. Evans, C. J. Doonan, *Coord. Chem. Rev*. **2016**, 307, 237

176- H.-L. Jiang, B. Liu, T. Akita, M. Haruta, H. Sakurai, Q. Xu, *J. Am. Chem. Soc*. **2009**, 131, 11302

177- D. Esken, S. Turner, O.I. Lebedev, G. Van Tendeloo, R.A. Fischer, *Chem. Mater*. **2010**, 22, 6393

178- Z. Li, H.C. Zeng, *Chem. Mater*. **2013**, 25, 1761

179- C. Avci, A. Yazdi, M. Tarrés, E. Bernoud, N. G. Bastús, V. Puntes, I. Imaz, X. Ribas, D. Maspoch, *ACS Appl. Mater. Interfaces* **2018**, 10, 23952

180- P. Wang, J. Zhao, X. Li, Y. Yang, Q. Yang, C. Li, *Chem. Commun*. **2013**, 49, 3330

181- C. J. Stephenson, J. T. Hupp, O. K. Farha, *Inorg. Chem*. **2015**, 2, 448

182- Y. Huang, Y. Zhang, X. Chen, D. Wu, Z. Yi, R. Cao, *Chem. Commun*. **2014**, 50, 10115.

183- A. K. Singh, Q. Xu, *ChemCatChem* **2013**, 5, 3000

184- M. Zhang, Y. Yang, C. Li, Q. Liu, C. T. Williams, C. Liang, *Catal. Sci. Technol*. **2014,** 4, 329

185- T. T. Dang, Y. Zhu, J. S. Y. Ngiam, S. C. Ghosh, A. Chen, A. M. Seayad, *ACS Catal.* **2013**, 3, 1406

186- Y. Pan, D. Ma, H. Liu, H. Wu, D. He, Y. Li, *J. Mater. Chem*. **2012**, 22, 10834

187- P. Wang, J. Zhao, X. Li, Y. Yang, Q. Yang, C. Li, *Chem. Commun*. **2013**, 49, 3330

188- M. Zahmakiran, *Dalton Trans.* **2012**, 41, 12690

189- C. H. Kuo, Y. Tang, L. Y. Chou, B. T. Sneed, C. N. Brodsky, Z. Zhao, C. K. Tsung, *J. Am. Chem. Soc*. **2012**, 134, 14345

190- Q. Liu, Z. X. Low, L. Li, A. Razmjou, K. Wang, J. Yao, H. Wang, *J. Mater. Chem. A* **2013**, 1, 11563

191- I. B. Vasconcelos, T. G. da Silva, G. C. G. Militão, T. A. Soares, N. M. Rodrigues, M. O. Rodrigues, N. B. da Costa, Jr., R. O. Freiree, S. A. Junior, *RSC Adv*. **2012**, 2, 9437

192- C.-Y. Sun, C. Qin, X.-L. Wang, G.-S. Yang, K.-Z. Shao, Y.-Q. Lan, Z.-M. Su, P. Huang, C.-G. Wang, E.-B. Wang, *Dalton Trans*. **2012**, 41, 6906

193- P. Kumar, V. Bansal, A. K. Paul, L. M. Bharadwaj, A. Deep, K.-H. Kim, *Appl*. *Nanosci*. **2016**, 6, 951

194- M. Hoop, C. F. Walde, R. Riccò, F. Mushtaq, A. Terzopoulou, X. Z. Chen, A. J. deMello, C. J. Doonan, P. Falcaro, B. J. Nelson, J. Puigmartí-Luis, S. Pané, *Appl*. *Mater. Today* **2018**, 11, 13

195- C. Avci, J. Ariñez-Soriano, A. Carné-Sánchez, V. Guillerm, C. Carbonell, I. Imaz, D. Maspoch, *Angew. Chem. Int. Ed*. **2015**, 54, 14417

196- H. Ren, L. Zhang, J. An, T. Wang, L. Li, X. Si, L. He, X. Wu, C. Wang, Z. Su, *Chem. Commun*. **2014**, 50, 1000

197- N. Liédana, A. Galve, C. Rubio, C. Téllez, J. Coronas, *ACS Appl. Mater. Interfaces* **2012**, 4, 9, 5016

198- O. M. Linder-Patton, T.J. de Prinse, S. Furukawa, S. G. Bell, K. Sumida, C. J. Doonan, C.J. Sumby, *CrystEngComm*, **2018**, 20, 4926

199- Y. Pan, D. Heryadi, F. Zhou, L. Zhao, G. Lestari, H. Sub, Z. Lai, *CrystEngComm* **2011**, 13, 6937

200- C. Avci, I. Imaz, A. Carné-Sánchez, J. Angel Pariente, N. Tasios, J.Pérez-Carvajal, M. Isabel Alonso, A. Blanco, M. Dijkstra, C. López, D. Maspoch, *Nat. Chem.* **2018**, 10, 78

201- A. F. Gross, E. Sherman, J. J. Vajo, *Dalton Trans.* **2012**, 41, 5458

202- K. Kida, M. Okita, K. Fujita, S. Tanaka, Y. Miyakeab, *CrystEngComm* **2013**, 15, 1794

203- N. L. Torad, M. Hu, Y. Kamachi, K. Takai, M. Imura, M. Naitoa, Y. Yamauchi, *Chem Commun.* **2013**, 49, 2521

204- M. Oh, C. A. Mirkin, *Nature* **2005**, 438, 651

205- A. Schejn, L. Balan, V. Falk, L. Aranda, G. Medjahdic, R. Schneider, *CrystEngComm* **2014**, 16, 4493

206- J. Cravillon, R. Nayuk, S. Springer, A. Feldhoff, K. Huber, M. Wiebcke, *Chem. Mater*. **2011**, 23, 2130

207- M. Q. Zhu, J. B. Jasinski, M. A. Carreon, *J. Mater. Chem*. **2012**, 22, 7684

208- H.-Y. Cho, J. Kim, S.-N. Kim, W.-S. Ahn, *Microporous Mesoporous Mater.* **2013**, 169, 180

209- J. Cravillon, C. A. Schroder, H. Bux, A. Rothkirch, J. Caro, M. Wiebcke, *CrystEngComm* **2012**, 14, 492

210- . X. Niu, S. L. Zheng, D. W. Wang, X. Q. Liu, H. J. Li, S. A. Han, J. Chen, Z. Y. Tang and G. B. Xu, *J. Am. Chem. Soc*. **2009**, 131, 697

211- T. Xing, Y. Lou, Q. Baoa, J. Chen, *CrystEngComm*, **2014**, 16, 8994

212- X. Fan, W. Wang, W. Li, J. Zhou, B. Wang, J. Zheng, X. Li, *ACS Appl. Mater. Interfaces* **2014**, 6, 17, 14994

213- S. Tanaka, K. Fujita, Y. Miyake, M. Miyamoto, Y. Hasegawa, T. Makino, S. Van der Perre, J.Cousin Saint Remi, T. Van Assche, G. V. Baron, J. F. M. Denayer, *J. Phys. Chem. C* **2015**, 119, 51, 28430

214- G. Zheng, Z. Chen, K. Sentosun, I. Pérez-Juste, S. Bals, L.M. Liz-Marzán, I. Pastoriza-Santos, J. Pérez-Juste, M. Hong, *Nanoscale* **2017**, 9, 43, 16645

215- F. Yang, H. Mu, C. Wang, L. Xiang, K. X. Yao, L. Liu, Y. Yang, Y. Han, Y. Li, Y. Pan, *Chem. Mater.* **2018**, 30, 10, 3467

216- H.J. Lee, W. Cho, M. Oh, *Chem. Commun*. **2012**, 48, 221

217- S. Jeoung, I. T. Ju, J. H. Kim, S. H. Joo, H. R. Moon, *J. Mater. Chem. A*, **2018**, 6, 18906

218- M. Hu, Y. Ju, K. Liang, T. Suma, J. Cui, F. Caruso, *Adv. Funct. Mater*. **2016**, 26, 5827

219- P. Zhang, B. Y. Guan, L. Y. X. W. (David) Lou, *Angew. Chem. Int. Ed.* **2017**, 56, 7141

220- P. Zhang, B. Y. Guan, L. Y. X. W. (David) Lou, *Chem* **2018**, 4, 162

221- L.-Y. Chou, P. Hu, J. Zhuang, J. V. Morabito, K. Chon, Y.-C. Kao, S.-C. Wang, F.-K. Shieh, C.-H. Kuo, C.-K. Tsung, *Nanoscale* **2015**, 7, 19408

222- J. Yang, F.J. Zhang, H.Y. Lu, X. Hong, H.L. Jiang, Y. Wu, Y.D. Li, *Angew. Chem. Int. Ed.* **2015**, 54, 10889

223- H. Chen, K Shen, J. Chen, X. Chen, Y. Li, *J. Mater. Chem. A* **2017**, 5, 9937

224- K. Shen, L. Zhang, X. Chen, L. Liu, D. Zhang, Y. Han, J. Chen, J. Long, R. Luque, Y. Li, B. Chen, *Science* **2018**, 359, 206

225- S. Furukawa, K. Hirai, Y. Takashima, K. Nakagawa, M. Kondo, T. Tsuruoka, O. Sakata, S. Kitagawa, *Chem. Commun*. **2009**, 0, 5097

226- K. Koh, A. G. Wong-Foya, A. J. Matzger, *Chem. Commun.* **2009**, 0, 6162

227- Z. Li, H. C. Zeng, *Chem. Mater.* **2013**, 25, 1761

228- J.Tang, R. R. Salunkhe, J. Liu, N. L. Torad, M. Imura, S. Furukawa, Y. Yamauchi, *J. Am. Chem. Soc.* **2015**, 137, 1572

229- P. Zhang, B. Y. Guan, L. Yu, X. W. (David) Lou, *Angew. Chem. Int. Ed*. **2017**, 56, 7141

230- J. Zhang, T. Zhang, K. Xiao, S. Cheng, G.Qian, Y.Wang, Y. Feng, *Cryst. Growth Des.* **2016**, 16, 6494

# CHAPTER 2

# Objectives

# OBJECTIVES

As highlighted in Chapter 1 (Section 2), since their discovery, MOFs have been conceived mostly as bulk materials exhibiting classical properties (e.g. gas sorption) that are somewhat related to their highly porous properties. Thus far, the quality of MOFs has been identified with parameters such as the surface area, pore structure, stability, internal chemistry (open metal sites and/or ligands with functional groups), among others. In this Thesis, we emphasize the importance of the modification of the morphology and the architecture of the MOF particles with nanoscopic precision. In this way, new functionalities beyond the classical can be attained. Even though some examples have been demonstrated regarding the controlled manipulation of the morphology of MOF materials at the nanoscale, the true potentials are far from being realized. Achieving such controls at the nanoscale can pave the way of unprecedented applications that will combine the MOF-related benefits with the new functions that arise from nano-engineering.

The aim of this Thesis is to demonstrate the size and shape engineering of colloidal MOF particles at the nanoscale and to emphasize the importance of these manipulations by exploiting new properties that are unconventional to MOFs. The anisotropic nature of these faceted crystals enables the size and shape engineering and nanostructuration of MOFs using simple wet-chemical methods. Here, we propose three main approaches, making use of the anisotropic nature of MOF particles, to manipulate them at the nanoscale:

1. Post-synthetic top-down approach. This approach is addressed in the first publication included in Chapter 3 regarding the post-synthetic anisotropic wet-chemical etching of ZIF crystals. The objective here is to reach unprecedented shapes that are unachievable by conventional synthetic methods, to explain the underlying mechanism of this etching of ZIF-8 to shed light on the applications to the other MOFs, and to prove the generality of the method by applying this etching to another ZIF, ZIF-67.

2. Post-synthetic bottom-up approach. The second publication that is presented in Chapter 4 is centered on developing a bottom-up approach where the size, shape, composition and architecture of ZIF-8 and ZIF-67 crystals are modified using post-synthetic wet-chemistry. Here, the aim is to show that ZIF particles can be manipulated by post-synthetic growing of another ZIF layer and functionalized with InNPs thereby opening new avenues for designing complex multi-layered and multi-component particles that can catalyze cascade reactions.

3. In-situ modulation and self-assembly of particles. This final approach is addressed in the third publication in Chapter 5. Here, the objectives can be summarized in four parts: i) Demonstrate that ZIF-8 particles can be produced with very high monodispersity with precise shapes using surfactants, which serve as size and shape modulators; ii) Generalize this approach to another MOF, such as UiO-66 that has a completely different chemistry with carboxylic ligands and Zr (IV) centers compared to the imidazolate ligands and Zn(II) centers of ZIF-8; iii) Prove the colloidal self-assembly of these MOF crystals to form ordered superstructures that can be used as 3D photonic crystals when the particle size is selected appropriately; and iv) Exploit the photonic properties of these MOF photonic crystals and evaluate their sensing capability against alcohol vapors.

# CHAPTER 3

# Post-Synthetic Anisotropic Wet-Chemical Etching of Colloidal Sodalite ZIF Crystals

MOF Processing

International Edition: DOI: 10.1002/anie.201507588
German Edition: DOI: 10.1002/ange.201507588

# Post-Synthetic Anisotropic Wet-Chemical Etching of Colloidal Sodalite ZIF Crystals

*Civan Avci, Javier Ariñez-Soriano, Arnau Carné-Sánchez, Vincent Guillerm, Carlos Carbonell, Inhar Imaz,* and Daniel Maspoch**

***Abstract:*** *Controlling the shape of metal–organic framework (MOF) crystals is important for understanding their crystallization and useful for myriad applications. However, despite the many advances in shaping of inorganic nanoparticles, post-synthetic shape control of MOFs and, in general, molecular crystals remains embryonic. Herein, we report using a simple wet-chemistry process at room temperature to control the anisotropic etching of colloidal ZIF-8 and ZIF-67 crystals. Our work enables uniform reshaping of these porous materials into unprecedented morphologies, including cubic and tetrahedral crystals, and even hollow boxes, by an acid–base reaction and subsequent sequestration of leached metal ions. Etching tests on these ZIFs reveal that etching occurs preferentially in the crystallographic directions richer in metal–ligand bonds; that, along these directions, the etching rate tends to be faster on the crystal surfaces of higher dimensionality; and that the etching can be modulated by adjusting the pH of the etchant solution.*

Chemical etching is an ancient fabrication method that was used by metal and glass craftsmen to obtain sophisticated surface designs. With the advent of controlling the etching orientation at the microscale and nanoscale, anisotropic wet-chemical etching has become highly useful for shaping many materials for diverse applications.[1,2] For example, the anisotropic wet-chemical etching of single-crystal silicon in the presence of a base is essential in microelectronics manufacturing.[1] Anisotropic etching can also be applied to preparation of metal nanocrystals from oxidative species and coordination ligands, for which it enables unprecedented morphologies and complexities, and unique physical properties.[2] Herein, we introduce the concept of anisotropic wet-chemical etching for metal–organic frameworks (MOFs) and, in particular, for the zeolitic–imidazolate framework (ZIF) subfamily.

MOFs (and by extension, ZIFs) are an emerging class of porous materials that show extremely large surface areas ($S_{BET}$) and potential for myriad applications, including gas sorption and separation, catalysis, sensing, and biomedicine, among others.[3,4] MOFs are built up from metal ions/clusters connected through organic linkers. Their exposed crystal facets, edges, and vertices can exhibit different chemical compositions. We hypothesized that agents capable of breaking the coordination bonds between the metal ions/clusters and the organic linkers could be exploited to preferentially etch specific external crystal surfaces (with more density of coordination bonds) over others. We envisioned that such control would enable us to post-synthetically tailor the shape of MOF crystals. To date, post-synthetic random etching of MOF crystals using $H^+$, $Na^+$, and quinone has already been demonstrated.[5,6] Inspired by similar results with zeolites, this strategy has enabled researchers to prepare hierarchical MOF crystals and/or create macropores on the MOF crystal surfaces.[7,8] However, to date, no one has demonstrated the ability to rationally and post-synthetically control the anisotropic etching of a porous MOF crystal as a property of its crystal planes, to shape it into different morphologies.

Isostructural ZIF-8 and ZIF-67 are among the most important porous MOF materials known today. They are isomorphous with zeolites, and their 3D frameworks, built up from connecting $Zn^{II}$ ions (ZIF-8) or $Co^{II}$ ions (ZIF-67) through 2-methylimidazole (2-MIM) linkers, show a sodalite topology featuring large cavities (11.6 Å) and small apertures (3.4 Å; Supporting Information, Figure S1).[9] Recently, several studies have shown that the crystal growth of ZIF-8 starts with formation of cubes exposing six {100} facets, which gradually evolve into truncated rhombic dodecahedra exposing six {100} and twelve {110} facets, and finally, into the thermodynamically more stable rhombic dodecahedra, in which only the twelve {110} facets are exposed (Figure 1 a).[10,11] Figure 1 a illustrates the different exposed crystallographic planes for the cubes and for the truncated and non-truncated rhombic dodecahedra. Each crystal shape has different exposed crystallographic planes, and each crystallographic plane has a distinct chemical composition. In ZIF-8, the {100} and {211} planes contain several Zn–2-MIM linkages, whereas the {110} and {111} planes do not contain any of these linkages (Figure 1 b).

By exploiting the aforementioned differences, we devised a method for anisotropic wet etching of colloidal crystals of isostructural ZIF-8 and ZIF-67. Our approach combines a simple acid–base reaction with metal ion sequestration, which occurs when mixing a colloidal aqueous solution (2.5 mL) of ZIF-8 or ZIF-67 crystals (25 mg; $pH_{ZIF\text{-}8} = 9.2$; $pH_{ZIF\text{-}67} = 10.5$) into an aqueous solution (2.5 mL) containing the weak acid xylenol orange (XO; 40 mg), whose pH is

[*] C. Avci,[+] J. Ariñez-Soriano,[+] Dr. A. Carné-Sánchez, Dr. V. Guillerm, Dr. C. Carbonell, Dr. I. Imaz, Prof. Dr. D. Maspoch
ICN2—Institut Catala de Nanociencia i Nanotecnologia
Campus UAB, 08193 Bellaterra, Barcelona (Spain)
E-mail: inhar.imaz@icn.cat
daniel.maspoch@icn.cat
Prof. Dr. D. Maspoch
Institució Catalana de Recerca i Estudis Avançats (ICREA)
08100 Barcelona (Spain)
[+] These authors contributed equally to this work.

Supporting information for this article is available on the WWW under http://dx.doi.org/10.1002/anie.201507588.

  

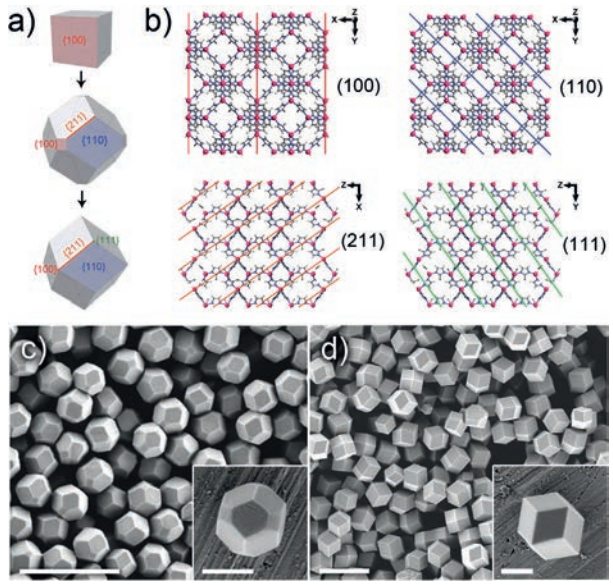


***Figure 1.*** a) Illustration of the change in crystal morphology during the crystal growth of ZIF-8. Note the change from cube to truncated rhombic dodecahedron to rhombic dodecahedron. The main exposed crystallographic planes are given for all crystal morphologies. {100}, {211}, {110}, and {111}crystallographic planes are represented in red, orange, blue, and green, respectively, throughout the manuscript. b) Representations of the crystal structure of ZIF-8 along different directions, with the exposed crystallographic planes highlighted. Zinc ions are represented as pink spheres, and carbon, nitrogen and hydrogen atoms as grey, blue, and white sticks, respectively. c, d) Representative FE-SEM images showing general views of the synthesized truncated (c) and non-truncated (d) rhombic dodecahedra ZIF-8 crystals, and corresponding single crystals (insets). Scale bars: 2 μm (c, d) and 500 nm (c, d insets).

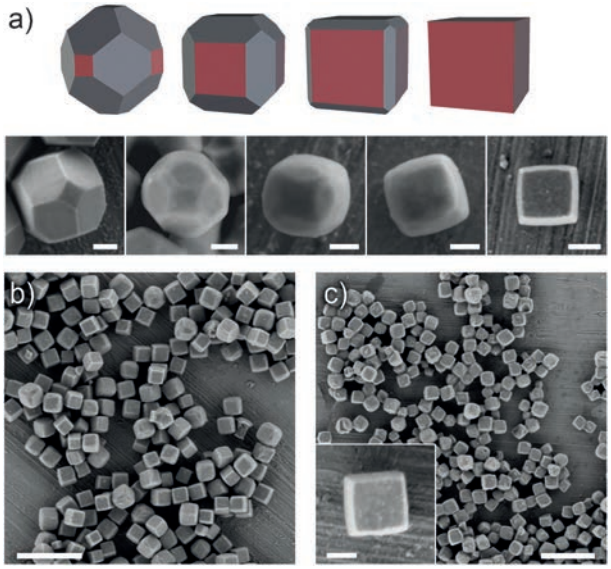


***Figure 2.*** a) Illustration and corresponding FE-SEM images (ZIF-8) of the change in crystal morphology during the etching of truncated rhombic dodecahedral ZIF-8 and ZIF-67 crystals. Note the change in each case, from truncated rhombic dodecahedron to cube. In each case, etching occurs preferentially in the <100> direction. b, c) Representative FE-SEM images showing general views of the ZIF-8 (b) and ZIF-67 (c) cubes. (Inset) Representative FE-SEM image of a single ZIF-67 cube. Scale bars: 1 μm (b, c) and 100 nm (a, c-inset).

adjusted using HCl or NaOH. When the two solutions are mixed, the 2-MIM linkers become protonated. This in turn breaks the Zn/Co–2-MIM bonds, and slowly and preferentially carves those external crystal surfaces having the highest density of Zn/Co–2-MIM bonds (that is, carves in the <100> and/or <211> directions). Simultaneously, XO also acts as a chelating agent that coordinates the liberated $Zn^{II}$ and $Co^{II}$ ions to form the well-known, stable, and water-soluble Zn–XO and Co–XO complexes (for example, $pKf_{Zn\text{-}XO} = 6.15$), respectively.[12] This reaction sequesters the metal ions, thereby preventing any further (undesired) reaction.

A first example of our method is shown in Figure 2, which illustrates the sequential, anisotropic, wet-chemical etching of truncated rhombic dodecahedral ZIF-8 crystals into well-defined cubes. To follow the morphologic evolution, colloidal solutions of ZIF-8 crystals (size = 605 ± 43 nm; Figure 1c) were systematically mixed with XO solutions that vary in pH (8.2, 8.0, 6.0, and 3.0). These mixtures, whose initial pHs changed to 8.3, 8.1, 6.8, and 5.8, respectively, were stirred at 300 rpm for 18 h. We quickly observed two trends from these initial incubations. First, over time, each mixture evolved towards a higher pH (Supporting Information, Figure S4), suggesting that an acid–base reaction had occurred in each one. Second, the initial orange mixtures turned violet, confirming the liberation of $Zn^{II}$ ions and their subsequent complexation with XO (Supporting Information, Figure S4). After 18 h, the resulting products were analyzed through field-emission scanning electron microscopy (FE-SEM), which indicated that they comprised crystals with the 6 {100} facets preferentially etched over the 12 {110} facets, and that the degree of etching increased with decreasing pH of the XO solution (Figure 2a). Consequently, when the XO solution at pH 3 was used, the areas of each one of the 6 etched {100} facets gradually increased until they merged to form well-defined cubes (size = 322 ± 40 nm) that exhibited only {100} facets (Figure 2b). This etching process clearly indicated a reversal of the reaction that had been observed during the original crystallization process described by Wiebcke and coworkers,[11] whereby {100}-faced cubes grow to become {100}- and {110}-faced truncated rhombic dodecahedra (Figure 1a). During this evolution, we also noticed the fingerprints of a slight etching in the {211} edges (Supporting Information, Figure S5). Our observations demonstrated that the surface-selective etching is connected to exposure of the metal clusters on the different external surfaces of the ZIF-8 crystal. Thus, the presence of Zn/Co–2-MIM linkages in {100} facets and {211} edges compared to {110} facets is correlated to the higher etching rate in the <100> and the <211> directions relative to the <110> directions. Furthermore, the relatively greater exposed 2-D area of the {100} facets compared to that of the 1-D {211} edges enabled the etching to proceed more rapidly in the <100> directions, ultimately affording the {100}-faced cubes.

Importantly, we were able to apply the same etching process in ZIF-67 crystals, to morph them from truncated

  

rhombic dodecahedra (size = 628 ± 66 nm; Supporting Information, Figure S3) into cubes (size = 415 ± 47 nm; Figure 2c). In this system, the optimum etching conditions were incubation of the ZIF-67 crystals with a XO solution at pH of 8.0 for 3 h. Also note that, for both ZIFs, the simulated (derived from the single-crystal structure) and experimental (from cubic crystals) X-ray powder diffraction (XRPD) patterns were consistent (Supporting Information, Figure S6), confirming that the etched cubic crystals were structurally identical to the starting (truncated rhombic dodecahedral) ZIF-8 and ZIF-67 crystals, and that the etching had not affected the initial crystalline integrity of the ZIFs.

We sought to explore the role of XO as a chelating agent in the etching process, beyond its importance as a proton source. To this end, we performed the ZIF-8 etching experiment without XO, using only HCl as the etchant solution, to which the crystals at pH 5.8 were exposed for 18 h. Close examination of the product revealed formation of etched ZIF-8 cubes with rougher surfaces than those in the corresponding experiment with XO, as well as a new, unknown crystalline phase that appeared as larger star-like crystals and was subsequently confirmed by XRPD (Supporting Information, Figure S7). These observations indicated that XO can coordinate with $Zn^{II}$ ions released from the etching of ZIF-8 crystals, thereby preventing the precipitation of new solids that would result from the reaction of leached $Zn^{II}$ ions and 2-MIM.

By varying the synthetic conditions of ZIF-8/ZIF-67, we were not only able to construct pure, truncated rhombic dodecahedral crystals, but also obtain perfect rhombic dodecahedral crystals, in which the preferentially etched {110} facets evolved into vertices. Under these new conditions, we expected that the etching would be different and thus, would yield distinct ZIF-8 and ZIF-67 crystal morphologies. To study the products formed, we conducted wet-chemical etching experiments similar to those described above, starting from these rhombic dodecahedral crystals (ZIF-8 size = 1.0 ± 0.1 μm and ZIF-67 size = 1.7 ± 0.3 μm; Figure 1d; Supporting Information, Figure S3). In a first experiment, a colloidal solution of rhombic dodecahedral ZIF-8 (or ZIF-67) crystals was mixed with a XO/HCl etchant solution (pH 2.5), and the resulting mixture was stirred at 300 rpm for 6 h (ZIF-8) or 3 h (ZIF-67). Here, chemical etching yielded hollow ZIF-8 and ZIF-67 microboxes with four openings and thin walls (thickness ca. 40 nm; Figure 3b,c; Supporting Information, Figure S8), as confirmed by FE-SEM and XRPD (Supporting Information, Figure S6). As expected from the etching mechanism (Figure 3a), the edge-length of the resulting boxes was in the range of that of the corresponding initial crystals.

Closer examination of the microboxes described above revealed that they had been formed by anisotropic etching of the original rhombic dodecahedral crystals, from four specific locations. When the process begins, rhombic dodecahedral crystals are preferentially etched from 12 {211} edges that define four equivalent threefold-vertices. As these etched uncovered areas become larger, etching at them becomes progressively faster, leading to formation of pinholes at these vertices, from which the ZIF-8/ZIF-67 are emptied. Note here

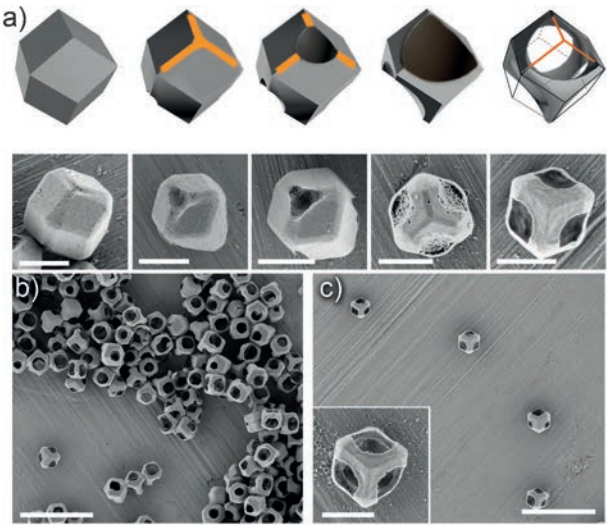


***Figure 3.*** a) Illustration and corresponding FE-SEM images (ZIF-67) of the change in crystal morphology during the etching of rhombic dodecahedral ZIF-8 and ZIF-67 crystals, using an etchant solution at pH 2.5. Note the change from rhombic dodecahedron to hollow box. Etching starts preferentially in the <211> directions. b,c) Representative FE-SEM images showing general views of hollow ZIF-67 microboxes. (Inset) Representative FE-SEM image of a single ZIF-67 microbox. Scale bars: 5 μm (b,c) and 1 μm (a,c-inset).

that although a rhombic dodecahedron has eight threefold-vertices, only half of them are etched, owing to the symmetric non-equivalency of the planes. We attributed this phenomenon to the crystallographic polarity[13] of the non-centrosymmetric ZIF-8/ZIF-67, which determines differences in the chemical behavior of the opposite planes (*hkl*) and ($\bar{h}\bar{k}\bar{l}$). These differences could explain etching of half of the 24 {211} edges. Interestingly, the same effect was observed by Anderson and co-workers in the growing mechanism of $Zn_3(PO_4)_2$ sodalite crystals,[14] which share the same $I\bar{4}3m$ space group as ZIF-8 and ZIF-67.

Formation of these boxes can be explained by the faster etching of the 1-D {211} edges compared to the 0-D {100} vertices in the rhombic dodecahedral crystals. However, increasing the pH of the etchant solution (to 3.5 for ZIF-8 and to 3.25 for ZIF-67) decreased the etching rate in the <211> directions, such that simultaneous etching in the <211> and the <100> directions came to dictate the resulting crystal morphology (Figure 4a). Consequently, etching of rhombic dodecahedra crystals for 18 h (ZIF-8) or 3 h (ZIF-67) afforded concave tetrahedra (ZIF-8 size = 614 ± 50 nm; and ZIF-67 size = 745 ± 83 nm; Figure 4b,c; Supporting Information, Figure S9). Note here that, in the case of ZIF-67, a further etching step using an etchant solution at pH 5.8 for 30 min was needed to obtain uniform tetrahedra. These tetrahedra are defined by four {111} facets and six {100} edges. Again, the XRPD patterns of the products were consistent with those of the initial ZIF-8 and ZIF-67 crystals, confirming that the etched tetrahedral crystals were also structurally identical to initial rhombic dodecahedral crystals. Based on this experiment, we confirmed that we could access com-

  

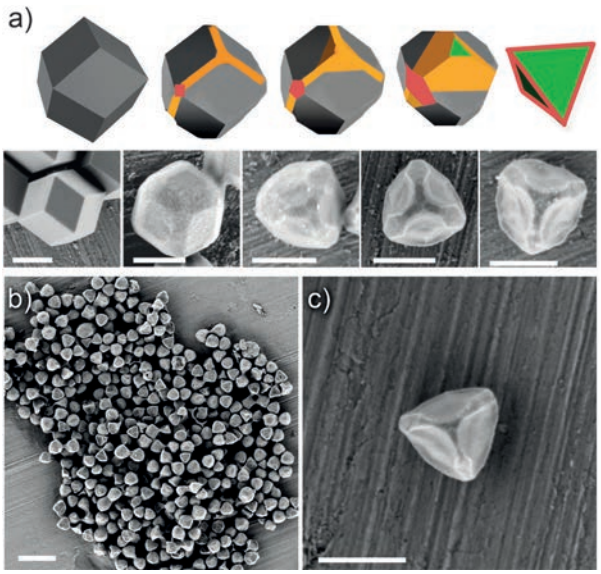


***Figure 4.*** a) Illustration and corresponding FE-SEM images (ZIF-8) of the change in crystal morphology during the etching of rhombic dodecahedral ZIF-8 and ZIF-67 crystals, using an etchant solution at pH 3.5. Note the change from rhombic dodecahedron to concave tetrahedron. Etching occurs preferentially in the <211> and <100> directions. b) Representative FE-SEM images showing general views of tetrahedral ZIF-8 crystals. (c) FE-SEM image of a single ZIF-8 tetrahedron. Scale bars: 500 nm (a, c) and 2 μm (b).

pletely different ZIF crystal morphologies starting from the same crystal; we realized that we could tune the wet-chemical anisotropic etching by simply changing the pH of the etchant solution.

It might be expected that the heavy chemical treatment in the etching process would affect the adsorption capabilities of the resulting etched ZIF-8/ZIF-67 crystal morphologies, but we did not observe this effect. Indeed, $N_2$ sorption measurements (taken at 77 K up to 1 bar) of all the etched ZIF-8 and ZIF-67 crystals proved that they had consistent sorption capacity (Table 1) as that of the initial crystals (Supporting Information, Figures S10–S20).[9,15] In fact, the newly etched materials exhibited slightly higher porosity, a difference that we attributed to the creation of defects[16] during etching.

In conclusion, we have demonstrated anisotropic etching of sodalite ZIF crystals. The etching solution in this process is acidified/basified XO, which serves to sequentially protonate the imidazolate linkers, break the coordination bonds, and sequester the liberated metal ions. We confirmed that etching is surface-selective and preferentially favors the metal–ligand bond-rich crystallographic directions and those crystal surfaces of higher dimensionalities. We were able to tune the etching (and consequently, the etched morphologies) by simply adjusting the pH of the etchant solution, demonstrating that different uniform crystal morphologies (including hollow boxes) can be obtained from the same initial crystal, without any loss in porosity. We consider wet-chemical anisotropic etching of MOFs/ZIFs to be an embryonic but promising method for better understanding their crystallization, and for post-synthetic, top-down production of these materials in unprecedented shapes that would be inaccessible through conventional chemistry. The access to a collection of crystal shapes for a certain MOF should expand their scope in numerous practical applications. For example, etched morphologies with higher surface-area-to-volume ratios with respect to the original shape (such as hollow boxes vs. rhombic dodecahedra) may prove advantageous for applications in chromatography (improving the separation of substances)[8] and in heterogeneous catalysis.[17,18] Also, as already observed in MFI zeolites,[19] etched porous morphologies may show changes in the adsorption/desorption rates because of the change in the number of defects present on the crystal surface. Finally, this novel post-synthetic method could encounter applications in some other fields, such as the synthesis of inorganic nanoparticles and hybrid carbons with new morphologies by the well-established calcination approach using MOF crystals as sacrificial templates.[20]

## Acknowledgements

This work was supported by the MINECO-Spain through projects PN MAT2012-30994, 2014-SGR-80 and EU FP7 ERC-Co 615954. I.I. and J.A. thank the MINECO for a RyC and FPU fellowship, respectively, and V.G. is grateful to the Generalitat de Catalunya for a Beatriu de Pinós Fellowship. ICN2 acknowledges the support of the Spanish MINECO

***Table 1:*** Summary of the BET surface areas and pore volumes of ZIF-8 and ZIF-67 crystals with different morphologies.

| MOF | Crystal Morphology | $S_{BET}$ at first step [$m^2 g^{-1}$] | Total pore volume [$cm^3 g^{-1}$] at $P/P_0 = 0.95$ |
|---|---|---|---|
| ZIF-8 | not defined (polyhedral)[9] | 1328 | 0.64[a] (Theo. = 0.54)[b] |
| | rhombic dodecahedra | 1235 | 0.59 |
| | truncated rhombic dodecahedra | 1385 | 0.68 |
| | cubes | 1425 | 0.71 |
| | boxes | 1310 | 0.69 |
| | tetrahedra | 1420 | 0.71 |
| ZIF-67 | not defined[15] | 1319 | 0.61 (Theo. = 0.55)[b] |
| | rhombic dodecahedra | 1175 | 0.58 |
| | truncated rhombic dodecahedra | 1370 | 0.68 |
| | cubes | 1540 | 0.80 |
| | boxes | 1410 | 0.71 |
| | tetrahedra | 1370 | 0.68 |

[a] Measured at $P/P_0 = 0.1$. [b] Extracted from solvent-free structure.

through the Severo Ochoa Centers of Excellence Program, under Grant SEV-2013-0295.

**Keywords:** anisotropic etching · hollow particles · metal–organic frameworks · porosity · zeolitic–imidazolate frameworks

**How to cite:** *Angew. Chem. Int. Ed.* **2015**, *54*, 14417–14421
*Angew. Chem.* **2015**, *127*, 14625–14629

[1] S. Franssila, *Introduction to Microfabrication*, Wiley, Chichester, **2010**.
[2] a) E. González, J. Arbiol, V. F. Puntes, *Science* **2011**, *334*, 1377–1380; b) A. R. Tao, S. Habas, P. Yang, *Small* **2008**, *4*, 310–325; c) Y. G. Sun, Y. N. Xia, *Science* **2002**, *298*, 2176–2179; d) Y. Yin, R. M. Rioux, C. K. Erdonmez, S. Hughes, G. A. Somorjai, A. P. Alivisatos, *Science* **2004**, *304*, 711–714.
[3] a) Special issue on metal-organic framework materials. *Chem. Soc. Rev.* **2014**, *43*, 5415; b) Special issue on metal-organic framework materials. *Chem. Soc. Rev.* **2009**, *38*, 1201.
[4] a) P. Horcajada, R. Gref, T. Baati, P. K. Allan, G. Maurin, P. Couvreur, G. Férey, R. E. Morris, C. Serre, *Chem. Rev.* **2012**, *112*, 1232–1268; b) M. D. Allendorf, V. Stavila, *CrystEngComm* **2015**, *17*, 229–246; c) N. Stock, S. Biswas, *Chem. Rev.* **2012**, *112*, 933–969; d) H. Furukawa, N. Ko, Y. B. Go, N. Aratani, S. B. Choi, E. Choi, A. Ö. Yazaydin, R. Q. Snurr, M. O'Keeffe, J. Kim, O. M. Yaghi, *Science* **2010**, *329*, 424–428.
[5] a) Y. Yoo, H.-K. Jeong, *Chem. Eng. J.* **2012**, *181–182*, 740–745; b) M. Hu, S. Furukawa, R. Ohtani, H. Sukegawa, Y. Nemoto, J. Reboul, S. Kitagawa, Y. Yamauchi, *Angew. Chem. Int. Ed.* **2012**, *51*, 984–988; *Angew. Chem.* **2012**, *124*, 1008–1012; c) M. Hu, A. A. Belik, M. Imura, Y. Yamauchi, *J. Am. Chem. Soc.* **2013**, *135*, 384–391.
[6] G. Wang, Z. Xu, Z. Chen, W. Niu, Y. Zhou, J. Guo, L. Tan, *Chem. Commun.* **2013**, *49*, 6641–6643.
[7] S. El-Hankari, J. Huo, A. Ahmed, H. Zhang, D. Bradshaw, *J. Mater. Chem. A* **2014**, *2*, 13479–13485.
[8] A. Ahmed, N. Hodgson, M. Barrow, R. Clowes, C. M. Robertson, A. Steiner, P. McKeown, D. Bradshaw, P. Myersa, H. Zhang, *J. Mater. Chem. A* **2014**, *2*, 9085–9090.
[9] a) K. S. Park, Z. Ni, A. P. Côté, J. Y. Choi, R. Huang, F. J. Uribe-Romo, H. K. Chae, M. O'Keeffe, O. M. Yaghi, *Proc. Natl. Acad. Sci. USA* **2006**, *103*, 10186–10191; b) J.-P. Zhang, Y.-B. Zhang, J.-B. Lin, X.-M. Chen, *Chem. Rev.* **2012**, *112*, 1001–1033.
[10] J. Cravillon, R. Nayuk, S. Springer, A. Feldhoff, K. Huber, M. Wiebcke, *Chem. Mater.* **2011**, *23*, 2130–2141.
[11] J. Cravillon, C. A. Schröder, H. Bux, A. Rothkirch, J. Caro, M. Wiebcke, *CrystEngComm* **2012**, *14*, 492–498.
[12] a) K. Studlar, I. Janoušek, *Talanta* **1961**, *8*, 203–208; b) K. Ogura, S. Kurakami, K. Seneo, *J. Inorg. Nucl. Chem.* **1981**, *43*, 1243–1247.
[13] a) P.-F. Fewster, P. A. C. Whiffin, *J. Appl. Phys.* **1983**, *54*, 4668–4670; b) E. P. Warekois, M. C. Lavine, A. N. Mariano, H. C. Gatos, *J. Appl. Phys.* **1962**, *33*, 690–696.
[14] M. A. Holden, P. Cubillas, M. P. Attfield, J. T. Gebbie, M. W. Anderson, *J. Am. Chem. Soc.* **2012**, *134*, 13066–13073.
[15] Q. Shi, Z. Chen, Z. Song, J. Li, J. Dong, *Angew. Chem. Int. Ed.* **2011**, *50*, 672–675; *Angew. Chem.* **2011**, *123*, 698–701.
[16] M. J. Katz, Z. J. Brown, Y. J. Colón, P. W. Siu, K. A. Scheidt, R. Q. Snurr, J. T. Hupp, O. K. Farha, *Chem. Commun.* **2013**, *49*, 9449–9451.
[17] R. Srivastava, M. Choi, R. Ryoo, *Chem. Commun.* **2006**, 4489–4491.
[18] X. Xu, Z. Zhang, X. Wang, *Adv. Mater.* **2015**, *27*, 5365–5371.
[19] P. Kortunov, S. Vasenkov, C. Chmelik, J. Kärger, D. M. Ruthven, J. Wloch, *Chem. Mater.* **2004**, *16*, 3552–3558.
[20] a) X.-Y. Yu, L. Yu, H. B. Wu, X. W. Lou, *Angew. Chem. Int. Ed.* **2015**, *54*, 5331–5335; *Angew. Chem.* **2015**, *127*, 5421–5425; b) W. Cho, Y. H. Lee, H. J. Lee, M. Oh, *Chem. Commun.* **2009**, 4756–4758; c) J. Tang, R. R. Salunkhe, J. Liu, N. L. Torad, M. Imura, S. Furukawa, Y. Yamauchi, *J. Am. Chem. Soc.* **2015**, *137*, 1572–1580.

Received: August 13, 2015
Revised: September 17, 2015
Published online: October 12, 2015

  

Angewandte Chemie
Eine Zeitschrift der Gesellschaft Deutscher Chemiker

Supporting Information

# Post-Synthetic Anisotropic Wet-Chemical Etching of Colloidal Sodalite ZIF Crystals

*Civan Avci, Javier Ariñez-Soriano, Arnau Carné-Sánchez, Vincent Guillerm, Carlos Carbonell, Inhar Imaz,* and Daniel Maspoch**

anie_201507588_sm_miscellaneous_information.pdf

## Experimental Section

**Materials.** 2-methylimidazole (2-MIM), $Zn(OAc)_2{\cdot}2H_2O$ and $Co(OAc)_2{\cdot}4H_2O$ were purchased from Sigma-Aldrich. Xylenol orange sodium salt (XO) was purchased from LOBA Feinchemie GmbH (Austria). All the chemicals were used as purchased without further purification.

**Synthesis of truncated and non-truncated rhombic dodecahedral ZIF-8 crystals.** A solution of 0.3 g of $Zn(OAc)_2{\cdot}2H_2O$ in 5 ml of deionized (DI) water was added into a solution of 1.12 g of 2-MIM in 5 ml of DI water, and the resulting mixture was homogenised by stirring it for a few seconds. Then, the mixture was let at room temperature for 5 h to form truncated rhombic dodecahedral ZIF-8 crystals. Non-truncated rhombic dodecahedral ZIF-8 crystals were prepared using the same procedure as for the truncated ones, except that the mixture was let for 24 h at room temperature. In both cases, white crystals were collected and washed several times with methanol. Finally, the powder was dried under vacuum for 5 h at room temperature.

**Synthesis of truncated and non-truncated rhombic dodecahedral ZIF-67 crystals.** A solution of 0.6 g of $Co(OAc)_2{\cdot}4H_2O$ in 5 ml of DI water was added into a solution of 2.24 g of 2-MIM in 5 ml of DI water, and the resulting mixture the resulting mixture was homogenised by stirring it for a few seconds. Then, the mixture was let at room temperature for 10 min to form truncated rhombic dodecahedral ZIF-67 crystals. Non-truncated rhombic dodecahedral ZIF-67 crystals were prepared using the same procedure as for the truncated ones, except that the mixture was let for 5 h at room temperature. In both cases, purple crystals were collected and washed several times with methanol. Finally, the powder was dried under vacuum for 5 h at room temperature.

**General route for etching ZIF-8/ZIF-67 crystals**. The general method starts with the preparation of a colloidal ZIF-8/ZIF-67 solution by ultrasonication of 25 mg of truncated or non-truncated rhombic dodecahedral ZIF-8/ZIF-67 crystals in 2.5 ml of DI water for 15 min. In parallel, 40 mg of XO was dissolved in 2.5 ml of DI water, and the *pH* of this etchant solution was adjusted by adding HCl or NaOH. The colloidal solution was then injected into the etchant solution, and the resulting mixture was stirred at 300 rpm for an optimized time (*t*). The final solid was collected by centrifugation and washed several times using methanol. The specific conditions for each etching process were: **ZIF-8 cubes:** pH of the etchant solution = 3.0 and t = 18 h; **ZIF-67 cubes:** pH = 8.0 and t = 3 h; **ZIF-8 microboxes:** pH = 2.5 and t = 6 h; **ZIF-67 microboxes:** pH = 2.5 and t = 3 h; **ZIF-8 tetrahedra:** pH = 3.5 and t = 18 h; and **ZIF-67 tetrahedra:** pH = 3.5 and t = 3 h. Note here that, only for ZIF-67 tetrahedra, a second etching step was needed to obtain a uniform sample. This second etching step consisted on washing the primarily etched crystals with water, re-dispersing them in 1 ml of DI water, and incubating them with 1 ml of XO etchant solution at pH = 5.80 for 30 min.

**Characterization.** Field-emission scanning electron microscopy (FE-SEM) images were collected on a scanning electron microscope (FEI Magellan 400L XHR) at acceleration voltage of 1.0 kV, using aluminium as support. The size of crystals was calculated from FE-SEM images by averaging the diameter of at least 100 particles from images of different areas of the same samples. X-ray powder diffraction (XRPD) measurements were done on an X'Pert PRO MPDP analytical diffractometer, $\lambda_{Cu}$ = 1.5406 Å (PANalytical). Volumetric $N_2$ sorption isotherms were collected at 77 K using an ASAP 2020 HD (Micromeritics). As reported by Yaghi *et al.* [K. S. Park, Z. Ni, A. P. Côté, J. Y. Choi, R. Huang, F. J.

Uribe-Romo, H. K. Chae, M. O'Keeffe, O. M. Yaghi, *Proc. Natl. Acad. Sci. U. S. A.* **2006**, *103*, 10186-10191], calculation of the BET area using the last step leads to high BET values but are likely unreliable (negative C constant). Thus, BET areas ($S_{BET}$) were calculated (using MicroActive software) from the first step of the isotherms, leading to significantly lower, but reliable BET values. Additionally, the total pore volumes (Pv) were calculated at $P/P_0 = 0.95$.

**Figure S1.** Representations of the crystal structure of ZIF-8/ZIF-67. Both isostructural ZIF-8 and ZIF-67 crystallize in the cubic space group $I\bar{4}3m$. In these structures, each Zn(II) ion (ZIF-8) or each Co(II) ion (ZIF-67) is tetrahedrally coordinated by four nitrogen atoms of four 2-MIM linkers (a) to form an infinite 3-D porous framework. This framework shows cages with a diameter of 11.6 Å (b) and effective hexagonal windows with a diameter of 3.4 Å. The ZIF-8/ZIF-67 3-D networks (c) resemble a regular zeolitic sodalite (SOD) topology.

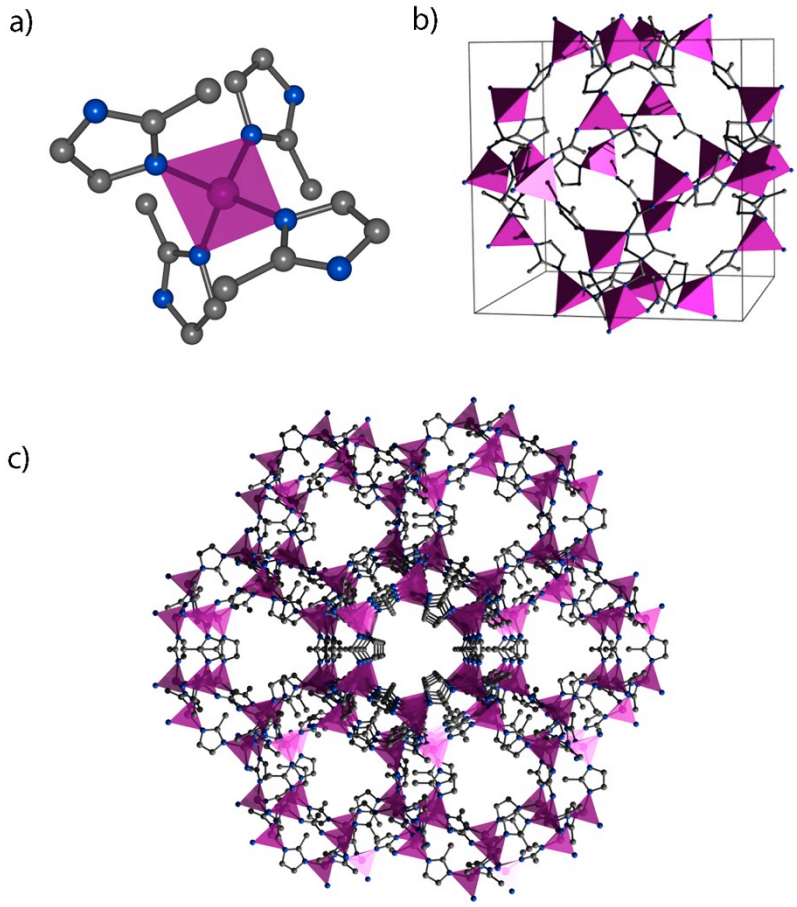

**Figure S2.** a) Representative FE-SEM images of the synthesized truncated rhombic dodecahedral ZIF-8 crystals (size = 605 ± 43 nm). b) Representative FE-SEM images of the synthesized rhombic dodecahedral ZIF-8 crystals (size = 1.0 ± 0.1 μm). Scale bars: 2 μm (a and b-left), and 1 μm (a and b-right).

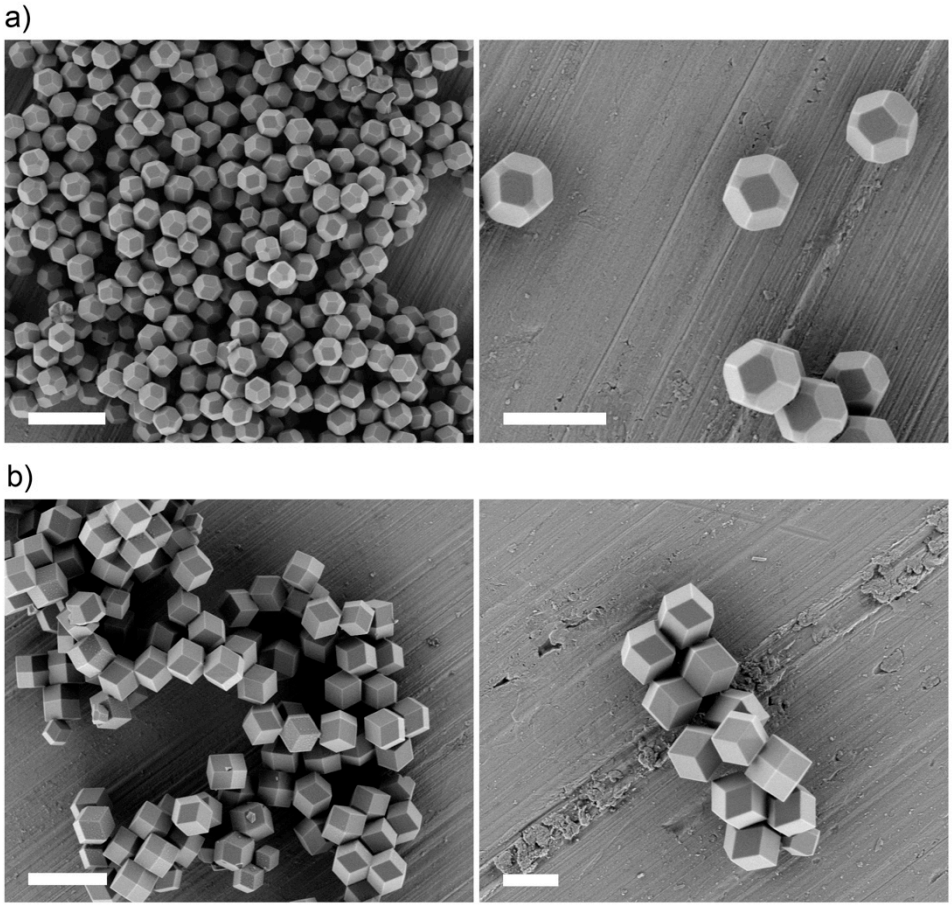

**Figure S3.** a) Representative FE-SEM images of the synthesized truncated rhombic dodecahedral ZIF-67 crystals (size = 628 ± 66 nm). b) Representative FE-SEM images of the synthesized rhombic dodecahedral ZIF-67 crystals (size = 1.7 ± 0.3 μm). Scale bars: 3 μm (a-left), 1 μm (a-right), 10 μm (b-left), and 5 μm (b-right).

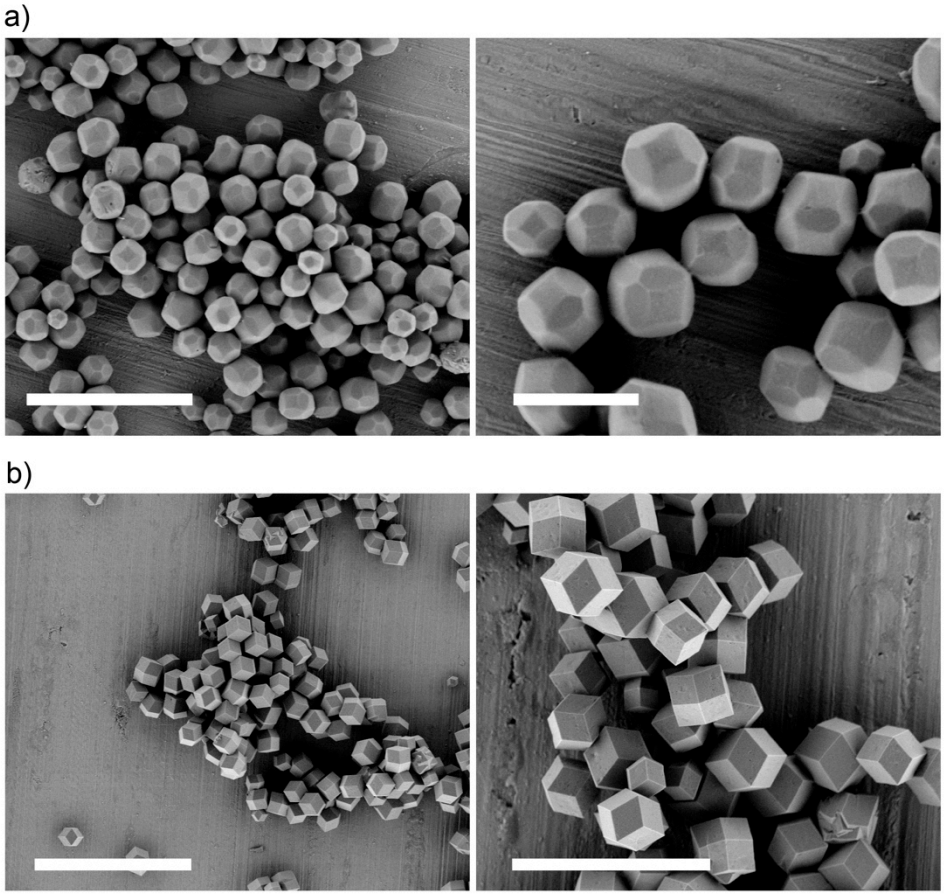

**Figure S4.** a) pH evolution during the etching process of the truncated rhombic dodecahedral ZIF-8 crystals to form cubic crystals. Note here that the pH continuously increases in all cases (from 5.8 to 7.5; from 6.8 to 8.8; from 8.0 to 10.3; and from 8.2 to 10.4 after 18 hours), suggesting that an acid-based reaction occurred. b) Photograph of an aqueous XO solution at pH = 5.8 (left) and the same solution containing ZIF-8 crystals at pH = 5.8 (right). Note here that the colour changed from orange to purple, confirming the complexation of XO with the leached Zn(II) ions.

a)

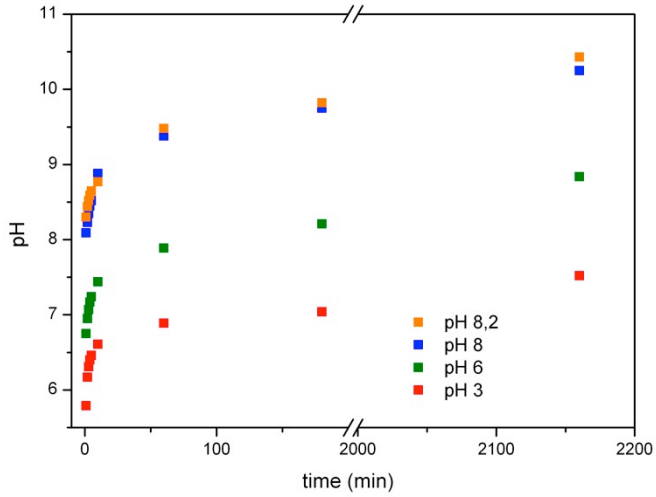


b)

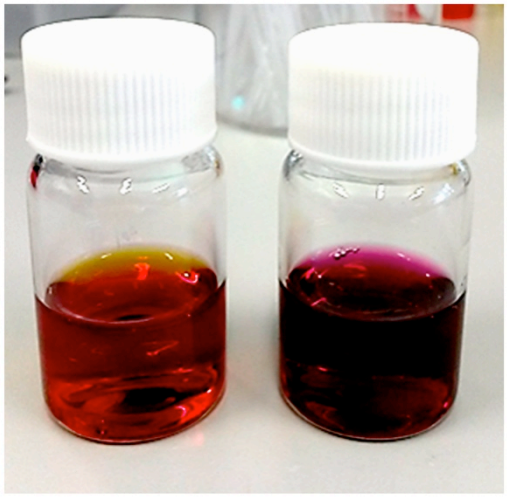

**Figure S5.** a) Representative FE-SEM image of the resulting "round-edged cubes" after etching a colloidal solution of truncated rhombic dodecahedral ZIF-8 crystals for 5 minutes. This early stage of etching reveals the fingerprints of a slight etching in the <211> directions (marked as red dashed lines in **b**) along with the preferential etching in the <100> directions (marked as blue dashed lines). In these etched crystals, the etching process in the <100> directions is not completed yet to form perfect cubes, and it can be observed that the {100} facets are not perfect squares. The concaveness in the {100} facets (marked as red dashed lines in **b**) is the result of a slight etching in the <211> directions. Also note that the concave square facet is more elongated in one axis than in the other. This is again explained by the same phenomenon of the crystallographic polarity. Scale bars: 3 μm (a), and 200 nm (b).

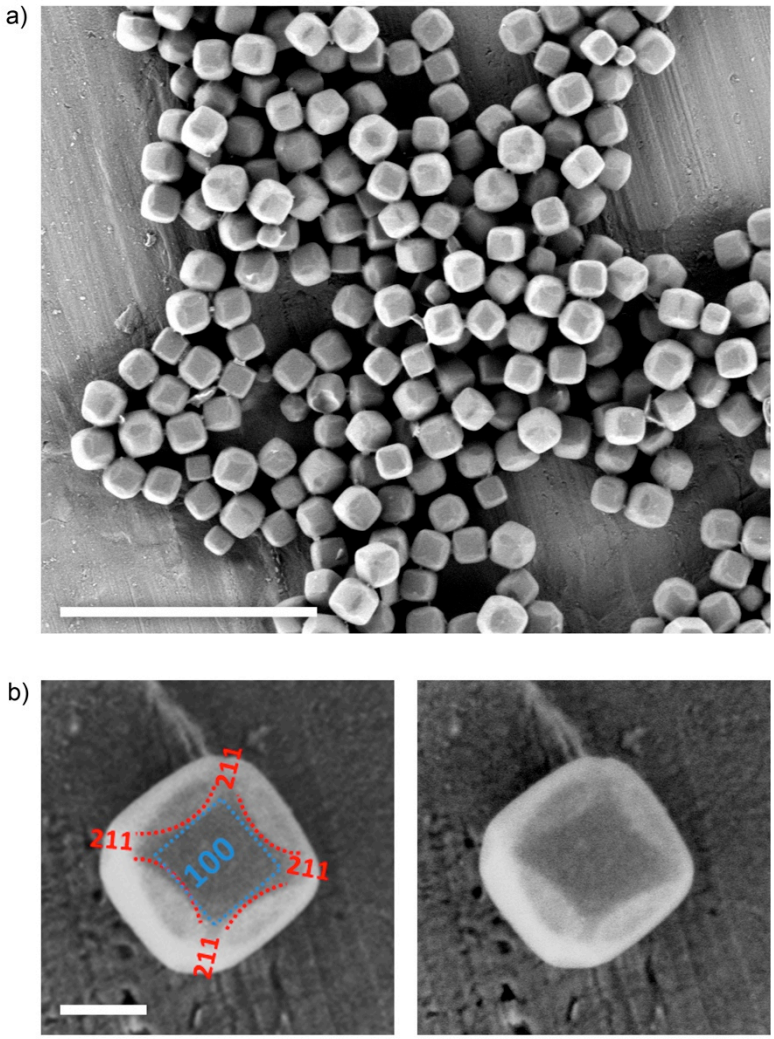

**Figure S6.** a) XRPD of the simulated patterns for ZIF-8 (grey), synthesized truncated (black) and non-truncated (red) rhombic dodecahedral ZIF-8 crystals, and ZIF-8 crystals etched in the form of cubes (pink), hollow microboxes (green) and tetrahedra (blue). b) XRPD of the simulated patterns for ZIF-67 (grey), synthesized truncated (black) and non-truncated (red) rhombic dodecahedral ZIF-67 crystals, and ZIF-67 crystals etched in the form of cubes (pink), hollow microboxes (green) and tetrahedra (blue).

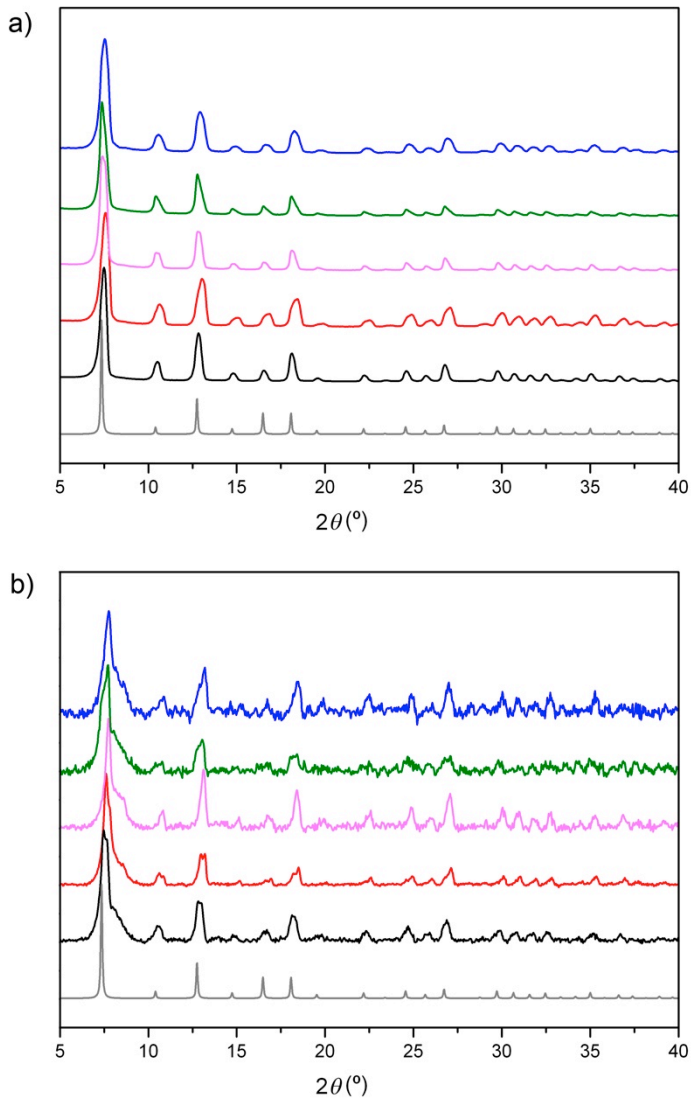

**Figure S7.** a) Representative FE-SEM images of the crystals resulting from etching a colloidal solution of truncated rhombic dodecahedral ZIF-8 crystals in HCl (without XO) for 1 hour (left) and 18 hours (right). Note here the formation of star-like crystals. b) XRPD of the simulated pattern for ZIF-8 (black) and ZIF-8 crystals etched in the absence of XO for 18 hours. Additional peaks that confirm the formation of a new crystalline phase are marked with asterisks. Scale bars: 2 μm (a).

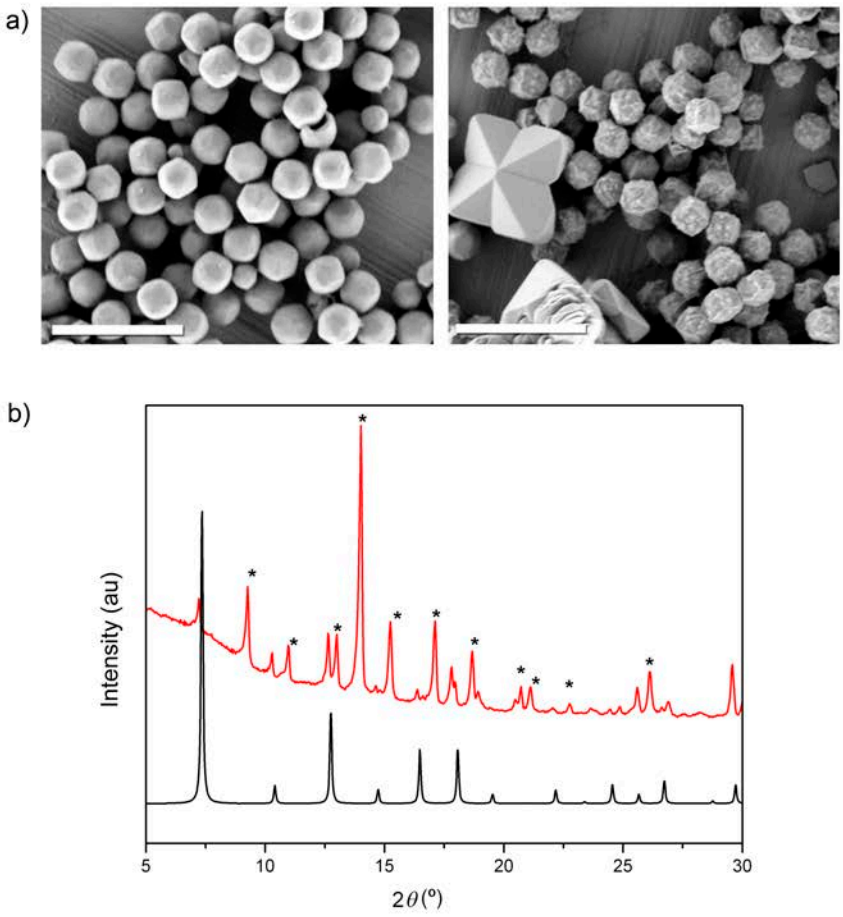

**Figure S8.** Representative FE-SEM images of hollow ZIF-8 microboxes. Scale bars: 10 μm (a), and 500 nm (b).

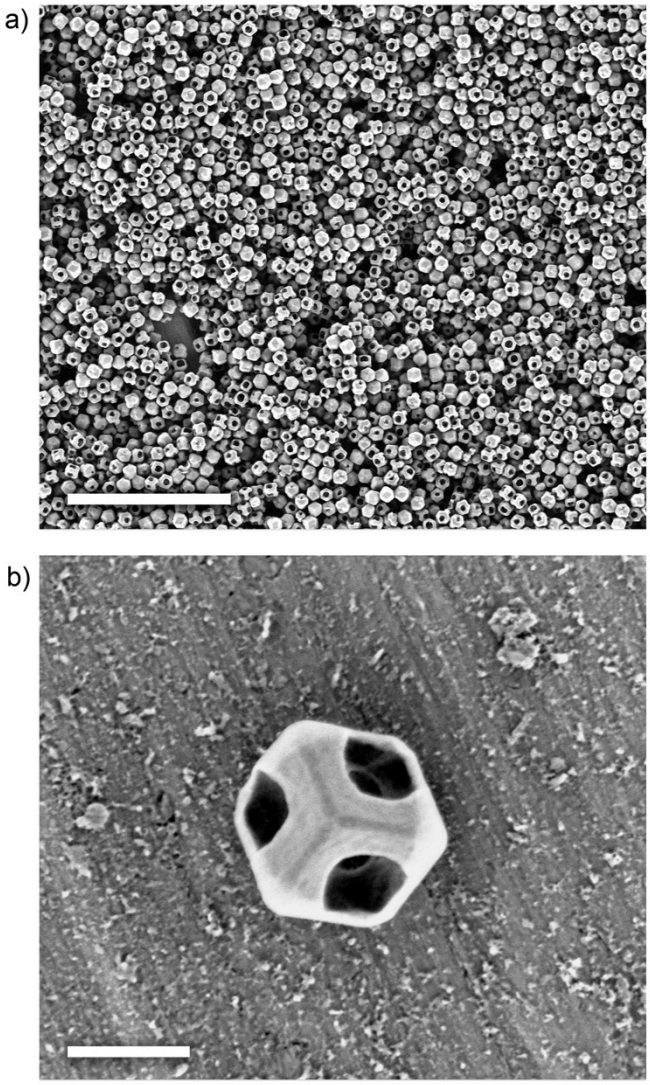

**Figure S9.** Representative FE-SEM images of tetrahedral ZIF-67 crystals. Scale bars: 5 μm (a), and 500 nm (b).

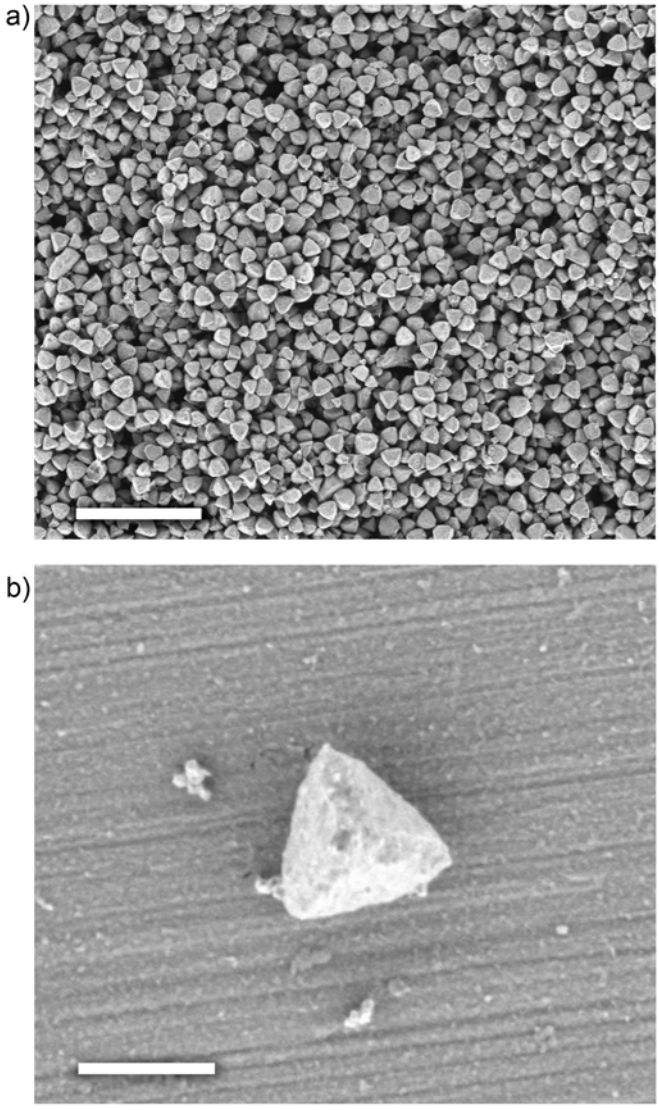

**Figure S10.** a) $N_2$ sorption isotherms at 77 K of synthesized truncated (black) and non-truncated (red) rhombic dodecahedral ZIF-8 crystals, and ZIF-8 crystals etched in the form of cubes (pink), hollow boxes (green) and tetrahedra (blue). b) $N_2$ sorption isotherms at 77 K of synthesized truncated (black) and non-truncated (red) rhombic dodecahedral ZIF-67 crystals, and ZIF-67 crystals etched in the form of cubes (pink), hollow boxes (green) and tetrahedra (blue).

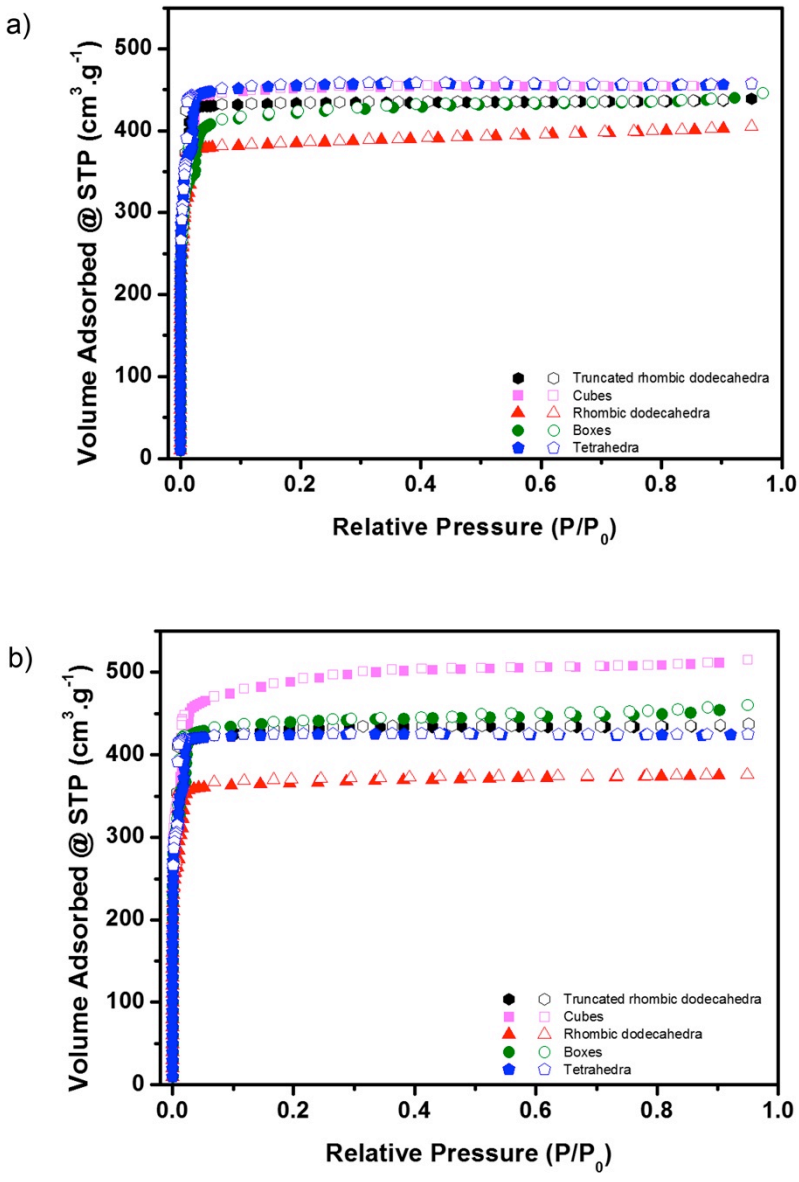

**Figure S11.** $N_2$ sorption isotherm at 77 K and BET linear fit for truncated rhombic dodecahedral ZIF-8 crystals.

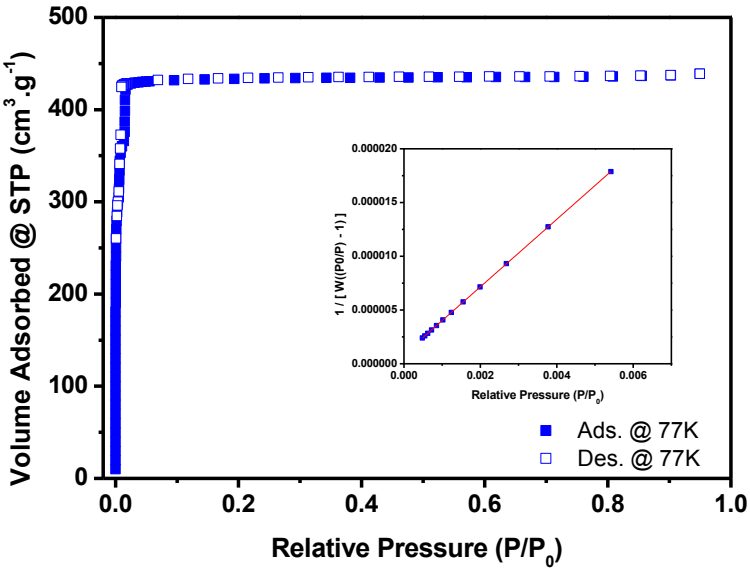


BET surface area: 1385.7726 ± 1.1302 $m^2/g$
Slope: 0.003140 ± 0.000003 $g/cm^3$ STP
Y-intercept: 0.000001 ± 0.000000 $g/cm^3$ STP
C: 3573.158085
Qm: 318.3797 $cm^3/g$ STP
Correlation coefficient: 0.9999967
Molecular cross-sectional area: 0.1620 $nm^2$

**Figure S12.** $N_2$ sorption isotherm at 77 K and BET linear fit for rhombic dodecahedral ZIF-8 crystals.

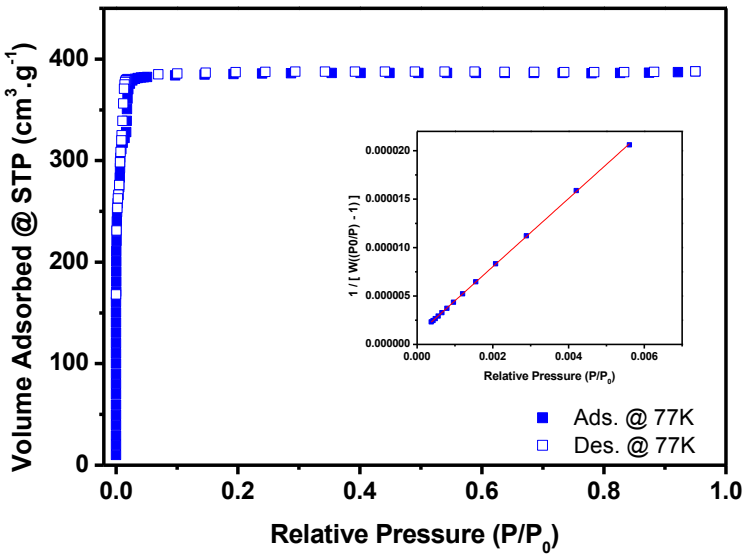


BET surface area: 1236.6999 ± 3.5102 m²/g
Slope: 0.003519 ± 0.000010 g/cm³ STP
Y-intercept: 0.000001 ± 0.000000 g/cm³ STP
C: 3543.120028
Qm: 284.1304 cm³/g STP
Correlation coefficient: 0.9999557
Molecular cross-sectional area: 0.1620 nm²

**Figure S13.** $N_2$ sorption isotherm at 77 K and BET linear fit for cubic ZIF-8 crystals.

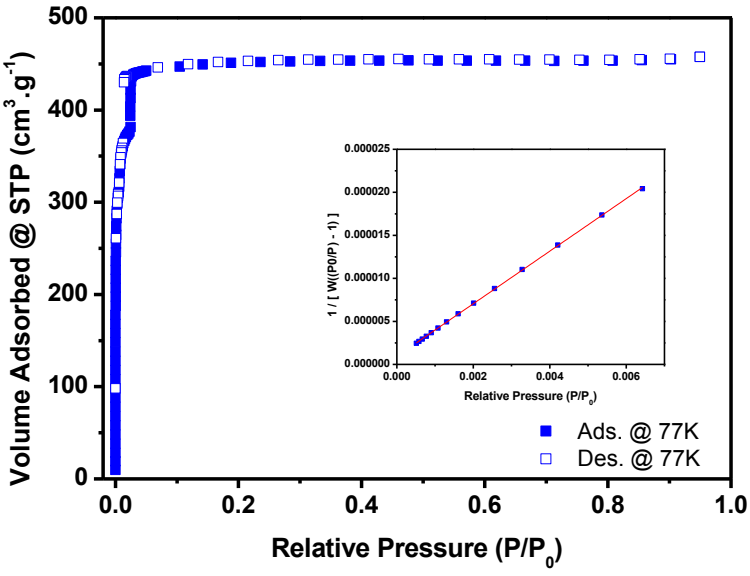


BET surface area: 1424.7266 ± 4.2834 m²/g
Slope: 0.003054 ± 0.000009 g/cm³ STP
Y-intercept: 0.000001 ± 0.000000 g/cm³ STP
C: 3235.061272
Qm: 327.3294 cm³/g STP
Correlation coefficient: 0.9999457
Molecular cross-sectional area: 0.1620 nm²

**Figure S14.** $N_2$ sorption isotherm at 77 K and BET linear fit for hollow ZIF-8 microboxes.

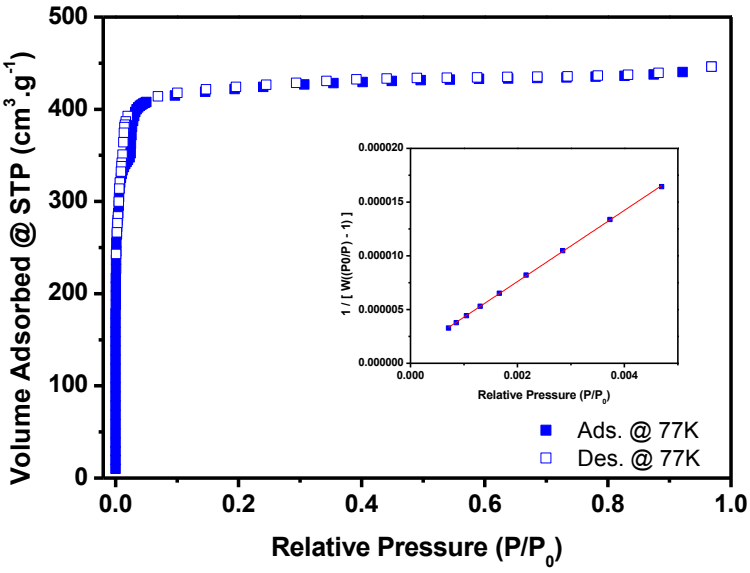


BET surface area: 1313.5323 ± 6.4830 m²/g
Slope: 0.003313 ± 0.000016 g/cm³ STP
Y-intercept: 0.000001 ± 0.000000 g/cm³ STP
C: 3376.395348
Qm: 301.7826 cm³/g STP
Correlation coefficient: 0.9999147
Molecular cross-sectional area: 0.1620 nm²

**Figure S15.** $N_2$ sorption isotherm at 77 K and BET linear fit for tetrahedral ZIF-8 crystals.

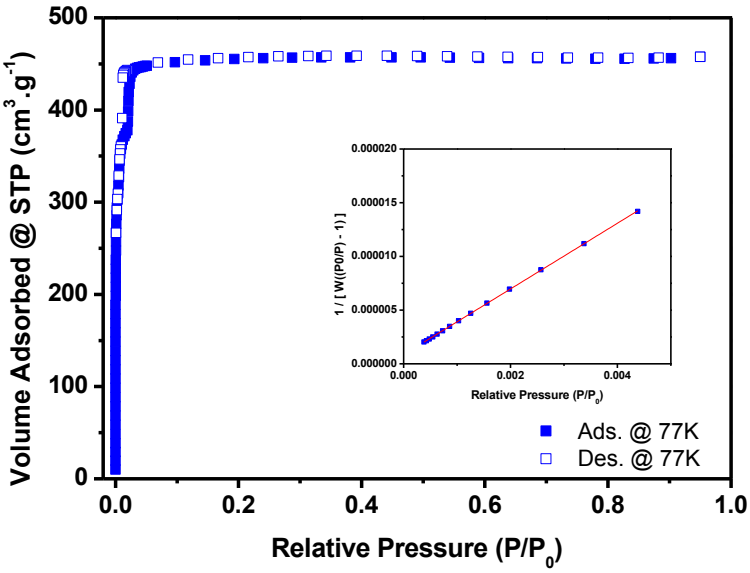


BET surface area: 1422.7822 ± 2.8484 $m^2/g$
Slope: 0.003058 ± 0.000006 $g/cm^3$ STP
Y-intercept: 0.000001 ± 0.000000 $g/cm^3$ STP
C: 3578.973526
Qm: 326.8826 $cm^3/g$ STP
Correlation coefficient: 0.9999759
Molecular cross-sectional area: 0.1620 $nm^2$

**Figure S16.** $N_2$ sorption isotherm at 77 K and BET linear fit for truncated rhombic dodecahedral ZIF-67 crystals.

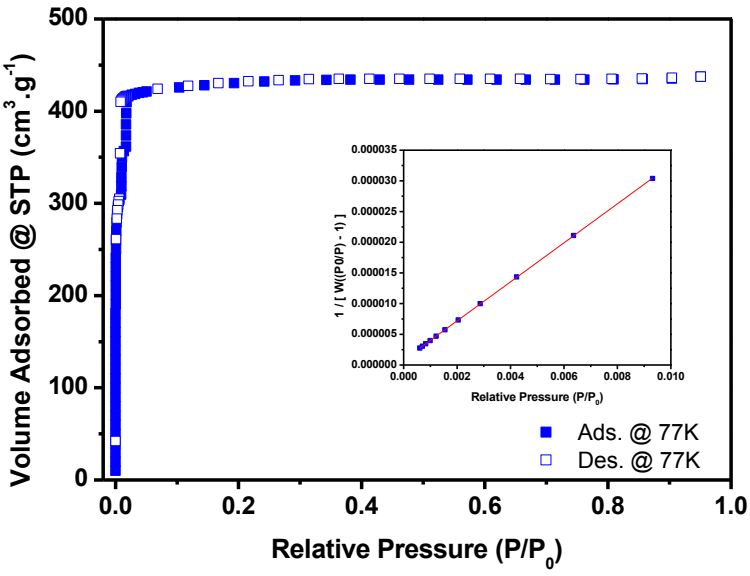


BET surface area: 1368.5073 ± 1.6407 m²/g
Slope: 0.003180 ± 0.000004 g/cm³ STP
Y-intercept: 0.000001 ± 0.000000 g/cm³ STP
C: 3831.988573
Qm: 314.4130 cm³/g STP
Correlation coefficient: 0.9999935
Molecular cross-sectional area: 0.1620 nm²

**Figure S17.** $N_2$ sorption isotherm at 77 K and BET linear fit for rhombic dodecahedral ZIF-67 crystals.

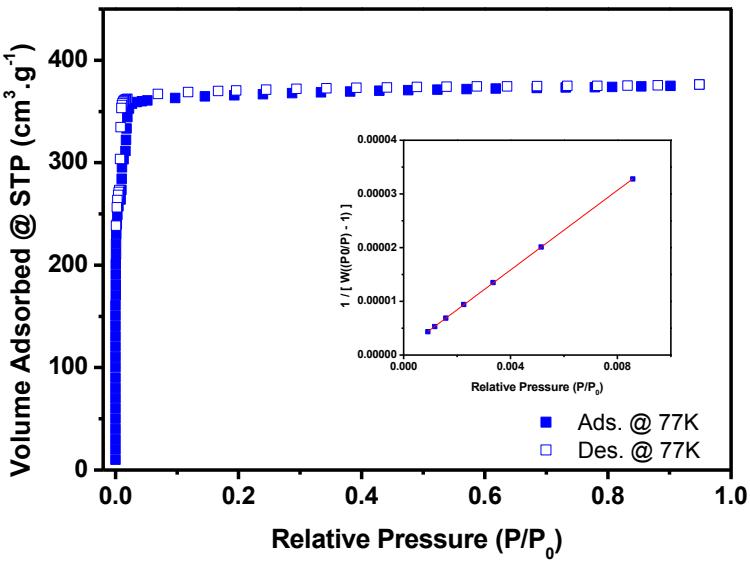


BET surface area: 1173.4649 ± 2.4957 m²/g
Slope: 0.003708 ± 0.000008 g/cm³ STP
Y-intercept: 0.000001 ± 0.000000 g/cm³ STP
C: 3670.777647
Qm: 269.6022 cm³/g STP
Correlation coefficient: 0.9999887
Molecular cross-sectional area: 0.1620 nm²

**Figure S18.** $N_2$ sorption isotherm at 77 K and BET linear fit for cubic ZIF-67 crystals.

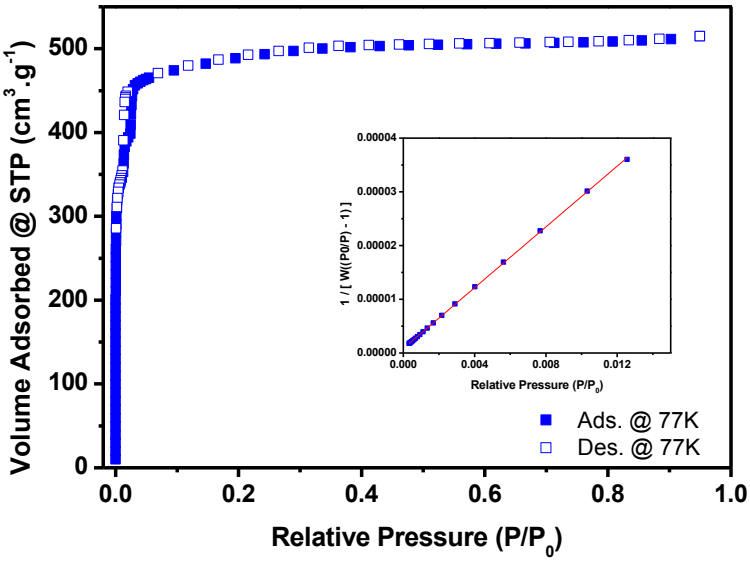


BET surface area: 1538.7033 ± 3.7827 m²/g
Slope: 0.002828 ± 0.000007 g/cm³ STP
Y-intercept: 0.000001 ± 0.000000 g/cm³ STP
C: 3332.438761
Qm: 353.5154 cm³/g STP
Correlation coefficient: 0.9999456
Molecular cross-sectional area: 0.1620 nm²

**Figure S19.** $N_2$ sorption isotherm at 77 K and BET linear fit for hollow ZIF-67 microboxes.

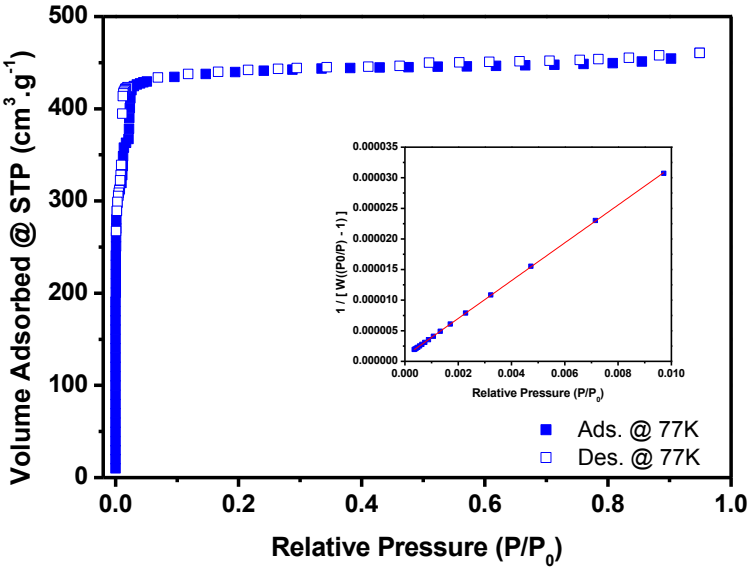


BET surface area: 1408.2787 ± 2.4638 m²/g
Slope: 0.003090 ± 0.000005 g/cm³ STP
Y-intercept: 0.000001 ± 0.000000 g/cm³ STP
C: 3727.327659
Qm: 323.5505 cm³/g STP
Correlation coefficient: 0.9999786
Molecular cross-sectional area: 0.1620 nm²

**Figure S20.** $N_2$ sorption isotherm at 77 K and BET linear fit for tetrahedral ZIF-67 crystals.

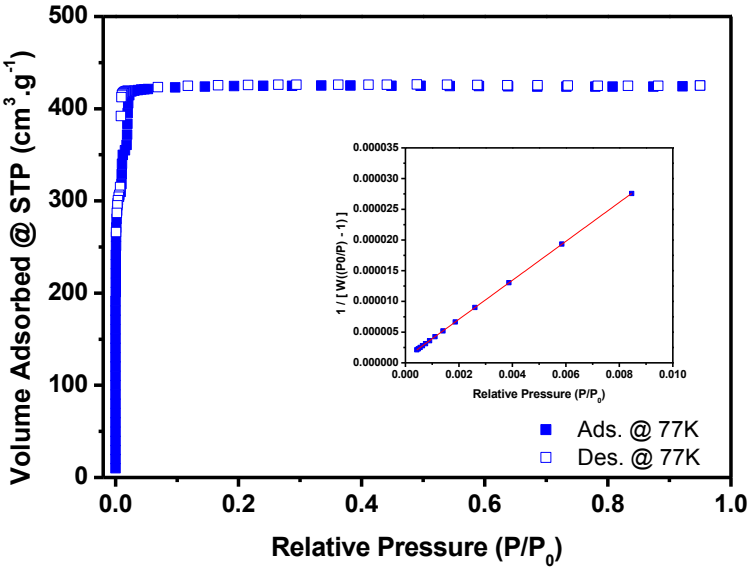


BET surface area: 1371.4704 ± 0.9498 m²/g
Slope: 0.003173 ± 0.000002 g/cm³ STP
Y-intercept: 0.000001 ± 0.000000 g/cm³ STP
C: 4252.386654
Qm: 315.0938 cm³/g STP
Correlation coefficient: 0.9999974
Molecular cross-sectional area: 0.1620 nm²

# CHAPTER 4

# Sequential Deconstruction–Reconstruction of Metal–Organic Frameworks: An Alternative Strategy for Synthesizing (Multi)-Layered ZIF Composites

ACS APPLIED MATERIALS & INTERFACES

Research Article

Cite This: ACS Appl. Mater. Interfaces 2018, 10, 23952−23960

www.acsami.org

# Sequential Deconstruction−Reconstruction of Metal−Organic Frameworks: An Alternative Strategy for Synthesizing (Multi)-Layered ZIF Composites

Civan Avci,[†] Amirali Yazdi,[†] Màrius Tarrés,[‡] Elise Bernoud,[‡] Neus G. Bastús,[†] Victor Puntes,[†,§] Inhar Imaz,[†] Xavi Ribas,[‡] and Daniel Maspoch*[,†,§]

[†]Catalan Institute of Nanoscience and Nanotechnology (ICN2), CSIC, and The Barcelona Institute of Science and Technology, Campus UAB, Bellaterra, Barcelona 08193, Spain

[‡]Institut de Química Computacional i Catàlisi (IQCC) and Departament de Química, Universitat de Girona, Campus Montilivi, Girona E-17071, Catalonia, Spain

[§]ICREA, Pg. Lluís Companys 23, Barcelona 08010, Spain

Supporting Information

**ABSTRACT:** Here, we report the synthesis of (multi)-layered zeolitic imidazolate framework (ZIF-8/-67) composite particles via a sequential deconstruction−reconstruction process. We show that this process can be applied to construct ZIF-8-on-ZIF-67 composite particles whose cores are the initially etched particles. In addition, we demonstrate that introduction of functional inorganic nanoparticles (INPs) onto the crystal surface of etched particles does not disrupt ZIF particle reconstruction, opening new avenues for designing (multi)-layered ZIF-on-INP-on-ZIF composite particles comprising more than one class of inorganic nanoparticles. In these latter composites, the location of the inorganic nanoparticles inside each single metal−organic framework particle as well as of their separation at the nanoscale (20 nm) is controlled. Preliminary results show that (multi)-layered ZIF-on-INP-on-ZIF composite particles comprising a good sequence of inorganic nanoparticles can potentially catalyze cascade reactions.

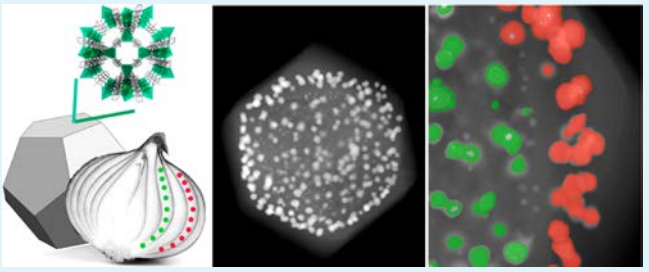

**KEYWORDS:** *metal−organic frameworks, inorganic nanoparticles, ZIF composites, etching, crystal growth, cascade catalysis*

## INTRODUCTION

A major obstacle to the practical application of diverse nanomaterials is the lack of methods to control their morphology.[1,2] To date, several top-down (e.g., etching, lithography, etc.)[3−5] and bottom-up (e.g., use of surfactants, controlled self-assembly, etc.)[6−8] approaches have been employed to design nanomaterials with specific shapes. However, most advanced nanomaterials are not produced and shaped in a single step but rather consecutively, via top-down and bottom-up strategies. A well-known example is the production of integrated circuits,[9] whereby multiple steps of material deposition (bottom-up) are followed by consecutive photolithographic processes (top-down) to reach complex patterns of heterogeneous composition. In the field of inorganic nanoparticles (INPs), a common approach is to combine oxidative etching (top-down) with growth methods (bottom-up), which yields nanoparticles with unprecedented shapes.[10−13]

Recent efforts to control the growth of metal−organic framework (MOF) particles have aimed at discovering new shapes[14] and at making more complex, multicomponent (composite) particles, built by growing one MOF on top of another (known as MOF-on-MOF systems)[15,16] and by combining MOFs with other functional materials, such as INPs[17−19] and biosystems.[20−22] Among the many reported MOFs, the most studied case by far is that of the zeolitic imidazolate frameworks ZIF-8 and ZIF-67, which are isostructural porous materials ($S_{BET}$ ∼ 1400−1700 $m^2/g$) made of Zn(II) and Co(II) ions, respectively. Each ZIF is very interesting because one can epitaxially grow on top of the other one (bottom-up) to afford either ZIF-8-on-ZIF-67 or ZIF-67-on-ZIF-8 particles.[23−26] Also, ZIF-8/ZIF-67 particles can be etched (top-down) into novel shapes[27,28] or synthesized as hollow or yolk-shelled particles.[29−34] Furthermore, both of these ZIFs can grow on the surface of INPs and biosystems, meaning that a rich variety of core−shell[35−44] and layered composites[17,23,45] could be designed.

With these advances, both MOF-on-MOF and etching approaches are now being combined, either sequentially (in said order) or simultaneously, to afford new ZIF-8/ZIF-67

Received: March 29, 2018
Accepted: June 22, 2018
Published: June 22, 2018







DOI: 10.1021/acsami.8b05098
ACS Appl. Mater. Interfaces 2018, 10, 23952−23960

particles. For instance, Li et al. and Muhler et al. reported formation of hollow Zn/Co ZIF particles in which ZIF-8-on-ZIF-67 particles were built and then the ZIF-67 core was etched due to its lower stability in MeOH compared to ZIF-8 under mild solvothermal conditions.[46,47] Similarly, Tsung et al. have shown that preformed ZIF-8 particles could be simultaneously regrown and etched to create hollow ZIF-8 particles.[31] And very recently, Liu et al. have applied regrowth processes followed by etching to build multishelled hollow particles of the well-known MIL-101.[29]

Herein, we report a novel strategy to construct ZIF-on-ZIF and (multi)-layered ZIF-on-INP-on-ZIF particles. Unlike the aforementioned combination (bottom-up/top-down) methods, our method begins with controlled etching followed by MOF-on-MOF growth. Recently, we have demonstrated that colloidal ZIF-8 and ZIF-67 particles can be anisotropically etched into well-defined, unprecedented morphologies. With this deconstructive method, truncated rhombic dodecahedral (tRD) and rhombic dodecahedral (RD) particles can be transformed into uniform cubic (C), hollow (H), or tetrahedral (T) particles (Figure S1). We show that these etched ZIF-8/-67 particles can be reversibly reconstructed to their initial shapes. This reconstruction entails growing ZIF-8 on the etched particles. Therefore, the sequential deconstruction−reconstruction process can be used to form ZIF-8-on-ZIF-67 particles whose cores are the initially etched particles. In addition, we demonstrate that the inclusion of functional INPs on the crystal surface of etched particles does not disrupt particle reconstruction. This observation opens the possibility of using this sequential process to design (multi)-layered ZIF-on-INP-on-ZIF composites formed by more than one class of INPs. In these onionlike composites, the sequence of the INPs can be controlled from outside to inside the ZIF crystal, paving the way for using them for innovative cascade catalytic reactions.

## EXPERIMENTAL SECTION

**Materials.** All materials were purchased from Sigma-Aldrich with no further modification.

**Synthesis of $tRD_{ZIF-67}$, $RD_{ZIF-67}$, and $tRD_{ZIF-8}$ Particles.** A solution of 0.6 g of $Co(OAc)_2{\cdot}4H_2O$ in 5 mL of deionized (DI) water was added into a solution of 2.24 g of 2-methylimidazole (2-MiM) in 5 mL of deionized (DI) water, and the resulting mixture was homogenized by stirring for a few seconds. Then, the mixture was let at room temperature for 10 min to form $tRD_{ZIF-67}$ particles. $RD_{ZIF-67}$ particles were prepared using the same procedure as for the truncated ones, except that the mixture was let for 5 h at room temperature. In both cases, purple crystals were collected and washed several times with methanol. Finally, the powder was dried under vacuum for 5 h at room temperature. In the case of $tRD_{ZIF-8}$ particles, a solution of 0.3 g of $Zn(OAc)_2{\cdot}2H_2O$ in 5 mL of DI water was added into a solution of 1.12 g of 2-MiM in 5 mL of DI water and the resulting mixture was homogenized by stirring for a few seconds. Then, the mixture was let at room temperature for 5 h to form $tRD_{ZIF-8}$ particles.

**General Route for Etching ZIF-67 Particles.** The general method starts with the preparation of a colloidal ZIF-67 solution by ultrasonication of 25 mg of tRD or RD ZIF-67 particles in 2.5 mL of DI water for 15 min. In parallel, 40 mg of xylenol orange (XO) was dissolved in 2.5 mL of DI water and the pH of this etchant solution was adjusted by adding HCl or NaOH. Note here that the etching solution in this process is acidified/basified XO, which protonates the 2-MiM linkers, breaks the coordination bonds, and sequesters the liberated Co(II) ions. The colloidal solution was then injected into the etchant solution, and the resulting mixture was stirred at 300 rpm for an optimized time ($t$). The final solid was collected by centrifugation and washed several times using methanol. The specific conditions for each etching process were $C_{ZIF-67}$: pH = 8.0 and $t$ = 3 h and $T_{ZIF-67}$: pH = 3.5 and $t$ = 3 h. Note here that, only for $T_{ZIF-67}$, a second etching step was needed to obtain a uniform sample. This second etching step consisted on washing the primarily etched crystals with water, redispersing them in 1 mL of DI water, and incubating them with 1 mL of XO etchant solution at pH = 5.80 for 30 min.

**General Route for Growing ZIF-8-on-ZIF-67 Particles.** The general method started with the preparation of a colloidal ZIF-67 solution by ultrasonication of 5 mg of core ZIF-67 particles in 5 mL of methanol for 15 min. 2-MiM (2.5 mL) and $Zn(NO_3)_2{\cdot}6H_2O$ (2.5 mL) with varying concentrations ($C$) were added to the colloidal solution, and the resulting mixture was let at room temperature for a time $t$. Finally, the regrown particles were collected by centrifugation, followed by washing steps with methanol. To make $RD_{ZIF-8}$-on-ZIF-67 crystals with $C_{ZIF-67}$ or $T_{ZIF-67}$ core: $C$ = 25 mM, $t$ = 1 day and with $H_{ZIF-67}$ core: $C$ = 25 mM, $t$ = 4 days. To make $tRD_{ZIF-8}$-on-ZIF-67 crystals with $C_{ZIF-67}$ or $T_{ZIF-67}$ core: $C$ = 10 mM, $t$ = 1 day and with $H_{ZIF-67}$ intermediate: $C$ = 25 mM, $t$ = 1 day.

**Synthesis of Au Nanoparticles (∼9 nm Diameter).** Au NPs were produced following a previously reported protocol.[48] In detail, a solution of 2.2 mM sodium citrate in DI water (150 mL) was heated with a heating mantle in a 250 mL three-necked round-bottomed flask for 15 min under vigorous stirring. A condenser was utilized to prevent the evaporation of the solvent. After boiling had commenced, 1 mL of $HAuCl_4$ (25 mM) was injected. The color of the solution changed from yellow to bluish gray and then to soft pink in 10 min. Under these conditions, the resulting particles (9 ± 2 nm, ∼$3 \times 10^{12}$ NPs/mL) were coated with negatively charged citrate ions and hence they were well suspended in $H_2O$. After the Au nanoparticle solution was cooled to room temperature, a solution of 0.5 g of poly(vinylpyrrolidone) (PVP, MW = 40 000) in water (20 mL) was added dropwise to the Au nanoparticle solution under continuous stirring, and the mixture was further stirred at room temperature for 24 h. Then, 600 mL of acetone was added to this mixture and left overnight. The supernatant was removed, and the resulting nanoparticles were washed three times with methanol, and finally dispersed in methanol at a concentration of 0.6 mg/mL.

**Synthesis of Au Nanoparticles (∼22 nm Diameter).** A solution of 2.2 mM sodium citrate in DI water (150 mL) was heated with a heating mantle in a 250 mL three-necked round-bottomed flask for 15 min under vigorous stirring. A condenser was utilized to prevent the evaporation of the solvent. After boiling had commenced, 1 mL of $HAuCl_4$ (25 mM) was injected. The color of the solution changed from yellow to bluish gray and then to soft pink in 10 min. Then, the reaction was cooled until the temperature of the solution reached 90 °C; after that, 1 mL of a $HAuCl_4$ solution (25 mM) was injected to the solution and stirred for 30 min. This process was repeated one more time. Under these conditions, the resulting particles (22 ± 2 nm, ∼$1.2 \times 10^{12}$ NPs/mL) were coated with negatively charged citrate ions and hence they were well suspended in $H_2O$. After the Au nanoparticle solution was cooled to room temperature, a solution of 0.5 g of PVP in water (20 mL) was added dropwise to the Au nanoparticle solution under continuous stirring, and the mixture was further stirred at room temperature for 24 h. Then, 600 mL of acetone was added to this mixture and left overnight. The supernatant was removed, and the resulting nanoparticles were washed three times with methanol, and finally dispersed in methanol at a concentration of 1.4 mg/mL.[48]

**Synthesis of Au Nanoparticles (∼4 nm Diameter).** A solution of 2.2 mM sodium citrate in DI water (300 mL) was heated up to 70 °C under vigorous stirring. Then, 0.2 mL of tannic acid (2.5 mM) and 2 mL of potassium carbonate ($K_2CO_3$, 150 mM) were added to the heated solution. Afterward, 2 mL of $HAuCl_4$ (25 mM) was injected and the color of the solution changed from yellow to bluish gray to reddish orange in 10 min. The solution was stirred at the same temperature for 2 h. Under these conditions, the resulting nanoparticles (3.6 ± 0.4 nm, 0.2 mg/mL) were coated with negatively charged citrate ions and hence they were well suspended in $H_2O$. The same coating producer as for Au nanoparticles (∼9 nm diameter) was used to functionalize these nanoparticles with PVP.[49]


DOI: 10.1021/acsami.8b05098
ACS Appl. Mater. Interfaces 2018, 10, 23952−23960

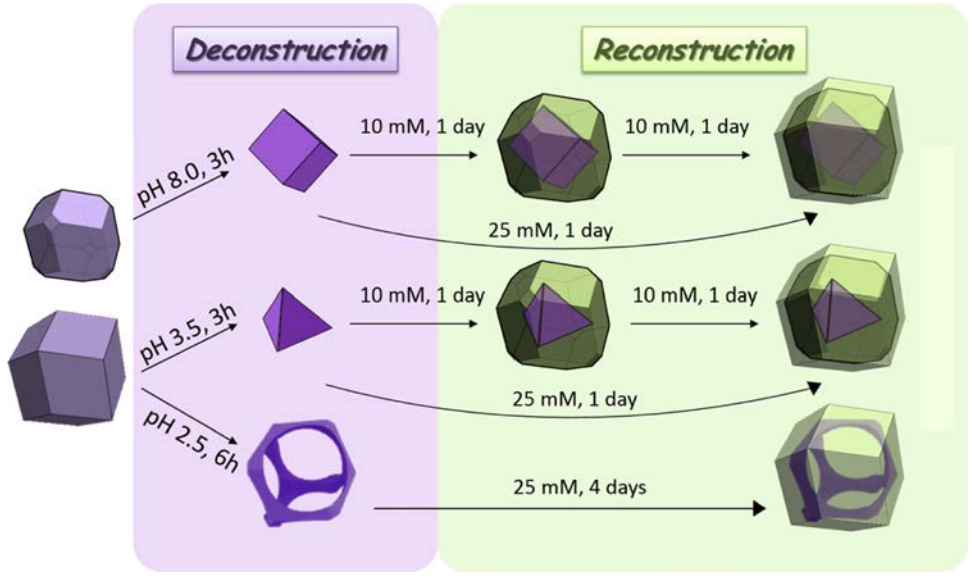


**Figure 1.** Schematic illustration of the synthetic conditions used to construct the different ZIF-8-on-ZIF-67 particles according to the sequential deconstruction–reconstruction strategy.

**Synthesis of Cubic Pd Nanoparticles (~18 nm Diameter).** KBr (547 mg), PVP (100 mg, MW = 55 000), $Na_2PdCl_4$ (51 mg), and L-ascorbic acid (55 mg) were added to 10 mL of DI water and heated to 80 °C under reflux and vigorous stirring for 3 h. After the nanoparticle solution was cooled to room temperature, the nanoparticles were washed twice with a mixture of acetone and water and one time with methanol and finally dispersed in methanol at a concentration of 0.5 mg/mL (size = 18 ± 2 nm).[6]

**Synthesis of Icosahedral Pd Nanoparticles (~13 nm Diameter).** In a standard procedure for the synthesis of Pd icosahedra, 160 mg of PVP and 20 μL of HCL (3 M) were introduced into 4 mL of diethylene glycol (DEG) hosted in a 20 mL vial. This mixture was preheated in an oil bath at 105 °C for 20 min under magnetic stirring. Subsequently, 2 mL of DEG solution containing 31 mg of $Na_2PdCl_4$ was added using a pipette. After the reaction had proceeded for 1 h, it was quenched by immersing the vial in an ice/water bath. Finally, the product was collected by centrifugation, washed once with acetone and twice with water to remove DEG and excess of PVP, and finally dispersed in methanol at a concentration of 0.6 mg/mL (size = 13 ± 4 nm).[50]

**Synthesis of Cu/Pd Nanoparticles (~10 nm Diameter).** In a typical process, 10 mg of $Na_2PdCl_4$, 36 mg of $CuSO_4$, and 240 mg of sodium citrate were added to a mixture of 40 mL of DI water and 20 mL of ethylene glycol. This mixture was then heated in an oil bath up to 160 °C in a 100 mL round-bottomed flask under vigorous stirring for 6 h. A condenser was utilized to prevent the evaporation of the solvent. After the nanoparticle solution was cooled to room temperature, a solution of 0.7 g of PVP (MW = 55 000) in water (10 mL) was added dropwise to the nanoparticle solution under continuous stirring and the mixture was further stirred at room temperature for 24 h. Then, 200 mL of acetone was added to this mixture and left overnight. The supernatant was removed, and the resulting nanoparticles were washed twice with water and twice with methanol, and finally dispersed in methanol at a concentration of 1.8 mg/mL (size = 10 ± 3 nm, Cu/Pd = 1:2).

**Synthesis of Au (9 nm)-on-ZIF-67 Composites.** $C/T/H_{ZIF\text{-}67}$ (10 mg) was dispersed in 5 mL of ethanol in a sonication bath for 10 min and then 10 mL of Au nanoparticle solution was added dropwise to the dispersion while stirring. The resulting composites were collected by centrifugation, washed twice with ethanol, and dried at 60 °C overnight.

**Synthesis of $tRD_{ZIF\text{-}8}$-on-Au (9 nm)-on-ZIF-67 Composites.** The same general route for growing $tRD_{ZIF\text{-}8}$-on-$C_{ZIF\text{-}67}$ was applied. The only difference is that we used Au (9 nm)-on-$C_{ZIF\text{-}67}$ cores in various shapes instead of only ZIF-67 cores.

**Synthesis of $RD_{ZIF\text{-}8}$-on-INPs-on-$tRD_{ZIF\text{-}8}$-on-Au (9 nm)-on-$C_{ZIF\text{-}67}$ Layered Composites.** $tRD_{ZIF\text{-}8}$-on-Au (9 nm)-on-$C_{ZIF\text{-}67}$ crystals (10 mg) were dispersed in 5 mL of ethanol in a sonication bath for 10 min. Then, desired amount of the corresponding INP (22 nm in diameter Au NPs, 13 nm in diameter icosahedral Pd NPs, or 18 nm in size cubic Pd NPs) solution was added dropwise to the dispersion while stirring. The resulting composites were collected by centrifugation, washed twice with ethanol, and dried at 60 °C overnight. The different INP-on-$tRD_{ZIF\text{-}8}$-on-Au (9 nm)-on-$C_{ZIF\text{-}67}$ composite crystals were finally subjected to a ZIF-8 growing using $C$ = 10 mM and $t$ = 1 day.

**Synthesis of INP-on-$tRD_{ZIF\text{-}8}$ Composites.** The same general route for growing Au (9 nm)-on-$C_{ZIF\text{-}67}$ was applied. $tRD_{ZIF\text{-}8}$ (10 mg) particles were dispersed in 5 mL of methanol in a sonication bath for 10 min. Then, 10 mL of Au (3 nm) nanoparticle solution, 1 mL of Cu/Pd (10 nm) nanoparticle solution, or a mixture of both nanoparticle solutions were added dropwise to this dispersion under continuous stirring. The different Au-on-$tRD_{ZIF\text{-}8}$, Cu/Pd-on-$tRD_{ZIF\text{-}8}$, and Au/Cu/Pd-on-$tRD_{ZIF\text{-}8}$ composites were collected by centrifugation, washed twice with ethanol, and dried at 60 °C overnight.

**Synthesis of INP-on-$tRD_{ZIF\text{-}8}$-on-INP-on-$tRD_{ZIF\text{-}8}$ Layered Composites.** A similar methodology used for growing $RD_{ZIF\text{-}8}$-on-INPs-on-$tRD_{ZIF\text{-}8}$-on-Au (9 nm)-on-$C_{ZIF\text{-}67}$ layered composites was applied. INP-on-$tRD_{ZIF\text{-}8}$ (10 mg) particles were dispersed in 10 mL of methanol in a sonication bath for 10 min. Then, 5 mL of 25 mM 2-MiM and 5 mL of 25 mM $Zn(NO_3)_2{\cdot}6H_2O$ in methanol were sequentially added to this dispersion in this order and left at room temperature without stirring for 10 min. The resulting particles were collected by centrifugation, washed twice with methanol, and dried at 60 °C overnight. Then, 10 mg of these particles were dispersed in 5 mL of methanol in a sonication bath for 10 min. Afterward, desired amount of the corresponding INP (Au (3 nm) or Cu/Pd (10 nm)) solution was added dropwise to the dispersion under continuous stirring. The final particles were collected by centrifugation, washed once with methanol, and dried at 60 °C overnight.

**General Route for the Catalytic Reactions.** A mixture of 1-(prop-2-yn-1-yloxy)naphthalene (**1**) (2.32 mg, 12.7 μmol), $K_2CO_3$ (3.52 mg, 25.5 μmol), iodobenzene (PhI; 1.42 μL, 12.7 μmol), xantphos (0.37 mg, 0.63 μmol), mesitylene as internal standard (0.35 μL, 5.1 μmol), and the desired ZIF-8-based catalyst (5 mol %) were mixed in 0.6 mL of dry toluene in a 2 mL sealed vial. The dispersion was sonicated for 15 min and stirred for 6 days at 110 °C. Afterward,


DOI: 10.1021/acsami.8b05098
ACS Appl. Mater. Interfaces 2018, 10, 23952–23960

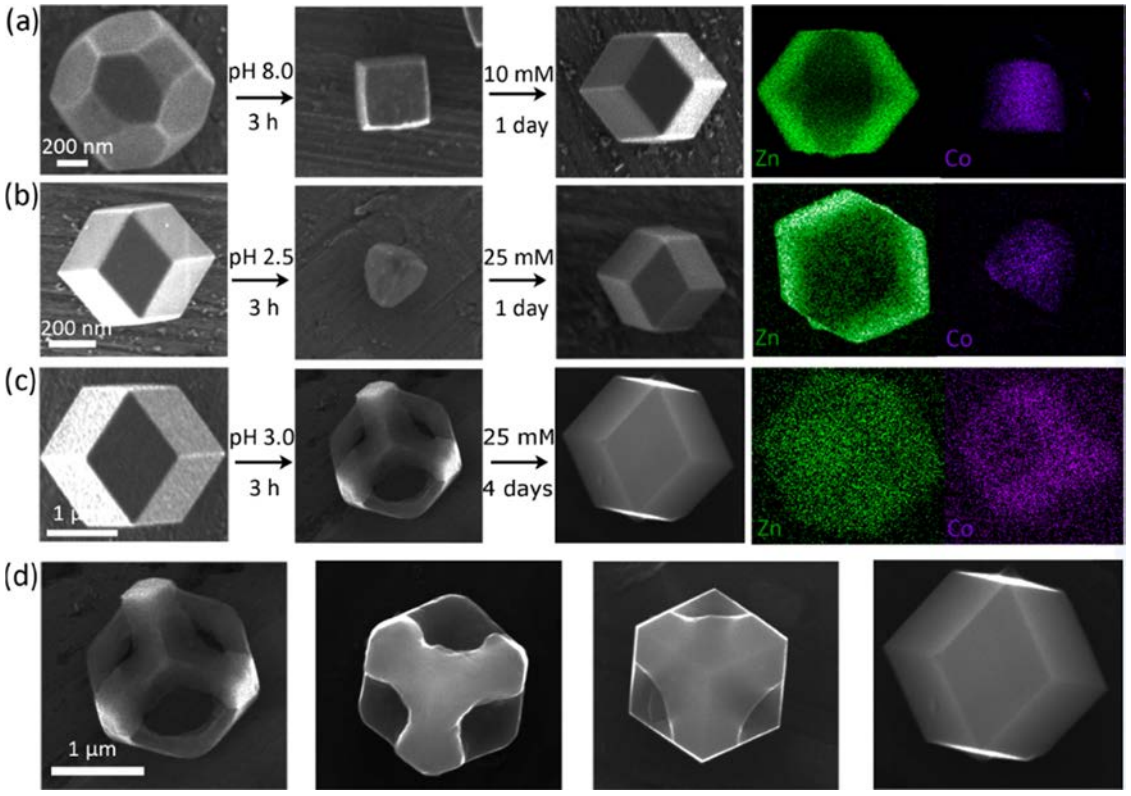


**Figure 2.** (a–c) FE-SEM images of single particles showing the formation of $RD_{ZIF\text{-}8}$-on-$C_{ZIF\text{-}67}$ (a), $RD_{ZIF\text{-}8}$-on-$T_{ZIF\text{-}67}$ (b), and $RD_{ZIF\text{-}8}$-on-$H_{ZIF\text{-}67}$ (c) particles built by the deconstruction–reconstruction strategy. Right-hand panel: the corresponding elemental mapping (energy-dispersive X-ray spectrometry, EDXS) results, showing the distribution of Zn (green) and Co (violet). (d) FE-SEM images showing the evolution of the formation of $RD_{ZIF\text{-}8}$-on-$H_{ZIF\text{-}67}$.

the raw solution was filtered through a silica pad and 4 mL of ethyl acetate were passed to elute all of the generated products. The obtained components were analyzed and quantified by means of gas chromatography and $^1$H NMR. Compounds **1**–**4** were synthesized and characterized according to the literature.[51−55]

**Characterization.** Powder X-ray diffraction (PXRD) patterns were collected on an X'Pert PRO MPDP analytical diffractometer (Panalytical) at 45 kV, 40 mA using Cu K$\alpha$ radiation ($\lambda$ = 1.5419 Å). Nitrogen adsorption and desorption measurements were done at 77 K using an Autosorb-IQ-AG analyzer (Quantachrome Instruments). Field-emission scanning electron microscopy (FE-SEM) images were collected on a FEI Magellan 400L scanning electron microscope at an acceleration voltage of 1.0–2.0 kV, using aluminum as support. High-angle annular dark-field scanning transmission electron microscopy (HAADF-STEM) images were obtained with a FEI Tecnai G2 F20 at 200 kV. Metal contents of all composites were determined by inductively coupled plasma optical emission spectroscopy (ICP-OES). These measurements were performed using an ICP-OES PerkinElmer, model Optima 4300DV by previous digestion of the composites in a mixture of $HNO_3$ and HCl (1:2) at 220 °C. Gas chromatography product analyses were performed on an Agilent 7820A gas chromatograph equipped with a HP-5 capillary column (30 m × 0.32 mm × 0.25 $\mu$m). The injection was carried out on a split/splitless automatic injector Agilent G4513A, in split mode with ratio 100:1 with an injected volume of 1 $\mu$L. The detection was conducted by a flame ionization detector (Agilent 7820A GC-System). $^1$H NMR data concerning product identity were collected with a Bruker 400 Avance (Serveis Tècnics de Recerca, University of Girona) spectrometer in the corresponding deuterated solvent ($CDCl_3$) and calibrated relative to the residual protons of the solvent. 1,3,5-Trimethoxybenzene (mesitylene) was used as internal standard.

## RESULTS AND DISCUSSION

Figure 1 depicts the different ZIF-8-on-ZIF-67 particles generated by sequential deconstruction–reconstruction. This process starts with anisotropic etching of the ZIF-67 particles to C, H, and T particles under our previously reported synthetic conditions.[27] The resulting etched particles are then dispersed in methanol (MeOH) and mixed with a solution of 2-methylimidazole (2-MiM) in MeOH at an optimized concentration. Afterward, a solution of $Zn(NO_3)_2{\cdot}6H_2O$ in MeOH at the same concentration is added, and the resulting mixture is left at room temperature for a certain time. Note that the required precursor concentration and the reaction time vary by the initial morphology of the etched core particle and that, in all cases, we could optimize them to selectively generate tRD or RD particles. For instance, when the core was a cubic or tetrahedral ZIF-67 particle, $tRD_{ZIF\text{-}8}$-on-$C_{ZIF\text{-}67}$ and $tRD_{ZIF\text{-}8}$-on-$T_{ZIF\text{-}67}$ particles were formed at a concentration of 10 mM and a reaction time of 1 day. In contrast, $RD_{ZIF\text{-}8}$-on-$C_{ZIF\text{-}67}$ and $RD_{ZIF\text{-}8}$-on-$T_{ZIF\text{-}67}$ particles were synthesized by increasing the concentration up to 25 mM and maintaining the reaction time at 1 day (for full synthetic procedures, see Experimental Section).

For the hollow microboxes, $RD_{ZIF\text{-}8}$-on-$H_{ZIF\text{-}67}$ particles were formed at a concentration of 25 mM and a reaction time of 4 days. With this core, controlled growth of an external $tRD_{ZIF\text{-}8}$ layer was not possible, since in etched hollow microboxes all six (100) vertices are already fully grown. However, the RD shape was fully recovered. Indeed, we found that these particles grew mainly inside of the hollow core, thus fully reversing the etching process (Figure 2d).


DOI: 10.1021/acsami.8b05098
ACS Appl. Mater. Interfaces 2018, 10, 23952–23960

Comparison of field-emission scanning electron microscopy (FE-SEM) images of the etched particles and the resulting ZIF-8-on-ZIF-67 particles confirmed their reconstruction into homogeneous tRD or RD particles (Figures 2 and S1). The internal composition of single particles was investigated by elemental mapping with energy-dispersive X-ray spectrometry (EDXS), which revealed a distribution of Co atoms following the shape of the initial etched ZIF-67 particles and a distribution of Zn atoms corresponding to the newly reconstructed layers (Figure 2). Moreover, powder X-ray diffraction (PXRD) patterns and Brunauer–Emmett–Teller (BET) surface areas ($RD_{ZIF\text{-}8}$-on-$C_{ZIF\text{-}67}$, $S_{BET}$ = 1417 $m^2/g$; $RD_{ZIF\text{-}8}$-on-$T_{ZIF\text{-}67}$, $S_{BET}$ = 1422 $m^2/g$; and $RD_{ZIF\text{-}8}$-on-$H_{ZIF\text{-}67}$, $S_{BET}$ = 1324 $m^2/g$) confirmed that these ZIF-on-ZIF systems are pure ZIF-8/ZIF-67 (Figures S3 and S4). Also note here that all $RD_{ZIF\text{-}8}$-on-$(C/T)_{ZIF\text{-}67}$ particles could be generated from the $tRD_{ZIF\text{-}8}$-on-$(C/T)_{ZIF\text{-}67}$ particles under the conditions described in Figure 1.

Altogether, these experiments showed that, even for the hollow microboxes, all etched cores can be reconstructed to its original shape by controlled regrowing. The fact that all the final shapes are similarly {110} dominant is the consequence of the difference in the growing kinetics in the ⟨100⟩, ⟨110⟩, and ⟨111⟩ directions, from which ⟨110⟩ is the slowest.

Having demonstrated that stepwise reconstruction of our etched particles from C/T to tRD to RD was possible, we envisioned using our strategy to make layered ZIF-8-on-INP-on-ZIF-67 composites by simply attaching the INPs onto the crystal surfaces of the etched ZIF-67 particles before their reconstruction. To this end, we began by investigating attachment of Au NPs (~9 nm diameter) to the crystal surface of C particles of ZIF-67. The formed Au NPs were previously coated with poly(vinylpyrrolidone) (PVP; see Supporting Information) and then quantitatively attached to the ZIF-67 particles by simply adding them dropwise to a colloidal solution of ZIF-67 particles in MeOH (5 mg/mL) under vigorous stirring. After 1 min, Au (9 nm)-on-$C_{ZIF\text{-}67}$ composites and a transparent supernatant were separated by centrifugation. Remarkably, the transparency of the supernatant indicated that it was deprived of Au NPs and therefore the Au NPs had attached to the ZIF-67 particles massively. Indeed, FE-SEM images of the Au (9 nm)-on-$C_{ZIF\text{-}67}$ composites revealed homogeneous attachment of the Au NPs to the crystal surface of ZIF-67 and showed neither any evidence of significant Au–Au aggregation, nor presence of isolated Au NPs in the background (Figure 3a,b).

We then attempted to grow a ZIF-8 layer on top of the Au (9 nm)-on-$C_{ZIF\text{-}67}$ composites, seeking to control the reconstruction into either tRD or RD shapes. Thus, we reproduced the same growing conditions as for $C_{ZIF\text{-}67}$ except that we used a dispersion of Au-on-$C_{ZIF\text{-}67}$ in MeOH (5 mg/mL). Figure 3c,d shows that, when a solution of 2-MiM/$Zn(NO_3)_2{\cdot}6H_2O$ was used at concentrations of 10 or 25 mM, $tRD_{ZIF\text{-}8}$-on-Au (9 nm)-on-$C_{ZIF\text{-}67}$ or $RD_{ZIF\text{-}8}$-on-Au (9 nm)-on-$C_{ZIF\text{-}67}$ composites, respectively, were formed. Remarkably, we could apply the same sequential process for the T and H particles, enabling us to generate the corresponding $RD_{ZIF\text{-}8}$-on-Au (9 nm)-on-$T_{ZIF\text{-}67}$ and $RD_{ZIF\text{-}8}$-on-Au (9 nm)-on-$H_{ZIF\text{-}67}$ particles (Figure 4). The homogeneity of the Au NP distribution observed in Figures 3 and 4 witnesses the ordered formation of the growing ZIF-8 layer in the experimental conditions.

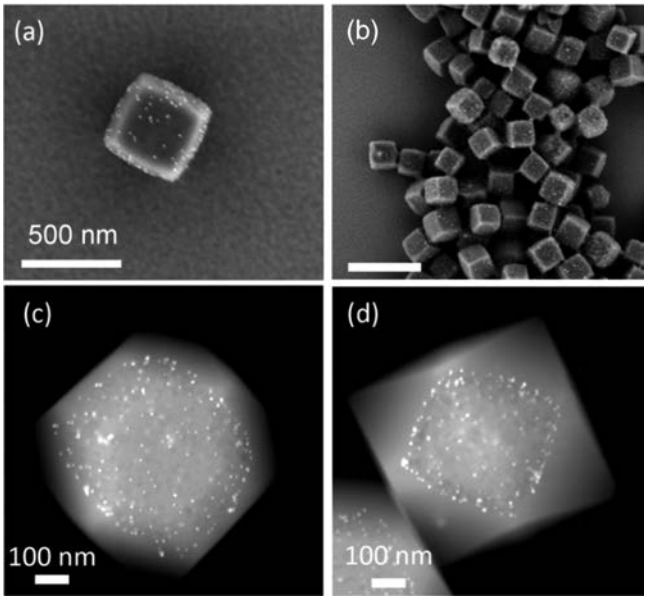


**Figure 3.** (a, b) FE-SEM images showing an individual (a) and a general view (b) of Au (9 nm)-on-$C_{ZIF\text{-}67}$ composites. (c, d) HAADF-STEM images of single $tRD_{ZIF\text{-}8}$-on-Au (9 nm)-on-$C_{ZIF\text{-}67}$ (c) and $RD_{ZIF\text{-}8}$-on-Au (9 nm)-on-$C_{ZIF\text{-}67}$ (d) composites.

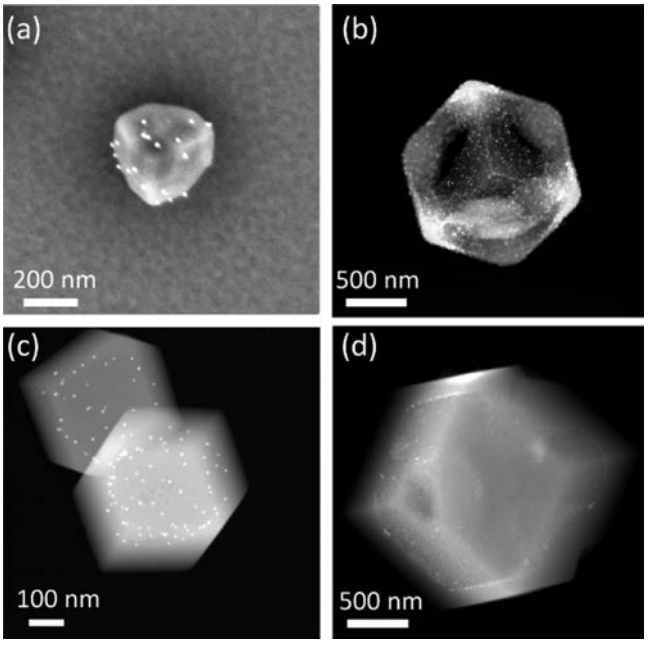


**Figure 4.** (a) FE-SEM image showing an individual Au-on-$T_{ZIF\text{-}67}$ composite. (b) HAADF-STEM image of a single Au-on-$H_{ZIF\text{-}67}$ composite. (c, d) HAADF-STEM images of single $RD_{ZIF\text{-}8}$-on-Au-on-$T_{ZIF\text{-}67}$ (c) and $RD_{ZIF\text{-}8}$-on-Au-on-$H_{ZIF\text{-}67}$ (d) composites.

Having shown that the layer of Au NPs does not preclude ZIF reconstruction and that reconstruction could be done stepwise, we next sought to use our strategy to construct onionlike composites made of (multi)-layered INPs (Figure 5a). To do this, we divided the $tRD_{ZIF\text{-}8}$-on-Au (9 nm)-on-$C_{ZIF\text{-}67}$ particles into three portions, to each of which we attached either PVP-coated Au NPs (~22 nm in diameter), icosahedral Pd NPs (~13 nm in diameter) or cubic Pd NPs (~18 nm in side length), using the same protocol. Then, similarly to the first reconstruction process, we deposited a


DOI: 10.1021/acsami.8b05098
ACS Appl. Mater. Interfaces 2018, 10, 23952–23960

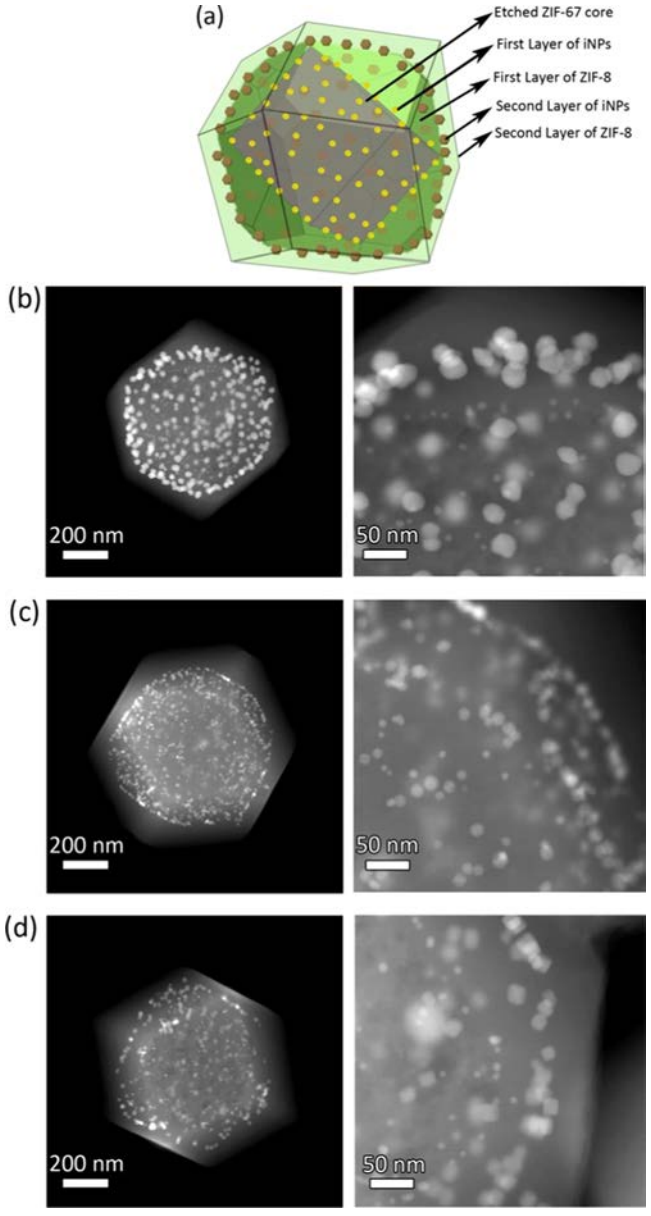


**Figure 5.** (a) Schematic illustration of the ZIF-based composites composed of two different layers of INPs. (b–d) HAADF-STEM images of single $RD_{ZIF\text{-}8}$-on-Au (22 nm)-on-$tRD_{ZIF\text{-}8}$-on-Au (9 nm)-on-$C_{ZIF\text{-}67}$ (b), $RD_{ZIF\text{-}8}$-on-Pd (icosahedral)-on-$tRD_{ZIF\text{-}8}$-on-Au (9 nm)-on-$C_{ZIF\text{-}67}$ (c), and $RD_{ZIF\text{-}8}$-on-Pd (cubic)-on-$tRD_{ZIF\text{-}8}$-on-Au (9 nm)-on-$C_{ZIF\text{-}67}$ (d) composites.

second ZIF-8 layer using a precursor concentration of 10 mM and a reaction time of 1 day. Figures 5b–d and S5 show high-angle annular dark-field scanning transmission electron microscopy (HAADF-STEM) images of three resulting multicomposites, revealing RD as the final shape and two different layers of INPs, that is, an internal layer of Au NPs (9 nm) and an external layer of either Au NPs (22 nm), icosahedral Pd NPs (13 nm) or cubic Pd NPs (18 nm). These (multi)-layered composites were found to retain the crystallinity and porosity of the starting ZIF particles (Figures S6 and S7). Interestingly, the two different layers of INPs inside a single ZIF particle could be separated by a distance of 40–50 nm (Figure 5b–d, right column).

MOF particles composed of separated layers of INPs should be useful for heterogeneous cascade catalysis because the involved reactions can be chronologically catalyzed in a stepwise manner. As a proof-of-concept, we studied a cascade reaction comprising a first Sonogashira coupling from 1-(prop-2-yn-1-yloxy)naphthalene (**1**) to 1-((3-phenylprop-2-yn-1-yl)oxy)naphthalene (**2**) catalyzed by Cu/Pd NPs, followed by a second cyclization reaction from **2** to 4-phenyl-2*H*-benzo[*h*]chromene (**3**) catalyzed by Au NPs (Figure 6a). We

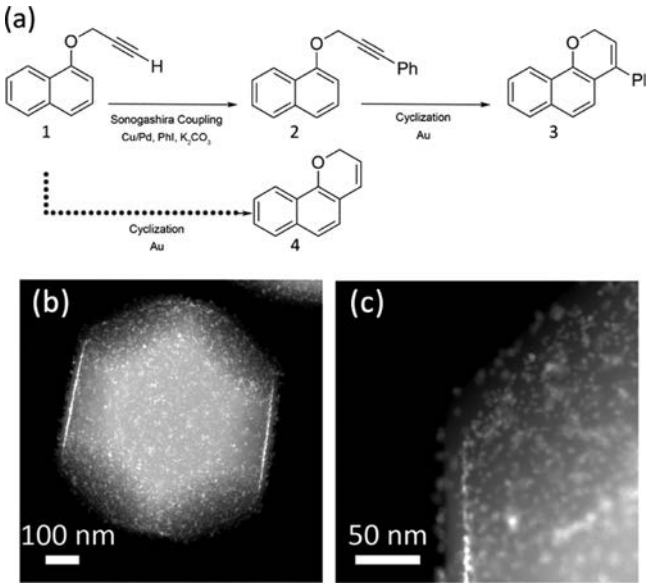


**Figure 6.** (a) Schematic illustration of the cascade reaction. (b, c) HAADF-STEM images of Cu/Pd-on-$tRD_{ZIF\text{-}8}$-on-Au-on-$tRD_{ZIF\text{-}8}$ composite.

selected this reaction because the cyclization of **1** to 2*H*-benzo[*h*]chromene (**4**) can occur either under thermal conditions[56] or can be catalyzed by Au NPs, thus highlighting the importance of the INP that starts catalyzing the reaction involving **1**.

Accordingly, we synthesized a composite composed of an internal layer of Au NPs (~4 nm in diameter) and an external layer of Cu/Pd NPs (~10 nm in diameter, Figure 6b). In this composite, both core and layer separating the INPs was ZIF-8 because it is more stable than ZIF-67. The thickness of the ZIF-8 layer was as small as 20 nm to facilitate the diffusion of the large reagents that occurs mainly through the framework and/or layer defects (Figure 6c).[57] The catalytic cascade reactions were then conducted by mixing **1**, $K_2CO_3$, iodobenzene (PhI), and xantphos in toluene with a toluene dispersion of Cu/Pd-on-$tRD_{ZIF\text{-}8}$-on-Au-on-$tRD_{ZIF\text{-}8}$ (Au: 2.2% w/w; Cu: 0.6% w/w; Pd: 1.3% w/w; metal content was estimated by analyzing the digested composite by ICP-OES) and reacted at 110 °C for 6 days under continuous stirring. As control experiments, we also reproduced the same reaction using $tRD_{ZIF\text{-}8}$ (without NPs), Au-on-$tRD_{ZIF\text{-}8}$ (Au: 2.1% w/w), Cu/Pd-on-$tRD_{ZIF\text{-}8}$ (Cu: 0.6% w/w; Pd: 1.2% w/w), Au-on-$tRD_{ZIF\text{-}8}$-on-Cu/Pd-on-$tRD_{ZIF\text{-}8}$ (Au: 2.2% w/w; Cu: 0.5% w/w; Pd: 1.0% w/w), and Au/Cu/Pd-on-$tRD_{ZIF\text{-}8}$ (Au: 2.1% w/w; Cu: 0.5% w/w; Pd: 1.2% w/w) as catalysts (Table 1).

In the case of ZIF-8 and the composite containing only Au NPs, Au-on-$tRD_{ZIF\text{-}8}$, they produced the nondesired **4** (yield: 21 and 31%, respectively, see Figure 6a). The 21% of **4**


DOI: 10.1021/acsami.8b05098
ACS Appl. Mater. Interfaces 2018, 10, 23952–23960

**Table 1. Summary of the Catalytic Reactions**

| entry | catalyst | 1 (%) | 2 (%) | 3 (%) | 4 (%) |
|---|---|---|---|---|---|
| 1[a] | ZIF-8 | 58 | | | 21 |
| 2[a] | Au-on-tRD$_{ZIF-8}$ | 40 | | | 31 |
| 3[a,b,c] | Au-on-tRD$_{ZIF-8}$ (reaction from **2** to **3**) | | 64 | 22 | |
| 4 | Cu/Pd-on-tRD$_{ZIF-8}$ | 20 | 35 | | 8 |
| 5 | Cu/Pd-on-tRD$_{ZIF-8}$-on-Au-on-tRD$_{ZIF-8}$ | | 53 | 11 | 1 |
| 6 | Au-on-tRD$_{ZIF-8}$-on-Cu/Pd-on-tRD$_{ZIF-8}$ | 45 | | | 18 |
| 7 | Au/Cu/Pd-on-tRD$_{ZIF-8}$ | | 28 | 4 | 2 |
| 9[a] | no ZIF-8 | 53 | | | 18 |
| 10[b] | ZIF-8 | | 71 | 8 | |
| 11[b] | no ZIF-8 | | 71 | 11 | |

[a]Without PhI and xantphos. [b]**2** as starting material. [c]3 days.

produced using only ZIF-8 was exclusively due to the thermal conditions of the reaction, as seen from blanks in Table 1 (entries 1 and 9). Note also here that a higher yield of **4** (65%) was obtained when Au-on-tRD$_{ZIF-8}$ was used without $K_2CO_3$. This yield increase demonstrates that $K_2CO_3$, which is necessary for the Sonogashira coupling, is detrimental for the cyclization reaction. For the composite containing only Cu/Pd NPs, Cu/Pd-on-tRD$_{ZIF-8}$, a mixture of **2** (yield: 35%) and **4** (yield: 8%) was synthesized. For the (multi)-layered composite with the incorrect sequence of INPs (external: Au NPs; internal: Cu/Pd NPs), it also produced **4** (yield: 18%) and not **2** or **3**, proving that the cyclization of **1** mainly takes place as it first encounters Au NPs and not Cu/Pd NPs, which were embedded further in the ZIF. For the composite that contains a mixture of both types of NPs on the external surface, Au/Cu/Pd-on-tRD$_{ZIF-8}$, **2** was mainly produced (yield: 28%). In this reaction, small proportions of **3** (yield: 4%) resulting from the cascade reaction and **4** (yield: 2%) were also formed. For the composite with the good sequence, Cu/Pd-on-RD$_{ZIF-8}$-on-Au-on-tRD$_{ZIF-8}$, we mainly obtained **2** (yield: 53%), a higher proportion of **3** (yield: 11%), and a small proportion of **4** (1%). The increase in the formation of **3** agrees with the occurrence of the cascade reaction, which is first catalyzed with Cu/Pd NPs and then with Au NPs. In addition, the yield of **3** also agrees with the expected value taking into account the independent performance of both reactions involved in the cascade process (Figure 6a). Indeed, as seen before, reaction of **1** in the presence of Cu/Pd-on-tRD$_{ZIF-8}$ gave **2** (yield: 35%), whereas the reaction of **2** in the presence of Au-on-tRD$_{ZIF-8}$ gave **3** (yield: 22%). These values result in an expected yield for the cascade reaction of 8%. Nevertheless, the fact that a higher yield of **3** could be obtained using Cu/Pd-on-tRD$_{ZIF-8}$-on-Au-on-tRD$_{ZIF-8}$ in comparison to the other binary Au-on-tRD$_{ZIF-8}$-on-Cu/Pd-on-tRD$_{ZIF-8}$ and Au/Cu/Pd-on-tRD$_{ZIF-8}$ composites is a first proof-of-concept that (multi)-layered MOF composites with a suitable sequence of INPs can potentially catalyze cascade reactions.

## CONCLUSIONS

In conclusion, we have reported that ZIF-8/ZIF-67 particles that have been etched can be fully reconstructed and that this reversibility can be used as an alternative strategy to synthesize novel ZIF-on-ZIF and layered ZIF-on-INP-on-ZIF composites. The first step of our approach comprises anisotropic etching of ZIF-8/ZIF-67 particles, which yields unprecedented C, T, and H morphologies. Second, exposing these etched particles to a ZIF precursor solution enables their reversible construction. Here, precursor concentration and regrowth time were critical variables for optimizing the final shape (tRD or RD) of the reconstructed particles. Moreover, we have demonstrated that even hollow microboxes can be recovered to a final RD shape by filling the inner space of the box with ZIF-8. Remarkably, the reconstruction step may also be accompanied with a step for attaching PVP-capped INPs onto the ZIF particle surface. This attachment, coupled with the ZIF-on-ZIF growth, affords layered ZIF-on-INP-on-ZIF composites. Furthermore, this latter process can be repeated to construct (multi)-layered composites composed of several types of INPs. In these composites, the different INPs are well separated by a nanometric layer of ZIF-8 that can be as small as 20 nm. These composites offer potential for diverse practical domains, such as catalysis, among other applications. Preliminary results obtained for a model cascade reaction paves the way to an improved design of new catalytic protocols for cascade reactions.

## ASSOCIATED CONTENT

### Supporting Information

The Supporting Information is available free of charge on the ACS Publications website at DOI: 10.1021/acsami.8b05098.

Additional FE-SEM and HAADF-STEM images, PXRD, and sorption isotherms (PDF)

## AUTHOR INFORMATION


### Corresponding Author

*E-mail: daniel.maspoch@icn2.cat.

### ORCID

Amirali Yazdi: 0000-0001-9420-8504
Neus G. Bastús: 0000-0002-3144-7986
Inhar Imaz: 0000-0002-0278-1141
Xavi Ribas: 0000-0002-2850-4409
Daniel Maspoch: 0000-0003-1325-9161


### Notes

The authors declare no competing financial interest.

## ACKNOWLEDGMENTS

This work was supported by the EU FP7 ERC-Co 615954, the Spanish MINECO (projects PN MAT2015-65354-C2-1-R, MAT2015-70725-R, and CTQ2016-77989-P), and the Catalan AGAUR (projects 2014 SGR 80, 2014 SGR 612 and 2014 SGR 862). It was also funded by the CERCA Program/Generalitat de Catalunya. N.G.B. acknowledges financial support by MINECO through the Ramon y Cajal program (RYC-2012-10991). ICN2 acknowledges the support of the Spanish MINECO through the Severo Ochoa Centers of Excellence Program under Grant SEV-2013-0295. X.R. is also grateful for ICREA-Acadèmia awards. We thank STR UdG for technical support.

## REFERENCES

(1) Lee, S. Y.; Gradon, L.; Janeczko, S.; Iskandar, F.; Okuyama, K. Formation of Highly Ordered Nanostructures by Drying Micrometer Colloidal Droplets. *ACS Nano* **2010**, *4*, 4717−4724.

(2) Meyer, R. A.; Green, J. J. Shaping the future of nanomedicine: anisotropy in polymeric nanoparticle design. *Wiley Interdiscip. Rev.: Nanomed. Nanobiotechnol.* **2016**, *8*, 191−207.

(3) Zeng, J.; Zhang, Q.; Chen, J.; Xia, Y. A comparison study of the catalytic properties of Au-based nanocages, nanoboxes, and nanoparticles. *Nano Lett.* **2010**, *10*, 30−35.


DOI: 10.1021/acsami.8b05098
*ACS Appl. Mater. Interfaces* 2018, 10, 23952−23960

(4) Chen, J.; Wiley, B.; McLellan, J.; Xiong, Y.; Li, Z.-Y.; Xia, Y. Optical Properties of Pd−Ag and Pt−Ag Nanoboxes Synthesized via Galvanic Replacement Reactions. *Nano Lett.* **2005**, *5*, 2058−2062.
(5) Merkel, T. J.; Herlihy, K. P.; Nunes, J.; Orgel, R. M.; Rolland, J. P.; DeSimone, J. M. Scalable, Shape-specific, Top-down Fabrication Methods for the Synthesis of Engineered Colloidal Particles. *Langmuir* **2010**, *26*, 13086−13096.
(6) Lim, B.; Jiang, M.; Tao, J.; Camargo, P. H. C.; Zhu, Y.; Xia, Y. Shape-Controlled Synthesis of Pd Nanocrystals in Aqueous Solutions. *Adv. Funct. Mater.* **2009**, *19*, 189−200.
(7) Moon, S. Y.; Kusunose, T.; Sekino, T. CTAB-Assisted Synthesis of Size- and Shape-Controlled Gold Nanoparticles in SDS Aqueous Solution. *Mater. Lett.* **2009**, *63*, 2038−2040.
(8) Gómez-Graña, S.; Goris, B.; Altantzis, T.; Fernández-López, C.; Carbó-Argibay, E.; Guerrero-Martínez, A.; Almora-Barrios, N.; López, N.; Pastoriza-Santos, I.; Pérez-Juste, J.; Bals, S.; Van Tendeloo, G.; Liz-Marzán, L. M. Au@Ag Nanoparticles: Halides Stabilize {100} Facets. *J. Phys. Chem. Lett.* **2013**, *4*, 2209−2216.
(9) Chen, C.; Hirdes, D.; Folch, A. Gray-scale photolithography using microfluidic photomasks. *Proc. Natl. Acad. Sci. U.S.A.* **2003**, *100*, 1499−1504.
(10) Liu, M.; Zheng, Y.; Zhang, L.; Guo, L.; Xia, Y. Transformation of Pd Nanocubes into Octahedra with Controlled Sizes by Maneuvering the Rates of Etching and Regrowth. *J. Am. Chem. Soc.* **2013**, *135*, 11752−11755.
(11) Wang, Z.; Wang, H.; Zhang, Z.; Yang, G.; He, T.; Yin, Y.; Jin, M. Synthesis of Pd Nanoframes by Excavating Solid Nanocrystals for Enhanced Catalytic Properties. *ACS Nano* **2017**, *11*, 163−170.
(12) Du, J.-H.; Sheng, T.; Xiao, C.; Tian, N.; Xiao, J.; Xie, A.-Y.; Liu, S.; Zhou, Z.-Y.; Sun, S.-G. Shape Transformation of {hk0}-Faceted Pt Nanocrystals from a Tetrahexahedron into a Truncated Ditetragonal Prism. *Chem. Commun.* **2017**, *53*, 3236−3238.
(13) Lee, J. H.; Gibson, K. J.; Chen, G.; Weizmann, Y. Bipyramid-Templated Synthesis of Monodisperse Anisotropic Gold Nanocrystals. *Nat. Commun.* **2015**, *6*, No. 7571.
(14) Choi, S.; Kim, T.; Ji, H.; Lee, H. J.; Oh, M. Isotropic and Anisotropic Growth of Metal-Organic Framework (MOF) on MOF: Logical Inference on MOF Structure Based on Growth Behavior and Morphological Feature. *J. Am. Chem. Soc.* **2016**, *138*, 14434−14440.
(15) Furukawa, S.; Hirai, K.; Takashima, Y.; Nakagawa, K.; Kondo, M.; Tsuruoka, T.; Sakata, O.; Kitagawa, S. A Block PCP Crystal: Anisotropic Hybridization of Porous Coordination Polymers by Face-selective Epitaxial Growth. *Chem. Commun.* **2009**, 5097−5099.
(16) Koh, K.; Wong-Foy, A. G.; Matzger, A. J. MOF@MOF: Microporous Core-Shell Architectures. *Chem. Commun.* **2009**, 6162−6164.
(17) Zhao, M.; Yuan, K.; Wang, Y.; Li, G.; Guo, J.; Gu, L.; Hu, W.; Zhao, H.; Tang, Z. Metal−Organic Frameworks as Selectivity Regulators for Hydrogenation Reactions. *Nature* **2016**, *539*, 76−80.
(18) Falcaro, P.; Ricco, R.; Yazdi, A.; Imaz, I.; Furukawa, S.; Maspoch, D.; Ameloot, R.; Evans, J. D.; Doonan, C. J. Application of Metal and Metal Oxide Nanoparticles@MOFs. *Coord. Chem. Rev.* **2016**, *307*, 237−254.
(19) Kim, C. R.; Uemura, T.; Kitagawa, S. Inorganic Nanoparticles in Porous Coordination Polymers. *Chem. Soc. Rev.* **2016**, *45*, 3828−3845.
(20) Cai, W.; Chu, C.-C.; Liu, G.; Wáng, Y.-X. J. Metal−Organic Framework-Based Nanomedicine Platforms for Drug Delivery and Molecular Imaging. *Small* **2015**, *11*, 4806−4822.
(21) Doonan, C.; Riccò, R.; Liang, K.; Bradshaw, D.; Falcaro, P. Metal−Organic Frameworks at the Biointerface: Synthetic Strategies and Applications. *Acc. Chem. Res.* **2017**, *50*, 1423−1432.
(22) Horcajada, P.; Chalati, T.; Serre, C.; Gillet, B.; Sebrie, C.; Baati, T.; Eubank, J. F.; Heurtaux, D.; Clayette, P.; Kreuz, C.; Chang, J.-S.; Hwang, Y. K.; Marsaud, V.; Bories, P.-N.; Cynober, L.; Gil, S.; Ferey, G.; Couvreur, P.; Gref, R. Porous Metal-Organic-Framework Nanoscale Carriers as a Potential Platform for Drug Delivery and Imaging. *Nat. Mater.* **2010**, *9*, 172−178.
(23) Li, Z.; Zeng, H. C. Surface and Bulk Integrations of Single-Layered Au or Ag Nanoparticles onto Designated Crystal Planes {110} or {100} of ZIF-8. *Chem. Mater.* **2013**, *25*, 1761−1768.
(24) Hu, Z.; Zhang, Z.; Li, Z.; Dou, M.; Wang, F. One-Step Conversion from Core−Shell Metal−Organic Framework Materials to Cobalt and Nitrogen Codoped Carbon Nanopolyhedra with Hierarchically Porous Structure for Highly Efficient Oxygen Reduction. *ACS Appl. Mater. Interfaces* **2017**, *9*, 16109−16116.
(25) Zhang, J.; Zhang, T.; Xiao, K.; Cheng, S.; Qian, G.; Wang, Y.; Feng, Y. Novel and Facile Strategy for Controllable Synthesis of Multilayered Core−Shell Zeolitic Imidazolate Frameworks. *Cryst. Growth Des.* **2016**, *16*, 6494−6498.
(26) Tang, J.; Salunkhe, R. R.; Liu, J.; Torad, N. L.; Imura, M.; Furukawa, S.; Yamauchi, Y. Thermal Conversion of Core-Shell Metal-Organic Frameworks: a New Method for Selectively Functionalized Nanoporous Hybrid Carbon. *J. Am. Chem. Soc.* **2015**, *137*, 1572−1580.
(27) Avci, C.; Ariñez-Soriano, J.; Carné-Sánchez, A.; Guillerm, V.; Carbonell, C.; Imaz, I.; Maspoch, D. Post-synthetic Anisotropic Wet-Chemical Etching of Colloidal Sodalite ZIF Crystals. *Angew. Chem., Int. Ed.* **2015**, *54*, 14417−14421.
(28) Pang, S. H.; Han, C.; Sholl, D. S.; Jones, C. W.; Lively, R. P. Facet-Specific Stability of ZIF-8 in the Presence of Acid Gases Dissolved in Aqueous Solutions. *Chem. Mater.* **2016**, *28*, 6960−6967.
(29) Liu, W.; Huang, J.; Yang, Q.; Wang, S.; Sun, X.; Zhang, W.; Liu, J.; Huo, F. Multi-shelled Hollow Metal−Organic Frameworks. *Angew. Chem., Int. Ed.* **2017**, *56*, 5512−5516.
(30) Hu, M.; Ju, Y.; Liang, K.; Suma, T.; Cui, J.; Caruso, F. Void Engineering in Metal-Organic Frameworks via Synergistic Etching and Surface Functionalization. *Adv. Funct. Mater.* **2016**, *26*, 5827−5834.
(31) Chou, L.-Y.; Hu, P.; Zhuang, J.; Morabito, J. V.; Ng, K. C.; Kao, Y.-C.; Wang, S.-C.; Shieh, F.-K.; Kuo, C.-H.; Tsung, C.-K. Formation of Hollow and Mesoporous Structures in Single-Crystalline Microcrystals of Metal-Organic Frameworks via Double-solvent Mediated Overgrowth. *Nanoscale* **2015**, *7*, 19408−19412.
(32) Chen, H.; Shen, K.; Chen, J.; Chen, X.; Li, Y. Hollow-ZIF-Templated Formation of a ZnO@C−N−Co Core−Shell Nanostructure for Highly Efficient Pollutant Photodegradation. *J. Mater. Chem. A* **2017**, *5*, 9937−9945.
(33) Jiang, Z.; Li, Z.; Qin, Z.; Sun, H.; Jiao, X.; Chen, D. LDH Nanocages Synthesized with MOF Templates and their High Performance as Supercapacitors. *Nanoscale* **2013**, *5*, 11770−11775.
(34) Zhang, P.; Guan, B. Y.; Yu, L.; Lou, X. W. D. Formation of Double-Shelled Zinc-Cobalt Sulfide Dodecahedral Cages from Bimetallic Zeolitic Imidazolate Frameworks for Hybrid Supercapacitors. *Angew. Chem., Int. Ed.* **2017**, *56*, 7141−7145.
(35) Li, S.; Dharmarwardana, M.; Welch, R. P.; Ren, Y.; Thompson, C. M.; Smaldone, R. A.; Gassensmith, J. J. Template-Directed Synthesis of Porous and Protective Core-Shell Bionanoparticles. *Angew. Chem., Int. Ed.* **2016**, *55*, 10691−10696.
(36) Lu, G.; Li, S.; Guo, Z.; Farha, O. K.; Hauser, B. G.; Qi, X.; Wang, Y.; Wang, X.; Han, S.; Liu, X.; DuChene, J. S.; Zhang, H.; Zhang, Q.; Chen, X.; Ma, J.; Loo, S. C.; Wei, W. D.; Yang, Y.; Hupp, J. T.; Huo, F. Imparting Functionality to a Metal-Organic Framework Material by Controlled Nanoparticle Encapsulation. *Nat. Chem.* **2012**, *4*, 310−316.
(37) Yazdi, A.; Mercoci, F.; Bastus, N. G.; Imaz, I.; Puntes, V.; Maspoch, D. The Influence of the MOF Shell Thickness on the Catalytic Performance of Composites made of Inorganic (Hollow) Nanoparticles Encapsulated into MOFs. *Catal. Sci. Technol.* **2016**, *6*, 8388−8391.
(38) Liang, K.; Ricco, R.; Doherty, C. M.; Styles, M. J.; Bell, S.; Kirby, N.; Mudie, S.; Haylock, D.; Hill, A. J.; Doonan, C. J.; Falcaro, P. Biomimetic Mineralization of Metal-Organic Frameworks as Protective Coatings for Biomacromolecules. *Nat. Commun.* **2015**, *6*, No. 7240.
(39) Jiang, H.-L.; Liu, B.; Akita, T.; Haruta, M.; Sakurai, H.; Xu, Q. Au@ZIF-8: CO Oxidation over Gold Nanoparticles Deposited to


DOI: 10.1021/acsami.8b05098
*ACS Appl. Mater. Interfaces* 2018, 10, 23952−23960

Metal-Organic Framework. *J. Am. Chem. Soc.* **2009**, *131*, 11302−11303.
(40) Schejn, A.; Mazet, T.; Falk, V.; Balan, L.; Aranda, L.; Medjahdib, G.; Schneider, R. $Fe_3O_4$@ZIF-8: Magnetically Recoverable Catalysts by Loading $Fe_3O_4$ Nanoparticles Inside a Zinc Imidazolate Framework. *Dalton Trans.* **2015**, *44*, 10136−10140.
(41) Yang, Q.; Xu, Q.; Yu, S.-H.; Jiang, H.-L. Pd Nanocubes@ZIF-8: Integration of Plasmon-Driven Photothermal Conversion with a Metal−Organic Framework for Efficient and Selective Catalysis. *Angew. Chem., Int. Ed.* **2016**, *55*, 3685−3689.
(42) Huang, Y.; Zhang, Y.; Chen, X.; Wu, D.; Yia, Z.; Cao, R. Bimetallic Alloy Nanocrystals Encapsulated in ZIF-8 for Synergistic Catalysis of Ethylene Oxidative Degradation. *Chem. Commun.* **2014**, *50*, 10115−10117.
(43) Jiang, H.-L.; Akita, T.; Ishida, T.; Haruta, M.; Xu, Q. Synergistic Catalysis of Au@Ag Core−Shell Nanoparticles Stabilized on Metal−Organic Framework. *J. Am. Chem. Soc.* **2011**, *133*, 1304−1306.
(44) Li, P.-Z.; Aranishi, K.; Xu, Q. ZIF-8 Immobilized Nickel Nanoparticles: Highly Effective Catalysts for Hydrogen Generation from Hydrolysis of Ammonia Borane. *Chem. Commun.* **2012**, *48*, 3173−3175.
(45) Chen, L.; Zhan, W.; Fang, H.; Cao, Z.; Yuan, C.; Xie, Z.; Kuang, Q.; Zheng, L. Selective Catalytic Performances of Noble Metal Nanoparticle@MOF Composites: The Concomitant Effect of Aperture Size and Structural Flexibility of MOF Matrices. *Chem. - Eur. J.* **2017**, *23*, 11397−11403.
(46) Rösler, C.; Aijaz, A.; Turner, S.; Filippousi, M.; Shahabi, A.; Xia, W.; Van Tendeloo, G.; Muhler, M.; Fischer, R. A. Hollow Zn/Co Zeolitic Imidazolate Framework (ZIF) and Yolk-Shell Metal@Zn/Co ZIF Nanostructures. *Chem. - Eur. J.* **2016**, *22*, 3304−3311.
(47) Yang, J.; Zhang, F.; Lu, H.; Hong, X.; Jiang, H.; Wu, Y.; Li, Y. Hollow Zn/Co ZIF Particles Derived from Core−Shell ZIF-67@ZIF-8 as Selective Catalyst for the Semi-Hydrogenation of Acetylene. *Angew. Chem., Int. Ed.* **2015**, *54*, 10889−10893.
(48) Bastús, N. G.; Comenge, J.; Puntes, V. Kinetically Controlled Seeded Growth Synthesis of Citrate-Stabilized Gold Nanoparticles of up to 200 nm: Size Focusing versus Ostwald Ripening. *Langmuir* **2011**, *27*, 11098−11105.
(49) Piella, J.; Bastús, N. G.; Puntes, V. Size-Controlled Synthesis of Sub-10-nanometer Citrate-Stabilized Gold Nanoparticles and Related Optical Properties. *Chem. Mater.* **2016**, *28*, 1066−1075.
(50) Huang, H.; Wang, Y.; Ruditskiy, A.; Peng, H.-C.; Zhao, X.; Zhang, L.; Liu, J.; Ye, Z.; Xia, Y. Polyol Syntheses of Palladium Decahedra and Icosahedra as Pure Samples by Maneuvering the Reaction Kinetics with Additives. *ACS Nano* **2014**, *8*, 7041−7050.
(51) Mézailles, N.; Ricard, L.; Gagosz, F. Phosphine Gold(I) Bis(trifluoromethanesulfonyl)imidate Complexes as New Highly Efficient and Air-Stable Catalysts for the Cycloisomerization of Enynes. *Org. Lett.* **2005**, *7*, 4133−4136.
(52) Worlikar, S. A.; Kesharwani, T.; Yao, T.; Larock, R. C. Synthesis of 3,4-Disubstituted 2*H*-Benzopyrans through C−C Bond Formation via Electrophilic Cyclization. *J. Org. Chem.* **2007**, *72*, 1347−1353.
(53) Efe, C.; Lykakis, I. N.; Stratakis, M. Gold Nanoparticles Supported on $TiO_2$ Catalyse the Cycloisomerisation/Oxidative Dimerisation of Aryl Propargyl Ethers. *Chem. Commun.* **2011**, *47*, 803−805.
(54) Lykakis, I. N.; Efe, C.; Gryparis, C.; Stratakis, M. $Ph_3PAuNTf_2$ as a Superior Catalyst for the Selective Synthesis of 2*H*-Chromenes: Application to the Concise Synthesis of Benzopyran Natural Products. *Eur. J. Org. Chem.* **2011**, 2334−2338.
(55) Arcadi, A.; Blesi, F.; Cacchi, S.; Fabrizi, G.; Goggiamani, A.; Marinelli, F. Gold versus Silver Catalyzed Intramolecular Hydroarylation Reactions of [(3-arylprop-2-ynyl)oxy]benzene Derivatives. *Org. Biomol. Chem.* **2012**, *10*, 9700−9708.
(56) Lutz, R. P. Catalysis of the Cope and Claisen rearrangements. *Chem. Rev.* **1984**, *84*, 205−247.
(57) Wu, X.; Yang, C.; Ge, J. Green Synthesis of Enzyme/metal-organic framework Composites with High Stability in Protein Denaturing Solvents. *Bioresour. Bioprocess.* **2017**, *4*, 24.


DOI: 10.1021/acsami.8b05098
*ACS Appl. Mater. Interfaces* 2018, 10, 23952−23960

**SUPPORTING INFORMATION**

# Sequential Deconstruction-Reconstruction of Metal-Organic Frameworks: an Alternative Strategy for Synthesizing (Multi)-Layered ZIF Composites

Civan Avci,[†] Amirali Yazdi,[†] Màrius Tarrés,[‡] Elise Bernoud,[‡] Neus G. Bastús,[†] Victor Puntes,[†,§] Inhar Imaz,[†] Xavi Ribas[‡] and Daniel Maspoch[*,†,§]

[†] Catalan Institute of Nanoscience and Nanotechnology (ICN2), CSIC and The Barcelona Institute of Science and Technology, Campus UAB, Bellaterra, 08193 Barcelona, Spain

[‡] Institut de Química Computacional i Catàlisi (IQCC) and Departament de Química, Universitat de Girona, Campus Montilivi, Girona, E-17071, Catalonia, Spain

[§] ICREA, Pg. Lluís Companys 23, 08010 Barcelona, Spain

*Corresponding author e-mail: daniel.maspoch@icn2.cat

**Figure S1.** Representative general FE-SEM images of a) $C_{ZIF-67}$ b) $T_{ZIF-67}$ and c) $H_{ZIF-67}$.

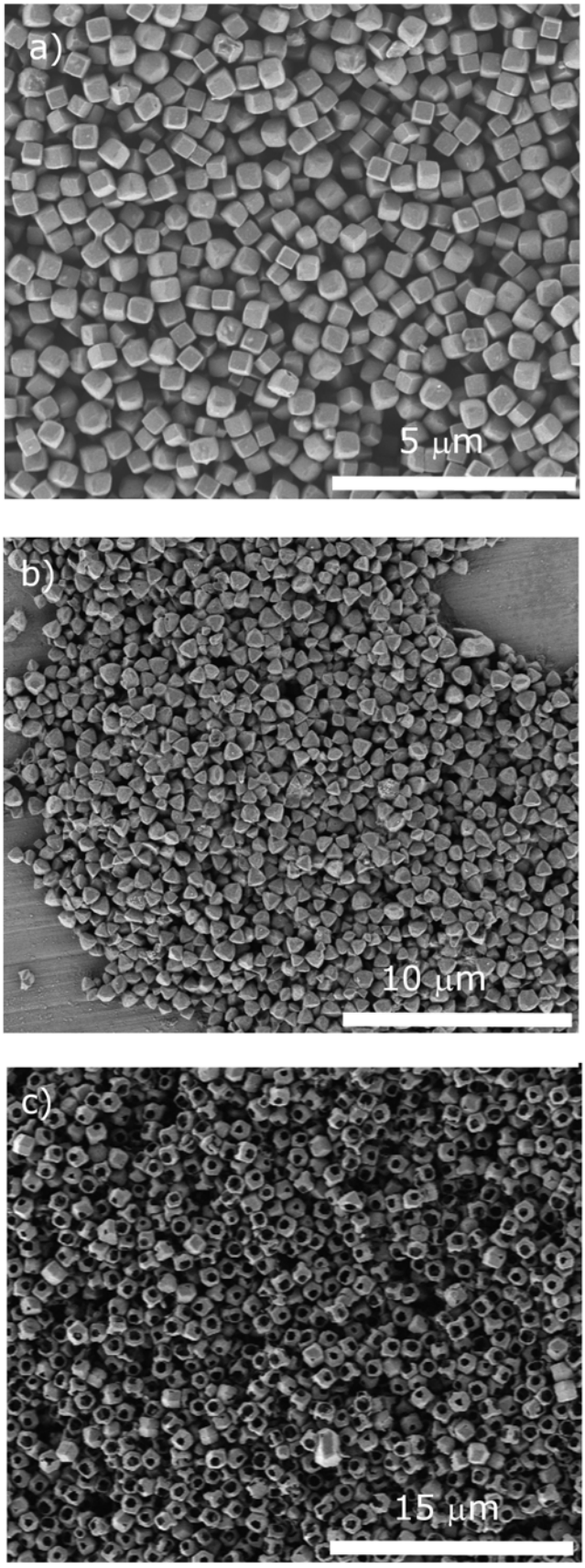

**Figure S2**. Representative general FE-SEM images of ZIF-8-on-ZIF-67 composites: a) $tRD_{ZIF\text{-}8}$-on-$C_{ZIF\text{-}67}$; and b) $RD_{ZIF\text{-}8}$-on-$C_{ZIF\text{-}67}$.

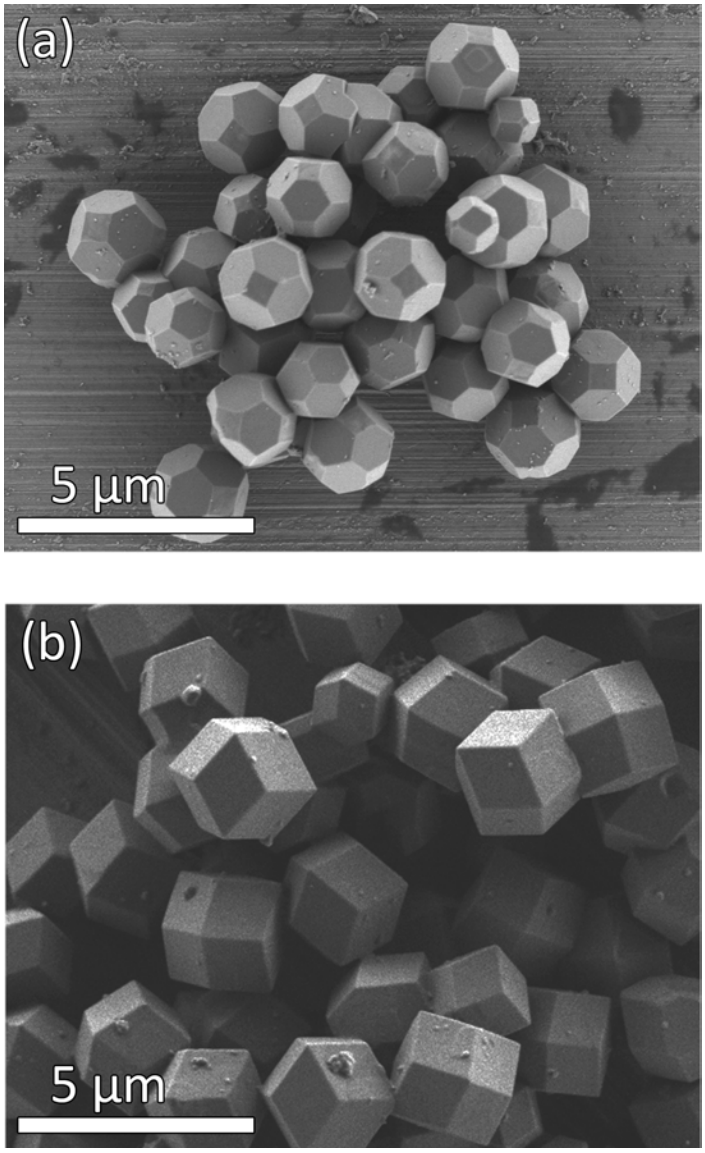

**Figure S3.** $N_2$ sorption isotherms of ZIF-8-on-ZIF-67 composites: a) $RD_{ZIF\text{-}8}$-on-$C_{ZIF\text{-}67}$; b) $RD_{ZIF\text{-}8}$-on-$T_{ZIF\text{-}67}$; and c) $RD_{ZIF\text{-}8}$-on-$H_{ZIF\text{-}67}$.

a)

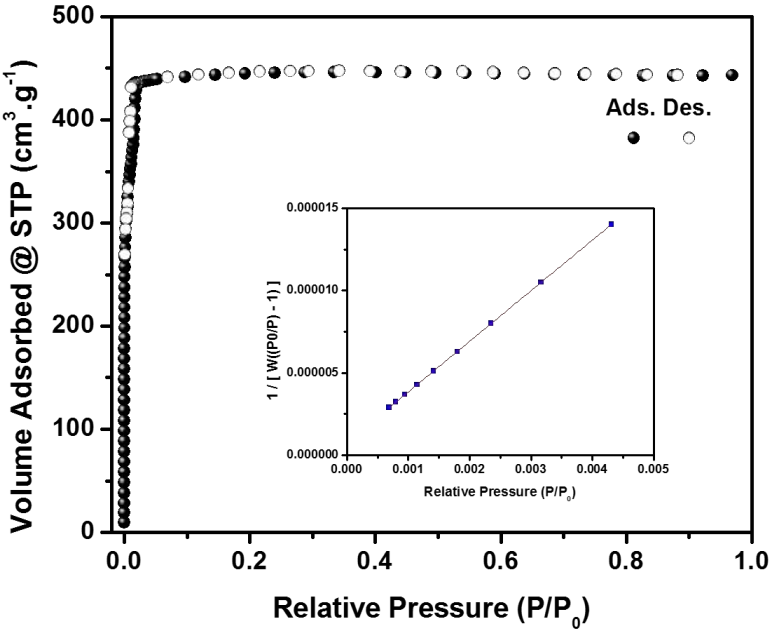


BET surface area = 1417 m²/g

Slope = 3.07

Intercept = 1.00 E-6

Correlation coefficient, r = 0.99999

C constant = 3935

b)

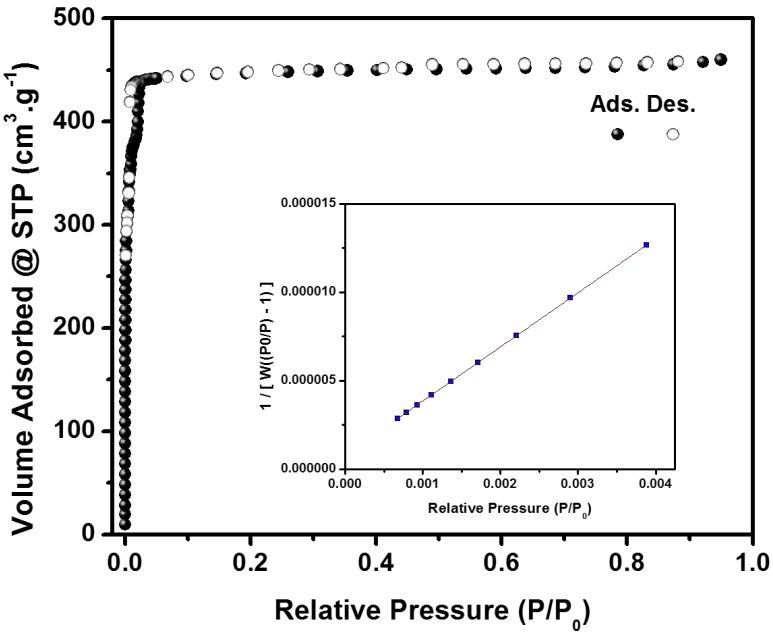


BET surface area = 1422 $m^2/g$

Slope = 3.06

Intercept = 1.00 E-6

Correlation coefficient, r = 0.99999

C constant = 3896

c)

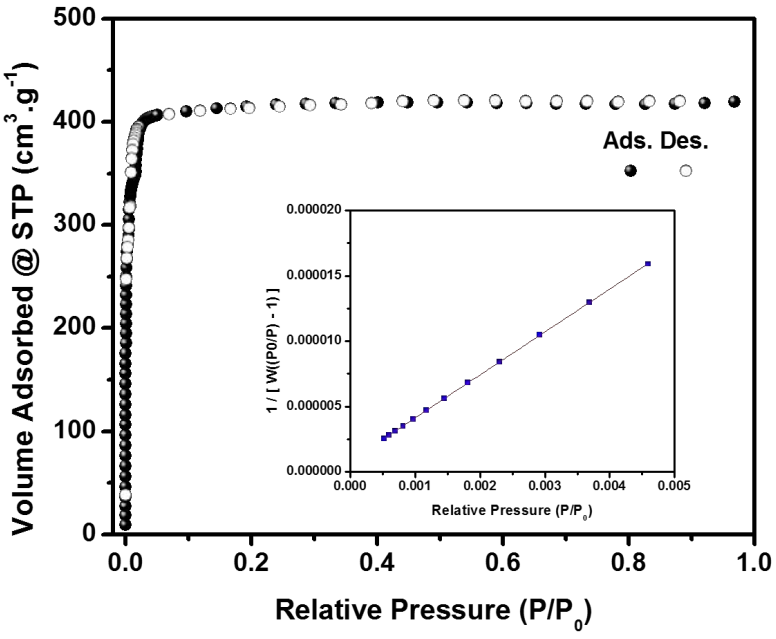


BET surface area = 1324 $m^2/g$

Slope = 3.29

Intercept = 1.00 E-6

Correlation coefficient = 0.99999

C constant = 3895

**Figure S4.** XRPD diffractograms of ZIF-8-on-ZIF-67 composites compared with the simulated powder pattern of ZIF-8 (black).

.

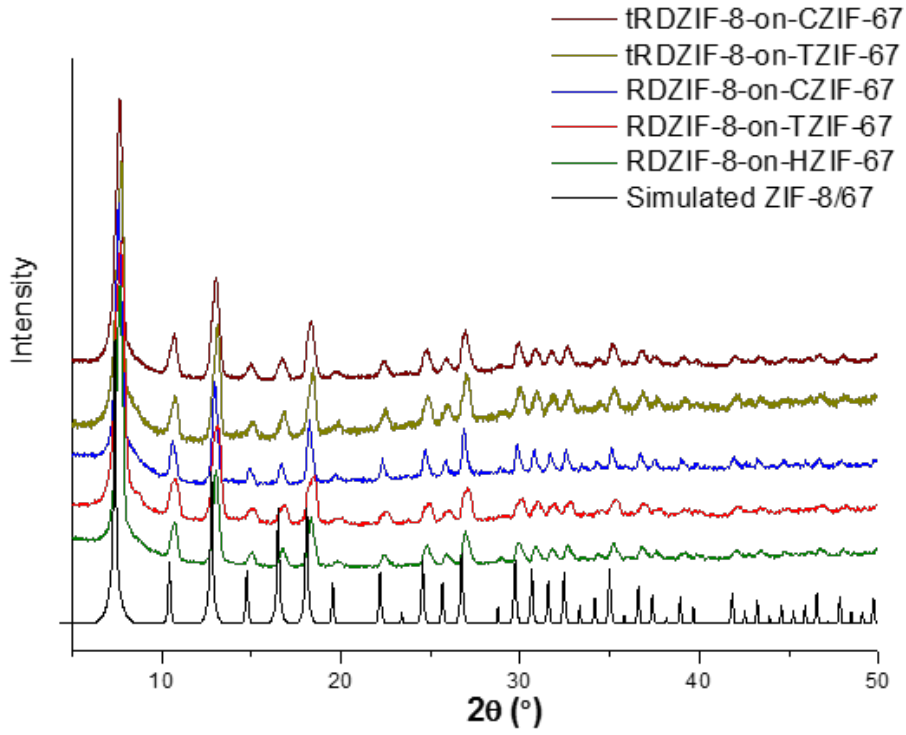

**Figure S5.** General HAADF-STEM images of layered ZIF-on-INP-on-ZIF composites: a) $RD_{ZIF\text{-}8}$-on-Au(22 nm)-on-$tRD_{ZIF\text{-}8}$-on-Au(9 nm)-on-$C_{ZIF\text{-}67}$; b) $RD_{ZIF\text{-}8}$-on-Pd (icosahedral)-on-$tRD_{ZIF\text{-}8}$-on-Au(9 nm)-on-$C_{ZIF\text{-}67}$; and c) $RD_{ZIF\text{-}8}$-on- Pd (cubic)-on-$tRD_{ZIF\text{-}8}$-on-Au(9 nm)-on-$C_{ZIF\text{-}67}$.

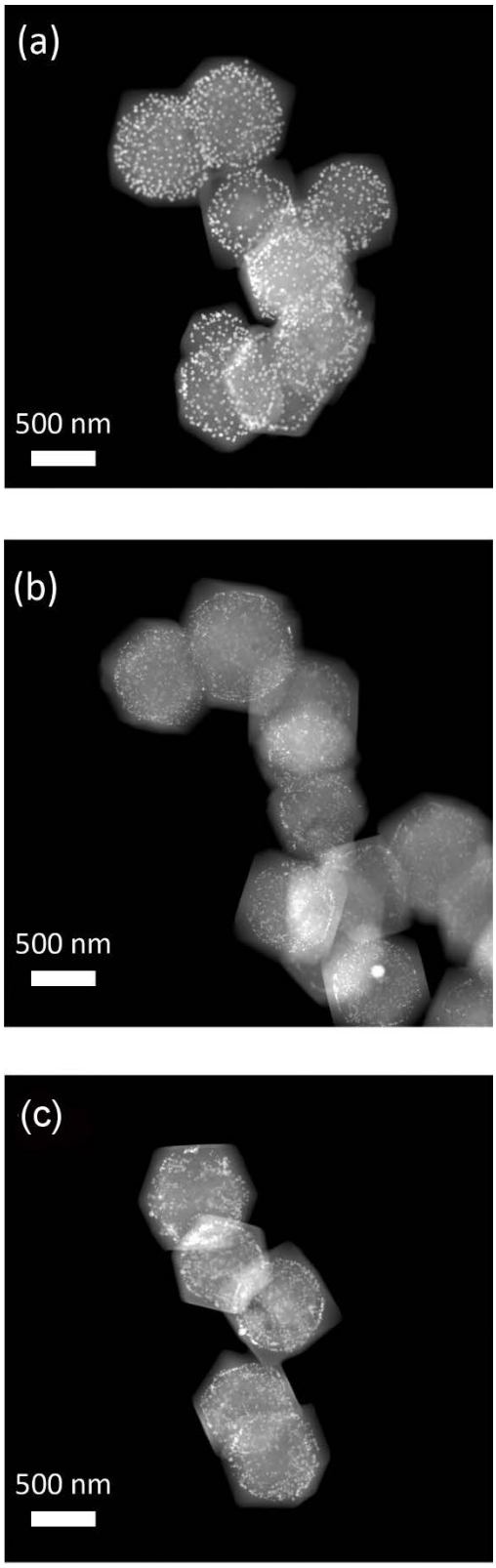

**Figure S6.** XRPD diffractograms of multilayered ZIF-on-INP-on-ZIF composites compared with the simulated powder pattern of ZIF-8 (black).

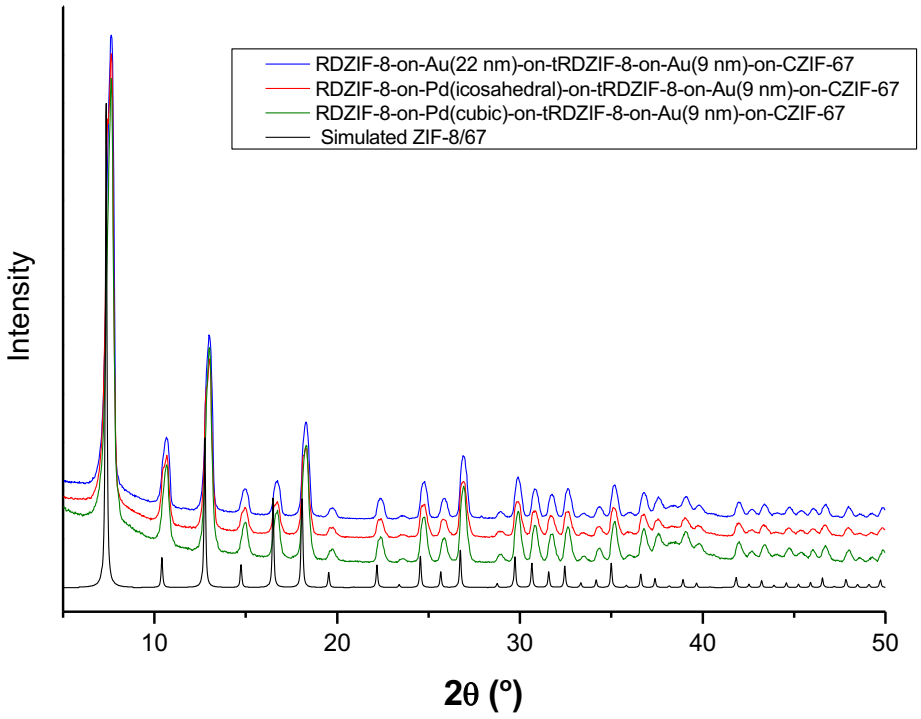

**Figure S7.** $N_2$ sorption isotherm of: a) $RD_{ZIF\text{-}8}$-on-Au(22 nm)-on-t$RD_{ZIF\text{-}8}$-on-Au(9 nm)-on-$C_{ZIF\text{-}67}$; b) $RD_{ZIF\text{-}8}$-on-Pd(icosahedral)-on-t$RD_{ZIF\text{-}8}$-on-Au(9 nm)-on-$C_{ZIF\text{-}67}$; and c) $RD_{ZIF\text{-}8}$-on-Pd(cubic)-on-t$RD_{ZIF\text{-}8}$-on-Au(9 nm)-on-$C_{ZIF\text{-}67}$.

a)

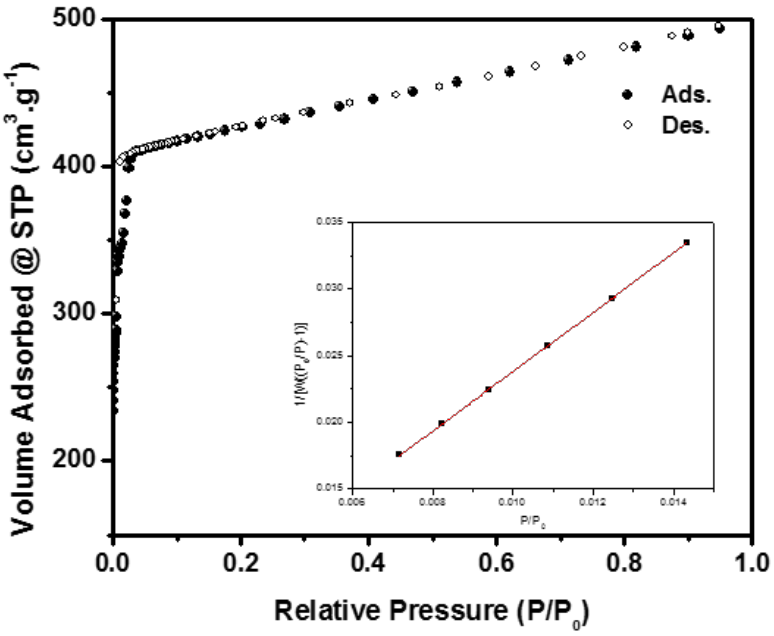


BET surface Area = 1562 $m^2/g$

Slope = 2.28

Intercept = 1.54 E-3

Correlation coefficient, r = 0.99996

C constant = 1462

b)

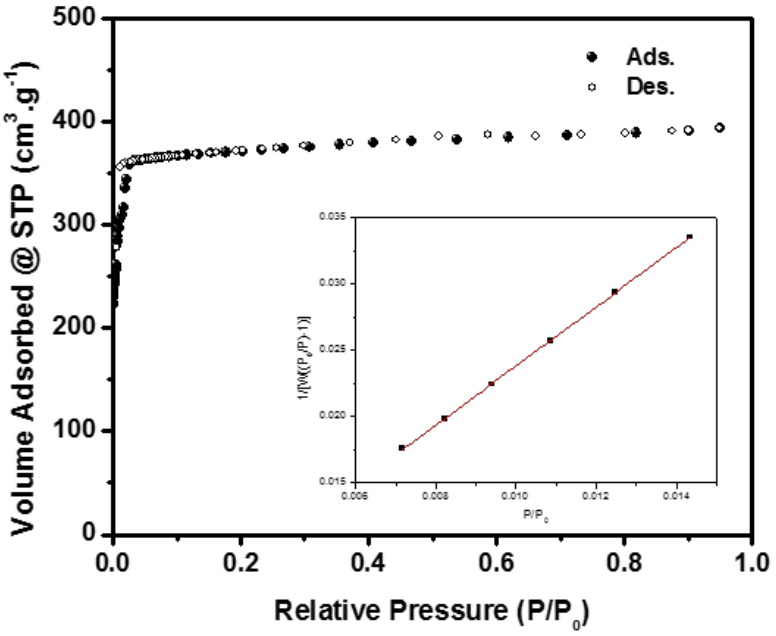


BET surface Area = 1467 m²/g

Slope = 2.37

Intercept = 3.40 E-3

Correlation coefficient, r = 0.9999

C constant = 680

c)

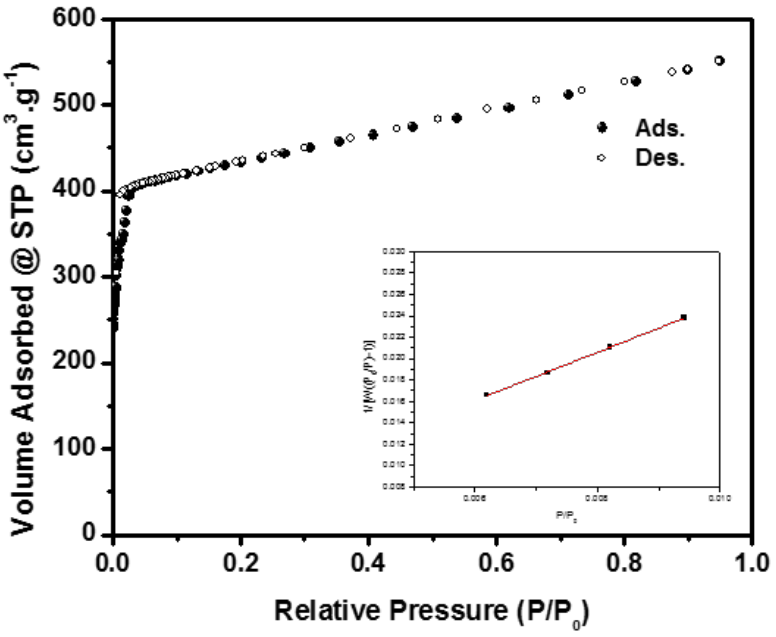


BET surface Area = 1539 $m^2/g$

Slope = 2.26

Intercept = 2.50 E-3

Correlation coefficient, r = 0.9996

C constant = 901

**Figure S8.** HAADF-STEM images of single and multiple: a,b) Au-on-$tRD_{ZIF-8}$; c,d) Cu/Pd-on-$tRD_{ZIF-8}$; and e,f) Cu/Pd-on-$tRD_{ZIF-8}$-on-Au-on-$tRD_{ZIF-8}$ composites.

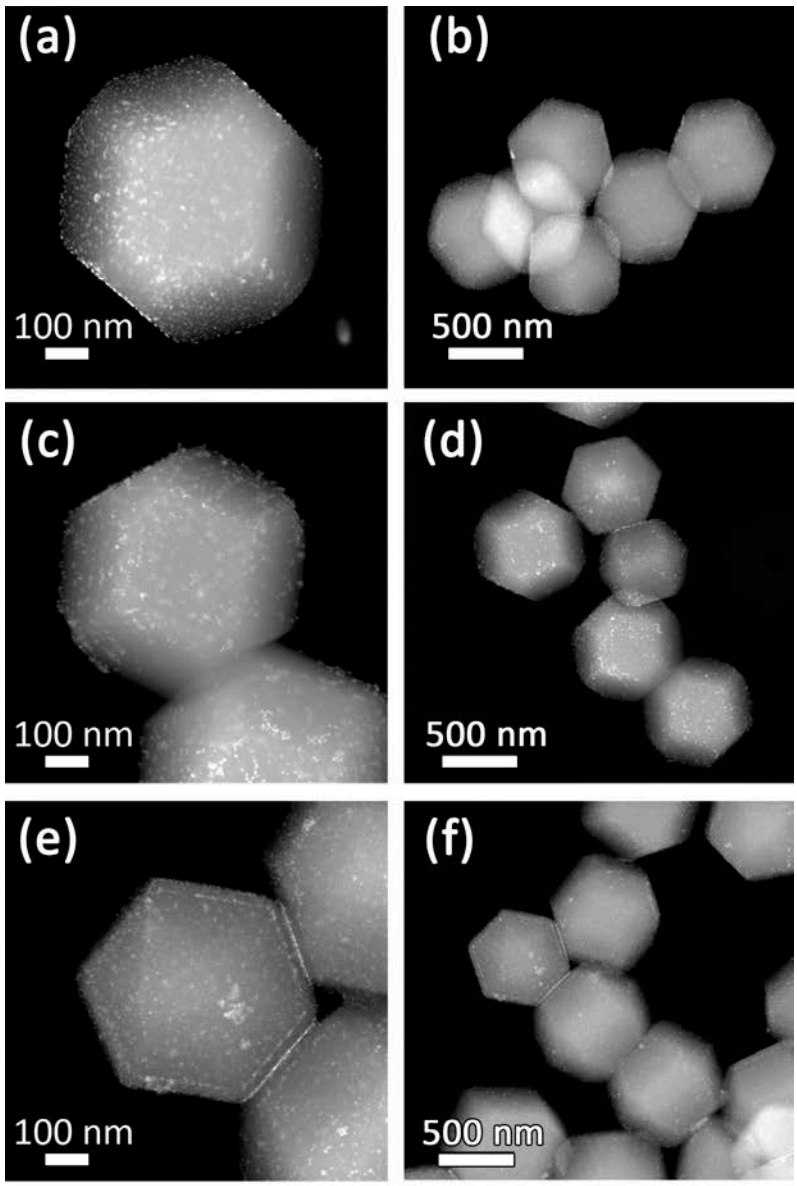

**Figure S9.** HAADF-STEM images showing a) a single and b) multiple Au/Cu/Pd-on-tRD$_{ZIF-8}$ composite. c) FE-SEM and d) HAADF-STEM images of Au-on-tRD$_{ZIF-8}$-on-Cu/Pd-on-tRD$_{ZIF-8}$ composite.

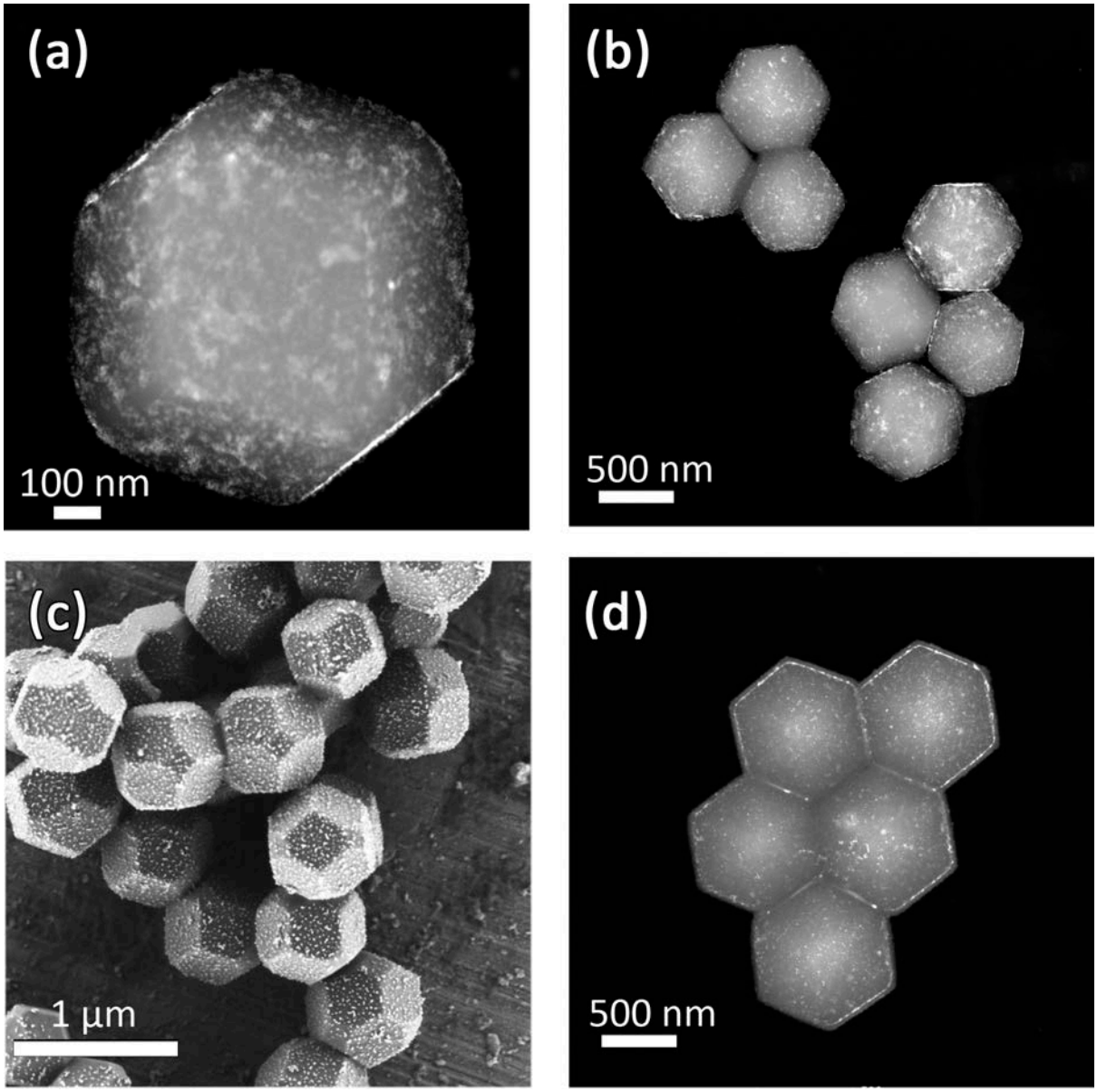

**Figure S10.** a) PXRD diffractograms of ZIF-8-based composites used in the catalysis experiments compared with the simulated powder pattern of ZIF-8 (black). b,c) HAADF-STEM images of Cu/Pd-on-$tRD_{ZIF\text{-}8}$-on-Au-on-$tRD_{ZIF\text{-}8}$ particles after one cycle of catalysis. d) PXRD diffractogram of Cu/Pd-on-$tRD_{ZIF\text{-}8}$-on-Au-on-$tRD_{ZIF\text{-}8}$ after one cycle of catalysis compared with the simulated powder pattern of ZIF-8 (black). Note that PXRD confirms the stability of ZIF-8 after one cycle but HAADF-STEM shows a certain degree of aggregation/sintering of the INPs.

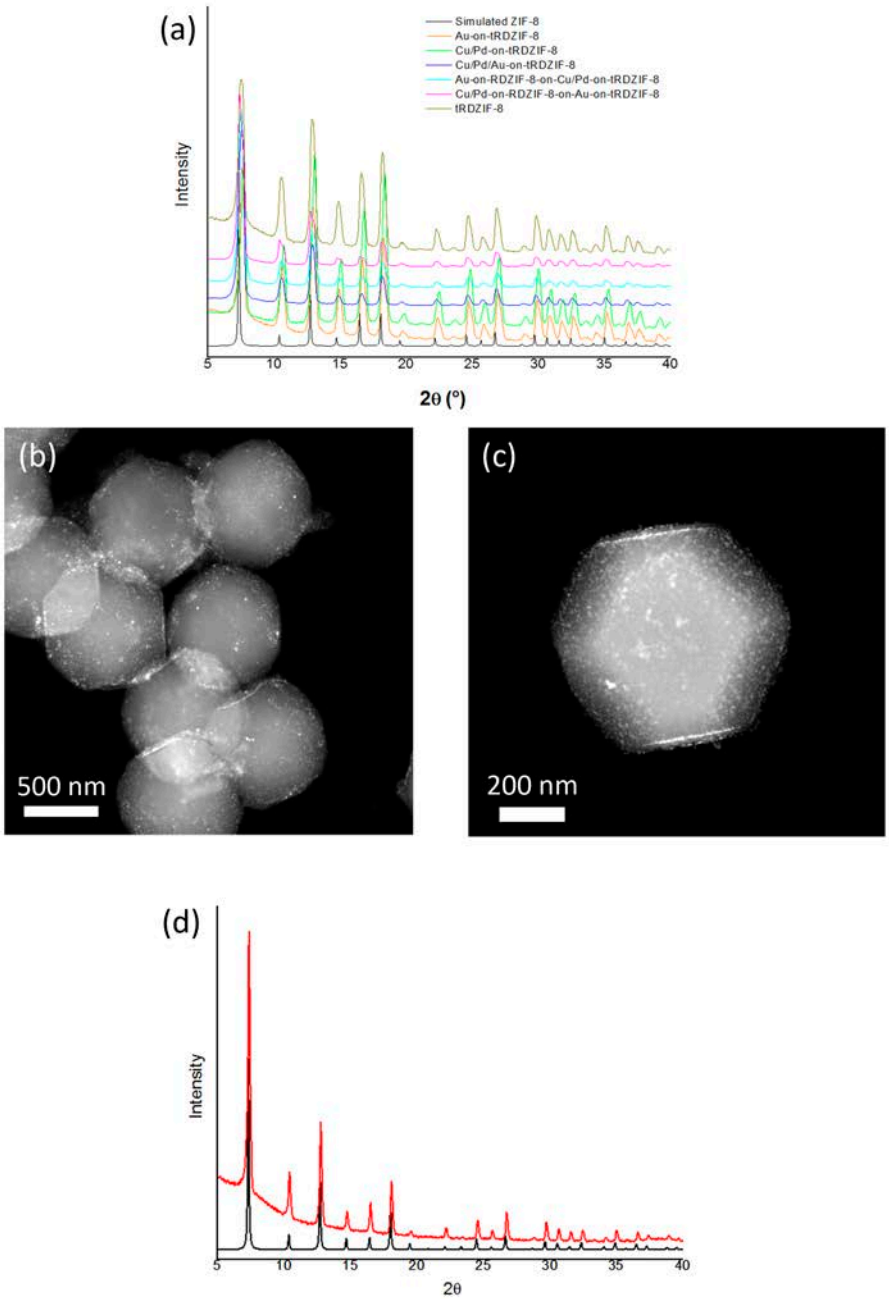

**Figure S11.** $^{1}$H NMR spectra of pure and isolated compounds **1-4.**

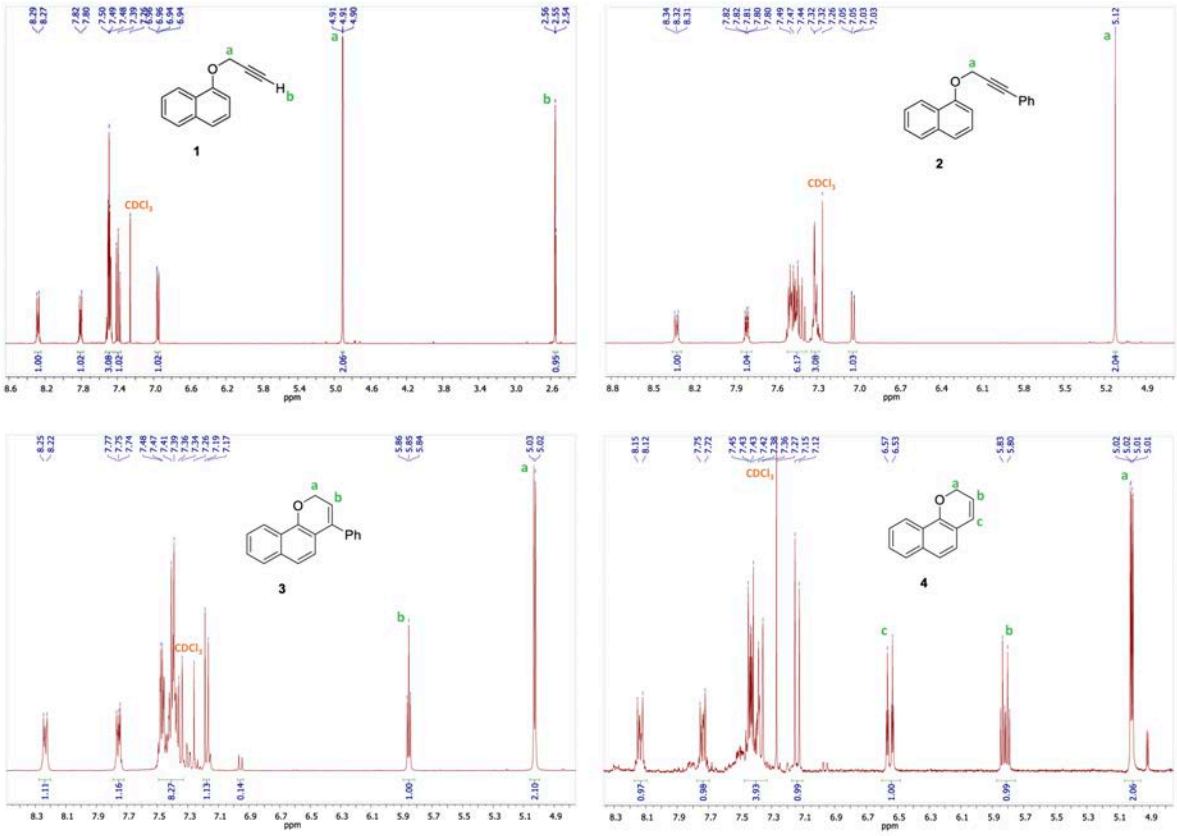

**Figure S12.** Representative example showing how the final compounds were characterised and quantified ($^1$H NMR and GC-FID). This example corresponds to Entry 2 of Table S1, in which reaction of **1** with Au-on-tRDZIF-8 yielded 40% of **1** and 31% of **4**. The $^1$H NMR of the raw material just passed through a silica pad clearly show two groups of signals, corresponding to compounds **1** and **4**.

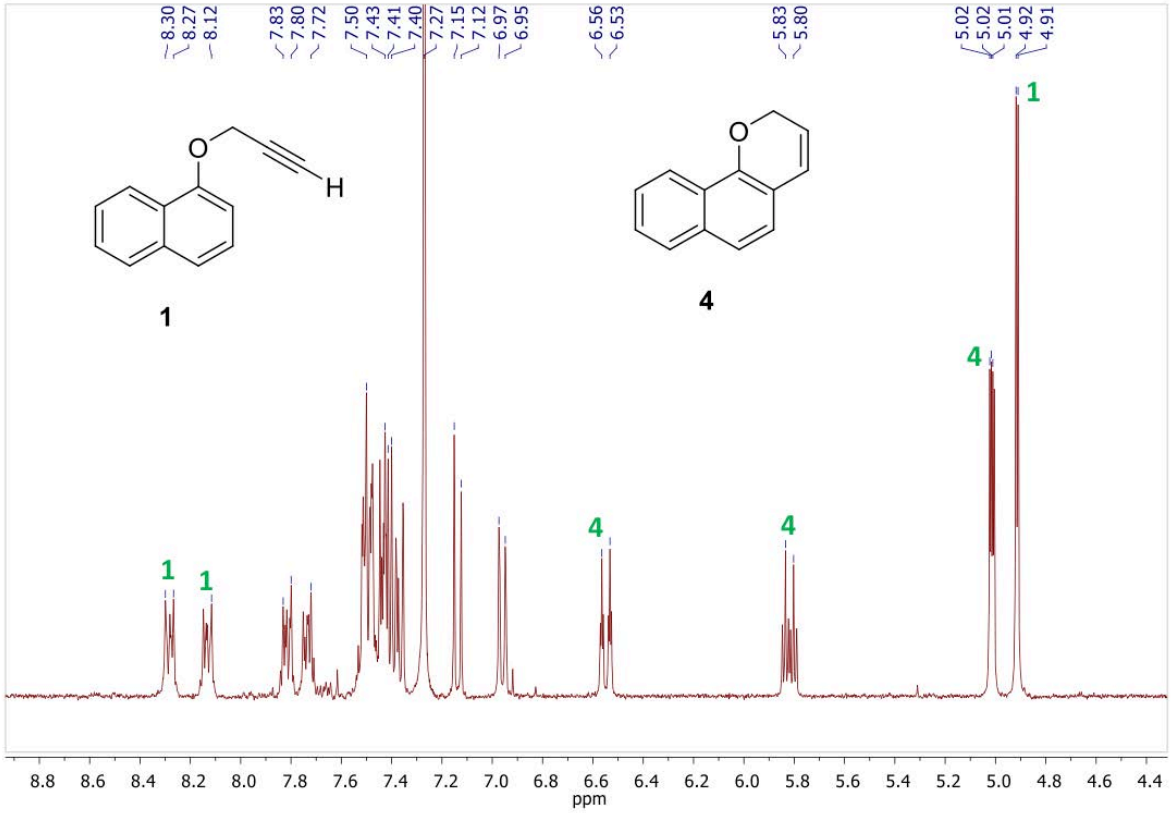


Thanks to a prior calibration of the GC instrument with the pure compounds, quantification of **1** and **4** was done by interpolation of the peak area in the calibration curve, bearing in mind the different retention times for each compound.

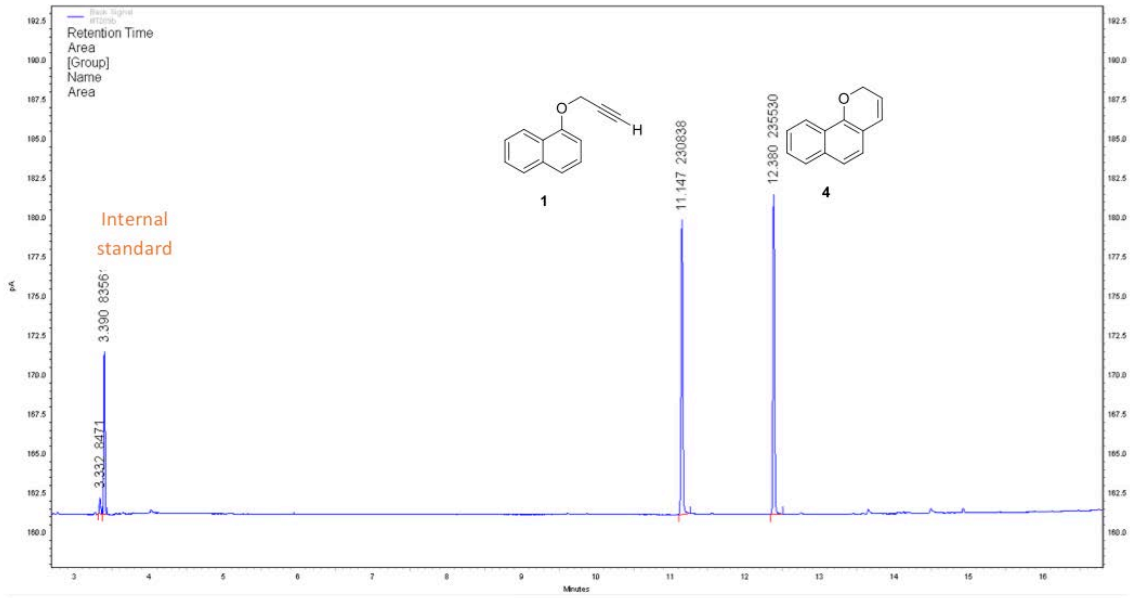

**Figure S13.** Representative example showing how the final compounds were characterised and quantified ($^1$H NMR and GC-FID). This example corresponds to Entry 5 of Table S1, in which reaction of **1** with Cu/Pd-on-tRDZIF-8-on-Au-on-tRDZIF-8 yielded 53% of **2** and 11% of **3**. As it could be seen in the following GC, both compounds appeared at the same retention time.

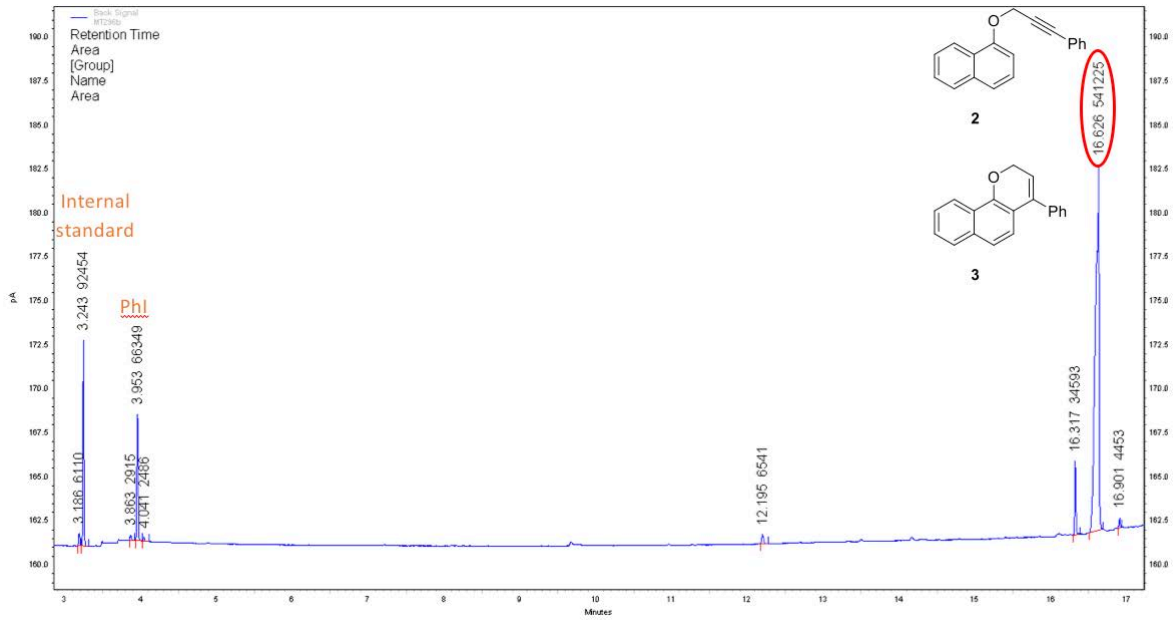


To clarify the final quantification of the two overlapped peaks from the GC, the $^1$H-NMR proportion of the signals integration allowed us to quantify **2** and **3** individually. As both signals correspond to one single H of each molecule, the proportion between both signals will be the proportion of both molecules in the peak area of the former GC.

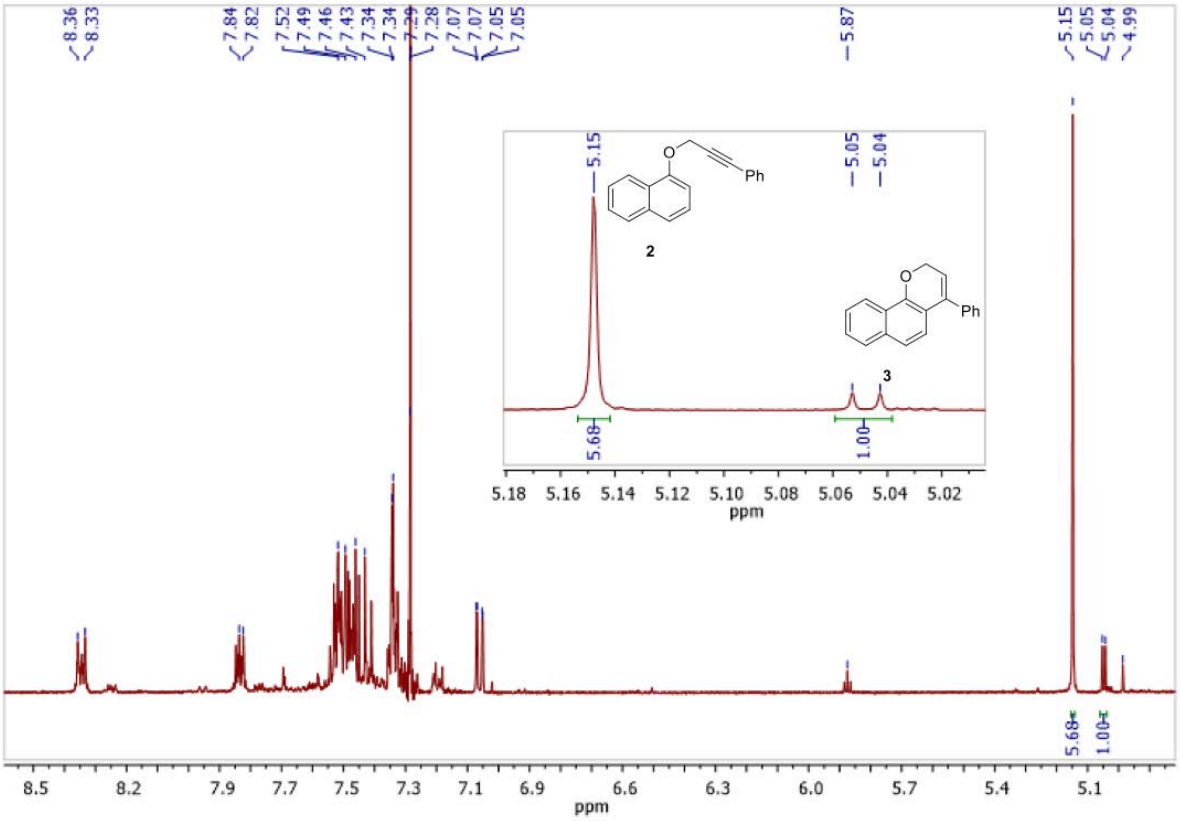

# CHAPTER 5

# Self-Assembly of Polyhedral Metal-Organic Framework Particles into Three-Dimensional Ordered Superstructures

ARTICLES
PUBLISHED ONLINE: 23 OCTOBER 2017 | DOI: 10.1038/NCHEM.2875
nature chemistry

# Self-assembly of polyhedral metal–organic framework particles into three-dimensional ordered superstructures

Civan Avci[1], Inhar Imaz[1], Arnau Carné-Sánchez[1], Jose Angel Pariente[2], Nikos Tasios[3], Javier Pérez-Carvajal[1], Maria Isabel Alonso[4], Alvaro Blanco[2], Marjolein Dijkstra[3], Cefe López[2]* and Daniel Maspoch[1,5]*

**Self-assembly of particles into long-range, three-dimensional, ordered superstructures is crucial for the design of a variety of materials, including plasmonic sensing materials, energy or gas storage systems, catalysts and photonic crystals. Here, we have combined experimental and simulation data to show that truncated rhombic dodecahedral particles of the metal–organic framework (MOF) ZIF-8 can self-assemble into millimetre-sized superstructures with an underlying three-dimensional rhombohedral lattice that behave as photonic crystals. Those superstructures feature a photonic bandgap that can be tuned by controlling the size of the ZIF-8 particles and is also responsive to the adsorption of guest substances in the micropores of the ZIF-8 particles. In addition, superstructures with different lattices can also be assembled by tuning the truncation of ZIF-8 particles, or by using octahedral UiO-66 MOF particles instead. These well-ordered, sub-micrometre-sized superstructures might ultimately facilitate the design of three-dimensional photonic materials for applications in sensing.**

Spherical colloidal particles (mainly silica or polymers such as polystyrene and acrylates) have traditionally been used to build self-assembled superstructures[1–4]. They tend to pack into the entropically favoured face-centred cubic (fcc) arrangement, although they can also adopt the less favoured, hexagonal close-packed (hcp) structure or the random, hexagonally close-packed (rhcp) lattice. Recently, the self-assembly of non-spherical polyhedral particles has begun to be considered as a viable method to diversify possible packing geometries[5–10], including the formation of crystals, liquid crystals, plastic crystals and quasicrystals[8,11,12]. Presently, these particles (mainly, metallic and metal chalcogenide particles such as gold[13,14], silver[15,16], cadmium/lead selenide/sulfide[17–19] and manganese oxide)[20] can be synthesized in multiple shapes, with high monodispersity and good colloidal stability, and can be coated with multiple organic polymers. Accordingly, several groups have observed, both experimentally and through simulations, that polyhedral particles form long-range ordered assemblies, corresponding to their densest packing, by alignment of the particle facets to maximize the entropy of the system[9,12,14,15,21,22].

So far, only a few studies have illustrated the use of polyhedral particles to generate long-range ordered arrangements that pack into different lattices. For example, Yang and co-workers have shown that polyvinylpyrrolidone-coated cubic, octahedral and truncated octahedral silver particles (dimensions of 100–300 nm) can be self-assembled by gravitational sedimentation into their corresponding densest lattice packings: the cubic, space-filling Kelvin structure or Minkowski packings, respectively[15]. Wang and co-workers demonstrated that, depending on their shape, cetyltrimethylammonium bromide (CTAB)-coated gold nanoparticles can self-assemble by water evaporation into different lattices[13]. They described self-assembly of gold rods, polyhedra, cubes and bipyramids into nematic/smectic-A, hexagonally packed, tetragonally packed and nematic/three-dimensionally ordered arrangements. More recently, Mirkin and co-workers have shown that depletion-based assembly allows cetyltrimethylammonium chloride (CTAC) or CTAB-coated gold nanoparticles with different shapes (rhombic dodecahedra, truncated cubes and octahedra) to self-assemble into multiple lattices (fcc, simple cubic and body-centred cubic, respectively) that are stable both in solution and in the solid state[14].

Strangely, rapid progress in the self-assembly of inorganic-based polyhedral particles has not led to the use of other families of the purely organic or hybrid metal–organic materials that are usually found as crystalline polyhedral particles, as functional building blocks to construct long-range self-assembled superstructures. The use of such crystalline particles has been precluded mainly by limited control over monodispersity, particle-shape homogeneity and colloidal stability. Here, we report that colloidal crystalline polyhedral MOF particles (in this case, zeolitic imidazolate framework-8 (ZIF-8)[23,24] and Universitetet i Oslo-66 (UiO-66)[25]) can be synthesized with the required size and shape homogeneity to subsequently self-assemble into well-ordered three-dimensional superstructures. These MOF-based superstructures show interesting features arising from their structures, in particular a photonic bandgap. Self-assembled spherical colloidal particles (mainly silica, polystyrene and acrylates) can form photonic crystals because they tend to order into superstructures capable of reflecting

[1]Catalan Institute of Nanoscience and Nanotechnology (ICN2), CSIC and The Barcelona Institute of Science and Technology, Campus UAB, Bellaterra, 08193 Barcelona, Spain. [2]Materials Science Factory, Instituto de Ciencia de Materiales de Madrid (ICMM), Consejo Superior de Investigaciones Científicas (CSIC), Calle Sor Juana Inés de la Cruz, 3, 28049 Madrid, Spain. [3]Soft Condensed Matter, Debye Institute for Nanomaterials Science, Utrecht University, Princetonplein 5, 3584 CC Utrecht, the Netherlands. [4]Institut de Ciència de Materials de Barcelona (ICMAB-CSIC), Campus UAB, 08193 Bellaterra, Spain. [5]ICREA, Pg. Lluís Companys 23, 08010 Barcelona, Spain. *e-mail: c.lopez@csic.es; daniel.maspoch@icn2.cat

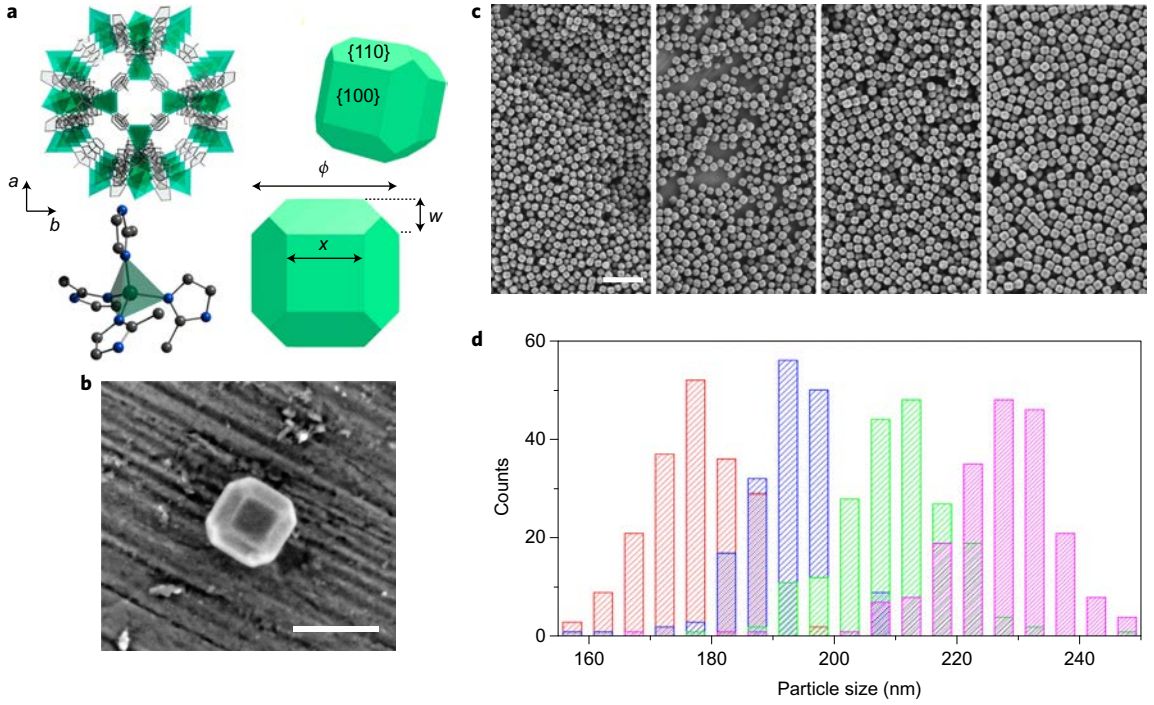


**Figure 1 | Structure and characterization of the TRD ZIF-8 particles. a**, Representation of the crystal structure of ZIF-8 showing that it is formed by the connection of tetrahedral Zn(II) ions (in green) through 2-methylimidazolate (2-MiM) linkers (in grey, top left). Bottom left: environment around one zinc centre. Atom colour code: Zn, green; C, grey; N, blue. Right: schematic illustrations of the ZIF-8 TRD particles, showing the {110} and {100} facets (top) and highlighting: particle size $\phi$; edge length $x$ of the {100} square facets; and chamfer $w$ (bottom). **b**, Representative FE-SEM image of a single TRD ZIF-8 particle. **c**, Representative FE-SEM images of TRD ZIF-8 particles of different sizes. From left to right: 178 ± 8 nm, 193 ± 8 nm, 210 ± 10 nm and 227 ± 10 nm. **d**, Size-distribution histograms of TRD ZIF-8 particles of different sizes: red, 178 ± 8 nm; blue, 193 ± 8 nm; green, 210 ± 10 nm; and purple, 227 ± 10 nm. Scale bars: 200 nm (**b**) and 1 μm (**c**).

**Table 1 | Length parameters of the particles. Lattice parameters and angles, interplanar distances, optical bandgaps and reflectance of the self-assembled superstructures.**

| Particle size $\phi$ (nm)* | $x$ (nm)* | $w$ (nm)† | $t$‡ | Lattice parameters $a, b, c$ (nm)§ | Lattice angles $\gamma, \beta, \alpha$ (deg)‖ | Interplanar distance $d$ (nm)¶ | Bandgap (nm)# | Reflectance (%)# |
|---|---|---|---|---|---|---|---|---|
| 178 ± 8 | 93 ± 4 | 43 ± 2 | 0.68 | 188 | 61 | 156 | 461 | 47 |
| 193 ± 8 | 101 ± 4 | 46 ± 2 | 0.69 | 204 | 61 | 169 | 500 | 50 |
| 210 ± 10 | 110 ± 5 | 50 ± 2 | 0.69 | 222 | 61 | 184 | 552 | 57 |
| 227 ± 10 | 119 ± 5 | 54 ± 2 | 0.69 | 239 | 61 | 199 | 600 | 43 |

*Measured from FE-SEM images. †Calculated from $(\phi - x)/2$. ‡Calculated from $x/(x + w)$. §Calculated from $(2w^2 + \phi^2)^{1/2}$. ‖Calculated from $\cos^{-1}[(w^2 + 2\phi w)/(2w^2 + \phi^2)]$. ¶Calculated from $[2w(w^2 - \phi w) + \phi(\phi^2 - w^2)]/[2(w^2 - \phi w)^2 + (\phi^2 - w^2)^2]^{1/2}$. #Measured from UV-vis reflectance spectra.

light at specific wavelengths and directions (photonic bandgap) due to the periodic refractive index distribution they create[2,3]. Here, the photonic bandgap of the MOF-based superstructures can not only be tuned by controlling the size of the MOF particles, but is also responsive to the sorption of guest substances.

## Results and discussion

**Synthesis of truncated rhombic dodecahedral ZIF-8 particles.** Highly monodisperse sub-micrometre-sized colloidal truncated rhombic dodecahedral (TRD) ZIF-8 particles in water were fabricated and stabilized by using CTAB as a cationic surfactant and a capping agent (Fig. 1a,b). ZIF-8 is a porous MOF made of Zn(II) ions and 2-methylimidazolate (2-MiM) linkers that exhibits a sodalite-type structure, a large surface area (~1,200–1,500 $m^2 g^{-1}$), good chemical and thermal stability, and is suited to many interesting porosity-related applications (for example, gas storage, separation and catalysis)[23,24,26]. ZIF-8 first crystallizes into cubic-shaped seeds, which gradually evolve into TRD particles and, finally, into the thermodynamically more stable rhombic dodecahedral (RD) particles due to the predominant (100) growth[27,28]. In this process, CTAB facilitates the synthesis of TRD ZIF-8 particles, as it selectively attaches to the {100} facets (*vide supra*)[29]. By controlling the amount of CTAB and 2-MiM, well-defined TRD ZIF-8 particles with sizes ranging from 178 ± 8 nm to 227 ± 10 nm were synthesized (with $\phi$ defined as the distance between opposing square facets; Fig. 1c,d and Table 1). In all cases, their size dispersity was ~5%. The TRD ZIF-8 particles exhibit six {100} square facets with edge length $x$ (Fig. 1a and Table 1) and twelve {110} irregular hexagonal facets with a surface area ratio of ~1:1.5 ({100}:{110}). These TRD particles, which can also be viewed as chamfered cubes (that is, cubes with bevelled edges), have a chamfer $w$ that increases with $\phi$ and a constant truncation $t$ of 0.68–0.69 (Table 1). X-ray powder diffraction (XRPD) indicated that all particles are crystalline ZIF-8 (Supplementary Fig. 1). Nitrogen physical sorption measurements on the ZIF-8 particles validated their microporosity. The measured Brunauer–Emmett–Teller (BET) surface area (1,154 $m^2 g^{-1}$) is fully consistent with previously reported values for ZIF-8[23]

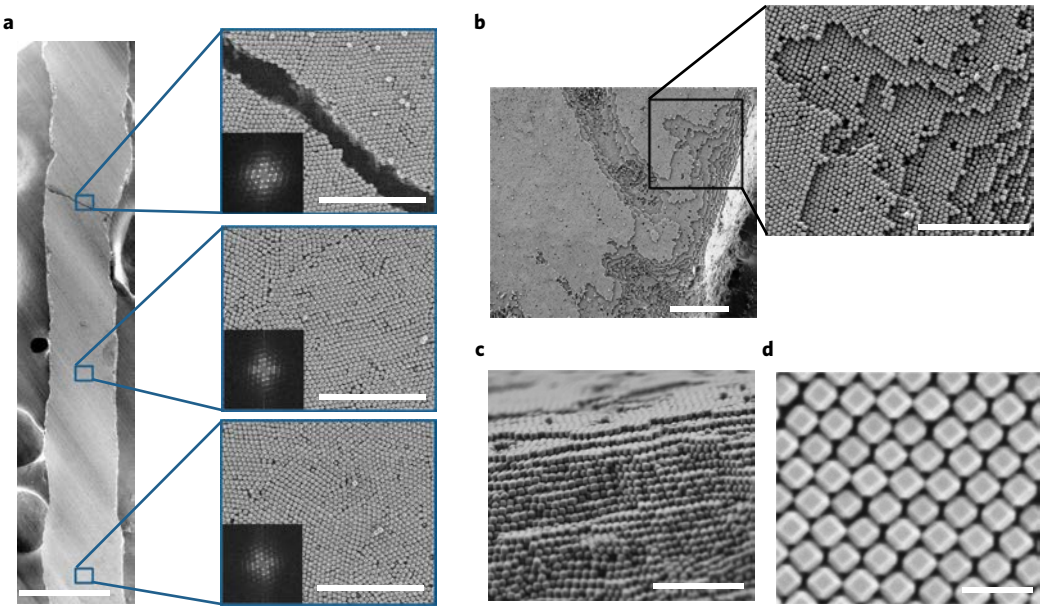


**Figure 2 | Ordered rhombohedral self-assembled superstructures.** Representative FE-SEM images of a self-assembled superstructure made of TRD ZIF-8 crystals (size 210 ± 10 nm). **a**, Low-magnification image of a self-assembled superstructure that extends over 1 mm. The three magnified sections reveal that the rhombohedral lattice is maintained across the self-assembled superstructure. Note here that—as in any other superstructure made of self-assembled particles—the ordering of TRD ZIF-8 crystals reveals domains with misfit dislocations and point defects. Insets: Fourier transforms of these sections showing different grain orientations. **b**, Edge of a self-assembled superstructure, showing order in the three dimensions. **c**, Cross-section of the self-assembled superstructure. **d**, Zoom of the packing structure. Scale bars: 200 μm (**a**), 5 μm (**a**, insets), 10 μm (**b**), 1 μm (**b**, inset), 2 μm (**c**) and 500 nm (**d**).

(Supplementary Fig. 2) and can be accounted for by internal porosity, as the external surface of the ZIF-8 is negligible in comparison.

**Self-assembly of TRD ZIF-8 particles.** In the self-assembly experiments, TRD ZIF-8 particles arranged into millimetre-sized three-dimensional superstructures by evaporation under heating. We began by placing a droplet of an aqueous colloidal solution of the particles (100 mg ml$^{-1}$) on a clean glass surface. Then, the surface was incubated in an oven at 65 °C until the droplet was dried. Field-emission scanning electron microscopy (FE-SEM) of the resulting dried solids revealed the formation of self-assembled superstructures in which the ZIF-8 particles are ordered along the three directions of space (Fig. 2 and Supplementary Fig. 3). The initial evaporation temperature optimized to ensure homogeneous three-dimensional ordering along the entire monolithic structure was found to be ~65 °C. Evaporation at room temperature yielded three-dimensional ordering but led to heterogeneity in the monolith thickness by generating thick surrounding walls around the droplet, which were formed by a concave meniscus formed over time (Supplementary Fig. 4). In contrast, a higher temperature (100 °C) led to quasi-amorphous packings caused by faster evaporation (Supplementary Fig. 4). Interestingly, other tested techniques, such as dip- and-spin-coating, vertical deposition and even simple centrifugation, all yielded similar self-assembled superstructures. However, in these cases the observed degree of three-dimensional ordering was much lower (Supplementary Figs 4 and 5).

Upon self-assembly, the TRD ZIF-8 particles adopted the densest rhombohedral packing, with a packing fraction of 0.86 (Figs 2 and 3a). Investigations using Floppy-Box Monte Carlo simulations based on a simulating-annealing approach in which the densest crystal structure is predicted by slowly increasing the pressure, also resulted in the formation of the same rhombohedral packing (Fig. 3b)[30,31]. The packing that we observed resulted from maximizing the density of the TRD particles. As shown in Fig. 3c–f, the maximum number of neighbours that can be adjacent to a given TRD particle is twelve (Fig. 3f). Of these neighbours, six are perfectly aligned through hexagonal {110} facets (in two groups of three that meet at two diagonally opposing vertexes; Fig. 3c), whereas the remaining six are connected through square {100} facets (Fig. 3d). In these latter connections, the {100} facets of neighbouring particles are touching and aligned but with a small shift (equal to $w$) in the two directions defined by the sides of the square (Fig. 3e). The resulting structure exhibits a rhombohedral Bravais lattice with a unit cell with lattice parameters $\vec{a}$, $\vec{b}$ and $\vec{c}$ and angles $\gamma$, $\beta$ and $\alpha$, as described in Table 1.

**Photonic crystal properties.** The MOF-based superstructures introduced here are periodic dielectrics made of ~200 nm MOF particles that also show angle-dependent opalescence arising from a photonic bandgap. Moreover, because the lattice period is comparable to visible wavelengths, this opalescence is visible to the naked eye (Fig. 4a). Figure 4b presents spectra recorded for superstructures assembled from TRD ZIF-8 particles of different sizes. These spectra were measured using reflectance spectrophotometry at normal incidence ($\theta = 0°$). A clear band in the optical reflectance spectrum was observed that is attributed to the opening of a bandgap in the (001) direction in reciprocal space, which is associated with the Bragg reflection from the (001) crystallographic planes of the rhombohedral lattice. Notice that these layers are not parallel to the square facet of the particles but form an angle given by $\cos\delta = (001)\cdot \vec{a}\times\vec{b}/|\vec{a}||\vec{b}| = (\phi^2 - w^2)/(\phi^2 + 2w^2)$. The magnitude of reflectance ranged from 40 to 57% (Table 1 and Supplementary Fig. 6), which is comparable with standard literature values for self-assembled three-dimensional photonic crystals made of spherical particles[3]. The reflectance spectra also showed (1) the Bragg reflection spectral position scales with particle size and (2) as expected, the Bragg reflection shifted linearly towards shorter wavelengths at smaller particle sizes.

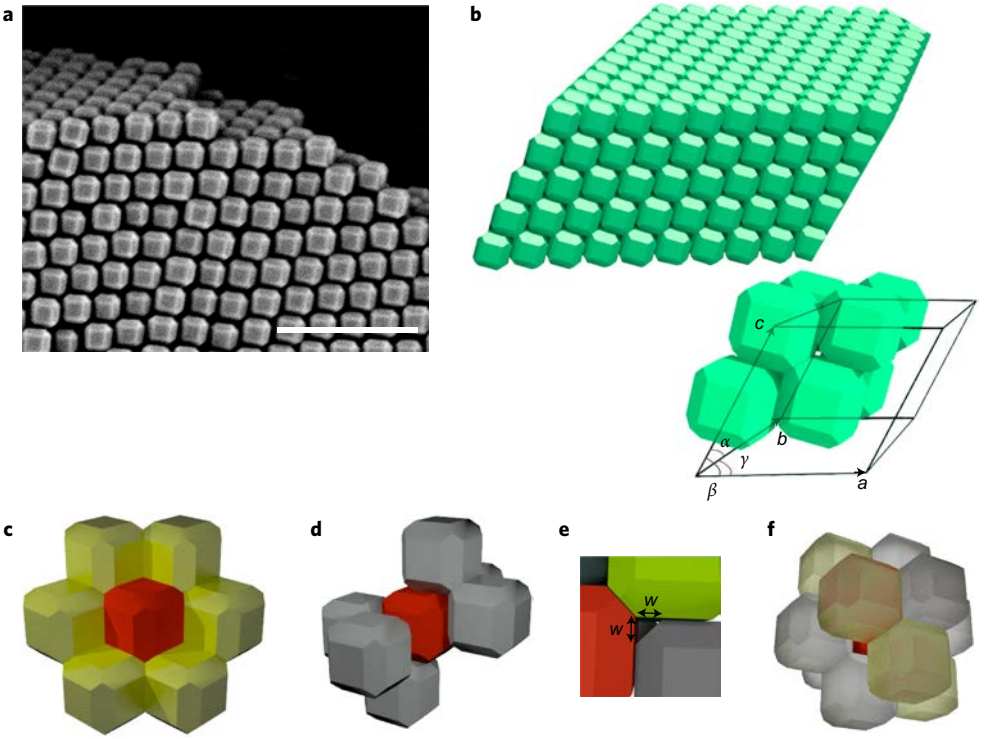


**Figure 3 | Computer simulation and FE-SEM image of the formation of the densest rhombohedral lattice. a**, Representative FE-SEM image of a cross-section of the self-assembled superstructure, showing the rhombohedral lattice. **b**, Densest packing obtained from Floppy-Box Monte Carlo simulations, confirming the same type of rhombohedral lattice obtained experimentally. Bottom right: unit cell of the rhombohedral lattice. **c**–**f**, Schematics showing the connectivity of a single TRD ZIF-8 particle in the rhombohedral lattice: six TRD particles perfectly aligned through the {110} facets (**c**); six TRD particles aligned through the {100} facets (**d**); representation showing the shift in two directions of these latter connections (**e**); combined 12 TRD particles aligned to a single TRD particle (**f**). Scale bar in **a**: 1 μm.

Figure 4c shows the Bragg reflection maximum or bandgap centre ($\lambda_c$) plotted against the interplanar distance $d$. Here, it is possible to fit $\lambda_c$ using the Bragg–Snell law for normal incidence, which is defined as $\lambda_c = 2nd$, where $n$ is the effective index of refraction of the superstructure. For our rhombohedral superstructure we calculated the interplanar distances by taking the normalized cross product of lattice vectors $\vec{a}$ and $\vec{b}$, which gives the normal to the plane defined by $\vec{a}$ and $\vec{b}$ (Table 1). Thus, from the slope of the fitted curve, we determined an effective refractive index of 1.49. This value is very close to the value (1.47) calculated by averaging the dielectric constant $\varepsilon = V_{fram}(n_{fram})^2 + V_{H_2O}(n_{H_2O})^2 + V_{air}(n_{air})^2$, where $V$ and $n$ are the volume fractions and effective refractive indexes of the different components, respectively (Supplementary Section 2 and Supplementary Table 1). This value of 1.49 is also in good agreement with the value (1.43) obtained by spectroscopic ellipsometry performed on the photonic crystal self-assembled from 210 nm TRD ZIF-8 particles (Supplementary Fig. 7)[32]. Importantly, the closely linear relationship between the interplanar distance (or particle size) and the maximum reflection wavelength (Fig. 4c) is a clear indication that the product packing fraction times average refractive index remains constant throughout the explored particle size range. That the refractive index of the MOF does not vary should not be surprising, given that all the TRD ZIF-8 particles are synthesized under the same conditions. However, only particles for which the proportions are preserved assemble into structures with the same packing fraction, as this is determined by the $w/x$ ratio. As observed in Table 1, $w$ very closely follows a linear relationship with $x$ (Supplementary Fig. 8). This indicates that the self-assembly proceeds similarly in all cases and is consistent with the fact that all the particles in the studied size range have the same geometry.

The microporosity of MOFs highly favours the use of these photonic structures for the development of sensing applications, because the adsorption of species in the MOF pore network can change their refractive index, resulting in a pronounced shift in the photonic bandgap spectral position $\lambda_c$. To realize this, the porous MOF particles should be activated, by driving out the water of the ZIF-8 particles without disrupting the well-ordered assembly so as to allow the adsorption of analyte molecules inside the empty pores. To this end, we studied the evacuation of the guest water molecules of the photonic structure self-assembled from 210 nm TRD ZIF-8 particles by heating it at 260 °C, a temperature at which thermogravimetric analysis (TGA) assured the complete removal of water molecules (Supplementary Fig. 9). Indeed, TGA of the heated superstructure indicated that no further weight loss had occurred up to 300 °C (Supplementary Fig. 9), confirming that all guest water molecules had been evacuated. Moreover, FE-SEM images demonstrated preservation of the rhombohedral packing, whereas an $N_2$ isotherm illustrated the typical type-I behaviour consistent with a BET surface area of 1,250 $m^2\ g^{-1}$, thus confirming the microporous character of the photonic structure (Supplementary Figs 10 and 11). Naturally, in this activated (fully dehydrated) photonic crystal, $\lambda_c$ displaced to shorter wavelengths (from 552 to 522 nm), which we expect for the replacement of water molecules with air (Supplementary Fig. 12).

As proof of concept, we subsequently exposed the activated photonic crystal to the vapour of different alcohols (methanol, ethanol, isopropanol and *n*-butanol) and to water vapour, while measuring the shift in the photonic bandgap. We found a redshift in $\lambda_c$ when the photonic crystal was exposed to alcohol vapour (methanol, $\lambda_c = 561$ nm; ethanol, $\lambda_c = 562$ nm; isopropanol,

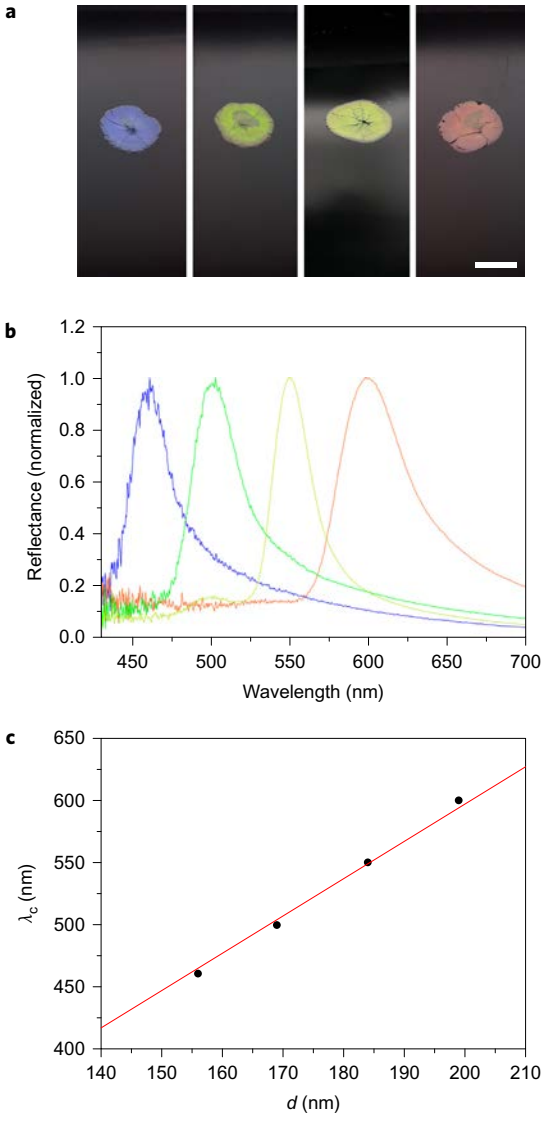


**Figure 4 | Photonic properties. a**,**b**, Photographs (**a**) and normalized optical reflection at $\theta = 0°$ of the self-assembled photonic crystals made of TRD ZIF-8 particles of different sizes (**b**): 178 ± 8 nm (blue); 193 ± 8 nm (green); 210 ± 10 nm (yellow); and 227 ± 10 nm (red). **c**, Bragg reflection maximum wavelength $\lambda_c$ plotted against interplanar distance $d$ and fit to the Bragg law (red line) constrained to intercept at zero. Scale bar in **a**: 1 cm.

$\lambda_c = 564$ nm; *n*-butanol, $\lambda_c = 568$ nm; Supplementary Figs 13 and 14) but not when it was exposed to water. This selectivity is somewhat expected for the inherent selective adsorption properties of ZIF-8, which is known to absorb alcohols but not water[33]. Considering a pore filling of 81% for methanol, ethanol or isopropanol and 86% for *n*-butanol (calculated from the adsorption isotherms; Supplementary Fig. 15), we concluded that these shifts correlate well with those calculated according to the corresponding effective refractive indices (determined by averaging the dielectric constant; Supplementary Section 2 and Supplementary Table 1). Thus, the replacement of water molecules with air in the pores of ZIF-8 at relatively low pressures changes the refractive index of the photonic crystal, causing the bandgap to shift. We envision that this feature could be exploited for the use of these materials as responsive materials or sensors.

**Extending the self-assembly to MOF particles with other morphologies.** Having demonstrated that well-ordered arrays can be fabricated from TRD ZIF-8 particles, we considered that the numerous MOFs reported to date could be an excellent source of crystalline polyhedral particles. We inferred that control of particle size, shape and self-assembly could enable new packing geometries. To this end, we extended the concept of using MOF particles to spontaneously generate ordered arrays by using ZIF-8 particles with other morphologies (that is, TRD with a lower degree of truncation and non-truncated RD), as well as octahedral particles of the UiO-66 MOF (Fig. 5). For the synthesis of TRD ZIF-8 particles with less truncation ($\phi = 263 \pm 13$ nm; $x = 107 \pm 5$ nm; $w = 78 \pm 4$ nm; $t = 0.57$ versus 0.69 for the previously synthesized TRD ZIF-8 particles), the capping effect of CTAB was used again. However, the amount of CTAB was reduced to accelerate the growth of the {100} facets (Supplementary Fig. 17). Complete removal of the CTAB resulted in either slightly truncated ($\phi = 319 \pm 14$ nm; $x = 76 \pm 3$ nm; $w = 122 \pm 5$ nm; $t = 0.38$; Supplementary Fig. 17) or non-truncated ($t = 0$) RD ZIF-8 particles, depending on the reaction time. The latter particles exhibited a $\phi$ (defined as the distance between opposing vertices) of 530 ± 30 nm and an edge size of 230 ± 12 nm (Supplementary Fig. 17).

Experimental observations confirmed that the new ZIF-8 particles self-assemble into ordered arrangements once their colloidal solutions are evaporated off at either 65 °C (TRD particles) or 120 °C (RD particles). A theoretical analysis of the densest packings as a function of $t$ of the ZIF-8 particles is shown in Fig. 5a. We found that the densest packing is a rhombohedral crystal for TRD particles with truncation $t$ higher than 0.66, whereas it is an fcc crystal for $t$ lower than 0.66. These theoretical findings corroborate the experimentally obtained self-assembled superstructures. As shown above, monodisperse TRD ZIF-8 particles with $t = 0.69$ adopted rhombohedral packing, whereas the newly synthesized particles with $t = 0.57$ crystallized into a plastic fcc crystal with a packing fraction of 0.68 (Fig. 5c). Note that the plastic fcc crystal differs from the regular one in the sense that no preferential facet-to-facet interactions exist between neighbouring ZIF-8 particles. We reasoned that the formation of a plastic—rather than a regular—fcc crystal was due to kinetic effects. Consistent with the simulation data, the slightly truncated ZIF-8 particles ($t = 0.38$) and the RD ZIF-8 particles ($t = 0$) each crystallized into an fcc regular crystal (Fig. 5d). In the latter crystals, each ZIF-8 particle is bound to 12 other particles by their 12 identical {110} facets. Importantly, the self-assembly experiments that we ran with as-synthesized, CTAB-free ZIF-8 particles all failed to produce ordered packings, which can be explained by the strong van der Waals attractions between the particles, which are not balanced by ionic surfactants (like CTAB). This result parallels observations on the assembly of polyhedral inorganic particles, in which adsorbed ionic surfactants/polymers on the particle surfaces are crucial to stabilize the suspension against irreversible colloidal aggregation[14,15]. We wish to remark here that non-adsorbed ionic surfactants/polymers in solution can be used to assist self-assembly by inducing depletion attractions between the particles.

Finally, we extended our approach to another MOF. We synthesized monodisperse octahedral particles of UiO-66[25] ($\phi = 340 \pm 30$ nm, defined as the distance between opposing vertices; edge size = 242 ± 18 nm) using acetic acid as a coordination modulator agent (Supplementary Fig. 17)[34]. UiO-66 is a promising MOF for catalysis and $CO_2$ capture due to its large surface area (1,100–1,400 $m^2\ g^{-1}$) and its high hydrothermal, chemical and thermal stability[35,36]. After synthesis, we functionalized the UiO-66 particles with CTAB and, using the evaporation method at 85 °C, left them to self-assemble. FE-SEM images revealed the formation of an ordered arrangement showing a hexagonal lattice closely related to the Minkowski lattice (Fig. 5b,e), as has been observed for octahedral silver particles[15].

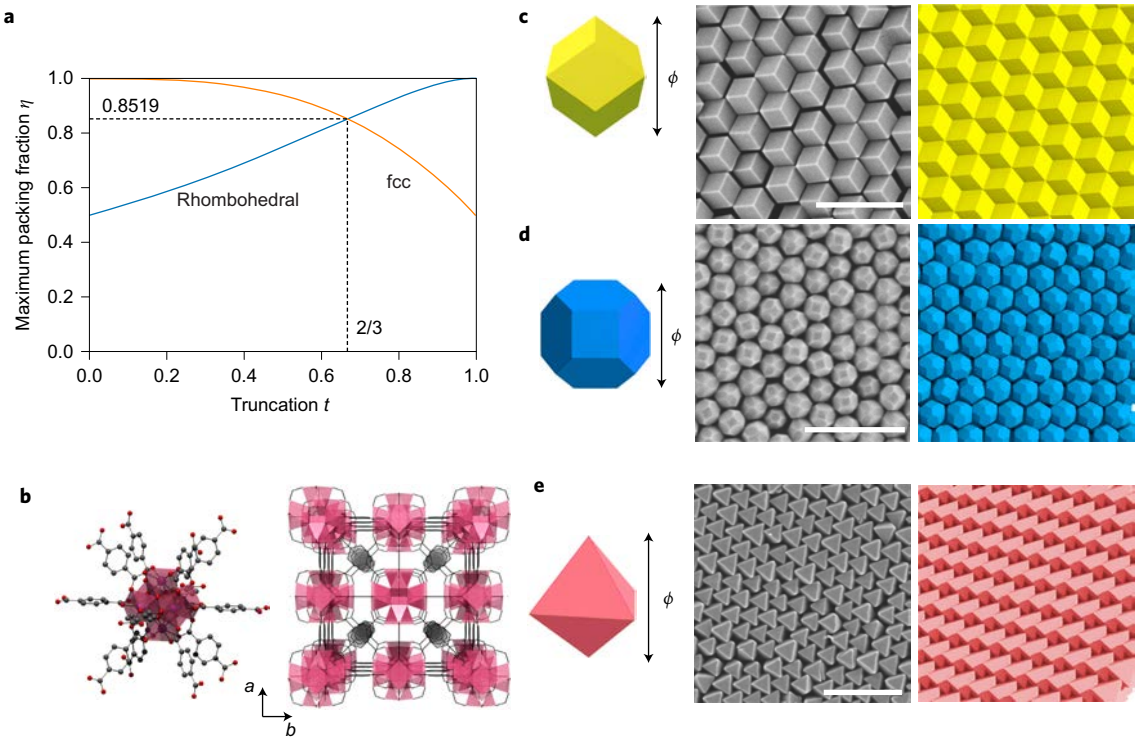


**Figure 5 | Ordered self-assembled superstructures made of MOF particles with other morphologies. a**, Maximum packing fraction $\eta$ as a function of truncation $t$ of the ZIF-8 particles for the two possible packing geometries: rhombohedral (blue) and fcc (orange). **b**, Representation of the crystal structure of UiO-66, showing that it is formed by connection of hexanuclear $[Zr_6O_4(OH)_4]$ oxoclusters through 12 terephthalate linkers (atom colour code: Zr, purple; C, grey; O, red). **c**–**e**, Left: schematic representation of the single MOF particles of the RD ZIF-8 particles (**c**), TRD ZIF-8 particles with $t$ = 0.57 (**d**) and octahedral UiO-66 particles (**e**), respectively. Middle: representative FE-SEM images of the crystals resulting from their respective self-assembly: a plastic fcc crystal (**c**), a regular fcc crystal (**d**) and a hexagonal packing closely related to the Minkowski lattice (**e**). Right: corresponding packings obtained from Floppy-Box Monte Carlo simulations. Scale bars in **c**–**e**: 1 μm.

## Conclusions

We have demonstrated that crystalline, polyhedral TRD ZIF-8 particles can be synthesized with good monodispersity, shape homogeneity and colloidal stability and that they subsequently (spontaneously) self-assemble into millimetre-sized three-dimensional ordered arrangements. The resulting superstructures, corresponding to the densest rhombohedral packings, are porous and show a photonic bandgap functionality that can be tuned by controlling the size of the ZIF-8 particles or by changing the substance adsorbed in the micropores of the ZIF-8 particles. These characteristics should enable the development of self-assembled, MOF-based photonic crystals for sensing applications. In addition, we have extended the formation of ordered arrangements showing different packing geometries to include the self-assembly of crystalline MOF particles with other shapes. These findings show that MOF particles and other molecular crystalline particles, in the same manner as purely organic particles, can be harnessed for the self-assembly of superstructures with long-range periodicities, which is attractive for designing the preparation of materials for applications such as sensing, storage, catalysis and photonics.

## Methods

**Synthesis of TRD ZIF-8 particles with truncation $t$ = 0.69 or 0.57.** In a typical synthesis, $Zn(CH_3COO)_2{\cdot}2H_2O$ (300 mg) dissolved in 5 ml of water was added to varying amounts of 2-methylimidazole (2-MiM) and CTAB (ref. 29) dissolved in 5 ml of water with gentle stirring for a few seconds. The resulting transparent mixture turned white after 15 s and was left undisturbed at room temperature for 2 h. The resulting ZIF-8 particles were washed three times with deionized (DI) water upon centrifugation at 9,000 r.p.m. in 50 ml Falcon tubes. The collected wet pellets were finally redispersed in DI water at a concentration of 100 mg $ml^{-1}$. Note that to prevent aggregation, the particles should be dispersed while they are still wet. The zeta potential of the resulting TRD ZIF-8 particles was approximately +40 mV. The conditions used to synthesize TRD ZIF-8 particles with $t$ = 0.69 were the following: for 178 ± 8 nm, [CTAB] = 0.54 mM and [2-MiM] = 2.72 M; for 193 ± 8 nm, [CTAB] = 0.5 mM and [2-MiM] = 2.72 M; for 210 ± 10 nm, [CTAB] = 0.54 mM and [2-MiM] = 2.58 M; for 227 ± 10 nm, [CTAB] = 0.44 mM and [2-MiM] = 2.72 M. The conditions used to synthesize the TRD ZIF-8 particles with $t$ = 0.57 were [CTAB] = 0.14 mM and [2-MiM] = 3.81 M.

**Synthesis of TRD ZIF-8 particles with truncation $t$ = 0.38 and RD ZIF-8 particles.** A 5 ml volume of an aqueous solution of $Zn(CH_3COO)_2{\cdot}2H_2O$ (300 mg) was added to 6.4 ml of an aqueous solution of 2.72 M 2-MiM with gentle stirring. After 15 s the transparent mixture turned white and was then left undisturbed at room temperature for either 15 min (TRD ZIF-8 particles with $t$ = 0.38) or 2 h (RD ZIF-8 particles). The resulting ZIF-8 particles were washed three times with DI water with centrifugation at 9,000 r.p.m. in 50 ml Falcon tubes. For functionalization, the particles were redispersed in 0.54 mM CTAB (aq.), stirred for 30 min and washed once more with DI water with centrifugation at 9,000 r.p.m. in 50 ml Falcon tubes. The collected wet pellets were finally redispersed in DI water at a concentration of 100 mg $ml^{-1}$. The zeta potential of the resulting ZIF-8 particles was approximately +50 mV.

**Synthesis of octahedral UiO-66 particles.** In a typical synthesis, $ZrCl_4$ (34.9 mg) and 1-4-benzendicarboxylic acid (BDC; 24.9 mg) were dissolved in 10 ml of 2.1 M acetic acid (DMF) and transferred to a scintillation vial, which was placed in a pre-heated oven at 120 °C for 12 h. The colloidal crystals were then recovered by centrifugation and washed twice with DMF and twice with methanol with centrifugation at 9,000 r.p.m. in a 50 ml Falcon tube. For functionalization, the particles were redispersed in 0.54 mM CTAB (aq.), stirred for 30 min and washed once more with DI water with centrifugation at 9,000 r.p.m. in 50 ml Falcon tubes. The collected wet pellets were finally redispersed in DI water at a concentration of 100 mg $ml^{-1}$. The zeta potential of the resulting octahedral UiO-66 particles was approximately +50 mV.

**Formation of the self-assembled superstructures.** Glass microscope slides were initially washed with water and ethanol, dried with a pressurized $N_2$ gun and subjected to plasma cleaning under $Ar^+$ for 2 min using a Zepto plasma cleaner (Diener Electronic). Then, 150 μl of each colloidal aqueous solution of MOF particles was added dropwise onto the clean substrate and the treated sample was left

to dry in an oven at varying temperatures. The temperatures used to fabricate the self-assembled superstructures were 65 °C (TRD ZIF-8), 120 °C (RD ZIF-8) or 85 °C (octahedral UiO-66).

**Floppy-Box Monte Carlo simulations.** To predict the densest crystal structure of hard MOF particles we performed Floppy-Box Monte Carlo simulations[30,31]. We carried out constant-pressure simulations of $N = 1, 2, 3$ or 4 particles in a simulation box with a variable box shape and periodic boundary conditions. We compressed the system by increasing the pressure stepwise, which enabled us to predict the densest packing. In all cases we obtained the densest packing, as presented in Figs 2 and 3.

**Data availability.** The data supporting the findings of this study are available upon request from the corresponding author (including data presented in the main text and in the Supplementary Information).

Received 24 July 2017; accepted 13 September 2017; published online 23 October 2017

## References


1. Li, F., Josephson, D. P. & Stein, A. Colloidal assembly: the road from particles to colloidal molecules and crystals. *Angew. Chem. Int. Ed.* **50,** 360–388 (2011).
2. Von Freymann, G., Kitaev, V., Lotsch, B. V. & Ozin, G. A. Bottom-up assembly of photonic crystals. *Chem. Soc. Rev.* **42,** 2528–2554 (2013).
3. Galisteo-López, J. F. *et al.* Self-assembled photonic structures. *Adv. Mater.* **23,** 30–69 (2011).
4. Kim, S.-H., Lee, S. Y., Yang, S.-M. & Yi, G.-R. Self-assembled colloidal structures for photonics. *NPG Asia Mater.* **3,** 25–33 (2011).
5. Glotzer, S. C. & Solomon, M. J. Anisotropy of building blocks and their assembly into complex structures. *Nat. Mater.* **6,** 557–562 (2007).
6. Quan, Z. & Fang, J. Superlattices with non-spherical building blocks. *Nano Today* **5,** 390–411 (2010).
7. Damasceno, P. F., Engel, M. & Glotzer, S. C. Predictive self-assembly of polyhedra into complex structures. *Science* **337,** 453–457 (2012).
8. Agarwal, U. & Escobedo, F. A. Mesophase behaviour of polyhedral particles. *Nat. Mater.* **10,** 230–235 (2011).
9. Torquato, S. & Jiao, Y. Dense packings of the Platonic and Archimedean solids. *Nature* **460,** 876–879 (2009).
10. Sacanna, S. & Pine, D. J. Shape-anisotropic colloids: building blocks for complex assemblies. *Curr. Opin. Colloid Interface Sci.* **16,** 96–105 (2011).
11. Gantapara, A. P., de Graaf, J., van Roij, R. & Dijkstra, M. Phase diagram and structural diversity of a family of truncated cubes: degenerate close-packed structures and vacancy-rich states. *Phys. Rev. Lett.* **111,** 015501 (2013).
12. Haji-Akbari, A. *et al.* Disordered, quasicrystalline and crystalline phases of densely packed tetrahedra. *Nature* **462,** 773–777 (2009).
13. Ming, T. *et al.* Ordered gold nanostructure assemblies formed by droplet evaporation. *Angew. Chem. Int. Ed.* **47,** 9685–9690 (2008).
14. Young, K. L. *et al.* A directional entropic force approach to assemble anisotropic nanoparticles into superlattices. *Angew. Chem. Int. Ed.* **52,** 13980–13984 (2013).
15. Henzie, J., Grünwald, M., Widmer-Cooper, A., Geissler, P. L. & Yang, P. Self-assembly of uniform polyhedral silver nanocrystals into densest packings and exotic superlattices. *Nat. Mater.* **11,** 131–137 (2011).
16. Tao, A. R., Ceperley, D. P., Sinsermsuksakul, P., Neureuther, A. R. & Yang, P. Self-organized silver nanoparticles for three-dimensional plasmonic crystals. *Nano Lett.* **8,** 4033–4038 (2008).
17. Miszta, K. *et al.* Hierarchical self-assembly of suspended branched colloidal nanocrystals into superlattice structures. *Nat. Mater.* **10,** 872–876 (2011).
18. Geuchies, J. J. *et al. In situ* study of the formation mechanism of two-dimensional superlattices from PbSe nanocrystals. *Nat. Mater.* **15,** 1248–1254 (2016).
19. Boneschanscher, M. P. *et al.* Long-range orientation and atomic attachment of nanocrystals in 2D honeycomb superlattices. *Science* **344,** 1377–1380 (2014).
20. Xie, S. *et al.* Supercrystals from crystallization of octahedral MnO nanocrystals. *J. Phys. Chem. C* **113,** 19107–19111 (2009).
21. Volkov, N., Lyubartsev, A. & Bergström, L. Phase transitions and thermodynamic properties of dense assemblies of truncated nanocubes and cuboctahedra. *Nanoscale* **4,** 4765–4771 (2012).
22. Damasceno, P. F., Engel, M. & Glotzer, S. C. Crystalline assemblies and densest packings of a family of truncated tetrahedra and the role of directional entropic forces. *ACS Nano* **6,** 609–614 (2012).
23. Park, K. S. *et al.* Exceptional chemical and thermal stability of zeolitic imidazolate frameworks. *Proc. Natl Acad. Sci. USA* **103,** 10186–10191 (2006).
24. Huang, X.-C., Lin, Y.-Y., Zhang, J.-P. & Chen, X -M. Ligand-directed strategy for zeolite-type metal–organic frameworks: zinc(II) imidazolates with unusual zeolitic topologies. *Angew. Chem. Int. Ed.* **45,** 1557–1559 (2006).
25. Cavka, J. H. *et al.* A new zirconium inorganic building brick forming metal organic frameworks with exceptional stability. *J. Am. Chem. Soc.* **130,** 13850–13851 (2008).
26. Chen, B., Yang, Z., Zhu, Y. & Xia, Y. Zeolitic imidazolate framework materials: recent progress in synthesis and applications. *J. Mater. Chem. A* **2,** 16811–16831 (2014).
27. Cravillon, J. *et al.* Controlling zeolitic imidazolate framework nano- and microcrystal formation: insight into crystal growth by time-resolved *in situ* static light scattering. *Chem. Mater.* **23,** 2130–2141 (2011).
28. Cravillon, J. *et al.* Formate modulated solvothermal synthesis of ZIF-8 investigated using time-resolved *in situ* X-ray diffraction and scanning electron microscopy. *CrystEngComm* **14,** 492–498 (2012).
29. Pan, Y. *et al.* Tuning the crystal morphology and size of zeolitic imidazolate framework-8 in aqueous solution by surfactants. *CrystEngComm* **13,** 6937–6940 (2011).
30. de Graaf, J., van Roij, R. & Dijkstra, M. Dense regular packings of irregular nonconvex particles. *Phys. Rev. Lett.* **107,** 155501 (2011).
31. Filion, L. *et al.* Efficient method for predicting crystal structures at finite temperature: variable box shape simulations. *Phys. Rev. Lett.* **103,** 188302 (2009).
32. Ahles, M. *et al.* Spectroscopic ellipsometry on opaline photonic crystals. *Opt. Commun.* **246,** 1–7 (2005).
33. Zhang, K. *et al.* Alcohol and water adsorption in zeolitic imidazolate frameworks. *Chem. Commun.* **49,** 3245–3247 (2013).
34. Schaate, A. *et al.* Modulated synthesis of Zr-based metal–organic frameworks: from nano to single crystals. *Chem. Eur. J.* **17,** 6643–6651 (2011).
35. Vermoortele, F. *et al.* Synthesis modulation as a tool to increase the catalytic activity of metal–organic frameworks: the unique case of UiO-66(Zr). *J. Am. Chem. Soc.* **135,** 11465–11468 (2013).
36. Wu, H. *et al.* Unusual and highly tunable missing-linker defects in zirconium metal–organic framework UiO-66 and their important effects on gas adsorption. *J. Am. Chem. Soc.* **135,** 10525–10532 (2013).


## Acknowledgements

This work was supported by EU FP7 ERC-Co 615954, the Spanish MINECO (projects PN MAT2015-65354-C2-1-R and MAT2015-68075-R [SIFE2]) and the Comunidad de Madrid project S2013/MIT-2740 (PHAMA_2.0). It was also funded by the CERCA Programme/Generalitat de Catalunya. The authors based at ICN2 and ICMAB acknowledge the support of the Spanish MINECO through the Severo Ochoa Centers of Excellence Program (grants SEV-2013-0295 and SEV-2015-0496). The authors thank J. Albalad and J. Saiz for their help in the TGA and reflectance measurements, respectively.

## Author contributions

C.A. and I.I. synthesized the ZIF-8 particles and the corresponding self-assembled superstructures. A.C.-S. synthesized the UiO-66 particles and the corresponding self-assembled superstructures. N.T. and M.D. performed the Floppy-Box Monte Carlo simulations. C.A., J.A.P., A.B. and C.L. performed and analysed the photonic measurements. M.I.A. performed the ellipsometry characterization, and C.A. and J.P.-C. performed the sorption measurements. D.M. conceived the project and drafted the manuscript. All authors discussed the results and commented on the manuscript.

## Additional information

Supplementary information is available in the online version of the paper. Reprints and permissions information is available online at www.nature.com/reprints. Publisher's note: Springer Nature remains neutral with regard to jurisdictional claims in published maps and institutional affiliations. Correspondence and requests for materials should be addressed to C.L. and D.M.

## Competing financial interests

The authors declare no competing financial interests.

nature chemistry

SUPPLEMENTARY INFORMATION

DOI: 10.1038/NCHEM.2875

In the format provided by the authors and unedited.

# Self-assembly of polyhedral metal–organic framework particles into three-dimensional ordered superstructures

Civan Avci, Inhar Imaz, Arnau Carné-Sánchez, Jose Angel Pariente, Nikos Tasios, Javier Pérez-Carvajal, Maria Isabel Alonso, Alvaro Blanco, Marjolein Dijkstra, Cefe Lopez, and Daniel Maspoch

# INDEX

**Supplementary Section 1: Characterisation**……..……5

A. Materials……...5

B. Instrumentation…….5

C. Guest Sorption Measurements……...……...……6

Supplementary Figure 1. Simulated (black) and synthesised XRPD patterns of ZIF-8 particles of different sizes: 178 ± 8 nm (blue); 193 ± 8 nm (green); 210 ± 10 nm (red); and 227 ± 10 nm (purple)……7

Supplementary Figure 2. Representative $N_2$ sorption isotherm of the synthesised ZIF-8 with a particle size of 210 ± 10 nm……...8

Supplementary Figure 3. Representative FE-SEM images of well-ordered superstructures self-assembled from ZIF particles of different sizes: a) 178 ± 8 nm; b) 193 ± 8 nm; and c) 227 ± 10 nm. Scale bars: 5 μm (left column) and 2 μm (right column)……9

Supplementary Figure 4. Representative FE-SEM images of the self-assembled superstructures obtained using different techniques: a) evaporation at RT; b) evaporation at 100 $^{o}$C; c) spin coating; d) dip coating; and e) vertical deposition. Scale bars: 10 μm (left column) and 5 μm (right column)……10

Supplementary Figure 5. a) Photograph of the self-assembled superstructures resulting from the centrifugation of an aqueous colloidal solution of ZIF-8 particles of different sizes. Note here the opalescence visible to the naked eye, which confirms a certain degree of ordering in these structures. b) Representative FE-SEM image of self-assembled superstructures resulting from this centrifugation step. Scale bars: 1 μm (b, left) and 5 μm (b, right)……...11

Supplementary Figure 6. Optical reflectance at θ = 0º for the photonic crystals made of TRD ZIF-8 particles of different sizes: 178 ± 8 nm (blue); 193 ± 8 nm (green); 210 ± 10 nm (yellow); and 227 ± 10 nm (red)……12

Supplementary Figure 7. Measured ellipsometric magnitudes (symbols) at several angles of incidence φ for the as-made photonic crystal made of TRD ZIF-8 particles sized 210 ± 10 nm, compared to the fittings, from which a refractive index *n* of 1.432 was deduced. Only the measured wavelength range (620 nm to 1030 nm) in which the material can be considered an effective medium is shown. (a) tan ψ and (b) cos Δ. The roughness-layer thickness obtained from the fitting was 64 ± 2 nm……..13

Supplementary Figure 8. Linear relation (r = 0.998) between the edge length *x* and the chamfer *w* of the different synthesised TRD ZIF-8 particles……..14

Supplementary Figure 9. TGA of the as-made (red) and activated (blue) photonic crystal made of TRD ZIF-8 particles sized 210 ± 10 nm……15

Supplementary Figure 10. (a,b) FE-SEM images of the activated photonic crystal made of TRD ZIF-8 particles sized 210 ± 10 nm. (c,d) FE-SEM images of the photonic crystal after alcohol adsorption experiments. Scale bars: 5 μm (a,c,d) and 3 μm (b)……16

Supplementary Figure 11. Representative $N_2$ sorption isotherm of the photonic crystal made of TRD ZIF-8 particles sized 210 ± 10 nm……17

Supplementary Figure 12. Optical reflectance at θ = 0º for the as-made and activated photonic crystal made of TRD ZIF-8 particles sized 210 ± 10 nm……18

Supplementary Figure 13. Optical reflectance at θ = 0º for the photonic crystal made of TRD ZIF-8 particles sized 210 ± 10 nm: as-made (light green), activated (black), and after exposure of the latter to MeOH (red), EtOH (blue), *i*-PrOH (violet), or *n*-BuOH (dark green)……...19

Supplementary Figure 14. Optical reflectance at θ = 0º for the photonic crystal made of TRD ZIF-8 particles sized 210 ± 10 nm: activated (black), and after exposure to water (blue)……20

Supplementary Figure 15. Alcohol and water sorption isotherms of the photonic crystal made of TRD ZIF-8 particles sized 210 ± 10 nm……21

Supplementary Figure 16. Measured ellipsometric quantities (symbols) at several angles of incidence φ for the activated photonic crystal made of TRD ZIF-8 particles sized 210 ± 10 nm compared to the fittings from which the refractive index $n$ = 1.40 was deduced for the activated sample. Only the measured wavelength range (620 nm to 1030 nm) in which the material can be considered an effective medium is shown. (a) tan ψ, (b) cos Δ. The roughness-layer thickness obtained from these fits was 87 ± 8 nm……22

Supplementary Figure 17. Representative FE-SEM images of (a,b) TRD ZIF-8 particles with $t$ = 0.57; (e,f) TRD ZIF-8 particles with $t$ = 0.38; (i,j) RD ZIF-8 particles; and (m,n) octahedral UiO-66 particles. Scale bars: 3 μm (a,e,i,m) or 500 nm (b,f,j,n). Size-distribution histograms of (c) TRD ZIF-8 particles with $t$ = 0.57; (g) TRD ZIF-8 particles with $t$ = 0.38; (k) RD ZIF-8 particles; and (o) octahedral UiO-66 particles. Simulated (black) and synthesised XRPD patterns of (d) TRD ZIF-8 particles with $t$ = 0.57; (h) TRD ZIF-8 particles with $t$ = 0.38; (l) RD ZIF-8 particles; and (p) octahedral UiO-66 particles……...……23

Supplementary Figure 18. Additional FE-SEM images of the self-assembled superstructures made of (a,b) TRD ZIF-8 particles with $t$ = 0.57; (c,d) TRD ZIF-8 particles with $t$ = 0.38; and (i,f) octahedral UiO-66 particles. Scale bars: 10 μm (c), 3 μm (a,e), 2 μm (b), and 1 μm (d,f)……24

Supplementary Figure 19. $N_2$ sorption isotherm of the plastic crystal made of TRD ZIF-8 particles with $t$ = 0.57……..25

Supplementary Figure 20. $N_2$ sorption isotherm of the ordered superstructure made of RD ZIF-8 particles……26

Supplementary Figure 21. $N_2$ sorption isotherm of the ordered superstructure made of octahedral UiO-66 particles……27

**Supplementary Section 2: Determination of the Effective Refractive Indexes and Shifts of the Photonic Band Gaps**……28

A. Effective refractive index of the dense ZIF-8 framework……28

B. Effective refractive index of the as-made (water-loaded) photonic crystal……29

C. Shifts in the band gaps of the photonic crystals upon exposure to alcohols……...30

Supplementary Table 1: Experimental and calculated refractive indices and band gaps of the as-made photonic crystal (particle size: 210 ± 10 nm) before evacuation and subsequent exposure to different alcohols……...31

References……...31

## Supplementary Section 1: Characterisation

**A. Materials.** All chemical reagents and solvents were purchased from Sigma Aldrich and used as received without further purification. Deionised (DI) $H_2O$ was obtained from a Milli-Q water purification system.

**B. Instrumentation.** Field-emission scanning electron microscopy (FE-SEM) images were collected on a scanning electron microscope (FEI Magellan 400L XHR) at an acceleration voltage of 1.0 kV, using conductive carbon tape. The size of crystals was calculated from FE-SEM images by averaging the distance of a {100} facet to its opposite {100} facet of 200 particles from images of different areas of the same samples. X-ray powder diffraction (XRPD) measurements were made on an X'Pert PRO MPD diffractometer (Panalytical), with $\lambda_{Cu}$ = 1.5406 Å. The surface charge of MOF particles (expressed as zeta potential ($\zeta$)) was measured using a Malvern Zetasizer, (Malvern Instruments, UK). Volumetric $N_2$ sorption measurements were collected at 77 K using an ASAP 2020 HD gas adsorption system (Micromeritics). The reflectance spectra were taken with a Hyperion 2000 FT-IR microscope coupled to a Vertex 80 Spectrometer (both from Bruker) with a 15× Schwarzschild standard objective, tungsten lamp (in the Vertex 80) and a Si-diode detector. Thermogravimetric analysis (TGA) measurements were performed under a nitrogen flow heating from 30ºC to 700ºC at a heating rate of 10ºC/min using a Pyris 8000 Thermo Gravimetric Analyzer. Ellipsometry measurements were made on a GES5E rotating polariser ellipsometer (SOPRALAB) at six angles of incidence: from 45º to 70º (at intervals of 5º) in a spectral range from *ca.* 230 nm to 1030 nm. The effective refractive index was evaluated for wavelengths that did not fulfil the Bragg condition. Since Bragg-like reflection features in the investigated self-assembled superstructure appeared in the wavelength range below 580 nm, we restricted the analysis of ellipsometry data to longer wavelengths (from 620 nm to 1030 nm). Moreover, as the sample surface was obviously rough, we included the roughness layer to model the ellipsometry data in a standard way. In order to compare the results to those from reflectometry, we considered a constant isotropic effective refractive index. The best-fit results for the as-made and activated photonic crystals exhibited constant refractive indexes of $n$ = 1.43 and 1.40, respectively. The roughness-layer thicknesses obtained from the fits were 64 ± 2 nm and 87 ± 8 nm in fair agreement with the step height ($w$) present in the stacking.

**C. Guest sorption measurements.** In order to track *in-situ* the change in band gap of the photonic crystal upon water evacuation, and alcohol and water sorption, we designed and assembled a custom vapour chamber. For the water evacuation, the as-prepared photonic crystal made from 210 nm TRD ZIF-8 particles was first activated in an oven at 260 $^{o}$C for 30 min, and then placed in a glass chamber that comprised a glass cuvette (used for UV-Vis spectroscopy) and a rubber sealing. A spectrum was collected from the activated sample. Then, the alcohol of interest or water was put in a separate bottle that had two plastic tubes on its cap. One end of the first tube was dipped into the alcohol/water and the other end was connected to the gas source that was used for bubbling the alcohol/water. The second tube in the bottle was used for transferring the alcohol/water vapours to the sample chamber. The alcohol/water vapours passed through the sample chamber by continuous air bubbling of the alcohol/water. In order to complete the vapour flow, we pierced the rubber sealing of the sample chamber with an empty needle. For the adsorption, the bubbling continued until (depending on the alcohol) the photonic superstructure did not exhibit any further shift in the band gap. Desorption was performed by purging with air the chamber until the band gap shifted back to its initial position of 522 nm. Additional heating (120 $^{o}$C for 10 min) in the oven was necessary in the cases of *i*-PrOH and *n*-BuOH, as the desorption of each was relatively slower than that of MeOH or EtOH.

**Supplementary Figure 1.** Simulated (black) and synthesised XRPD patterns of ZIF-8 particles of different sizes: 178 ± 8 nm (blue); 193 ± 8 nm (green); 210 ± 10 nm (red); and 227 ± 10 nm (purple).

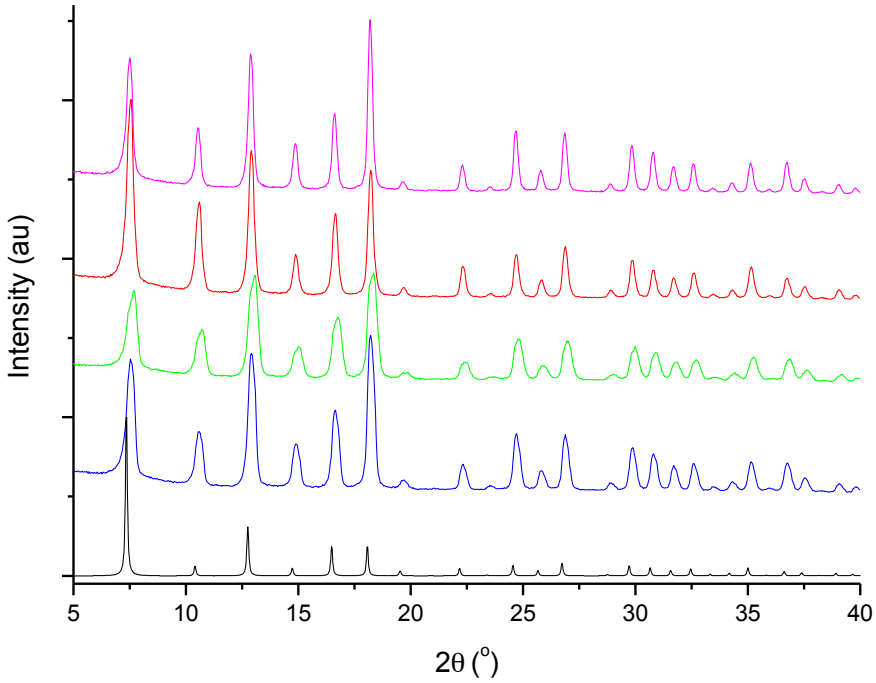

**Supplementary Figure 2.** Representative $N_2$ sorption isotherm of the synthesised ZIF-8 with a particle size of 210 ± 10 nm.

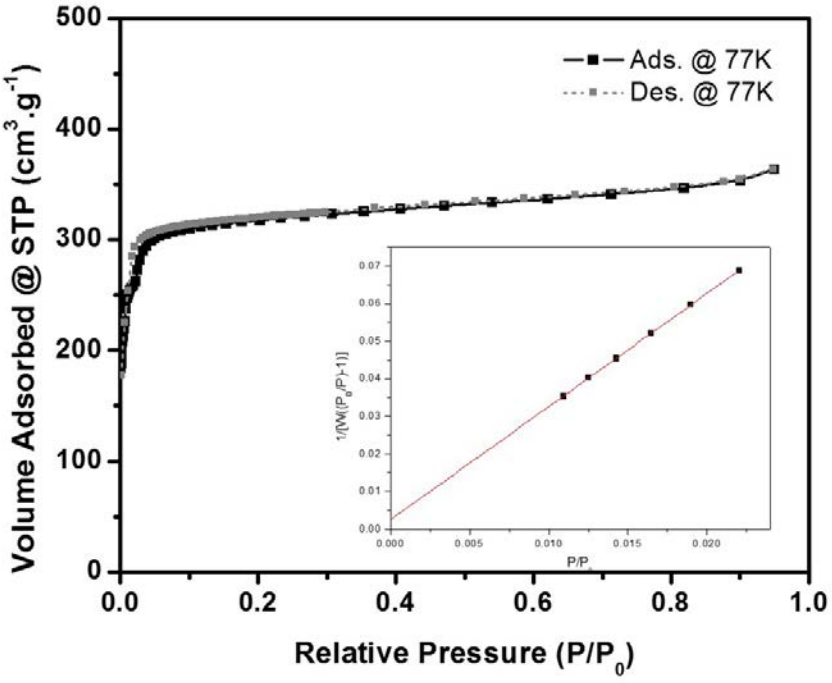


**Surface area** = 1154 m²/g

**Slope** = 3.013

**Intercept** = 2.469e-03

**Correlation coefficient, r** = 0.999954

**C constant** = 1221

**Pore volume** = 0.50 $cm^3/g$

**Supplementary Figure 3.** Representative FE-SEM images of well-ordered superstructures self-assembled from ZIF particles of different sizes: a) 178 ± 8 nm; b) 193 ± 8 nm; and c) 227 ± 10 nm. Scale bars: 5 μm (left column) and 2 μm (right column).

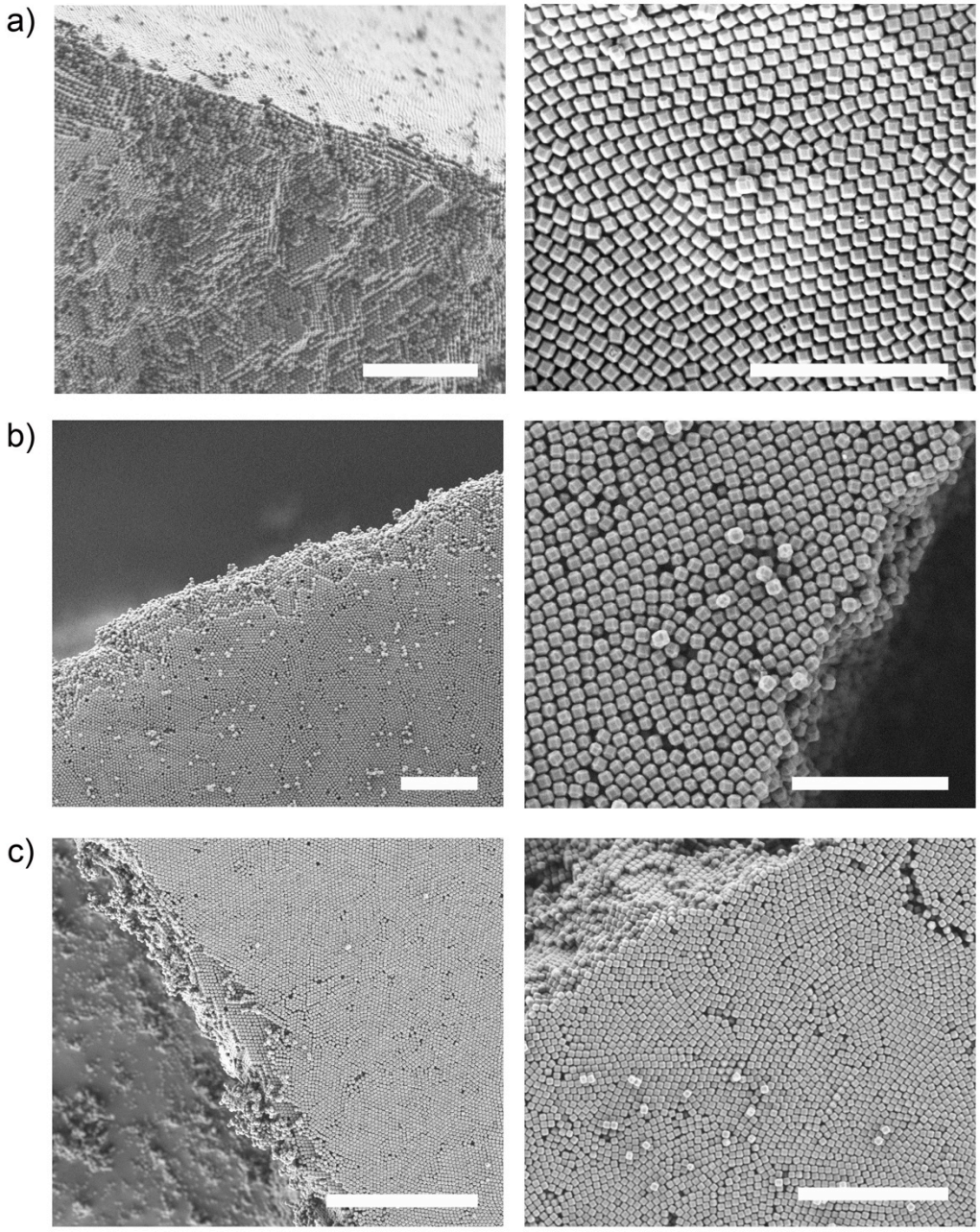

**Supplementary Figure 4.** Representative FE-SEM images of the self-assembled superstructures obtained using different techniques: a) evaporation at RT; b) evaporation at 100 $^{o}$C; c) spin coating; d) dip coating; and e) vertical deposition. Scale bars: 10 μm (left column) and 5 μm (right column).

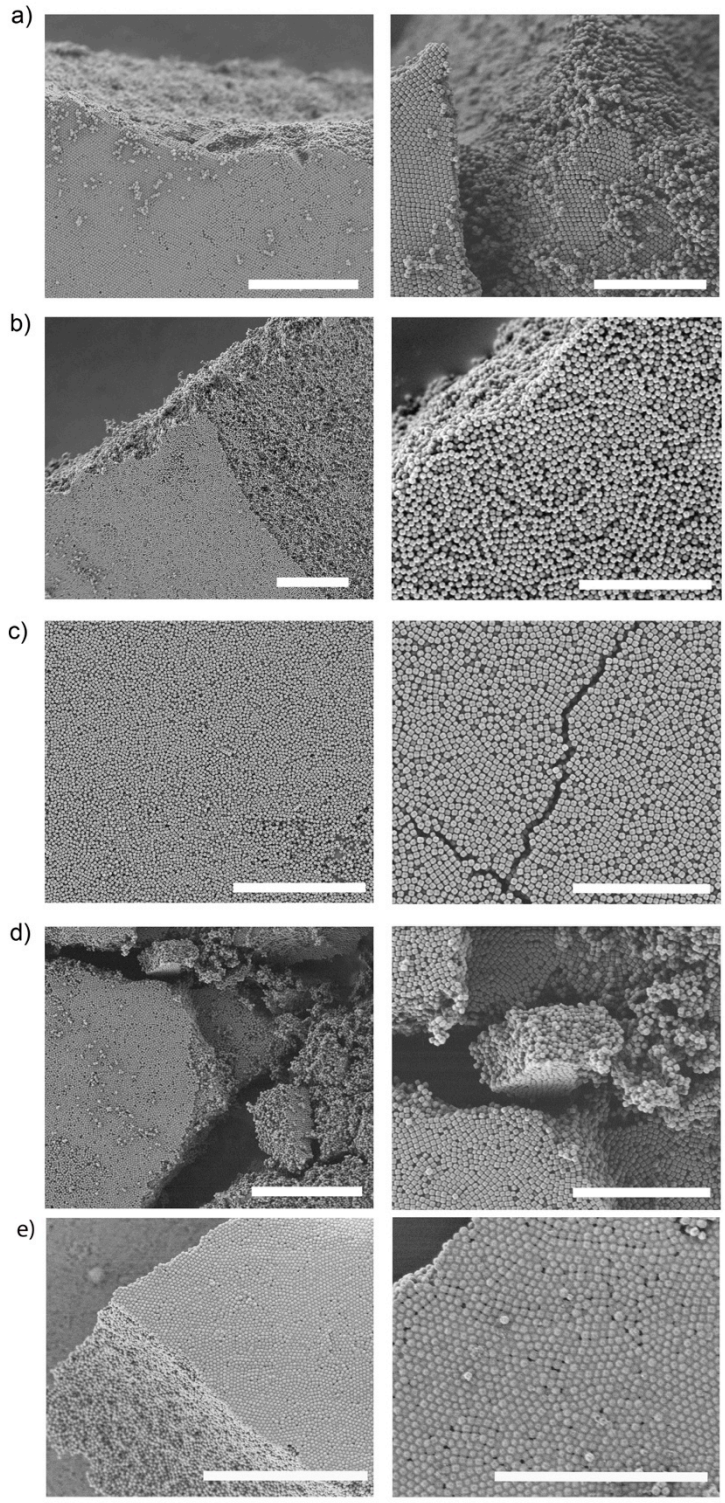

**Supplementary Figure 5.** a) Photograph of the self-assembled superstructures resulting from the centrifugation of an aqueous colloidal solution of ZIF-8 particles of different sizes. Note here the opalescence visible to the naked eye, which confirms a certain degree of ordering in these structures. b) Representative FE-SEM image of self-assembled superstructures resulting from this centrifugation step. Scale bars: 1 μm (b, left) and 5 μm (b, right).

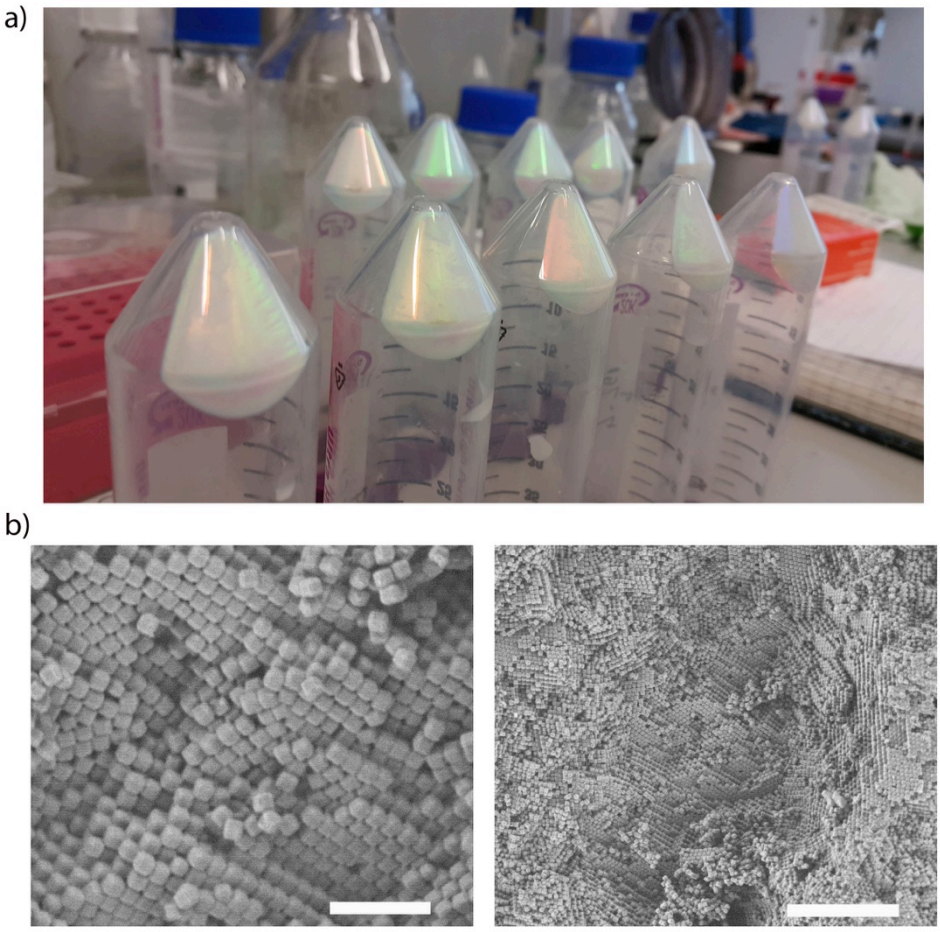

**Supplementary Figure 6.** Optical reflectance at θ = 0º for the photonic crystals made of TRD ZIF-8 particles of different sizes: 178 ± 8 nm (blue); 193 ± 8 nm (green); 210 ± 10 nm (yellow); and 227 ± 10 nm (red).

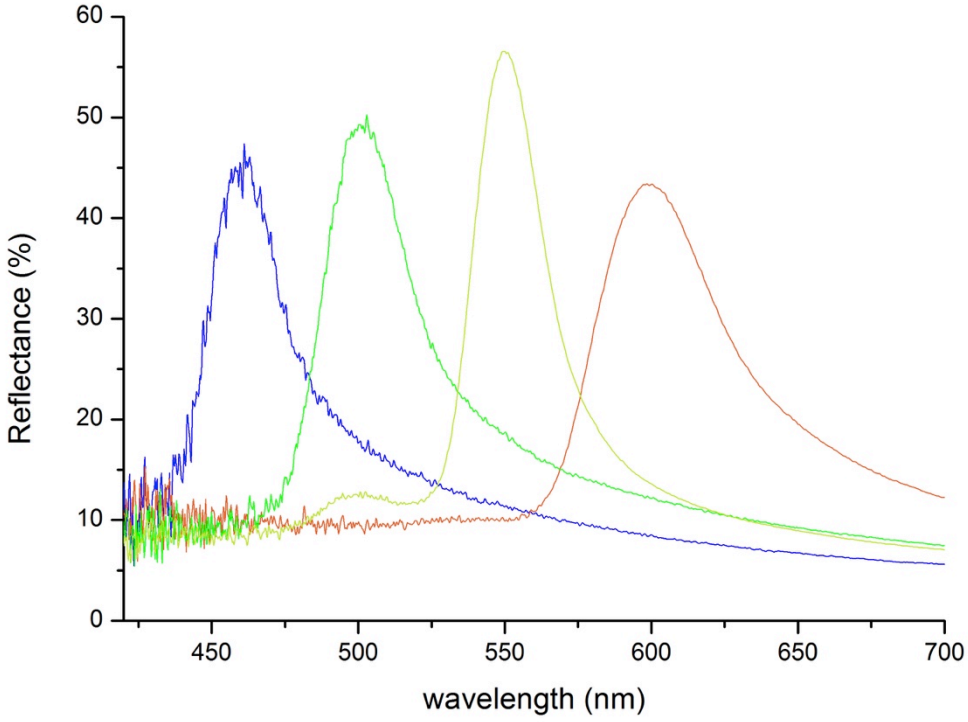

**Supplementary Figure 7.** Measured ellipsometric magnitudes (symbols) at several angles of incidence φ for the as-made photonic crystal made of TRD ZIF-8 particles sized 210 ± 10 nm, compared to the fittings, from which a refractive index *n* of 1.432 was deduced. Only the measured wavelength range (620 nm to 1030 nm) in which the material can be considered an effective medium is shown. (a) tan ψ and (b) cos Δ. The roughness-layer thickness obtained from the fitting was 64 ± 2 nm.

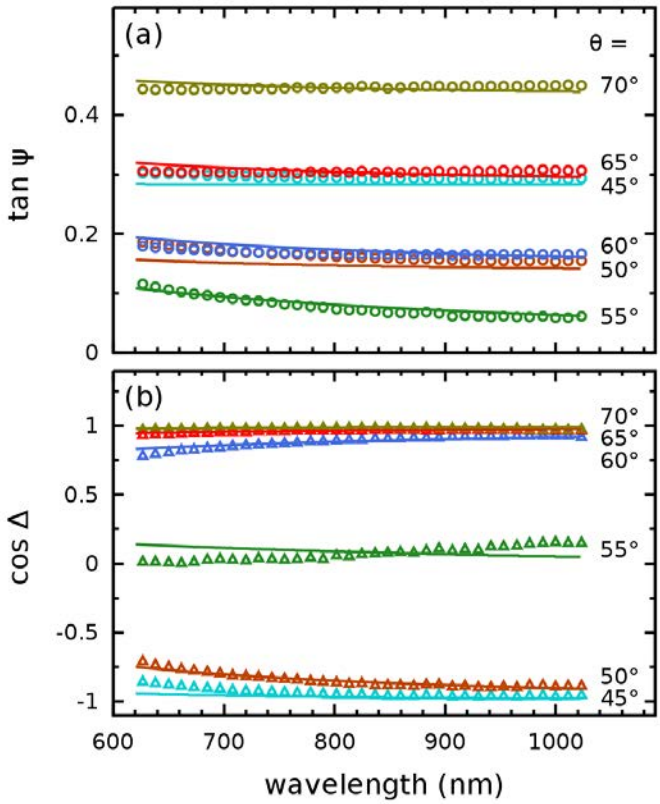

**Supplementary Figure 8.** Linear relation (r = 0.998) between the edge length *x* and the chamfer *w* of the different synthesised TRD ZIF-8 particles.

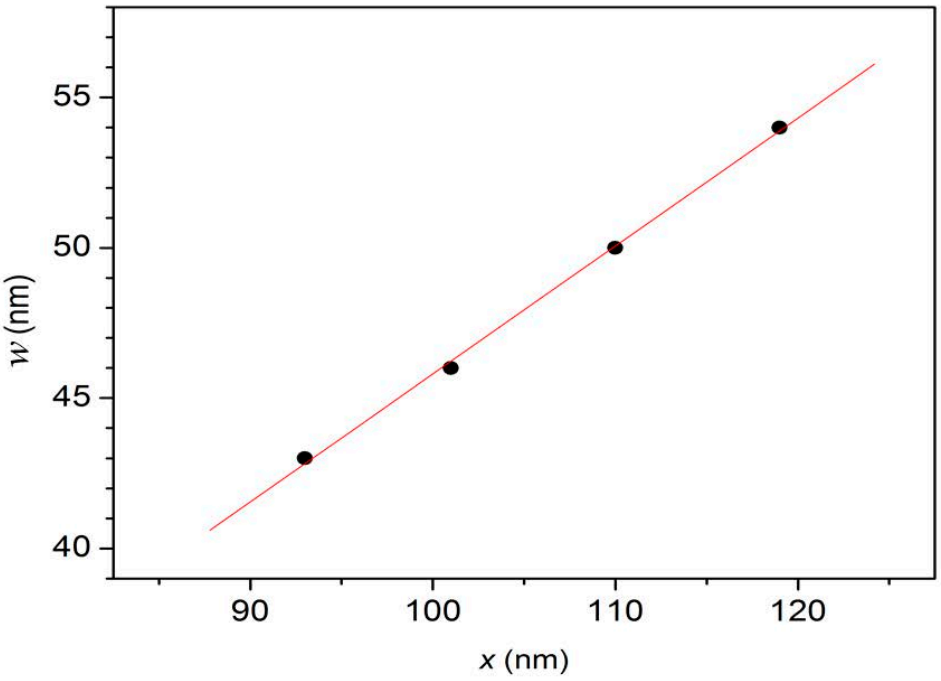

**Supplementary Figure 9.** TGA of the as-made (red) and activated (blue) photonic crystal made of TRD ZIF-8 particles sized 210 ± 10 nm.

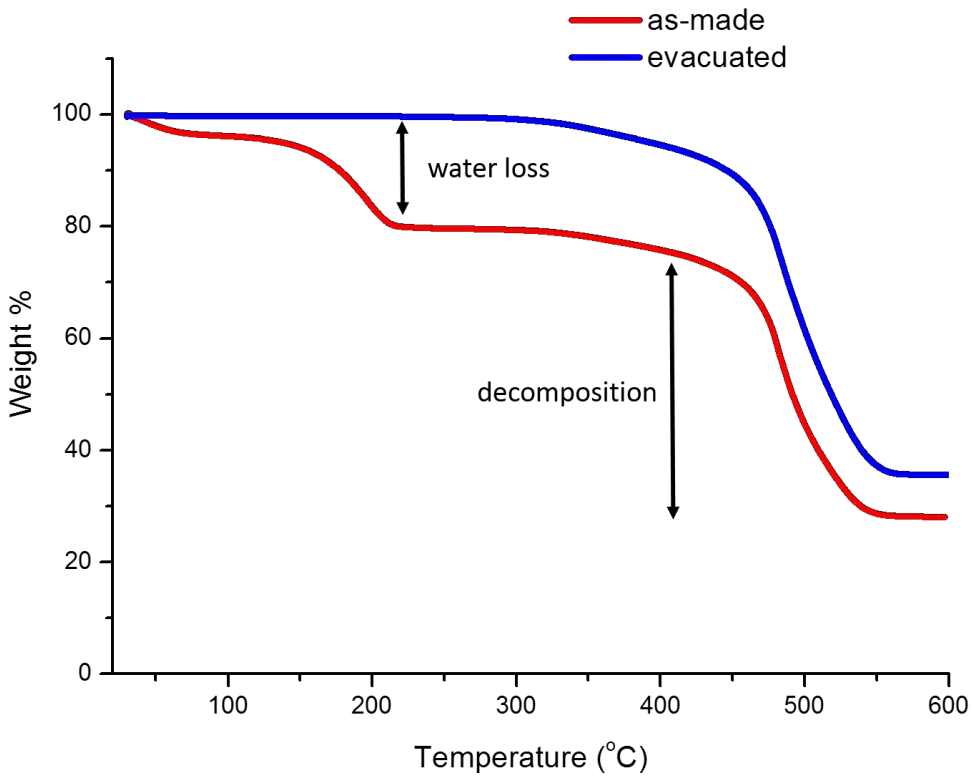

**Supplementary Figure 10.** (a,b) FE-SEM images of the activated photonic crystal made of TRD ZIF-8 particles sized 210 ± 10 nm. (c,d) FE-SEM images of the photonic crystal after alcohol adsorption experiments. Scale bars: 5 μm (a,c,d) and 3 μm (b).

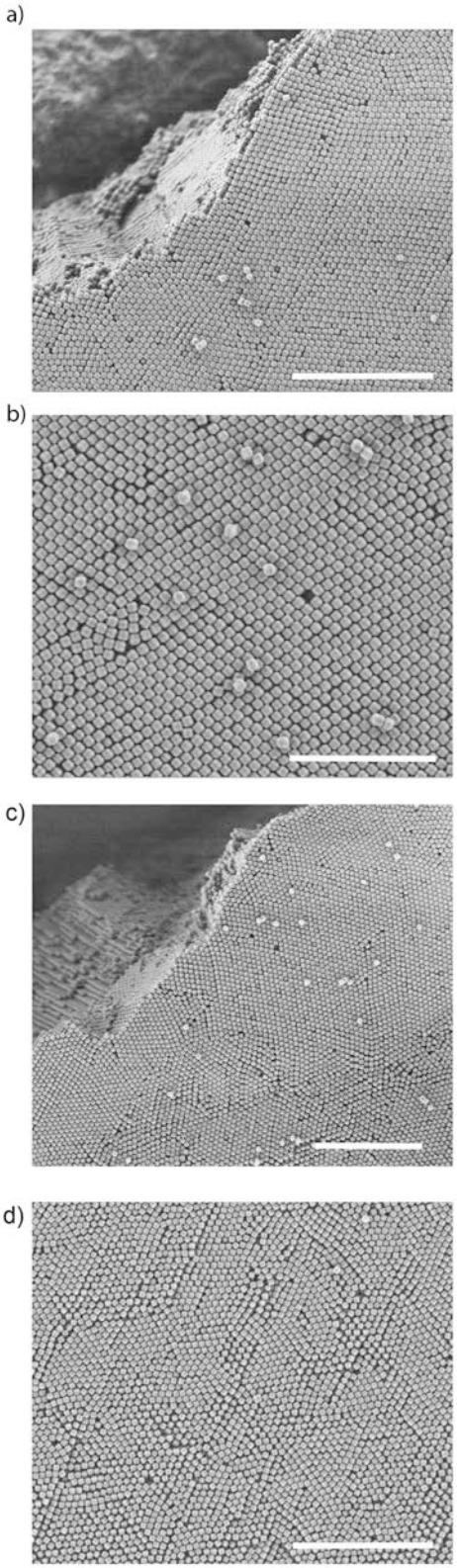

**Supplementary Figure 11.** Representative $N_2$ sorption isotherm of the photonic crystal made of TRD ZIF-8 particles sized 210 ± 10 nm.

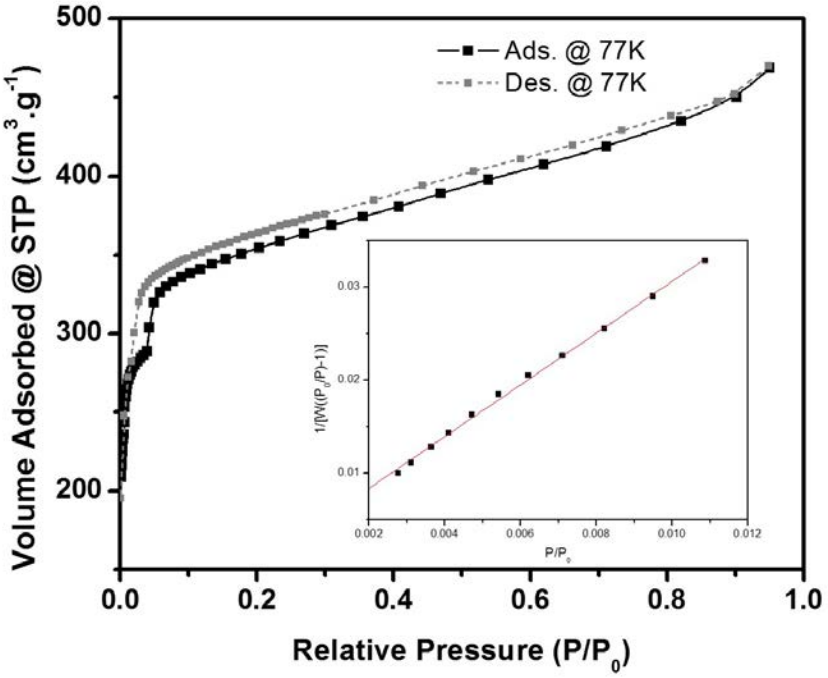


**Surface area** = 1250 m²/g

**Slope** = 2.784

**Intercept** = 2.788e-03

**Correlation coefficient, r** = 0.9989

**C constant** = 999

**Pore volume** = 0.57 $cm^3/g$

**Supplementary Figure 12.** Optical reflectance at θ = 0º for the as-made and activated photonic crystal made of TRD ZIF-8 particles sized 210 ± 10 nm.

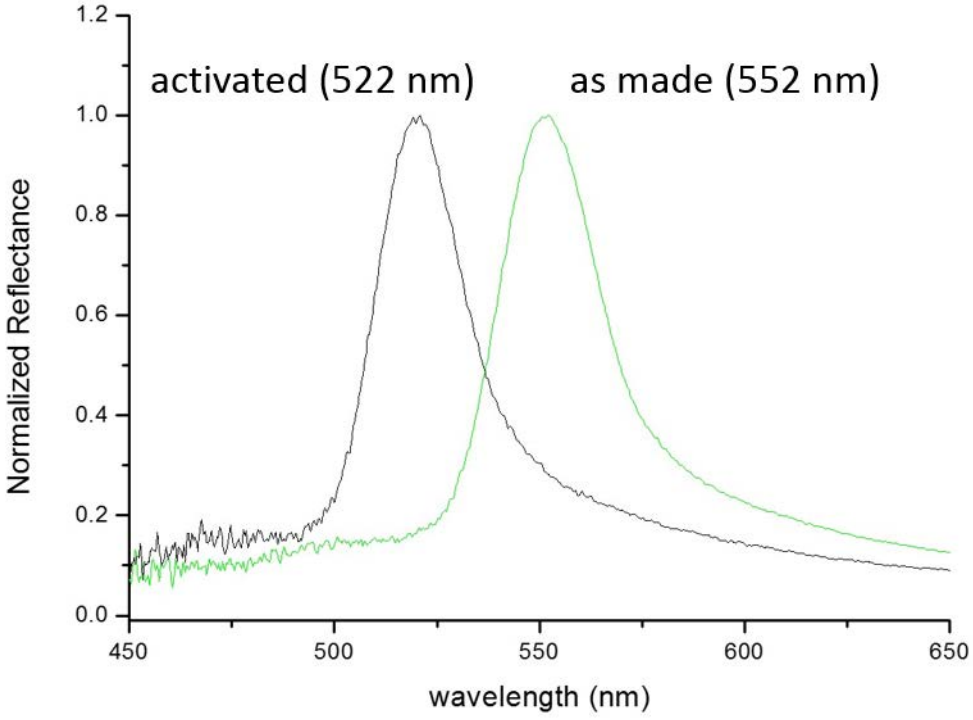

**Supplementary Figure 13.** Optical reflectance at θ = 0º for the photonic crystal made of TRD ZIF-8 particles sized 210 ± 10 nm: as-made (light green), activated (black), and after exposure of the latter to MeOH (red), EtOH (blue), *i*-PrOH (violet), or *n*-BuOH (dark green).

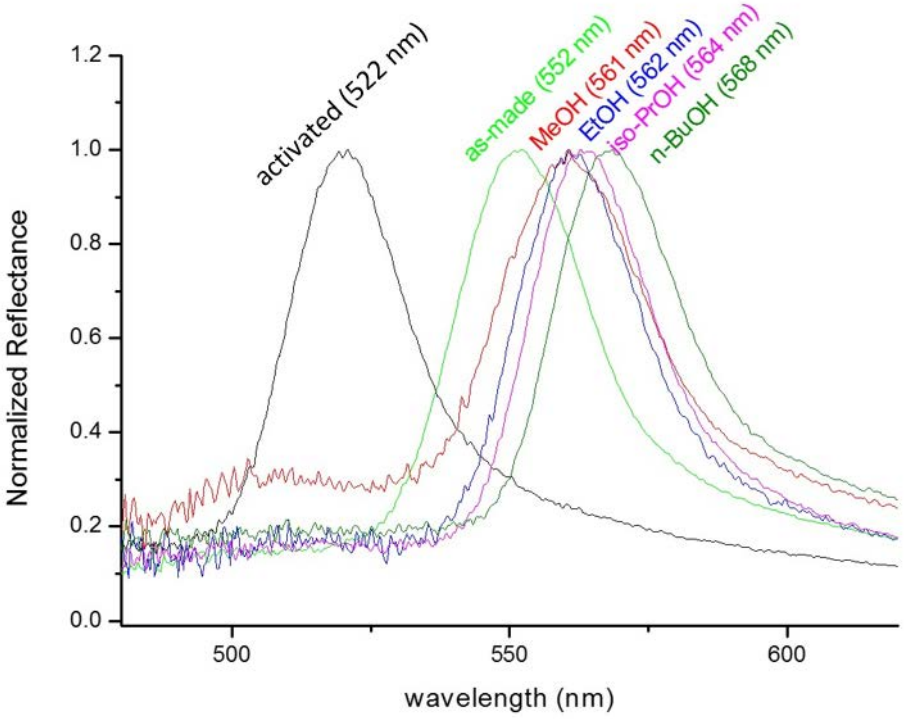

**Supplementary Figure 14.** Optical reflectance at θ = 0º for the photonic crystal made of TRD ZIF-8 particles sized 210 ± 10 nm: activated (black), and after exposure to water (blue).

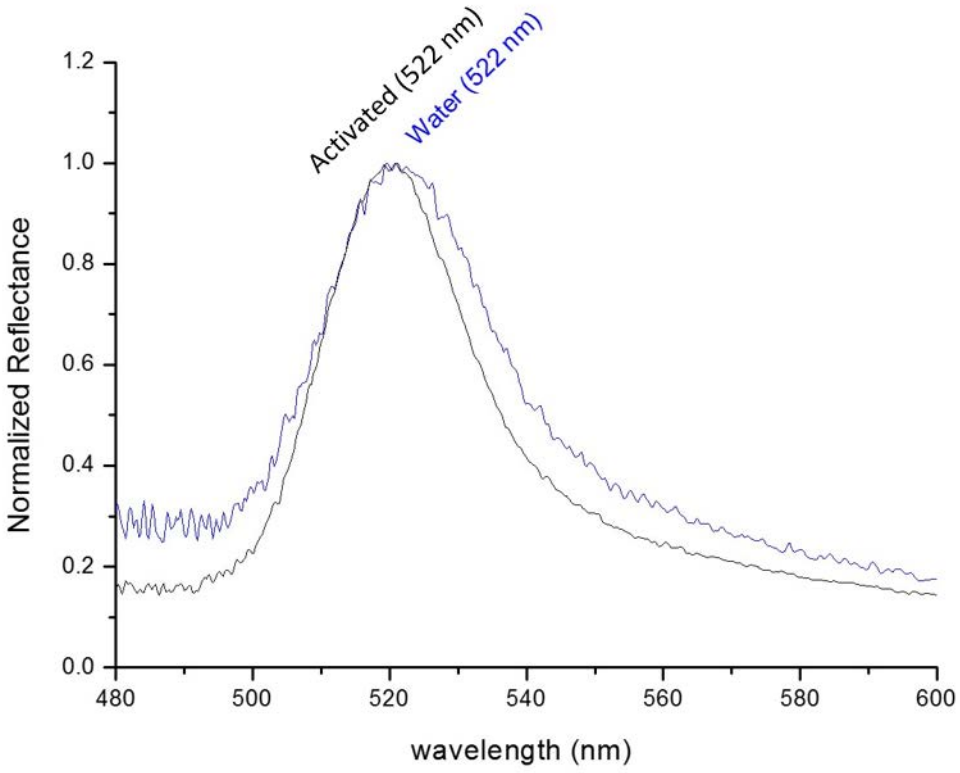

**Supplementary Figure 15**. Alcohol and water sorption isotherms of the photonic crystal made of TRD ZIF-8 particles sized 210 ± 10 nm.

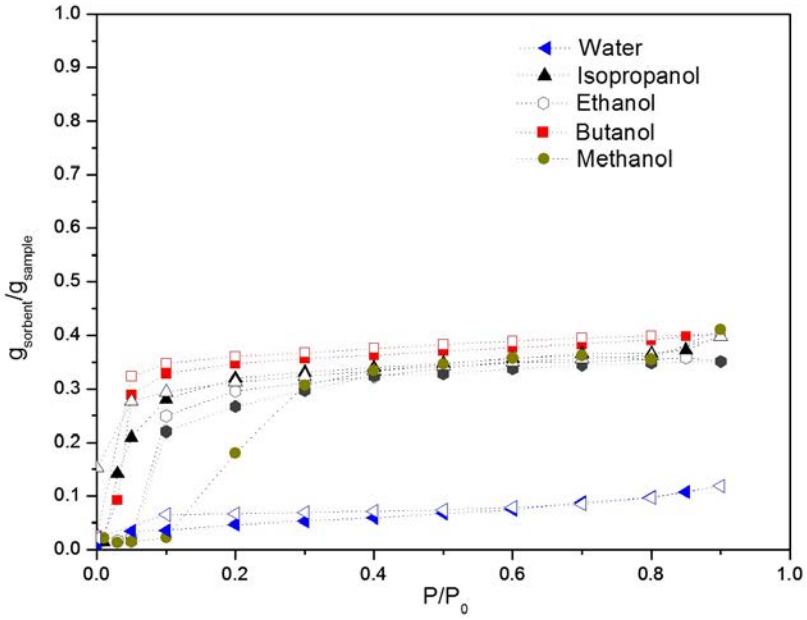

**Supplementary Figure 16.** Measured ellipsometric quantities (symbols) at several angles of incidence φ for the activated photonic crystal made of TRD ZIF-8 particles sized 210 ± 10 nm compared to the fittings from which the refractive index $n$ = 1.40 was deduced for the activated sample. Only the measured wavelength range (620 nm to 1030 nm) in which the material can be considered an effective medium is shown. (a) tan ψ, (b) cos Δ. The roughness-layer thickness obtained from these fits was 87 ± 8 nm.

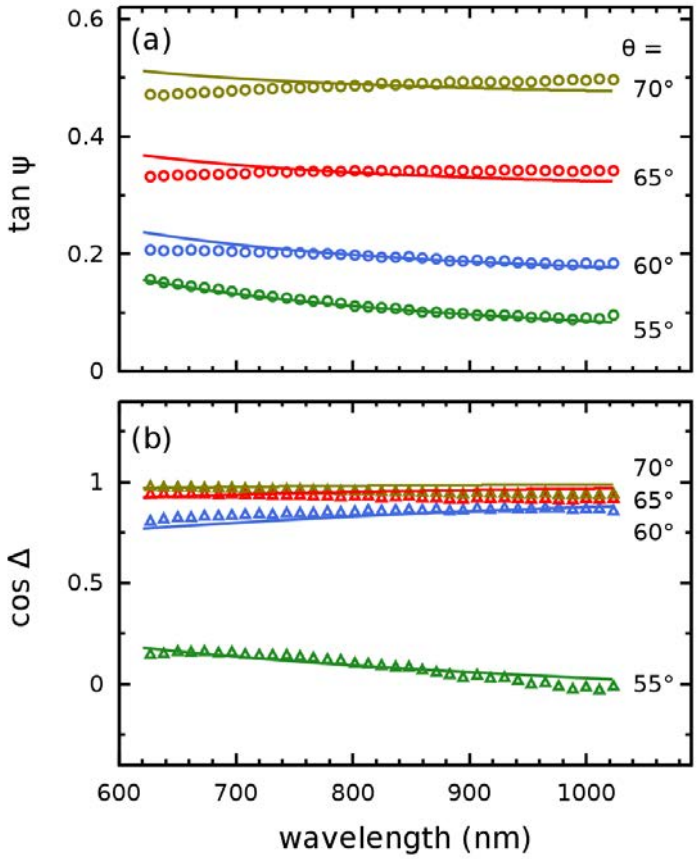

**Supplementary Figure 17.** Representative FE-SEM images of (a,b) TRD ZIF-8 particles with $t$ = 0.57; (e,f) TRD ZIF-8 particles with $t$ = 0.38; (i,j) RD ZIF-8 particles; and (m,n) octahedral UiO-66 particles. Scale bars: 3 μm (a,e,i,m) or 500 nm (b,f,j,n). Size-distribution histograms of (c) TRD ZIF-8 particles with $t$ = 0.57; (g) TRD ZIF-8 particles with $t$ = 0.38; (k) RD ZIF-8 particles; and (o) octahedral UiO-66 particles. Simulated (black) and synthesised XRPD patterns of (d) TRD ZIF-8 particles with $t$ = 0.57; (h) TRD ZIF-8 particles with $t$ = 0.38; (l) RD ZIF-8 particles; and (p) octahedral UiO-66 particles.

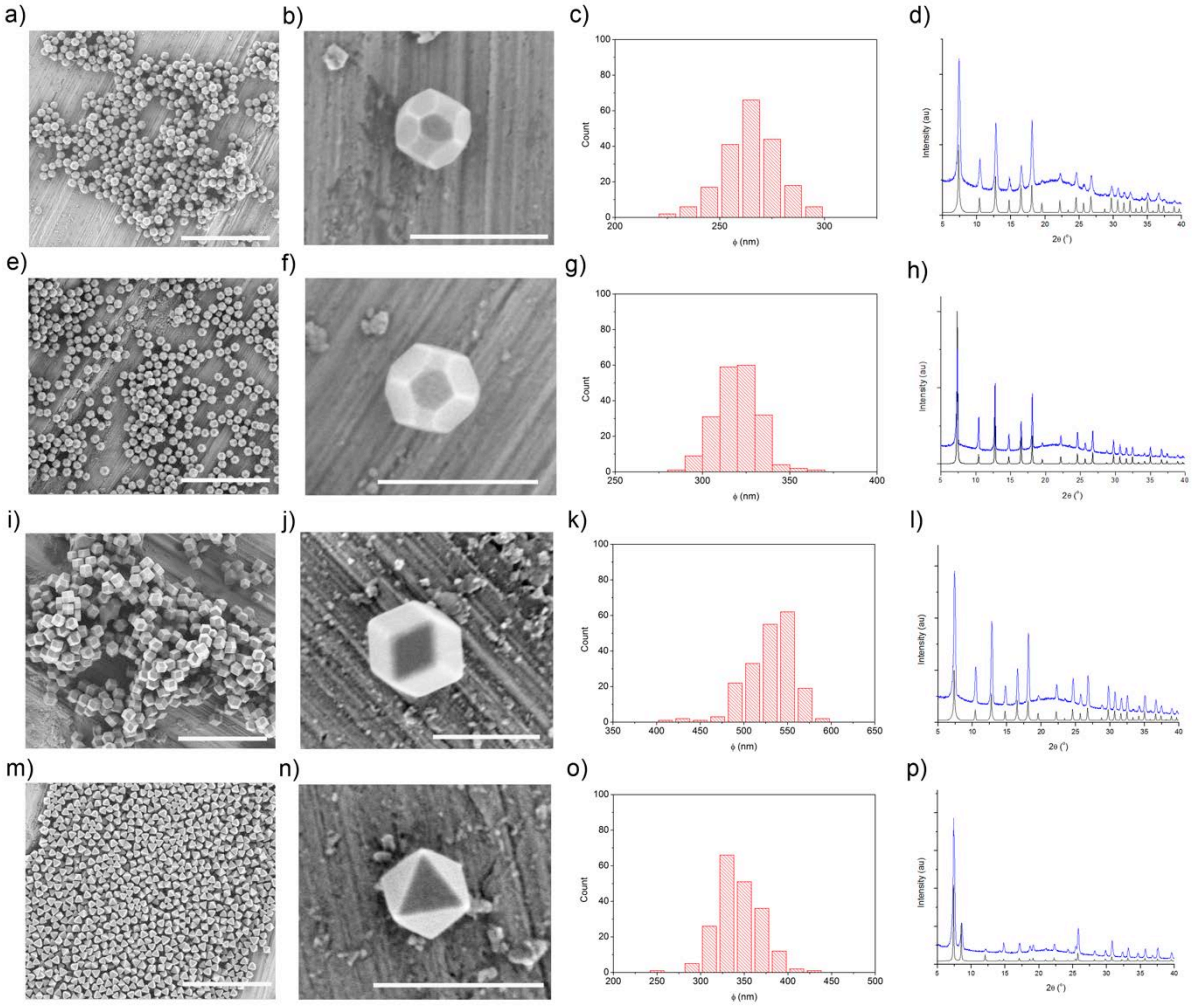

**Supplementary Figure 18.** Additional FE-SEM images of the self-assembled superstructures made of (a,b) TRD ZIF-8 particles with $t = 0.57$; (c,d) TRD ZIF-8 particles with $t = 0.38$; and (i,f) octahedral UiO-66 particles. Scale bars: 10 μm (c), 3 μm (a,e), 2 μm (b), and 1 μm (d,f).

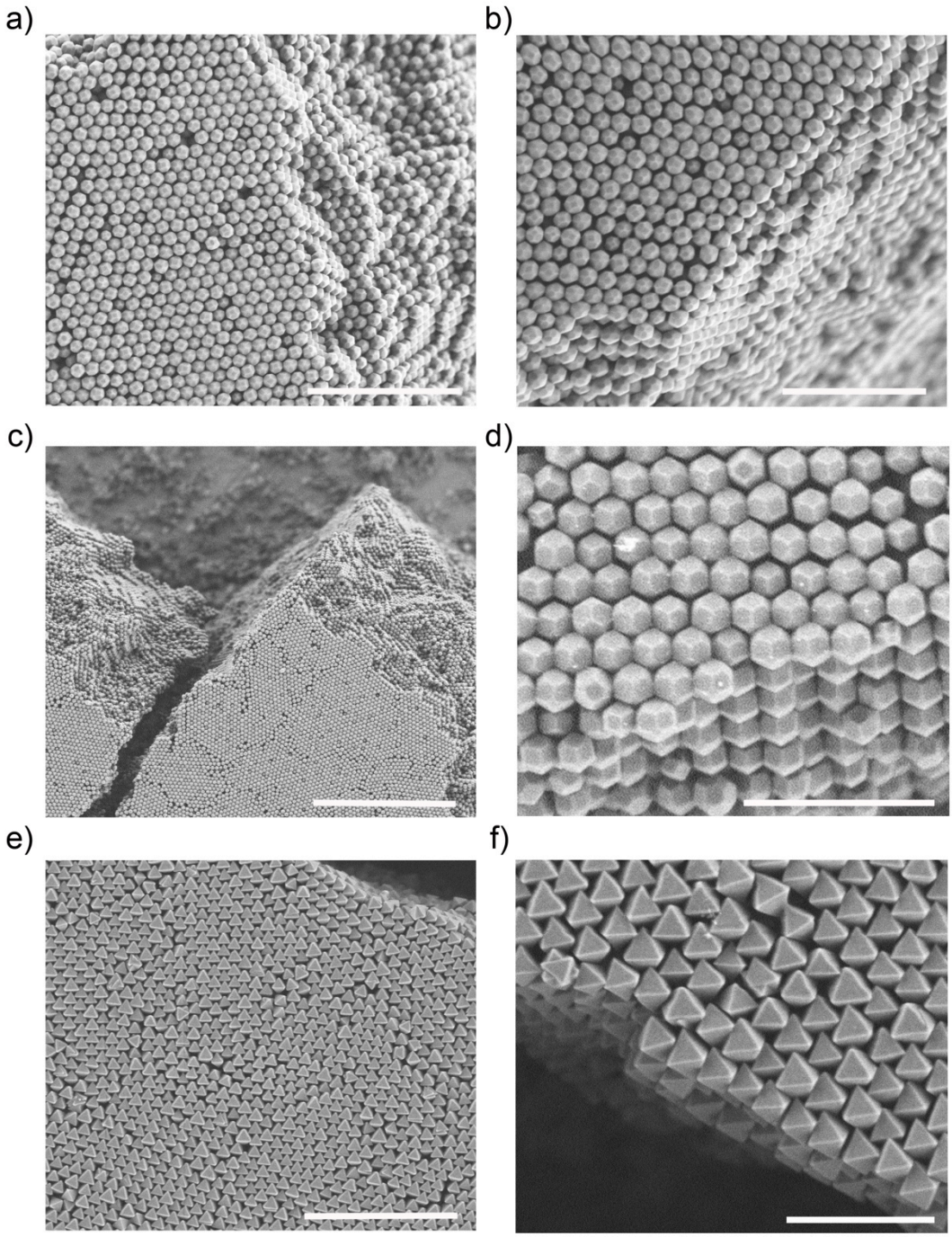

**Supplementary Figure 19.** $N_2$ sorption isotherm of the plastic crystal made of TRD ZIF-8 particles with $t = 0.57$.

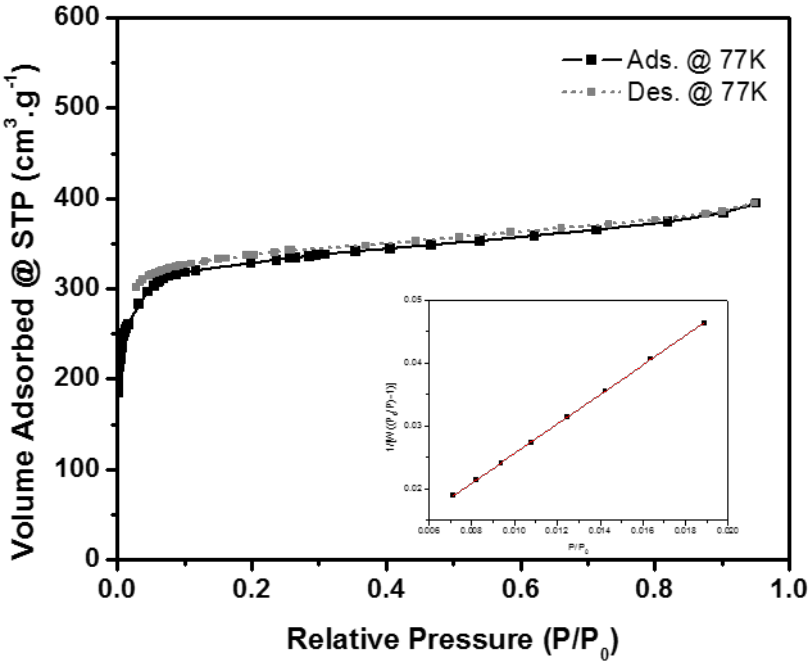


**Surface area** = 1201 m²/g

**Slope** = 2.343

**Intercept** = 2.15e-03

**Correlation coefficient, r** = 0.9999

**C constant** = 1086

**Pore volume** = 0.52 $cm^3/g$

**Supplementary Figure 20.** $N_2$ sorption isotherm of the ordered superstructure made of RD ZIF-8 particles.

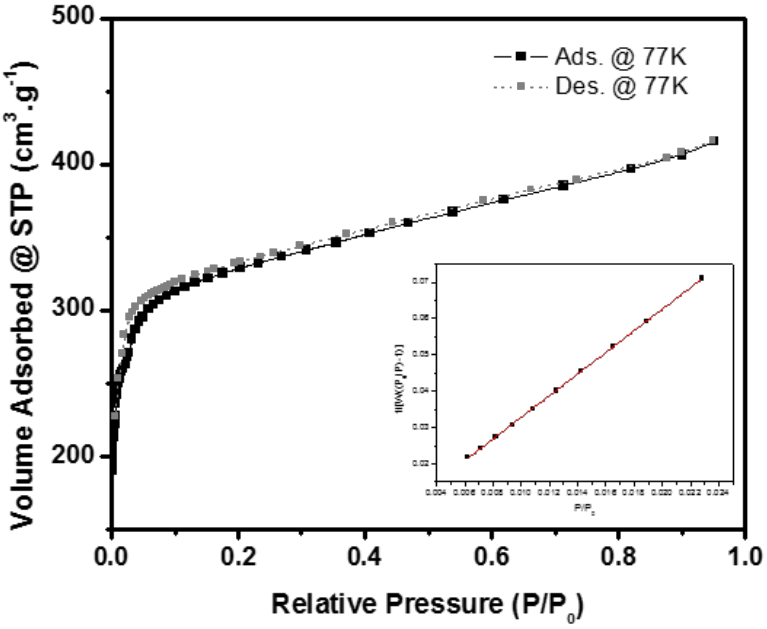


**Surface area** = 1168 m²/g

**Slope** = 2.977

**Intercept** = 2.788e-03

**Correlation coefficient, r** = 0.9999

**C constant** = 990

**Pore volume** = 0.53 $cm^3/g$

**Supplementary Figure 21.** $N_2$ sorption isotherm of the ordered superstructure made of octahedral UiO-66 particles.

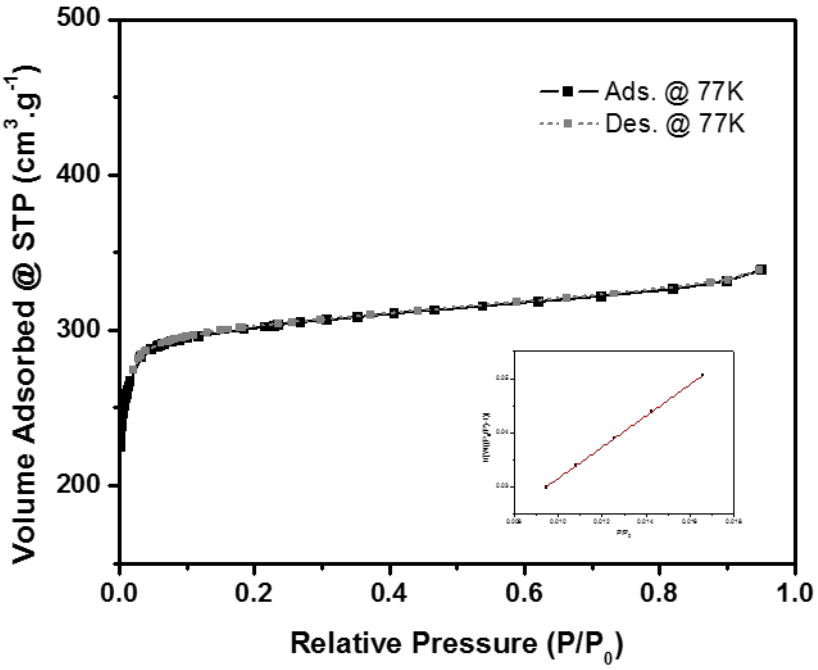


**Surface area** = 1240 m²/g

**Slope** = 2.827

**Intercept** = 0.033

**Correlation coefficient, r** = 0.9999

**C constant** = 835

**Pore volume** = 0.47 $cm^3/g$

## Supplementary Section 2: Determination of the Effective Refractive Indexes and Shifts of the Photonic Band Gaps

### A. Effective refractive index of the dense ZIF-8 framework

In order to calculate the theoretical shifts of the band gap of the photonic crystal made of TRD ZIF-8 particles (size: 210 ± 10 nm) due to the inclusion of guest molecules, we first determined the effective refractive index of the dense ZIF-8 framework ($n_{fram}$) without considering the pores. To do this, we determined the effective refractive index of the activated photonic crystal using the Bragg-Snell law (Equation 1):

$$\lambda_{activated} = 2dn_{activated} \quad (1)$$

where $\lambda_{activated}$ is 522 nm (as measured from the reflectance spectra; Figure S8) and $d$ is the interplanar distance of 184 nm. The effective refractive index $n_{activated}$, which corresponds to the photonic crystal free of water, was found to be 1.42. This value is in good agreement with the value (1.40) obtained by spectroscopic ellipsometry performed on the activated photonic crystal self-assembled from 210-nm TRD ZIF-8 particles (Supplementary Fig. S16).

We then calculated the occupancy of the interparticle voids in the photonic crystal according to Equation 2:

$$V_{void} = 1 - f \quad (2)$$

where $f$ is the packing fraction of the rhombohedral packing ($f$ = 0.86) and $V_{void}$ is 0.14. Owing to their porous nature, ZIF-8 crystals comprise the solid framework and the micropores. The theoretical micropore volume of ZIF-8 is 0.54 $cm^3/g$, which corresponds to a volumetric occupancy of 50%. From the $N_2$ sorption isotherm of the photonic crystal, we measured a pore volume of 0.57 $cm^3/g$, which is quite close to this theoretical value. Accordingly, in the photonic crystal the fraction of volume that corresponds to the dense ZIF-

8 framework ($V_{fram}$) is 0.43; that which corresponds to accessible micropores ($V_{micro}$), is also 0.43; and that representing interparticle voids ($V_{void}$), is 0.14. Combining the volume fractions for the micropores and the interparticle voids, and considering then that the resulting space is filled with air, yields an air-volume fraction ($V_{air}$) of 0.57 in the photonic crystal.

The effective refractive index of the activated photonic crystal can also be calculated according to Equation 3:

$$n_{activated} = \sqrt{V_{fram} n_{fram}^2 + V_{air} n_{air}^2} \quad (3)$$

where $n_{air}$ is 1.00.[1] From this equation, the effective refractive index of the dense ZIF-8 framework ($n_{fram}$) is calculated to be 1.83.

**B. Effective refractive index of the as-made (water-loaded) photonic crystal**

The TGA of the as-made photonic crystal shows that it contains 21% (w/w) water (Figure S8). Considering that the density of ZIF-8 is 0.925 g/cm$^3$,[2] this amount of water corresponds to a volume fraction of water ($V_{water}$) of 0.21 in the total photonic crystal. Therefore, the as-made photonic crystal is composed of the dense ZIF-8 framework ($V_{fram}$ = 0.43, $n_{fram}$ = 1.83), water ($V_{water}$ = 0.21, $n_{water}$ = 1.33)[3] and air ($V_{air}$ = 0.36, $n_{air}$ = 1.00). From Equation 4, the effective refractive index of the as-made photonic crystal is calculated to be 1.47 (see also Table S1).

$$n_{as\text{-}made} = \sqrt{V_{fram} n_{fram}^2 + V_{H2O} n_{H2O}^2 + V_{air} n_{air}^2} \quad (4)$$

**C. Shifts in the band gaps of the photonic crystals upon exposure to alcohols**

The alcohol sorption isotherms measured for the photonic crystal (Figure S12) revealed that it can take up to 35% (w/w) of MeOH, EtOH, or *i*-PrOH, or up to 38% (w/w) of *n*-BuOH. These uptake values are equivalent to a volume fraction of 0.35 for MeOH, EtOH, and *i*-PrOH ($V_{MeOH}$, $V_{EtOH}$ and $V_{i\text{-PrOH}}$ ), or 0.37 for *n*-BuOH ($V_{n\text{-BuOH}}$). With these values, the micropore filling of ZIF-8 particles is 81% for MeOH, EtOH, or *i*-PrOH, or 86% for *n*-BuOH. Using Equation 4, but substituting the water molecules with the corresponding alcohol molecules, the effective refractive indexes of the photonic crystal upon exposure to each alcohol is calculated to be: 1.51 for MeOH; 1.52 for EtOH; 1.53 for *i*-PrOH; and 1.54 for *n*-BuOH. The expected band gaps can then be calculated using the Bragg-Snell law. The obtained values are 556 nm for MeOH, 559 nm for EtOH, 561 nm for *i*-PrOH, and 567 nm for *n*-BuOH. These results and the experimental ones are summarised together in Table S1.

**Supplementary Table 1: Experimental and calculated refractive indices and band gaps of the as-made photonic crystal (particle size: 210 ± 10 nm) before evacuation and subsequent exposure to different alcohols.**

| Guest molecule | Refractive index of guest molecule $n_{guest}$ | Pore filling of the guest molecule (%) | Experimental refractive index $n_{exp}$ [§] | Calculated refractive index $n_{cal}$ * | Experimental band gap $\lambda_c$ [††] (nm) | Calculated band gap $\lambda_c$ ** (nm) |
|---|---|---|---|---|---|---|
| Water | 1.33 | 49 [†] | 1.49 | 1.47 | 552 | 543 |
| Methanol | 1.33[4] | 81 [‡] | 1.52 | 1.51 | 561 | 556 |
| Ethanol | 1.36[4] | 81 [‡] | 1.53 | 1.52 | 562 | 559 |
| isopropanol | 1.38[4] | 81 [‡] | 1.53 | 1.53 | 564 | 561 |
| *n*-Butanol | 1.40[4] | 86 [‡] | 1.54 | 1.54 | 568 | 567 |

[†] Measured from TGA

[‡] Measured from sorption isotherms

[§] Measured from the slope of the interplanar distance vs. the experimental band-gap plot

* Calculated using the equation $n_{eff} = \sqrt{V_{fram}n_{fram}^2 + V_{guest}n_{guest}^2 + V_{air}n_{air}^2}$.

[††] Measured from UV-Visible reflectance spectra

** Calculated using the Bragg-Snell law

## References


1. Ciddor, P. E. Refractive index of air: new equations for the visible and near infrared. *Appl. Opt.* **35,** 1566–1573 (1996).
2. Radhakrishnan, D. & Narayana, Effect of pore occupancy on the acoustic properties of zeolitic imidazolate framework (ZIF)-8: A Brillouin spectroscopic study at ambient and low temperatures. *J. Chem. Phys.* **143,** 234703 (2015).
3. Hale, G. M. & Querry, M. R. Optical constants of water in the 200-nm to 200-µm wavelength region. *Appl. Opt.* **12,** 555–563 (1973).
4. O'Brien, R. N. & Quon, D. Refractive index of some alcohols and saturated hydrocarbons at 6328 A. *J. Chem. Eng. Data* **13,** 517 (1968).

# CHAPTER 6

# Conclusions

# CONCLUSIONS

The main goal of this Thesis was to emphasize the importance of the morphology control on the MOF materials at the nano-scales. Our work showed that, apart from the classical aspects of MOFs that are related to the bulk properties, controlling the morphology, especially at the nano-scale, is another tool yet embryonic to be developed. Here, we showed with three examples that the morphology and the architecture of the MOF particles can be –controllably-manipulated (nano-engineered) by making use of the anistropic nature of the MOF crystals.

Three approaches have been adopted in order to do this nano-engineering in our prototypical MOF, ZIF-8.

The first approach mainly constituted of post-synthetic top-down etching of MOF crystals, which was explained in the first publication entitled "Post-Synthetic Anisotropic Wet-Chemical Etching of Colloidal Sodalite ZIF Crystals" in Chapter 3. In this work we demonstrated the anisotropic etching of ZIF-8 and ZIF-67 crystals. Xylenol Orange (XO) played a key role in the etching process as a chelating agent.

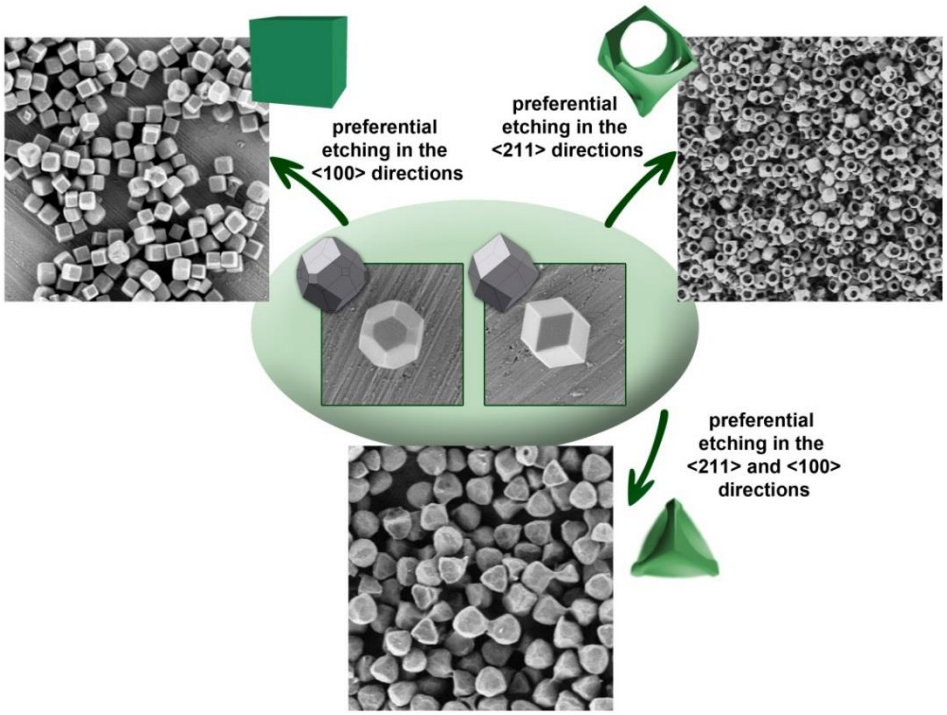

The etchant, which was an acidified or basified XO solution, served to sequentially protonate the imidazolate linkers, broke the coordination bonds, and sequestered the liberated metal ions by forming soluble complexes. We confirmed that etching was surface-selective and preferentially favored the metal–ligand bond-rich crystallographic directions and those crystal surfaces of higher dimensionalities. The progression of the etching of the ZIF crystals depended on different parameters including the pH of the etchant solution and the morphology of the initial crystals. We were able to tune the etching (and consequently, the etched morphologies) by simply adjusting the pH of the etchant solution, demonstrating that different uniform crystal morphologies including cubes, tetrahedra and hollow boxes can be obtained from the same initial crystal. Among the obtained shapes, tetrahedra and hollow boxes were new. It might be expected that the heavy chemical treatment in the etching process would affect the adsorption capabilities of the resulting etched ZIF-8/ZIF-67 crystal morphologies, but we observe neither an amorphization nor a loss in porosity. We consider this top-down shaping of MOFs/ZIFs using anisotropy of the facets of the MOF crystal to be a promising method for better understanding their crystallization, and for the post-synthetic, top-down production of these materials in unprecedented shapes that would be inaccessible through conventional chemistry.

The second approach for designing nano-engineered MOF materials was the post-synthetic bottom-up growing explained in the second publication entitled ”Sequential Deconstruction−Reconstruction of Metal−Organic Frameworks: An Alternative Strategy for Synthesizing (Multi)-Layered ZIF Composites” in Chapter 4.

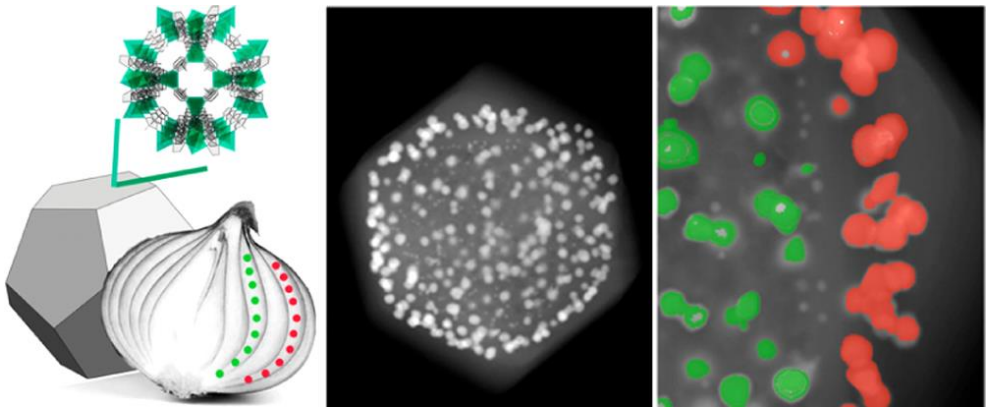

In this work, we demonstrated that ZIF-8/ZIF-67 particles, which have been etched according to the previous procedures explained in the publication in Chapter 3, could be fully reconstructed to their initial shapes. Exposing the etched particles to a ZIF precursor solution enabled their reversible construction to tRD or RD morphologies. The precursor concentration and regrowth time were critical variables for optimizing the final shape (tRD or RD) of the reconstructed particles. In all of our growth cases, the growth rate was higher than the nucleation rate. This enabled a proper growing without the formation of secondary ZIF particles. Moreover, given enough time, we have demonstrated that even hollow microboxes can be recovered to a final RD shape by filling the inner space of the box with ZIF-8. This reversibility also enabled the synthesis of novel ZIF-on-ZIF and layered ZIF-on-INP-on-ZIF composites. Remarkably, the reconstruction step may also be accompanied with a step for attaching PVP-capped INPs onto the ZIF particle surface. This attachment, coupled with the ZIF-on-ZIF growth, affords layered ZIF-on-INP-on-ZIF composites. Furthermore, this latter process can be repeated to construct (multi)-layered composites composed of several types of INPs. In these composites, the different INPs are well separated by a nanometric layer of ZIF-8 that can be as small as 20 nm. These composites offer potential for diverse practical domains, such as catalysis, among other applications. Preliminary results obtained for a model cascade reaction paves the way to an improved design of new catalytic protocols for cascade reactions.

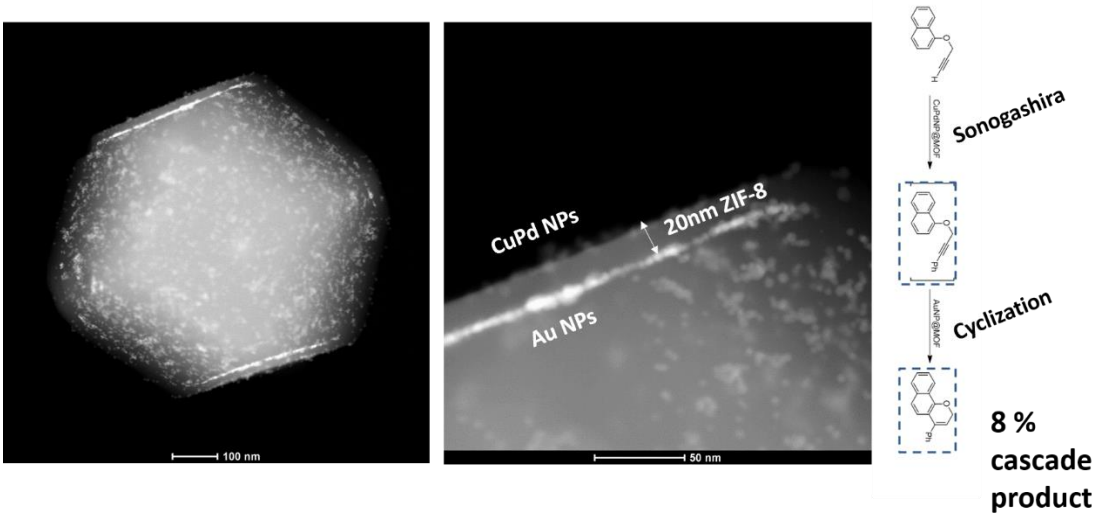

The third approach that is based on in-situ modulation and self-assembly of particles has been employed in the publication entitled “Self-Assembly of Polyhedral Metal–Organic Framework Particles into Three-Dimensional Ordered Superstructures” in Chapter 5.

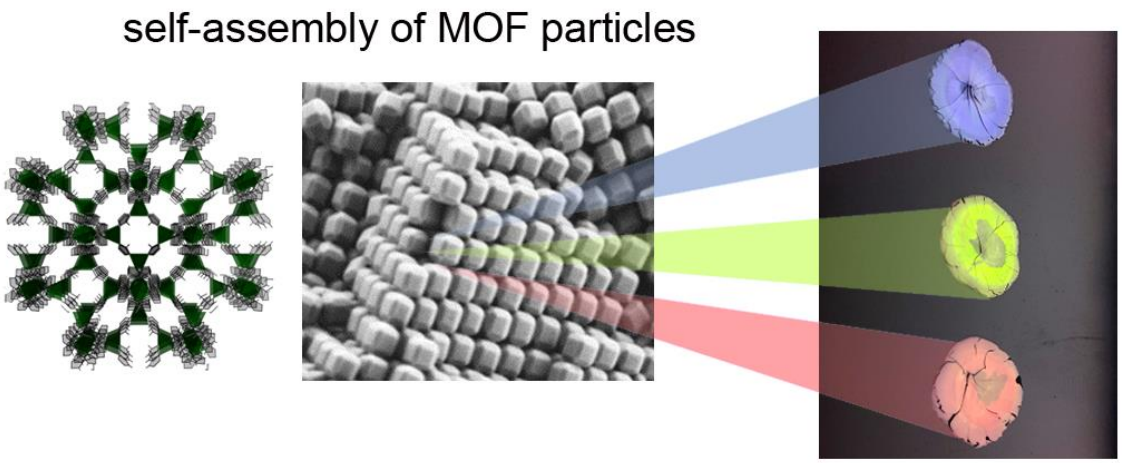


Here we demonstrated that ZIF-8 particles can be produced with very high monodispersity (PD <5 %) with precise shapes using CTAB that serves as size and shape modulators. The in-situ modulation of the size and shape of the MOF particles was achieved by the anisotropic interest of the CTAB molecules to the facetet polyhedral MOF crystals, specifically, through their selective attachment to the {100} facets, hindering the growth in <100> directions. Different shapes of MOF particles could be obtained by varying the surfactant concentration and the Zn:2-mim ratio. Monodisperse ZIF-8 particles with different truncations (*t*) (where *t* is 0.00, 0.38, 0.57, 0.62, 0.69 and 1.00) were obtained. Interestingly, these uni-shaped colloidal particles self-assembled into ordered superstructures with a fast evaporation method. Based on the truncation of the ZIF-8 particles, the final ordered superstructure adopted the fcc or rhombohedral superlattice in order to reach the corresponding densest packing.

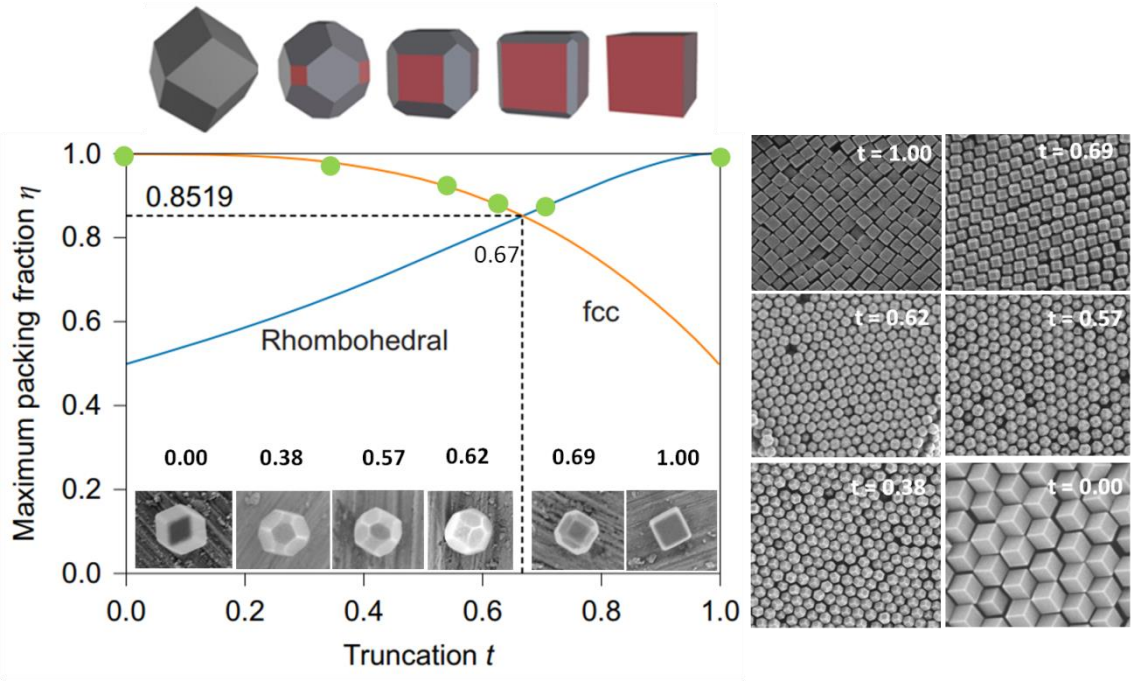


The obtained monoliths also served as 3D photonic crystals with a bright visible color when the particle size was selected appropriately. In contrast to the previously reported methods that are mainly based on particle sedimentation, the fast evaporation method enables the formation of opalline structures in very short times, which is expressed only in few minutes. Here, upon putting the droplet on the substrate in the oven, the particles are forced to move towards the surface of the droplet to form densely packed structures. The presence of CTAB on the droplet surface enhances the mobility and helps the re-organization of the particles. Then, the evaporation of the droplet leaves behind an ordered structure that was already formed in the colloidal state. The observation of the opalline colors on the droplet surface while the evaporation did not start is evidence to these explanations.

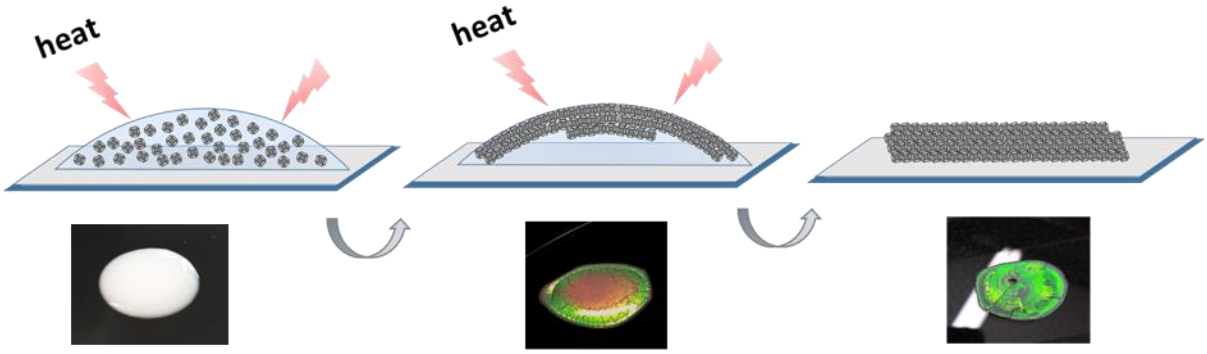

The study showed in Chapter 5 has a lot of novelty in terms of nano-engineering of MOF particles. We were able to demonstrate that highly monodisperse MOF particles with different sizes that are only ~15 nm different from each other can be produced. The self-assembled superstructures were one of the first examples to a 3D self-assembly of nonspherical particles that exhibit photonic properties. These ZIF-8 monolithic photonic crystals can serve as an alcohol sensor and exhibit water selectivity due to the intrinsic porous nature of ZIF-8. We believe we demonstrated a nice example to the exploitation of new properties of MOFs by bridging the classical aspects (porosity, selective adsorption) with nano-engineneering (crystal size and shape design and self-assembly of ordered superstructures).

To conclude, MOFs are naturally anisotropic materials and there is plenty of engineering in the anisotropy.